

Progress in Theoretical Chemistry and Physics A 29

Series Editors: J. Maruani · S. Wilson

M.A.C. Nascimento

Jean Maruani

Erkki J. Brändas

Gerardo Delgado-Barrio *Editors*

Frontiers in Quantum Methods and Applications in Chemistry and Physics

Selected Proceedings of QSCP-XVIII
(Paraty, Brazil, December, 2013)



Springer

Frontiers in Quantum Methods and Applications in Chemistry and Physics

Progress in Theoretical Chemistry and Physics

VOLUME 29

Honorary Editors

Sir Harold W. Kroto (*Florida State University, Tallahassee, FL, USA*)

Prof. Yves Chauvin (*Institut Français du Pétrole, Tours, France*)

Editors-in-Chief

J. Maruani (*formerly Laboratoire de Chimie Physique, Paris, France*)

S. Wilson (*formerly Rutherford Appleton Laboratory, Oxford, UK*)

Editorial Board

E. Brändas (*University of Uppsala, Uppsala, Sweden*)

L. Cederbaum (*Physikalisch-Chemisches Institut, Heidelberg, Germany*)

G. Delgado-Barrio (*Instituto de Matemáticas y Física Fundamental, Madrid, Spain*)

E.K.U. Gross (*Freie Universität, Berlin, Germany*)

K. Hirao (*University of Tokyo, Tokyo, Japan*)

E. Kryachko (*Bogolyubov Institute for Theoretical Physics, Kiev, Ukraine*)

R. Lefebvre (*Université Pierre-et-Marie-Curie, Paris, France*)

R. Levine (*Hebrew University of Jerusalem, Jerusalem, Israel*)

K. Lindenberg (*University of California at San Diego, San Diego, CA, USA*)

A. Lund (*University of Linköping, Linköping, Sweden*)

R. McWeeny (*Università di Pisa, Pisa, Italy*)

M.A.C. Nascimento (*Instituto de Química, Rio de Janeiro, Brazil*)

P. Piecuch (*Michigan State University, East Lansing, MI, USA*)

M. Quack (*ETH Zürich, Zürich, Switzerland*)

S.D. Schwartz (*Yeshiva University, Bronx, NY, USA*)

A. Wang (*University of British Columbia, Vancouver, BC, Canada*)

Former Editors and Editorial Board Members

I. Prigogine (†)

W.F. van Gunsteren (*)

J. Rychlewski (†)

H. Hubač (*)

Y.G. Smeyers (†)

M.P. Levy (*)

R. Daudel (†)

G.L. Malli (*)

M. Mateev (†)

P.G. Mezey (*)

W.N. Lipscomb (†)

N. Rahman (*)

H. Ågren (*)

S. Suhai (*)

V. Aquilanti (*)

O. Tapia (*)

D. Avnir (*)

P.R. Taylor (*)

J. Cioslowski (*)

R.G. Woolley (*)

†: deceased; *: end of term

More information about this series at <http://www.springer.com/series/6464>

M.A.C. Nascimento · Jean Maruani
Erkki J. Brändas · Gerardo Delgado-Barrio
Editors

Frontiers in Quantum Methods and Applications in Chemistry and Physics

Selected Proceedings of QSCP-XVIII
(Paraty, Brazil, December, 2013)



Springer

Editors

M.A.C. Nascimento

Department of Physical Chemistry
Federal University of Rio de Janeiro
Rio de Janeiro
Brazil

Erkki J. Brändas

Department of Quantum Chemistry
Uppsala University
Uppsala
Sweden

Jean Maruani

Laboratoire de Chimie Physique
CNRS & UPMC
Paris
France

Gerardo Delgado-Barrio

Instituto de Fisica Fundamental, CSIC
Madrid
Spain

ISSN 1567-7354

ISSN 2215-0129 (electronic)

Progress in Theoretical Chemistry and Physics

ISBN 978-3-319-14396-5

ISBN 978-3-319-14397-2 (eBook)

DOI 10.1007/978-3-319-14397-2

Library of Congress Control Number: 2015931807

Springer Cham Heidelberg New York Dordrecht London

© Springer International Publishing Switzerland 2015

This work is subject to copyright. All rights are reserved by the Publisher, whether the whole or part of the material is concerned, specifically the rights of translation, reprinting, reuse of illustrations, recitation, broadcasting, reproduction on microfilms or in any other physical way, and transmission or information storage and retrieval, electronic adaptation, computer software, or by similar or dissimilar methodology now known or hereafter developed.

The use of general descriptive names, registered names, trademarks, service marks, etc. in this publication does not imply, even in the absence of a specific statement, that such names are exempt from the relevant protective laws and regulations and therefore free for general use.

The publisher, the authors and the editors are safe to assume that the advice and information in this book are believed to be true and accurate at the date of publication. Neither the publisher nor the authors or the editors give a warranty, express or implied, with respect to the material contained herein or for any errors or omissions that may have been made.

Printed on acid-free paper

Springer International Publishing AG Switzerland is part of Springer Science+Business Media
(www.springer.com)

PTCP Aim and Scope

Progress in Theoretical Chemistry and Physics

A series reporting advances in theoretical molecular and material sciences, including theoretical, mathematical and computational chemistry, physical chemistry and chemical physics and biophysics.

Aim and Scope

Science progresses by a symbiotic interaction between theory and experiment: theory is used to interpret experimental results and may suggest new experiments; experiment helps to test theoretical predictions and may lead to improved theories. Theoretical Chemistry (including Physical Chemistry and Chemical Physics) provides the conceptual and technical background and apparatus for the rationalization of phenomena in the chemical sciences. It is, therefore, a wide ranging subject, reflecting the diversity of molecular and related species and processes arising in chemical systems. The book series *Progress in Theoretical Chemistry and Physics* aims to report advances in methods and applications in this extended domain. It will comprise monographs as well as collections of papers on particular themes, which may arise from proceedings of symposia or invited papers on specific topics as well as from initiatives from authors or translations.

The basic theories of physics—classical mechanics and electromagnetism, relativity theory, quantum mechanics, statistical mechanics, quantum electrodynamics—support the theoretical apparatus which is used in molecular sciences. Quantum mechanics plays a particular role in theoretical chemistry, providing the basis for the valence theories, which allow to interpret the structure of molecules, and for the spectroscopic models, employed in the determination of structural information from spectral patterns. Indeed, Quantum Chemistry often appears synonymous with Theoretical Chemistry; it will, therefore, constitute a major part of this book series. However, the scope of the series will also include other areas of theoretical chemistry, such as mathematical chemistry (which involves the use of algebra and

topology in the analysis of molecular structures and reactions); molecular mechanics, molecular dynamics, and chemical thermodynamics, which play an important role in rationalizing the geometric and electronic structures of molecular assemblies and polymers, clusters, and crystals; surface, interface, solvent, and solid state effects; excited-state dynamics, reactive collisions, and chemical reactions.

Recent decades have seen the emergence of a novel approach to scientific research, based on the exploitation of fast electronic digital computers. Computation provides a method of investigation which transcends the traditional division between theory and experiment. Computer-assisted simulation and design may afford a solution to complex problems which would otherwise be intractable to theoretical analysis, and may also provide a viable alternative to difficult or costly laboratory experiments. Though stemming from Theoretical Chemistry, Computational Chemistry is a field of research in its own right, which can help to test theoretical predictions and may also suggest improved theories.

The field of theoretical molecular sciences ranges from fundamental physical questions relevant to the molecular concept, through the statics and dynamics of isolated molecules, aggregates and materials, molecular properties and interactions, to the role of molecules in the biological sciences. Therefore, it involves the physical basis for geometric and electronic structure, states of aggregation, physical and chemical transformations, thermodynamic and kinetic properties, as well as unusual properties such as extreme flexibility or strong relativistic or quantum-field effects, extreme conditions such as intense radiation fields or interaction with the continuum, and the specificity of biochemical reactions.

Theoretical Chemistry has an applied branch (a part of molecular engineering), which involves the investigation of structure-property relationships aiming at the design, synthesis and application of molecules and materials endowed with specific functions, now in demand in such areas as molecular electronics, drug design or genetic engineering. Relevant properties include conductivity (normal, semi- and super-), magnetism (ferro- and ferri-), optoelectronic effects (involving nonlinear response), photochromism and photoreactivity, radiation and thermal resistance, molecular recognition and information processing, biological and pharmaceutical activities, as well as properties favouring self-assembling mechanisms and combination properties needed in multifunctional systems.

Progress in Theoretical Chemistry and Physics is made at different rates in these various research fields. The aim of this book series is to provide timely and in-depth coverage of selected topics and broad-ranging yet detailed analysis of contemporary theories and their applications. The series will be of primary interest to those whose research is directly concerned with the development and application of theoretical approaches in the chemical sciences. It will provide up-to-date reports on theoretical methods for the chemist, thermodynamician or spectroscopist, the atomic, molecular or cluster physicist, and the biochemist or molecular biologist who wish to employ techniques developed in theoretical, mathematical and computational chemistry in their research programs. It is also intended to provide the graduate student with a readily accessible documentation on various branches of theoretical chemistry, physical chemistry, and chemical physics.

Preface

This volume collects 15 selected papers from the scientific contributions presented at the Eighteenth International Workshop on Quantum Systems in Chemistry, Physics, and Biology (QSCP-XVIII), which was organized by Prof. M.A.C. Nascimento at the *Casa da Cultura* in Paraty (Rio de Janeiro), Brazil, from December 1 to 7, 2013. Over 100 scientists from 25 countries attended this meeting. Participants of the QSCP-XVIII workshop discussed the state of the art, new trends, and future evolution of methods in molecular quantum mechanics, and their applications to a wide variety of problems in chemistry, physics, and biology.

The high-level attendance attained in this conference was particularly gratifying. It is the renowned interdisciplinary nature and friendly feeling of QSCP meetings that make them such successful discussion forums.

Paraty is located on the south coast of Brazil, 250 km from Rio de Janeiro, the state capital. This historical town, nestled on the *Costa Verde*, is a living memory of the Gold Cycle: gold extracted from the mines of the state of Minas Gerais was transported by mule along the Estrada Real down to Paraty and from there shipped to Rio de Janeiro. The area of Paraty is probably the only place on the planet that brings together a native forest about 80 % preserved, a bay protected from the open sea by over a hundred islands, and a seventeenth-century town which is regarded by UNESCO as the most harmonious baroque location in the world. From this past originate the relics and traditions that so enchant the visitors: a wonderful wealth of cultural and ecological attractions, as well as a tourist infrastructure consisting of cosy inns and picturesque restaurants.

Details of the Paraty meeting, including the scientific program, can be found on the web site: <http://www.qscp2013.iq.ufrj.br>. Altogether, there were 18 morning and afternoon sessions, where 55 plenary talks were given, and two evening poster sessions, with 18 flash presentations for a total of 38 displayed posters. We are grateful to all participants for making the QSCP-XVIII workshop a stimulating experience and a great success. QSCP-XVIII followed the traditions established at previous workshops:

QSCP-I, organized by Roy McWeeny in 1996 at San Miniato (Pisa, Italy);
QSCP-II, by Stephen Wilson in 1997 at Oxford (England);
QSCP-III, by Alfonso Hernandez-Laguna in 1998 at Granada (Spain);
QSCP-IV, by Jean Maruani in 1999 at Marly-le-Roi (Paris, France);
QSCP-V, by Erkki Brändas in 2000 at Uppsala (Sweden);
QSCP-VI, by Alia Tadjer in 2001 at Sofia (Bulgaria);
QSCP-VII, by Ivan Hubac in 2002 near Bratislava (Slovakia);
QSCP-VIII, by Aristides Mavridis in 2003 at Spetses (Athens, Greece);
QSCP-IX, by Jean-Pierre Julien in 2004 at Les Houches (Grenoble, France);
QSCP-X, by Souad Lahmar in 2005 at Carthage (Tunisia);
QSCP-XI, by Oleg Vasyutinskii in 2006 at Pushkin (St Petersburg, Russia);
QSCP-XII, by Stephen Wilson in 2007 near Windsor (London, England);
QSCP-XIII, by Piotr Piecuch in 2008 at East Lansing (Michigan, USA);
QSCP-XIV, by Gerardo Delgado-Barrio in 2009 at El Escorial (Madrid, Spain);
QSCP-XV, by Philip Hoggan in 2010 at Cambridge (England);
QSCP-XVI, by Kiyoshi Nishikawa in 2011 at Kanazawa (Japan);
QSCP-XVII, by Matti Hotokka in 2012 at Turku (Finland).

The lectures presented at QSCP-XVIII were grouped into nine areas in the field of *Quantum Systems in Chemistry, Physics, and Biology*, ranging from Concepts and Methods in Quantum Chemistry and Physics through Molecular Structure and Dynamics, Reactive Collisions and Chemical Reactions, to Computational Chemistry, Physics, and Biology.

The width and depth of the topics discussed at QSCP-XVIII are reflected in the contents of this volume of proceedings in the book series *Progress in Theoretical Chemistry and Physics*, which includes four sections:

- I. Quantum Methodology (3 papers);
- II. Structure and Properties (4 papers);
- III. Molecular Dynamics (4 papers);
- IV. Fundamental Theory (3 papers).

In addition to the scientific program, the workshop had its usual share of cultural events. There was a boat cruise in the Paraty bay and a show by the internationally known group *Contador de Estórias*. The award ceremony of the CMOA Prize and Medal took place during the congress banquet in the most traditional restaurant of Paraty, *Margarida Café*.

The CMOA Prize was shared between two selected nominees: Jer-Lai Kuo and Yuan-Chung Cheng, both from Taiwan. Two other nominees, Jhih-Wei Chu (from Taiwan) and Andriy Loboda (from Ukraine) received a certificate of nomination and a gift. The prestigious CMOA Medal for senior scientists was awarded to Prof. Lorentz Cederbaum (University of Heidelberg, Germany). According to a custom of QSCP meetings, the venue of the next yearly workshop was announced to be in Odessa, Ukraine, in 2015, followed by one in Taipei, Taiwan, in 2016. However, due to the political events, the dates of the two meetings were later reversed.

We are pleased to acknowledge the generous support given to the QSCP-XVIII conference by *Coordenação de Aperfeiçoamento de Pessoal de Nível Superior* (CAPES), the City of Paraty Convention Bureau and *Casa da Cultura* of Paraty. We are most grateful to all members of the Local Organizing Committee for their work and dedication, which made the stay and work of participants both pleasant and fruitful. We also thank the members of the International Scientific Committee and the Honorary Committee for their invaluable expertise and advice.

We hope the readers will find as much interest in consulting these proceedings as the participants in attending the meeting.

M.A.C. Nascimento
Jean Maruani
Erkki J. Brändas
Gerardo Delgado-Barrio

Contents

Part I Quantum Methodology

The Importance of Orbital Analysis	3
Rebecca Weber, George Schoendorff and Angela K. Wilson	
1 Introduction	3
2 Computational Methods	7
3 Results and Discussion	8
3.1 Main Group Diatomics	9
3.2 S-Block Diatomics	12
3.3 Transition Metal Diatomics	14
4 Conclusion	26
References	27
A General Geometric Representation of Sphere-Sphere	
Interactions	29
Ho-Kei Chan, Eric B. Lindgren, Anthony J. Stace	
and Elena Bichoutskaia	
1 Introduction	29
2 Introduction to the Bispherical Coordinate System	31
3 Derivation of the Scaled Surface-to-Surface Separation	32
4 Graphical Representation of the Scaled Surface-to-Surface	
Separation	35
5 Conclusions	36
References	36
Understanding the Electronic Structure Properties of Bare	
Silver Clusters as Models for Plasmonic Excitation	37
Lindsey R. Madison, Mark A. Ratner and George C. Schatz	
1 Introduction	38
2 Methods	40

2.1	RT-TDDFT	40
2.2	FD-TDDFT	42
3	Results and Discussion	43
3.1	Comparison of RT-TDDFT and FD-TDDFT	43
4	Insights into Hot Electron Properties	48
5	Conclusions	50
	References	51

Part II Structure and Properties

Optimized Perturbation Theory for Calculating the Hyperfine Line Shift and Broadening of Heavy Atoms in a Buffer Gas	55	
Olga Yu. Khetselius		
1	Introduction	55
2	Optimized Atomic Perturbation Theory and Advanced Kinetic Theory of Spectral Lines	58
3	Relativistic Many-Body Perturbation Theory with the Kohn-Sham Zeroth Approximation and the Dirac-Sturm Method	62
3.1	Relativistic Many-Body Perturbation Theory with the Kohn-Sham Zeroth Approximation	62
3.2	The Dirac-Sturm Approach	65
4	Shift and Broadening of Hyperfine Spectral Lines for Multielectron Atoms in an Atmosphere of a Buffer Gas	67
4.1	Shift and Broadening of the Thallium and Ytterbium Hyperfine Lines in an Atmosphere of the Inert Gas	67
4.2	Shift and Broadening of the Alkali Atom Hyperfine Lines in an Atmosphere of the Inert Gas	71
5	Conclusion	73
	References	74
Proton Quantum Confinement on Symmetric Dimers of Ammonia and Lower Amine Homologs	77	
Jake A. Tan, Jheng-Wei Li and Jer-Lai Kuo		
1	Introduction	77
2	Calculation Methods	79
2.1	Density Functional Methods	80
2.2	Ab Initio Path Integral Molecular Dynamics (PIMD)	81
2.3	Vibrational Hamiltonian at Reduced Dimensions	83
3	Results and Discussion	84
3.1	An Intuitive Trend Based on a Static Picture	84

3.2 A Counter Intuitive Trend Arose from Quantum Nature	86
3.3 Possible Experimental Observables	87
4 Conclusion	88
References	89
 Ab-Initio and DFT Study of the Muchimangin-B Molecule	 91
Liliana Mammino, Mireille K. Bilonda and Tendamudzimu Tshiwawa	
1 Introduction	92
2 Computational Details	92
3 Results	95
3.1 Results in Vacuo	95
3.2 Results in Solution	107
3.3 Adducts with Explicit Water Molecules	110
4 Discussion and Conclusions	113
References	113
 Molecular Dynamics Analysis of FAAH Complexed with Anandamide	 115
Sérgio F. Sousa, João T.S. Coimbra, Pedro A. Fernandes, Tiziana Marino, Maria J. Ramos and Nino Russo	
1 Introduction	116
2 Methodology	117
3 Results and Discussion	118
3.1 Root Mean Square Deviation (RMSD) Analysis	119
3.2 Root Mean Square Fluctuation (RMSF) Analysis	119
3.3 SASA Analysis	121
4 Conclusions	126
References	127
 Part III Molecular Dynamics	
 Intense Field Molecular Photodissociation: The Adiabatic Views	 135
R. Lefebvre	
1 Introduction	135
2 The Time-Dependent Wave-Equation	136
3 The Instantaneous Solutions	137
4 The Quasi-Adiabatic Solutions	139
5 The Solution of the Time-Dependent Schrödinger Equation	144
6 Conclusion	145
References	145

Photoionization Spectra and Ionization Potentials of Energetic Molecules	147
Itamar Borges Jr. and Elmar Uhl	
1 Introduction	147
2 Methods	149
3 Results and Discussion	151
3.1 Nitromethane	151
3.2 The Photoionization Spectra of the Four Molecules	154
4 Conclusion	156
References	156
Theoretical Study of Coherent π-Electron Rotations in a Nonplanar Chiral Aromatic Molecule Induced by Ultrafast Linearly Polarized UV Pulses	159
H. Mineo and Y. Fujimura	
1 Introduction	160
2 Coherent π -Electron Angular Momentum and Current	161
2.1 Equations of Motion for π -Electrons in a Pulsed Laser Field	161
2.2 Coherent Electric Angular Momentum and Current for a Chiral Aromatic Molecule with Two Aromatic Rings	162
3 Results and Discussion	165
3.1 Geometry and Excited States of (P)-2,2'-Biphenol	165
3.2 Creation of Coherent Two Electronic Excited States by the Linearly Polarized UV Laser Pulses	166
3.3 Four Initial Directional Patterns of Ring Currents and Angular Momentum	167
3.4 Time Evolution of Coherent Ring Currents	167
3.5 Time Dependent Angular Momentum for Three Types of Electron Coherence	170
3.6 Design of Ultrafast Multi-dimensional Quantum Switching	170
3.7 Coherent π -Electron Rotations in Aromatic Chain Molecules	172
4 Summary and Conclusion	174
References	175
Full Quantum Calculations of the Diffusion Rate of Adsorbates	177
Thiago Firmino, Roberto Marquardt, Fabien Gatti, David Zanuttini and Wei Dong	
1 Introduction	177
2 Theory and Methods	179
2.1 Dynamical Structure Factor	179
2.2 Models	180

2.3	Quantum Dynamics	181
3	Results	183
3.1	CO/Cu(100) System	183
3.2	H/Pd(111) System	189
4	Conclusions	191
	References	192

Part IV Fundamental Theory

Relativistic Quantum Chemistry: An Advanced Approach to the Construction of the Green Function of the Dirac Equation with Complex Energy and Mean-Field Nuclear Potential 197

A.V. Glushkov, A.A. Svinarenko, O.Yu. Khetselius, V.V. Buyadzhi,
T.A. Florko and A.N. Shakhman

1	Introduction	198
2	Dirac Equation with Complex Energy: Fundamental Solutions	201
3	Non-Singular Nuclear Potential of the Dirac Equation: Relativistic Mean-Field and Fermi Models	203
4	Construction of the Optimal One-Quasi-Electron Representation	207
5	Procedure for Determination of the Second Fundamental Solution of the Dirac Equation and Anti-Wronscian	209
6	General Scheme of Calculation for a Three-Electron System	211
7	Calculation Results for Self-Energy Shifts to Atomic Level Energies: Li-like Ions	212
	References	214

Spacetime-Based Foundation of Quantum Mechanics and General Relativity 219

John A. Macken

1	Introduction	219
2	Zero Point Energy and the Spacetime Field	220
3	Spacetime Model of a Fundamental Particle	225
4	Testing of the Particle Model	226
4.1	Energy and Angular Momentum Test	226
4.2	Curved Spacetime Test	227
4.3	Gravitational and Electrostatic Force Test	230
4.4	Unification of Forces	231
4.5	Point Particle Test	235
4.6	Inertia Test	237

5	Charge, Electric Fields and Black Holes	238
6	Summary and Conclusion	243
	References	244
A Zero Energy Universe Scenario: From Unstable Chemical States to Biological Evolution and Cosmological Order		247
Erkki J. Brändas		
1	Introduction	247
2	Conjugate Variables and Einstein's Law of Special Relativity	250
3	Einstein's Laws of General Relativity and the Schwarzschild Gauge	252
4	Gödel's Theorem and the Law of Self-Reference	254
5	Non-Hermitian Quantum Mechanics	259
6	Statistical Mechanics far from Equilibrium—Off-Diagonal Long-Range Order	261
7	The Liouville Equation and the Prigogine Energy Operator	264
8	Free Energy Configurations and the Correlated Dissipative Ensemble, CDE	267
9	The CDE as a Spatio-Temporal Mnemonic Configuration, STEM	270
10	The Poisson Distribution and its Implication for STEM	273
11	Memory and Communication on Channel SELF	275
12	Conclusion	278
	References	282
Index		285

Obituary

Osvaldo Goscinski (1938–2013)

Osvaldo Goscinski, retired professor of Quantum Chemistry at Uppsala University, died on October 30, 2013, the day after his 75th birthday.

Osvaldo Goscinski grew up in Peron's Argentina and received a classical education at the prestigious Colegio Nacional de Buenos Aires, a special gymnasium organized in collaboration with Universidad de Buenos Aires, which taught several generations of famous authors, artists, scientists, and politicians.

With his first PhD. in Chemistry from the University of Florida, he arrived in Uppsala in 1966, where he continued his graduate studies to a Swedish Fil. Dr. in 1970. In 1982 he became Per-Olov Löwdin's successor on the chair in Quantum Chemistry at Uppsala University. In addition to prominent international positions like editorships, organizer of international meetings, collaborations and distinctions, e.g., the Prize of the International Academy of Quantum Molecular Science in 1980, he served at important national duties as being a vice chairman of the Swedish National Science Research Council and presiding over its program committee for Physics.

Osvaldo Goscinski's main contribution to science was the development of sophisticated quantum chemical methods and their application to contemporary problems in theoretical chemistry. In particular, he was instrumental in extending fundamental theories of his teacher and mentor Per-Olov Löwdin to modern quantum chemistry. One of his objectives has been to increase accuracy and precision in analyzing the properties of various quantum chemical systems via model independent investigations and analysis. His renowned recognition as an accomplished expert on propagator and perturbation theory led him to achieve unique results in, e.g., the determination of van der Waals forces, excitation and ionization energies, lifetimes, etc. His general passion for an erudite understanding of nature

led him to find pathways to fundamental problems like symmetry violations in nature, limitation aspects of information theory and to voice the challenges of the density matrix N-representability conundrum.

With his double competence in chemistry and physics, including considerable interests in mathematics, philosophy, and the humanities, Osvaldo Goscinski was particularly well suited to lead a cross-scientific institute like the department of quantum chemistry. As an avid and devoted spokesman for his field he “let thousand flowers bloom,” as exemplified by the numerous multifaceted research projects that flourished under the parasol of quantum chemistry, from the chemistry of free radicals, surface science, dissipative systems, information theory, complex antimatter, and quantum computers. He also fought successfully for an additional professorship in applied quantum chemistry at the department. He was a very inspiring teacher, he enjoyed lecturing, and he was heavily engaged in research education as established during his term as associate dean of the Faculty of Science and Technology.

For most of us, working with him as a teacher and scientist, the acquaintance and association with Osvaldo led to important consequences in more than one way. He represented the gateway to science. His playfulness and creativity inspired original questions and nontrivial scientific contributions. Finally, when we tried to stand on our own legs, it turned out that he did not always buy our new ideas. Not until later did we understand that critique prompts carefulness and persistence, a necessity for the mental process to continue and never halt.

For us as young doctoral students, pursuing our studies in the late 1960s and beginning of the 1970s, it was a priceless privilege to share the brilliant creativity, flow of ideas, humor, and inventiveness, which always emerged around Osvaldo at seminars, discussions, and coffee breaks. The happy, spirited, and playful joker from Jorge Luis Borges Argentina did spoil us with adventurous anecdotes and puns, combined with refined and subtle argumentation—all from the renaissance reclaim of the classical antiquity to Edda-inspired Old-Norse mythology to Planck, Einstein, Bohr, and Popper.

For us who worked closely with Osvaldo during many years since the 1960s and 1970s, it is impossible to express in a few words what he meant to us. He was always there with his understanding, his personal engagement, his knowledge, not only in delicate scientific interpretations but also in private and difficult problems of a more personal and confidential kind. His amazing courage, not to give in, despite an exceptionally long and severe illness has more than overwhelmed us. This courage combined with his wife Gunilla’s strength to organize and arrange so that Osvaldo with the same sincerity as before, could participate in every gathering and invitation that concerned the department, science and the arts, but also in private parties and celebrations has manifested respect and admiration.

We will miss Osvaldo tremendously. Even when we are trying to understand and realize that life in the end must be completed, nothing can take away and destroy the joy of life and creativity that emerged from Rundelsgränd 2A and 2B, about 50 years ago. In this melting pot of contemporary scientific leaders in quantum chemistry, Osvaldo was a natural central point and visionary.

Behind Osvaldo's humorous and witty style existed an ardent feeling for freedom, justice, and integrity. We all mourn today an honest, courageous, and generous family man, friend, and colleague who always with empathy and resolution shared with us his engagement and unique wisdom of life.

Erkki Brändas
Sten Lunell
Department of Theoretical Chemistry
Uppsala University
Sweden

Obituary

Ricardo de Carvalho Ferreira: A Pioneer of Theoretical Chemistry in Latin America

Ricardo de Carvalho Ferreira was born on January 16, 1928 in the city of Recife, Brazil. He died on July 30, 2013 in this same city. He was a physical chemist who pioneered the fields of theoretical chemistry and biophysics in Brazil. Ricardo showed a strong inclination toward physics and chemistry at an early age. In spite of the reduced number of Brazilian institutions harboring scientific research, Ricardo published his first scientific contribution when he was 19 years old [1]. At 25 years old, he submitted a contribution to *Nature*, which was published in the same volume reporting the discovery of the structure of the DNA by James Watson and Francis Crick [2]. More than 130 peer-reviewed papers and several book chapters followed these first reports. Among them is, what is believed to be the first theoretical chemistry publication fully thought and conducted in Latin America [3]. The post-doctoral years at CALTECH (1959–1960) in contact with Linus Pauling, and Norman Davidson allowed Ricardo to expand his interests onto theoretical biophysics and biochemistry. During these years, Ricardo was strongly influenced by the ideas of Michel J.S. Dewar who was then visiting CALTECH. The discussions with Dewar and later with Robert S. Mulliken during a short visit to the University of Chicago led to publications on the principles of electronegativity equalization [4–6].

Ricardo contributed to Brazilian science far beyond his publication record. He helped to shape important scientific societies as the Sociedade Brasileira para o Progresso da Ciéncia (SBPC) and the Sociedade Brasileira de Química (SBQ) both of which he presided over upon election. He was part of the commission for the



Fig. 1 Robert Oppenheimer speaks at CBPF in 1961. Ricardo Ferreira is the first one in the first row from *left to right* (Revista O. Cruzeiro, October 7, 1961)

creation of the University of Brasilia and funded the Department of Fundamental Chemistry of the Federal University of Pernambuco, where he remained as Emeritus Professor until his death. Ricardo was associated with several research and teaching institutions in Brazil and abroad: the California Institute of Technology, Indiana University, Columbia University and Earlham College in the United States, l'Université de Genève and the Oxford University in Europe, the Brazilian Center of Physical Research (CBPF) (Fig. 1), Universidade de São Paulo, Universidade Federal de São Carlos and Universidade Federal de Pernambuco in Brazil. He was awarded a number of honors, in special the Grã-Cruz da Ordem Nacional do Mérito Científico from the Brazilian Presidency (1995), Almirante Alvaro Alberto Price from CNPq (1996), Medalha Simão Mathias from the SBQ (1997), Emeritus Researcher of the CBPF (1999) and Emeritus Professor of the Federal Universities of Pernambuco, UFPE (2001) and Alagoas, UFAL (1979). As a last tribute, the asteroid 158520 discovered by the amateur astronomers Paulo Holvoem and Charles Juels was named after him. It is remarkable that among these distinguished honors, the one most cherished by Ricardo was an annual scholarship named after him to support chemistry undergraduate students enrolled at Earlham College, USA. The "Ferreira Scholarship" is funded by a generous donation of a former student tutored by Ricardo many decades ago.

Ricardo had a life-lasting impact on his students and colleagues. He influenced two generations of Brazilian physicists, chemists, and biologists. The eminent Brazilian physicist Constantino Tsallis wrote [7]: *I have met, during my life, only two people to whom I would immediately and heartily reserve the title of natural*

philosopher ... They are Murray Gell-Mann, the Nobel laureate in Physics, and Ricardo Ferreira. Ricardo was all this, and above all a humanist. Brazilian science has lost one of his most inspiring scientists.

Thereza A. Soares
Arnóbio A.S. da Gama
Roberto D. Lins
Gilberto F. de Sá
Oscar L. Malta

Department of Fundamental Chemistry
Federal University of Pernambuco, Recife, PE
50740-560, Brazil

Marco Antonio Chaer do Nascimento
Department of Physical Chemistry
Federal University of Rio de Janeiro, Rio de Janeiro, RJ
21941-909, Brazil

References

1. Ferreira RC (1947) The central angle of the tetrahedron. *J Chem Educ* 24, 246
2. Ferreira RC (1953) Resolution of racemic mixtures by symmetrical agents. *Nature* 171, 39
3. De Giambiagi MS, Giambiagi M, Ferreira RC (1964) Une Approximation pour les Paramètres Semi-Empiriques dans les Molécules Conjuguées. *Journal de Chimie Physique et de Physico-Chimie Biologique* 61, 697–705
4. Ferreira RC (1960) Dipole moment data and hyperconjugation. *Nature* 188, 848
5. Ferreira RC (1963) Principle of electronegativity equalization. Part 1. Bond moments and force constants. *Trans Faraday Soc* 59, 1064–1074
6. Ferreira RC (1963) Principle of electronegativity equalization. Part 2. Bond-dissociation energies. *Trans Faraday Soc* 59, 1075–1079
7. Tsallis C (2008) My friend Ricardo Ferreira, an impressive natural philosopher. *J Braz Chem Soc* 19, 203–205

Part I

Quantum Methodology

The Importance of Orbital Analysis

Rebecca Weber, George Schoendorff and Angela K. Wilson

Abstract It has long been known that there are multiple solutions to the self-consistent Hartree-Fock equations. This can be problematic if careful attention is not given to the orbital occupation and electronic state in the converged wave function. The issues with convergence have been demonstrated through the calculation of potential energy curves for O₂, F₂, Cl₂, Br₂, LiF, NaCl, CaO, MgO, ScO, FeO, TiO, YO, and ZrO. Hartree-Fock (HF) calculations were used to compute the points on the potential energy surface, with dynamic electron correlation included through the use of the completely renormalized coupled cluster, including singles, doubles, and perturbative triples [CR-CC(2,3)]. Even in regions with little to no multireference character, as determined by the T₁/D₁ diagnostics, HF does not always converge to the ground electronic state. As HF provides the reference wave function for CR-CC(2,3), and other post-Hartree-Fock ab initio methods, treatment of electron correlation does not necessarily result in a smooth potential energy curve, especially if HF is unable to produce a smooth curve. Even the convergence rate of multireference methods can be affected as the initial orbitals that form the basis for multireference calculations are frequently obtained from HF calculations.

Keywords Hartree-Fock · Electronic states · Wavefunction · Coupled cluster · Diatomic · Potential energy curve · Ground state · Excited state

1 Introduction

In the early days of computational chemistry, it was routine to check the stability of the optimized Hartree-Fock (HF) wave function. As the field of computational chemistry has grown to include more neophytes utilizing a theoretical approach in

R. Weber · G. Schoendorff · A.K. Wilson (✉)

Department of Chemistry, Center for Advanced Scientific Computing and Modeling (CASCaM), University of North Texas, Denton, TX 76203-5017, USA
e-mail: akwilson@unt.edu

© Springer International Publishing Switzerland 2015

M.A.C. Nascimento et al. (eds.), *Frontiers in Quantum Methods and Applications in Chemistry and Physics*, Progress in Theoretical Chemistry and Physics 29, DOI 10.1007/978-3-319-14397-2_1

the course of research, however, this practice has fallen into disuse. This can be problematic in the prediction of the structural and energetic properties of the systems under investigation, especially when determination of the correct electronic state is essential to achieve results that are even qualitatively correct.

It is known that there is more than one solution to the Hartree-Fock equations [1–3]. In fact, within a finite basis there can be $O(3^N)$ solutions for a closed-shell system, where N is equal to the number of basis functions used [1]. Most HF algorithms populate the initial orbitals based on the *aufbau* principle, wherein the lowest energy orbitals subject to the initial guess of LCAO coefficients are populated to determine the lowest energy solution and thus the ground state of the molecule [4–6]. There are cases, however, when the algorithm can produce an excited state determinant rather than the ground state as has been noted in the literature [3, 7, 8]. Optimization to an excited state can happen when there is a small HOMO-LUMO gap, when there are nearly degenerate determinants, or in other cases where a multireference treatment is more appropriate such as when bonds are broken or formed. Even multireference calculations depend upon single-reference methods as the source of the initial orbitals from which an active space is chosen, and this is often reflected in the rate of convergence of the multireference wave function.

Optimization of an excited state determinant with Hartree-Fock orbitals forms the basis of extended Hartree-Fock theory for excited states [9]. However, it has been shown that in the case of a closed shell system, an electron in a virtual orbital does not experience the full interaction of the $2N$ electrons, and so a modified Fock operator should be employed to obtain a well-defined excited state in terms of a single determinant of Hartree-Fock orbitals. When the excited states are obtained unintentionally through population based on orbital energies, the Fock operator is not modified to account for the missing electronic interactions. Therefore, while the excited states obtained may be representative of the dominant configuration of a multiconfigurational excited state wave function, they do not include the entire mean field correlation.

It is imperative that the optimized Hartree-Fock wave function be scrutinized to ensure that the correct state has been determined. While there are some systems for which optimization to an excited state determinant is not detrimental to geometry optimizations (e.g. situations in which the potential energy curves (PEC) are mostly parallel, such as with Ln(III) -halide bonds), [10] this frequently is not the case. The optimized orbitals need to be investigated to ensure that the appropriate orbitals are being populated, a process that generally can rely on chemical intuition.

A condition of Hartree-Fock convergence is that the orbital gradient is zero, i.e. $\partial E / \partial C_i = 0$. However, as this condition can be met at several places on the orbital potential energy surface, the stability of the solution may need to be tested through the calculation of the orbital Hessian matrix [11]. Negative eigenvalues indicate that there is still a lower energy solution that can be reached; essentially, this indicates that a saddle point in the potential energy surface has been found, rather than a minimum. Such a situation could be remedied in a black-box manner by performing a Hartree-Fock instability test. However, this is only beneficial when the Hartree-Fock solution is a saddle point on the orbital potential energy surface.

Often testing the stability of the wave function based on the orbital Hessian matrix can be unnecessary due to the optimization technique employed. One such situation is when a Newton-Raphson (NR) optimization technique is used. This technique depends on the calculation of both the orbital gradient and orbital Hessian at each step as shown in Eq. 1.

$$C_{i,n+1} = C_{i,n} - \frac{\frac{\partial E}{\partial C_{i,n}}}{\frac{\partial^2 E}{\partial C_{i,n}^2}} \quad (1)$$

The orbital Hessian is used as in the denominator of the second term of Eq. 1, and thus, the NR method ensures that a local minimum on the orbital potential energy surface is located rather than a saddle point. However, the NR method only determines the nearest minimum rather than the global minimum. There exists a basin of attraction that is bounded by saddle points on the orbital potential energy surface. Only the minimum in this region is located and there is no knowledge of any other minima outside the basin of attraction. Each local minimum on the orbital potential energy surface corresponds to a unique single determinant solution of the Hartree-Fock equations, i.e. a unique electronic state. Thus, the NR method guarantees convergence to a local minimum as long as $\partial E / \partial C_i \neq 0$ at the initial guess.

Due to the expense involved in the computation of the full orbital Hessian, other convergence aides such as an approximate NR method or direct inversion of iterative subspace (DIIS) is frequently employed [12]. Approximate NR methods frequently use an exact orbital gradient with an approximate orbital Hessian. Even the approximate orbital Hessian is often sufficient to ensure both convergence and convergence to a minimum, but the minimum will be the nearest minimum in the same basin of attraction. DIIS achieves convergence in an entirely different manner. An error vector is used to determine convergence as shown in Eq. 2.

$$\mathbf{e} = \mathbf{FDS} - \mathbf{SDF} \quad (2)$$

The error vector is constructed from the Fock matrices (\mathbf{F}), density matrices (\mathbf{D}), and overlap matrices (\mathbf{S}) from previous SCF iterations. Convergence is reached when the DIIS error goes to zero. However, the error vector is related to the orbital gradient and not the orbital Hessian. So with DIIS, there may occasionally be a need to test the stability of the Hartree-Fock solution since it converges to the nearest stationary point rather than the nearest minimum on the orbital potential energy surface.

For ease of both convergence and the determination of the correct ground state, a good initial guess of the LCAO coefficients used to construct the molecular orbitals is essential. The initial guess is the only control anyone has over which solution is obtained since this determines the basin of attraction. There are several different options for the initial guess within each commonly available software package. One popular method is the diagonalization of a Fock matrix that contains only the one-electron terms, referred to as the core Hamiltonian matrix. Within this paper, this is

referred to as the H_{core} guess, following the nomenclature in GAMESS [13]. While this initial guess is usually fairly poor, it has the advantage of being implemented in most computational codes [5]. Another common approach is to use the guess generated by a semi-empirical procedure such as Extended Hückel Theory (referred to in this paper as the Hückel guess) and projected onto the current basis. The initial guess provided by Hückel theory is generally superior to that provided by H_{core} , yet can still have difficulty assigning the initial electronic configuration based on the orbital population [13]. Another approach that can be useful, especially when calculating a potential energy curve, is to use the optimized orbitals from a nearby point on the potential energy surface, as is done automatically during a gradient driven geometry optimization.

As Hartree-Fock does not account for electron correlation beyond mean field correlation, a myriad of correlated electron methods have been developed that are based upon a Hartree-Fock reference wave function. Configuration interaction (CI), coupled cluster (CC), and many body perturbation theory are examples of such theories designed to recover electron correlation energy. Full CI calculations do not depend on the quality of the reference wave function, yet full CI with an appropriately large basis set quickly becomes computationally intractable. Because of this increase in computational cost (in terms of memory and CPUs required for the calculation), more approximate methods are used. An example of a more approximate method would be coupled cluster including single and double excitations, with perturbative triples [CCSD(T)]. Although truncated, CCSD(T) has been shown to calculate ground state properties such as heats of formation, at times achieving more accurate results (i.e. closer to results achieved by full CI) than less approximate methods such as CCSDT [14].

However, the accuracy of truncated correlated methods can be sensitive to the choice of the reference wave function. CCSD(T) is a single reference post-Hartree-Fock method, generally based upon a HF wave function. If the reference wave function as determined by HF corresponds to an excited state determinant, truncated correlated methods are not necessarily able to produce the correct ground state. Even single reference theories such as the completely renormalized coupled cluster method, including singles, doubles, and perturbative triples [CR-CC(2,3)] that have been shown to treat some multireference problems [15, 16] (i.e. bond breaking, singlet-triplet gaps in biradical systems, and other systems with strong static correlation) still are subject to the limitations of the reference wave function. Furthermore, while it is possible to converge to a ground state wave function while using an excited state reference, the amplitudes can be much more challenging to converge.

There are other single-reference methodologies that use more than one determinant within their formulation, for example the spin flip method [17, 18]. The spin flip method and its variants use multiple determinants (the reference state and additional excited states that result from a spin flip of an electron) and are able to better describe events such as bond breaking. The description of the reference state can increase to higher correlated methods, yet this would increase the computational cost involved within the calculation. Additionally, for the simplest version of

the spin-flip method, Hartree-Fock is used to describe the reference system, so there is still some dependence on HF being able to determine the correct electronic configuration.

Multireference methods such as the multiconfigurational self-consistent field (MCSCF) [19] and complete active space perturbation theory, second order (CASPT2) [20], among many others, are designed specifically to recover non-dynamical correlation energy. However, there are drawbacks to these methods [21, 22]. The scaling of these methods is such that it is generally limited to systems of no more than sixteen active electrons within sixteen active orbitals [19]. Furthermore, the selection of an appropriate active space can be system dependent and ensures that these methods are by no means “black box”. The HF wavefunction generally serves as the reference wavefunction for these methods as well and can be used to help determine the orbitals that should be included within the active space. A wavefunction that has converged to the wrong state can lead to very slow convergence or to completely inappropriate orbitals included within the active space.

Another popular approach to incorporate some degree of electron correlation is density functional theory (DFT). It has found use in the calculation of ground state properties for organic and inorganic molecules [23]. DFT has the benefit of including correlation within the calculation beyond the mean field correlation that is included within Hartree-Fock, yet the computational cost is on par with a Hartree-Fock calculation. DFT generally achieves a reasonable balance between computational cost and accuracy [23]. However, as a single reference method, it may suffer from some of the same limitations as Hartree-Fock theory.

The molecules included in this study were chosen for illustrative purposes only. While the molecules all have been the focus of prior extensive theoretical and experimental studies, our goal is not to provide a broad review of the literature, but rather to illustrate some of the problems that can manifest when the optimized orbital occupancy is not considered.

2 Computational Methods

The diatomic molecules chosen for this study were O₂, F₂, Cl₂, Br₂, LiF, NaCl, CaO, MgO, ScO, FeO, TiO, YO, and ZrO. These molecules cover many parts of the periodic table including main group diatomics with light and heavy atoms, diatomics containing *s*-block elements, and diatomics containing transition metals. Additionally, both closed shell and open shell species are included. All molecules studied were the neutral species. The experimental bond lengths were taken from the NIST Chemistry WebBook (<http://www.webbook.nist.gov>) [24].

To gauge the possible multireference character of the molecules, T₁ and D₁ diagnostic values were calculated [25–27]. The T₁ and D₁ diagnostic values are related to the magnitude of the oscillator strength of single excitations and thus are frequently used to estimate the multireference character of a molecule. A T₁ value of 0.02 and a D₁ value of 0.05 are considered the multireference thresholds

for main group and *s*-block containing molecules, while the more recently proposed thresholds of T_1 greater than 0.05 and D_1 greater than 0.15 are used for transition metal-containing compounds [28].

Calculations were performed using GAMESS [13]. Restricted Hartree-Fock (RHF or ROHF) calculations were performed for all of the molecules. Unrestricted HF (UHF) calculations also were performed for O₂ and FeO as UHF can describe multireference character arising from bond breaking, albeit with the disadvantage of producing wave functions that are not spin eigenfunctions. CR-CC(2,3) calculations also were performed to examine the impact of the Hartree-Fock reference on a correlated wave function method. The Sapporo-2012 triple- ζ all-electron basis sets were used for all calculations [29]. The Sapporo-2012 basis sets were chosen because they cover most of the periodic table and are generally more compact than other correlation consistent basis sets. Potential energy curves (PECs) for each diatomic were calculated from about 1.4 Å to about 3.5 Å in 0.1 Å increments, then decreased to 0.01 Å and then 0.001 Å around the minimum of the curve, when possible in order to determine the equilibrium bond length accurate to 10⁻³ Å. Restricted open-shell (RO) DFT also was used to calculate PECs for FeO using four popular DFT functionals: B3LYP [30, 31], PBE0 [32, 33], M06 [34], and M11 [35]. All calculations were restricted to C_{2v} symmetry.

When single point energy calculations resulted in an excited state for FeO, the full excited state potential energy curves were constructed using the Maximum Overlap Method (MOM) of Gilbert, Besley, and Gill [2]. In this approach, excited state solutions to the Hartree-Fock equations are determined by populating the orbitals that overlap the most with the previously occupied orbitals in contrast to occupation according to the *aufbau* principle, in which the lowest energy orbitals are always populated first. Using this approach keeps the wave function from collapsing to the lowest energy solution.

3 Results and Discussion

The calculated ground state of each molecule, the experimental bond lengths, and the equilibrium bond lengths based on the computed potential energy curves at both the HF and CR-CC(2,3) levels of theory are shown in Table 1. Bond lengths computed using both the H_{core} and Hückel guesses are reported, as well as the mean signed deviation (MSD), mean absolute deviation (MAD), and root-mean-square deviation (RMSD).

On average, HF underestimates the bond lengths by 0.014 and 0.020 Å, while CR-CC(2,3) overestimates the bond lengths by 0.033 and 0.039 Å for the H_{core} and Hückel guesses, respectively, as accounting for electron correlation tends to make the electron density more diffuse [36, 37]. Two notable exceptions from this trend are NaCl and FeO. The HF calculated equilibrium bond length for NaCl is 0.027 Å too long using either guess. In the case of FeO, the HF calculated bond length using the H_{core} guess is 0.054 Å too long, while the Hückel guess is unable to produce a

Table 1 Equilibrium bond distances (Å), determined from experiment (r_{eq}) and from the potential energy curves (r_{PEC})

Molecule	Calc. ground state	r_{eq}	r_{PEC}			
			ROHF		CR-CC(2,3)	
			H_{core}	Hückel	H_{core}	Hückel
O ₂	³ A ₂	1.208	-0.057	-0.056	+0.004	+0.004
F ₂	¹ A ₁	1.412	-0.084	-0.084	+0.003	+0.006
Cl ₂	¹ A ₁	1.988	-0.012	-0.012	+0.022	+0.021
Br ₂	¹ A ₁	2.281	-0.017	-0.017	+0.016	+0.022
LiF	¹ A ₁	1.564	-0.005	-0.005	+0.018	+0.020
NaCl	¹ A ₁	2.361	+0.027	+0.027	+0.040	+0.034
MgO	¹ A ₁	1.749	-0.012	-0.012	+0.015	+0.014
CaO	¹ A ₁	1.822	-0.005	-0.005	+0.134	+0.140
ScO	² A ₁	1.668	-0.020	-0.020	+0.036	+0.042
FeO	⁵ A ₁	1.626	+0.054	-	-	-
TiO	³ A ₁	1.620	-0.025	-0.020	0.000	+0.031
YO	² A ₁	1.790	-0.022	-0.022	+0.050	+0.053
ZrO	³ A ₁	1.712	-0.010	-0.010	+0.059	+0.082
		MSD	-0.014	-0.020	0.033	0.039
		MAD	0.027	0.024	0.033	0.039
		RMSD	0.035	0.033	0.048	0.054

All experimental values came from the NIST chemistry WebBook. Mean signed deviation (MSD), mean absolute deviation (MAD), and the root-mean-squared deviation (RMSD) are reported

smooth curve in the region of equilibrium, so an estimation of the equilibrium bond length cannot be made. The bond length for CaO calculated with CR-CC(2,3) is significantly too long with a deviation greater than 0.1 Å. Finally, HF produces the same equilibrium bond lengths for each molecule, regardless of initial guess. Overall, the equilibrium bond lengths calculated with CR-CC(2,3) vary between the different initial guesses, as each method populates the orbitals in a slightly different manner. Generally, the deviation between guesses is not large (e.g. 0.001 Å between the H_{core} and Hückel guess for Cl₂). However, in some cases, the deviation can be quite large, as for ZrO with a deviation of 0.023 Å between the two guesses.

3.1 Main Group Diatomics

The main group diatomics that were included within this study are O₂, F₂, Cl₂, and Br₂. The T₁/D₁ diagnostic values are shown in Table 2. The halide diatomics are well-behaved systems, in that they have low multireference character and the curves that are calculated are smooth and continuous at all points considered. This is to be expected, given that they are all closed shell singlets. The multireference character of the molecule increases as the bond is stretched, yet ROHF still optimizes to a

Table 2 T_1/D_1 diagnostics for the main group molecules

	r (Å)			
O_2	1.1	1.3	2.1	3.3
T_1	0.011	0.017	0.037	—
D_1	0.031	0.047	0.097	—
F_2	1.1	1.3	1.8	2.5
T_1	0.008	0.009	0.018	0.030
D_1	0.016	0.023	0.059	0.105
Cl_2	1.6	2.0	2.7	3.5
T_1	0.008	0.009	0.014	0.022
D_1	0.017	0.022	0.045	0.080
Br_2	1.8	2.3	3.0	3.7
T_1	0.007	0.008	0.013	0.020
D_1	0.014	0.019	0.041	0.071

For O_2 at 3.3 Å, the CCSD amplitudes did not converge, which is an indication of either significant multireference character or a poor reference wavefunction

single state wave function for each molecule. Of the main group diatomics, triplet O_2 exhibits the most multireference character throughout the entire calculated PEC. Even at equilibrium, the T_1/D_1 values for triplet O_2 approach the multireference threshold, while the CCSD amplitudes do not even converge further towards dissociation (i.e. 3.5 Å). This is indicative of significant multireference character in this area of the curve due to the breaking of the bonds and demonstrates that the single reference wave function determined with HF is not a suitable reference. The multireference character is manifested by the oscillation between different states throughout the entire curve (see Fig. 1).

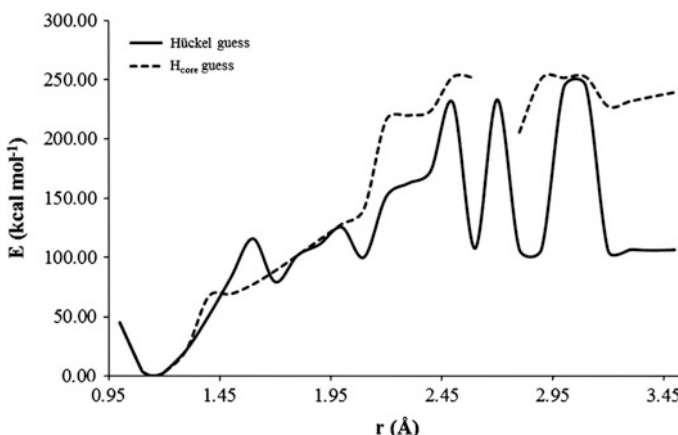


Fig. 1 Points calculated for O_2 at the ROHF level of theory, using the H_{core} and Hückel initial guess. The point at 2.7 Å using the H_{core} guess did not converge

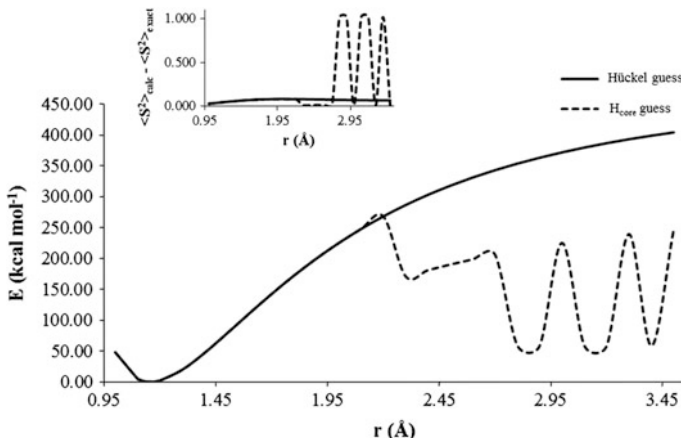


Fig. 2 Points calculated for O₂ at the UHF level of theory, using the H_{core} and Hückel initial guesses. The difference between the calculated $\langle S^2 \rangle$ and the $\langle S^2 \rangle$ for the pure spin state ($\langle S^2 \rangle_{\text{calc}} - \langle S^2 \rangle_{\text{exact}}$) are inset

Both initial guesses produce vastly different results at large internuclear distances. Near the equilibrium region, a $^3\text{A}_2$ state is found which is a direct product of B₁ and B₂ orbitals in the C_{2v} point group. These orbitals correspond to the π^* antibonding orbitals that result from the linear combination of 2p_x atomic orbitals and 2p_y atomic orbitals, respectively. In the region of intermediate internuclear distances (IID, the area of the potential energy curve between equilibrium and dissociation) the points fall on a curve belonging to a state of $^3\text{A}_1$. This state results from the direct product of two singly occupied B₁ orbitals corresponding to the π and π^* orbitals from the overlap of p_x atomic orbitals. This gives an overall bond order of 1, which is clearly on a different PEC than the ground state. As the internuclear distance grows, the curve resulting from the Hückel initial guess begins to oscillate drastically between different states. The upper state produced by the Hückel guess leads to homolytic dissociation, while the lower state leads to a heterolytic dissociation.

The triplet O₂ PEC also was calculated via UHF, as the unrestricted formalism should be able to better describe the bond breaking region of the curve (see Fig. 2).

It is important to note that the ROHF wave function is an eigenvalue of the S² operator while the UHF wave function is not [38]. This means that UHF suffers from spin contamination, as contributions from higher spin states are included in the wave function. The $\langle S^2 \rangle_{\text{calc}}$ expectation value is used as a measure of the spin contamination within an unrestricted calculation. The $\langle S^2 \rangle_{\text{exact}}$ for a spin pure state is $S_z(S_z + 1)$. As increasingly higher spin states are included $\langle S^2 \rangle_{\text{calc}}$ increases. $\langle S^2 \rangle_{\text{calc}}$ for each curve is compiled in Table 3.

The UHF curve calculated from Hückel guess produces one smooth, continuous curve in the $^3\text{A}_1$ state. $\langle S^2 \rangle_{\text{calc}}$ indicates that, although there is slight mixing of higher spin states, particularly in the IID region, the same state is found throughout

Table 3 $\langle S^2 \rangle_{\text{calc}} - \langle S^2 \rangle_{\text{exact}}$ at 0.1 Å increments along the UHF curve for triplet O₂

O ₂	H _{core} guess	Hückel guess
r (Å)	$\langle S^2 \rangle_{\text{calc}} - \langle S^2 \rangle_{\text{exact}}$	$\langle S^2 \rangle_{\text{calc}} - \langle S^2 \rangle_{\text{exact}}$
1.0	0.026	0.026
1.1	0.034	0.034
1.2	0.043	0.043
1.3	0.051	0.051
1.4	0.058	0.058
1.5	0.065	0.065
1.6	0.070	0.070
1.7	0.074	0.074
1.8	0.076	0.076
1.9	0.078	0.078
2.0	0.079	0.079
2.1	0.078	0.078
2.2	0.010	0.078
2.3	0.010	0.077
2.4	0.010	0.076
2.5	0.010	0.074
2.6	0.010	0.073
2.7	0.010	0.071
2.8	1.011	0.070
2.9	1.013	0.069
3.0	0.010	0.067
3.1	1.015	0.066
3.2	1.015	0.065
3.3	0.010	0.064
3.4	1.016	0.064
3.5	0.009	0.063

the entire curve. The H_{core} guess, however, does not remain in one state throughout the curve. At 2.3 Å, a lower energy state is found, with an even lower energy state appearing at 2.8 Å. While each state has ³A₁ symmetry, the $\langle S^2 \rangle_{\text{calc}}$ indicates increasing spin contamination.

3.2 S-Block Diatomics

The s-block diatomics included in this study are LiF, NaCl, CaO, and MgO. The T₁/D₁ diagnostic values are listed in Table 4.

As expected, the multireference character increases as the bond breaks when the internuclear separation increases. LiF and NaCl are well-behaved with both H_{core}

Table 4 T_1/D_1 diagnostics for the *s*-block-containing molecules

	r (Å)			
LiF	1.4	1.6	2.5	3.5
T_1	0.013	0.015	0.023	0.040
D_1	0.024	0.027	0.049	0.108
NaCl	2.0	2.4	3.3	4.0
T_1	0.005	0.006	0.009	0.011
D_1	0.010	0.011	0.021	0.029
MgO	1.4	1.7	2.5	3.5
T_1	0.069	0.043	0.115	0.087
D_1	0.191	0.107	0.308	0.245
CaO	1.5	1.8	2.5	3.5
T_1	0.022	0.050	0.089	—
D_1	0.044	0.132	0.181	—

For CaO at 3.5 Å, the CCSD amplitudes did not converge, which is an indication of either significant multireference character or a poor reference wavefunction

and Hückel guesses producing the same smooth PECs. MgO and CaO both exhibit some multireference character throughout the entire potential energy curve as indicated by the T_1/D_1 diagnostics, even near the equilibrium bond length. However, with the exception of the large internuclear distances for MgO (see Fig. 3), ROHF optimizes to a single state wave function for each of these molecules.

Although MgO is significantly multireference throughout the entire curve with T_1 and D_1 values greater than 0.02 and 0.05, respectively, ROHF produces a smooth, continuous curve describing both the equilibrium region and most of the non-equilibrium region quite well. There is only a small discrepancy between the results from the two initial guesses as the bond length is increased.

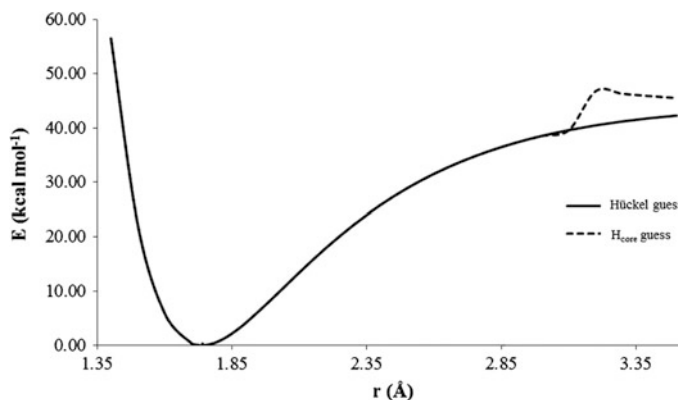
**Fig. 3** Points calculated for MgO at the ROHF level of theory, using the H_{core} and Hückel initial guesses

Table 5 T_1/D_1 diagnostics for the transition metal-containing molecules

	r (Å)			
ScO (2A_1)	1.4	1.6	2.5	3.5
T_1	0.026	0.035	—	—
D_1	0.043	0.056	—	—
FeO (5A_2)	1.3	1.7	2.4	4.0
T_1	0.049	0.090	0.026	0.179
D_1	0.097	0.188	0.060	0.665
TiO (3A_1)	1.4	1.6	2.4	3.5
T_1	0.034	0.046	0.029	0.059
D_1	0.058	0.075	0.058	0.104
YO (2A_1)	1.6	1.8	2.5	3.5
T_1	0.025	0.033	0.088	0.076
D_1	0.040	0.054	0.175	0.155
ZrO (3A_1)	1.5	1.7	2.5	3.5
T_1	0.026	0.035	0.126	—
D_1	0.044	0.060	0.258	—

For ScO and ZrO, the HF wavefunction did not converge, as ROHF is a high-spin theory. At this point on the curve, the low-spin case is enforced on the system

3.3 Transition Metal Diatomics

The transition metal diatomics in the test set are ScO, FeO, TiO, YO, and ZrO. The T_1/D_1 diagnostic values are listed in Table 5. All of the molecules exhibit some multireference character throughout the PECs, although with the exception of FeO, all of the molecules have low diagnostic values around the minimum of the curve. As will become evident throughout the discussion of transition metal diatomics, the possible multireference character and the initial guess of the bond length can affect the convergence of geometry optimizations.

3.3.1 ROHF Results

Both ScO and YO are doublets with one unpaired electron (2A_1 ground states). For these diatomics, the calculated PECs are well-behaved around the minimum of the curves (see Figs. 4 and 5, respectively).

Problems arise as the bond distance increases to the intermediate internuclear distances (IID) between equilibrium and dissociation. While the lowest energy state for ScO is still a 2A_1 state, it is 21.4 kcal mol⁻¹ lower in energy than the rest of the curve (see Fig. 4). The PECs for YO exhibits state switching, beginning at 2.6 Å (see Fig. 5). This is the area of the PEC that has the highest multireference character, with a T_1 value of 0.088 and a D_1 of 0.175, and the multireference character manifests itself in the inability of ROHF calculations to find one ground state at each point of the curve.

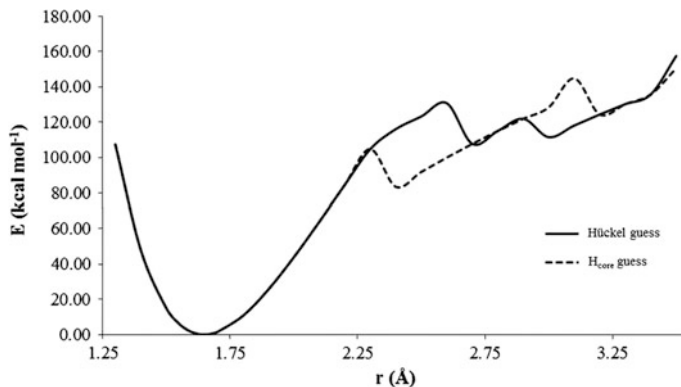


Fig. 4 Points calculated for ScO at the ROHF level of theory, using both the H_{core} and Hückel initial guesses

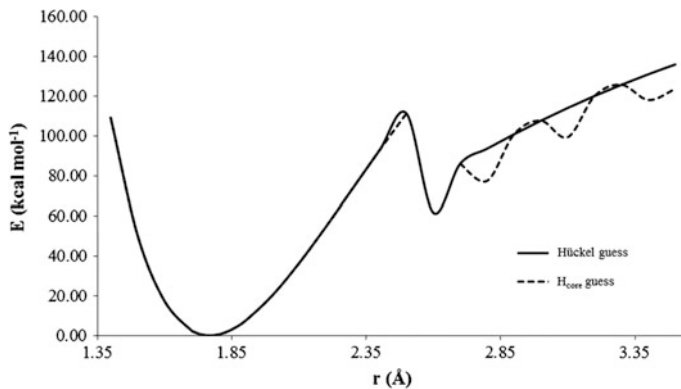


Fig. 5 Points calculated for YO at the ROHF level of theory, using both the H_{core} and Hückel initial guesses

The initial guess for the wave function, either the H_{core} or the Hückel guess, had little impact on the smoothness (or lack thereof) on the PECs for ScO. The Hückel guess for YO was able to determine a single state as the bond length was increased, whereas the H_{core} guess produced oscillations between two distinct states near dissociation.

The ground state for ZrO is 3A_1 (see Fig. 6) along with a degenerate 3A_2 state, yet at 2.6 Å, the lowest energy state is found to be 3B_2 when the H_{core} initial guess is used. When using the Hückel guess, at 2.4 Å, the PEC jumps to a 3B_1 state, which is the direct product of A_1 and B_1 singly occupied orbitals. Then at 2.6 Å the calculation settles to a 3A_1 state. However, this A_1 state results from the direct product of two B_1 orbitals instead of two A_1 orbitals, as with the ground state around the minimum of the curve. This is a direct result of different d -orbital

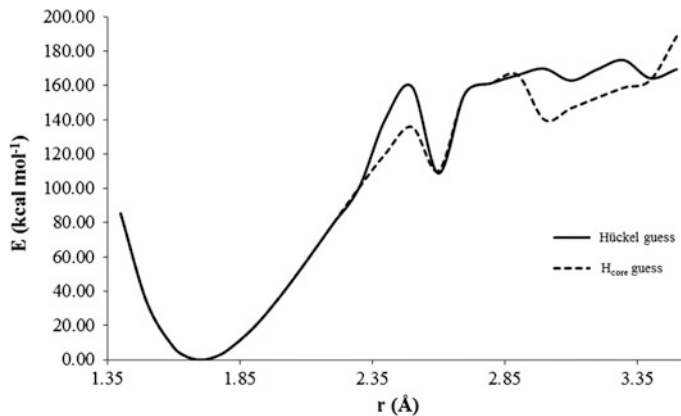


Fig. 6 Points calculated for ZrO at the ROHF level of theory, using both the H_{core} and Hückel initial guesses

occupation. TiO is also a triplet and the PECs show that the initial guess for the wave function can have an effect as well (see Fig. 7).

With either initial guess, the ground state near equilibrium is 3A_1 , which results from the direct product of two A_1 orbitals (an s and a d_{x^2} orbital) localized on Ti. Yet at 2.1 Å, the H_{core} guess finds the lowest energy state for TiO as 3B_1 resulting from the combination of a p_x orbital of B_1 symmetry localized on O and an s orbital with A_1 symmetry localized on Ti. The tail of the PEC oscillates between the 3A_1 and 3B_1 states. As is shown in Fig. 7, when using the H_{core} initial guess, it is not obvious that the wave function has changed states. The Hückel guess, however, falls into the higher energy 3B_1 state around the minimum of the curve, which can be problematic for gradient-driven optimizations. Even given an initial geometry

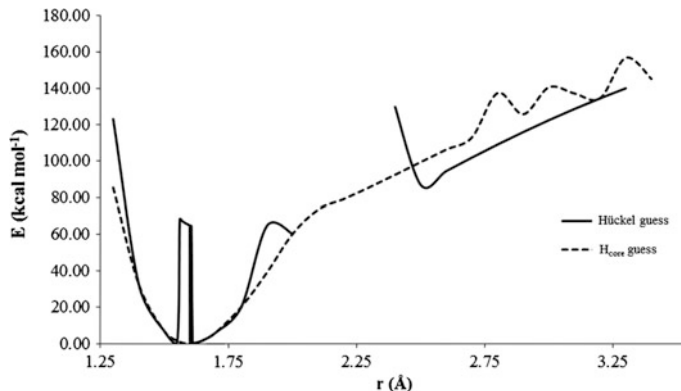


Fig. 7 Points calculated for TiO at the ROHF level of theory, using the H_{core} and Hückel initial guesses. The points between 2.1 and 2.3 Å on the Hückel curve do not converge

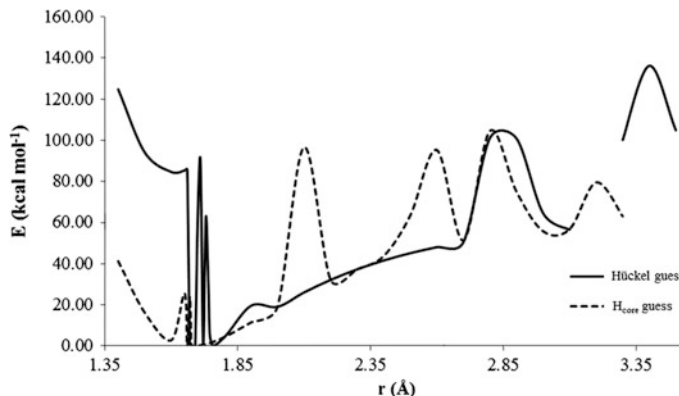


Fig. 8 Points calculated for FeO at the ROHF level of theory, using the H_{core} and Hückel initial guesses. The point at 3.4 Å on the H_{core} curve and 3.2 Å on the Hückel curve do not converge

close to the equilibrium bond length, HF could still optimize to an excited state resulting in an incorrect geometry, especially if the ground and excited PECs are not parallel. Non-parallel PECs can be problematic as a bad initial guess can result in an incorrect optimized geometry, especially when a gradient-driven optimization algorithm is used. In this case the two different initial guesses produce PECs with two different equilibrium bond lengths, 1.595 Å for the H_{core} guess and 1.600 Å for the Hückel guess, indicating that the curves resulting from the two different guesses are not parallel. While this is only a 0.005 Å difference in the calculated bond length, there could be a greater difference for other molecules. Fortunately, the initial guesses had no effect on the calculated bond length for the rest of the molecules investigated in the present work.

FeO is an open shell quintet. Unsurprisingly, the T_1/D_1 diagnostics indicate that FeO exhibits multireference character at all internuclear distances. Notably, the area that shows the least multireference character according to the T_1/D_1 diagnostic is at 2.4 Å, firmly in the IID region of the curve, an area that is typically the most multireference due to bond breaking. The ROHF reference curves using the H_{core} and Hückel initial guesses demonstrate this quite clearly (see Fig. 8).

The H_{core} guess is able to produce a smooth curve close to the minimum, yet there is an excited state found at distances just short of equilibrium. The curve also quickly degenerates into several different states in the IID region. The Hückel guess, however, is unable to produce a smooth curve around the minimum. The lowest energy state between 1.4 and 1.66 Å is 5A_2 , while the lowest energy state from 1.67 Å is 5A_1 . The orbital occupation for the 5A_2 has some mixing between the Fe 3d and O 2p orbitals with the 3d and 4p orbitals singly occupied, while only the 3d orbitals are singly occupied in the 5A_1 state.

An attempt was made to calculate the separate ROHF curves for FeO using the Maximum Overlap Method (MOM) approach [2] beginning from an H_{core} initial guess, yet even this was unable to isolate the different states towards dissociation

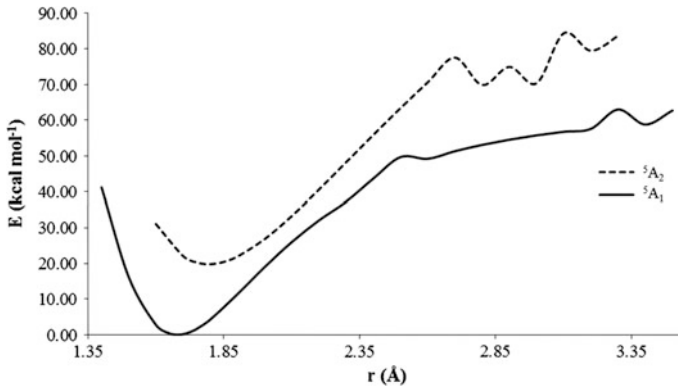


Fig. 9 Ground state (${}^5\text{A}_1$) and excited state (${}^5\text{A}_2$) curves for FeO, using the maximum overlap method (MOM), calculated at the ROHF level of theory. The optimized orbitals from a point on the excited state curve were used as the initial guess for subsequent points. Orbital rotations were restricted to attempt to stay in the same electronic state. The curves are smooth and continuous around the minima, yet are unable to stay on the same curve as the bond length increases. These curves also demonstrate that the ground state and excited state curves are not always parallel, as the equilibrium bond distance for the ground state is 1.680 Å and for the excited state is 1.790 Å

(see Fig. 9). Around equilibrium, two distinct states are produced, yet the IID region shows several different states. The different curves have different equilibrium bond lengths as well. The ${}^5\text{A}_1$ ground state produces an equilibrium bond length of 1.68 Å, while the higher ${}^5\text{A}_2$ state has a bond length of 1.79 Å.

The inability to produce a smooth potential energy curve is a basis set independent phenomenon. The Dunning-style correlation consistent polarized valence triple- ζ basis sets [28, 29] were also utilized with ROHF to calculate the potential energy curves for FeO as shown in Fig. 10.

As ROHF tends to enforce heterolytic dissociation, UHF was also utilized to calculate points on the potential energy curve for FeO (see Fig. 11). The Hückel initial guess identifies the ground state as ${}^5\text{A}_1$. Notably, the curve is much smoother around the minimum, which is the region that ROHF was unable to describe. At 2.0 Å, the calculation converges to an excited ${}^5\text{A}_1$ state. The H_{core} initial guess in conjunction with UHF is unable to produce a smooth curve at equilibrium. There is oscillation between the ${}^5\text{B}_1$ ground state and an excited ${}^5\text{B}_1$ that is noticeably not parallel to the ground state curve. This demonstrates that even a reasonable initial guess of the geometry for FeO can result in the incorrect state and a different equilibrium bond length.

The spin contamination for the points on the calculated PEC are shown by the inset graph of Fig. 11 and in Table 6. When the calculation converges to an excited state curve, there is an accompanying increase in the $\langle \text{S}^2 \rangle$ value.

It is clear that calculation of the FeO potential energy curve will benefit from a multireference treatment. This is a result of near degeneracies arising from the 4s and 3d orbitals in addition to the breaking of the Fe–O bond at long internuclear

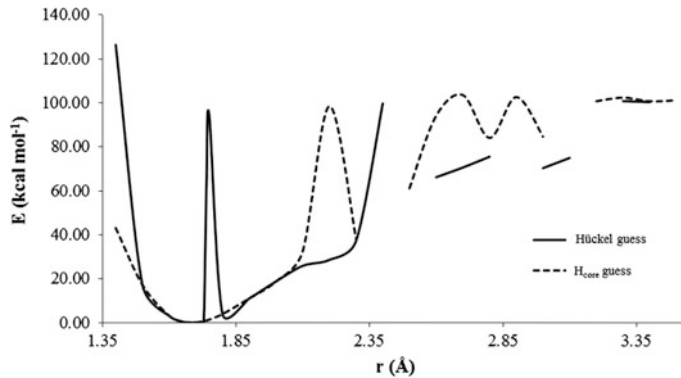


Fig. 10 Points calculated for FeO at the ROHF level of theory, using the H_{core} and Hückel initial guesses and cc-pVTZ basis sets. The points at 2.4 and 3.1 Å on the H_{core} curve and 2.5, 2.9, 3.2, and 3.5 Å on the Hückel curve do not converge

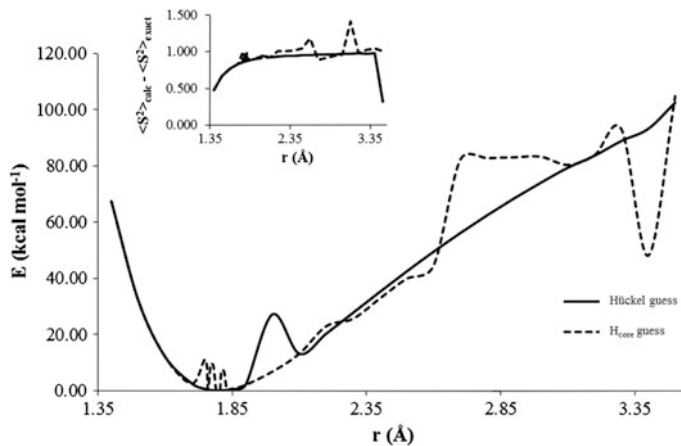


Fig. 11 Points calculated for FeO at the UHF level of theory, using the H_{core} and Hückel initial guesses. The difference between the calculated $\langle S^2 \rangle$ and $\langle S^2 \rangle$ for the pure spin state ($\langle S^2 \rangle_{calc} - \langle S^2 \rangle_{exact}$) are inset

distance. Thus, any active space employed must account for both sources of multireference character. A sensible active space would then include the Fe 4s and 3d orbitals and the O 2p orbital set. While only two O 2p orbitals may take part in bonding to Fe, the full set should initially be included due to the degeneracy of the O 2p orbital set. Given this initial (12,9) active space, it may be possible to truncate the active space if it can be shown that occupation of any orbitals remains constant (doubly occupied or unoccupied) for all internuclear distances. It is known that the ground state term of FeO is $^5\Delta$ with A_2 symmetry, [21] while there also is a low-lying $^5\Sigma^+$ state with A_1 symmetry known [39, 40]. If it is assumed that FeO exists as

Table 6 $\langle S^2 \rangle_{\text{calc}} - \langle S^2 \rangle_{\text{exact}}$ at 0.1 Å increments along the UHF curve for FeO

FeO	H_{core} guess	Hückel guess
r (Å)	$\langle S^2 \rangle_{\text{calc}} - \langle S^2 \rangle_{\text{exact}}$	$\langle S^2 \rangle_{\text{calc}} - \langle S^2 \rangle_{\text{exact}}$
1.40	0.471	0.471
1.50	0.666	0.666
1.60	0.773	0.773
1.70	0.833	0.833
1.75	0.970	0.854
1.80	0.871	0.871
1.90	0.896	0.896
2.00	0.913	0.944
2.10	0.925	0.925
2.20	1.005	0.935
2.30	1.008	0.942
2.40	1.015	0.948
2.50	1.046	0.953
2.60	1.186	0.957
2.70	0.885	0.960
2.80	0.919	0.963
2.90	0.943	0.966
3.00	0.960	0.969
3.10	1.416	0.971
3.20	0.983	0.984
3.30	1.028	0.976
3.40	1.047	0.979
3.50	1.013	0.321

$\text{Fe}^{2+}\text{O}^{2-}$, then Fe exists in the ^5D state with a valence configuration of $4s^03d^6$. Thus, it may be possible to cut the 4s orbital out of the active space if it is shown to have negligible occupation at all internuclear distances, i.e. Fe is Fe(II) at all internuclear distances. This would allow for a reduced active space of (12,8). The smooth potential energy curve with this active space is shown in Fig. 12.

3.3.2 CR-CC(2,3) Results

If the ROHF wave function providing the reference for correlated calculations is not correct, then the correlated calculations may be incorrect as well. The exception to this would be full CI calculations, or coupled cluster or many-body perturbation theory calculations that converge to full CI in the full expansion. These results are independent of the reference wave function, yet a good reference will speed up convergence. This is demonstrated by the PECs for O_2 , YO , and FeO (see Figs. 13, 14 and 15). The PECs for O_2 show the same oscillating behavior between the homolytic and heterolytic dissociation states, yet the H_{core} guess produces only the

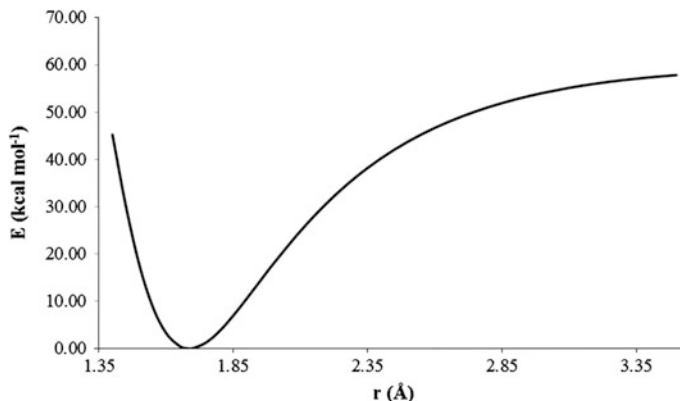


Fig. 12 Points calculated for FeO at the CASSCF level of theory, using a (12,8) active space

heterolytic curve (see Fig. 13). The ROHF PEC for YO using the H_{core} initial guess (Fig. 5) has some oscillation between states beginning in the IID region of the PEC, extending out towards dissociation. This same problem is evident for CR-CC(2,3) as shown in Fig. 14. The calculations based on the Hückel guess result in a smoother curve, although still not in one single state, as evidenced by the small “kink” in the curve at 2.7 Å.

The PECs for FeO exhibit much less oscillation between two different states, yet the curve resulting from the Hückel guess has a discontinuity between 1.7 and 1.8 Å (see Fig. 15). From 1.4 to 1.7 Å, the curve calculated using the Hückel guess follows the higher energy $^5\text{A}_2$ state, and then at 1.8 Å shifts to the lower energy $^5\text{A}_1$ state.

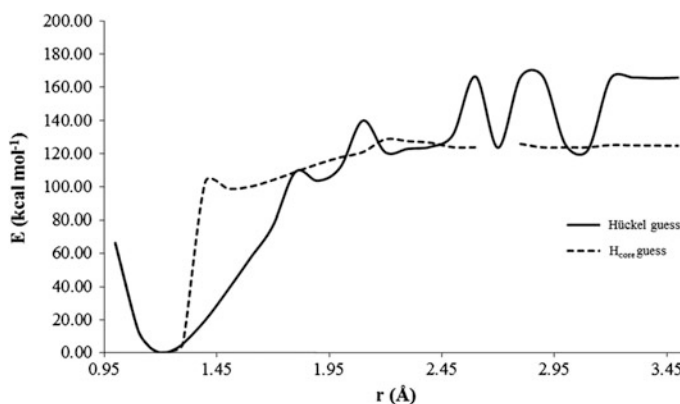


Fig. 13 Points calculated for O_2 at the CR-CC(2,3) level of theory, using the H_{core} and Hückel initial guesses. The point at 2.7 Å using the H_{core} guess did not converge

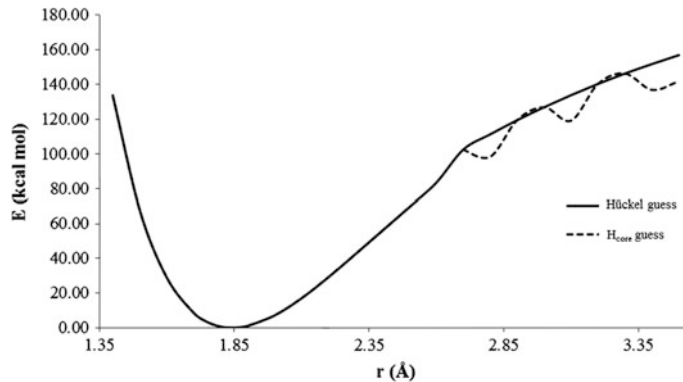


Fig. 14 Points calculated for YO at the CR-CC(2,3) level of theory, using the H_{core} and Hückel initial guesses

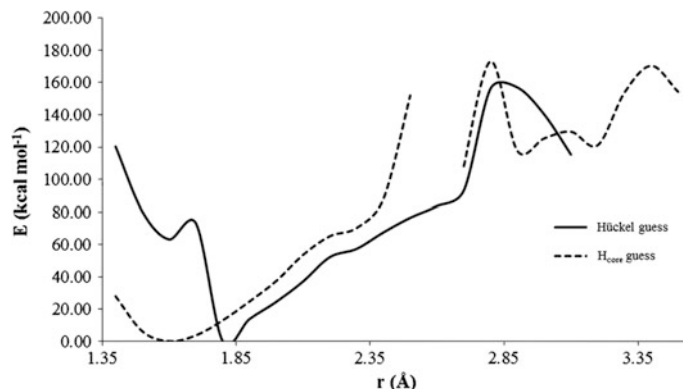


Fig. 15 Points calculated for FeO at the CR-CC(2,3) level of theory, using the H_{core} and Hückel initial guesses. The point at 2.6 Å using the H_{core} guess and the points at 3.2, 3.4, and 3.5 Å using the Hückel guess do not converge

3.3.3 DFT Results

PECs for FeO were calculated using RODFT with the B3LYP, PBE0, M06, and M11 functionals (Figs. 16, 17, 18 and 19, respectively). Using B3LYP and the H_{core} initial guess, a smooth curve is computed for the region between 1.4 and 2.2 Å, with a ground electronic state of 5A_1 resulting from the direct product of an A_1 orbital, an A_2 orbital, a B_1 orbital, and a B_2 orbital, all of which are d orbitals on iron. However, B3LYP calculations are unable to converge to any state after 2.2 Å (Fig. 16). The Hückel guess produces two electronic states close to equilibrium. The ground state is a 5A_1 state that results from single occupation of an A_1 orbital, an A_2 orbital, a B_1 orbital, and a B_2 orbital, all of which are also iron d orbitals. The

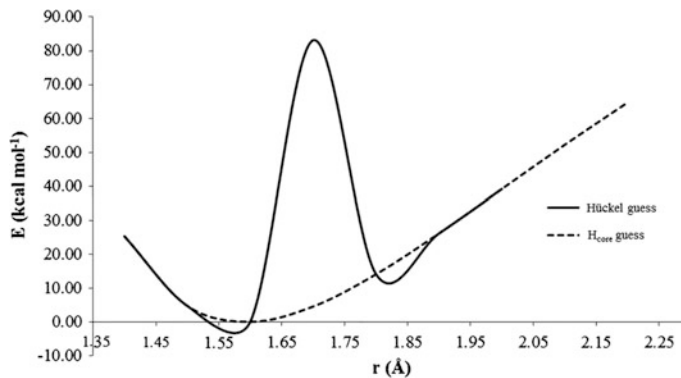


Fig. 16 Points calculated for FeO at the B3LYP level of theory, using the H_{core} and Hückel initial guesses. The calculations do not converge past 2.0 Å using the Hückel guess or 2.2 Å using the H_{core} guess

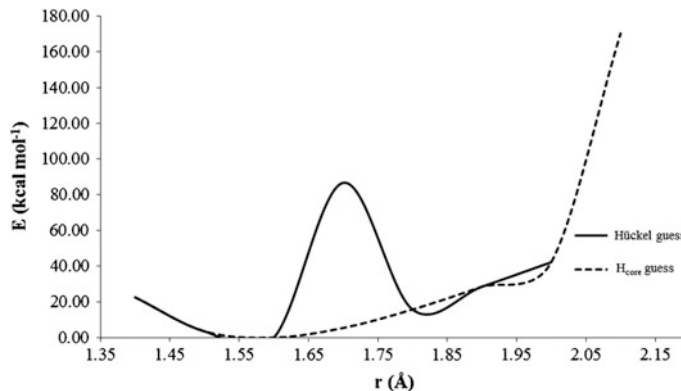


Fig. 17 Points calculated for FeO at the PBE0 level of theory, using the H_{core} and Hückel initial guesses. The calculations do not converge past 2.0 Å using the Hückel guess or 2.1 Å using the H_{core} guess

other electronic state is found at 1.7 Å, which is a 5A_2 state that results from a combination of an s orbital and a d_{z^2} orbital localized on iron with A_1 symmetry, a B_2 orbital, and a B_1 orbital, both of which are d orbitals. The 5A_2 excited state is 83 kcal mol⁻¹ higher than the ground state. Beyond 2.0 Å, the calculations that utilize the Hückel guess do not converge.

PBE0 does not perform much better (Fig. 17) than B3LYP. Around the minimum of the curve, the H_{core} guess produces a smooth curve corresponding to a 5A_2 state. This state is a combination of a B_1 orbital, a B_2 orbital, and two A_1 orbitals, all of which are d orbitals. At 2.1 Å the calculation optimizes to an excited 5A_1 state, which results from a combination of two d orbitals localized on iron with B_1 and B_2 symmetry, and the $2p_x$ and $2p_y$ orbitals, with B_1 and B_2 symmetry

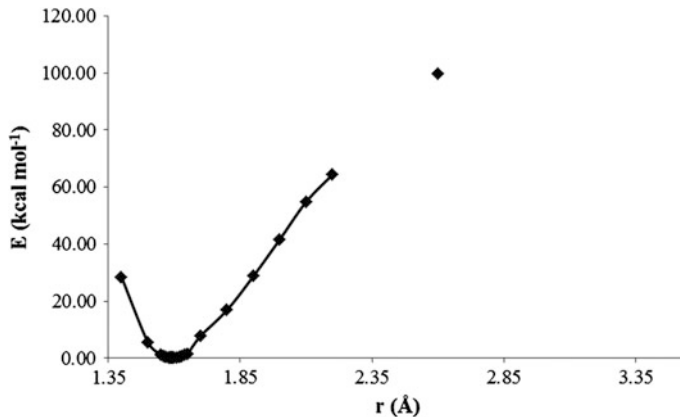


Fig. 18 Points calculated for FeO at the M06 level of theory, using the H_{core} initial guess. The calculations do not converge past 2.2 Å using the H_{core} guess. Only four points on the curve converged using the Hückel guess

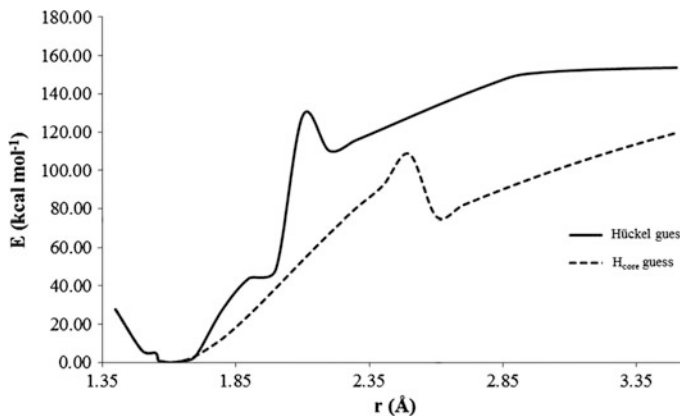


Fig. 19 Points calculated for FeO at the M1 level of theory, using the H_{core} and Hückel initial guesses

respectively, localized on oxygen. Past 2.1 Å with the H_{core} guess and 2.0 Å with the Hückel guess, PBE0 is also unable to converge to any state. The Hückel guess once again lands in an excited state at 1.7 Å that is 86 kcal mol⁻¹ above the ground state. The ground state is a ⁵A₁ and the excited state found at 1.7 Å is a ⁵A₂ state. The ground ⁵A₁ state is a combination of an A₂ orbital, an A₁ orbital, a B₁ orbital, and a B₂ orbital, all of which are *d* orbitals on iron. The excited state ⁵A₂ results from the occupation of two A₁ orbitals, a B₂ orbital, and a B₁ orbital, similar to the population of the excited state calculated with B3LYP.

Although the M06 functional was fairly broadly parameterized in the course of its construction, problems still arise when calculating a potential energy curve for FeO (Fig. 18). Using the H_{core} initial guess, only the points between 1.7 and 2.0 Å converged successfully. From this point, however, the optimized orbitals from a converged point were used as the initial guess for the next point on the curve with orbital rotations restricted. Similar to the MOM method, this does ensure that the calculated curve is constrained to one electronic state. However, with the exception of a converged point at 2.6 Å, the points for the remainder of the curve past 2.2 Å do not converge. Using the Hückel initial guess results in only two points that converged, at 1.8 and 2.0 Å. With the optimized orbitals from these two points, points at 1.7 and 1.9 Å were converged. For the remainder of the curve, however, even utilizing the optimized orbitals as an initial guess did not provide a good enough starting guess for the calculations to converge.

The M11 functional performed by far the best of the tested functionals in calculating the potential energy curve for FeO (Fig. 19). Using the H_{core} initial guess a curve was produced that was mostly smooth around the minimum with the exception of a point at 1.55 Å. The calculated electronic state is 5A_1 , a state that results from a combination of an A_2 , A_1 , B_2 , and B_1 orbitals, all of which are iron d orbitals. The H_{core} initial guess was sufficient for the points to converge from 1.4 to 1.64 Å. At 1.65 Å, the optimized orbitals were used for the starting guess, but it was not necessary to restrict orbital rotations to reach convergence until points in the IID region of the curve (specifically, 2.2, 2.3, 2.5, 3.2, and 3.3 Å). The point at 2.5 Å is a 5A_2 electronic state, from the occupation of a B_1 , B_2 , and two A_1 orbitals, all of which are still iron d orbitals. At 2.6 Å, there is a discontinuity in the curve and a lower energy electronic state is followed for the remainder of the curve. This electronic state is 5B_2 , from the occupation of a B_1 orbital that is a combination of an iron d orbital and an oxygen p orbital, and A_1 , B_2 , and B_1 orbitals, all of which are iron d orbitals. This is a limitation inherent in using a restricted open shell formulation to describe dissociation.

The Hückel initial guess is sufficient for points to converge from 1.4 to 2.1 Å, however the curve is not continuous, especially beginning at 2.0 Å. From 2.2 to 2.5 Å, the optimized orbitals had to provide the initial guess in order for the calculation to converge, and from 2.6 Å orbital rotations had to be restricted as well. The calculated electronic ground state at the minimum is a 5A_1 state. The occupation is in iron d orbitals of symmetry A_2 , A_1 , B_2 , and B_1 . At 2.0 Å, the electronic state changes to 5B_1 (the direct product of B_2 , A_1 , A_2 , and A_1 orbitals), with an oxygen p_x orbital included within the singly occupied orbitals. The excited state at 2.2 Å results from the occupation of an iron s orbital as well as an oxygen p_x orbital and is a 5A_1 state. At 3.0 Å, the electronic state is still a 5A_1 state, yet this is a result of a combination of oxygen p_x and p_y orbitals being populated. The potential energy curve generated by the Hückel guess demonstrates that, although the calculations converged to an answer fairly easily, inspection of the singly occupied orbitals shows that an excited state has been determined to be the ground state.

In addition to determining the equilibrium bond length from the minimum of the calculated potential energy curve, gradient-drive geometry optimizations were

performed using the M11 functional as well, beginning with both the H_{core} and Hückel initial guesses. The optimized bond length determined using the H_{core} initial guess was 1.607 Å, the same as the bond length determined from the minimum of the potential energy curve. The optimized bond length resulting from the Hückel initial guess was 1.643, 0.036 Å longer than the bond length at the bottom of the potential energy curve (also 1.607 Å). The experimental bond length is 1.626 Å, as seen in Table 1. The H_{core} -optimized bond length and the PEC-determined bond lengths are all 0.019 Å too short, while the optimized bond length from the Hückel guess is 0.017 Å too long.

These calculated curves demonstrate that DFT is not immune to the excited state optimization problems either. While using a combination of DFT and the H_{core} initial guess, along with an initial bond length close to equilibrium, a correct bond distance can be computed. However, using the Hückel guess can result in optimization to the wrong state and neither method is able to produce good initial orbitals at large internuclear distances.

4 Conclusion

Potential energy curves for a set of diatomic molecules were calculated using Hartree-Fock, CR-CC(2,3), and DFT with the B3LYP and PBE0 functionals. For some systems, HF erroneously converged to an excited state instead of the ground state of the molecule. Inspection of the optimized orbitals is imperative to determine that the calculation has converged to the intended state. While optimization techniques such as the Newton-Raphson method will converge to a local minimum with respect to the orbital coefficients, the initial orbital guess must be correctly populated as the Newton-Raphson method finds the nearest minimum rather than the global minimum. The initial guess can be generated through several commonly used options within computational chemistry software packages, but care must still be taken that the correct orbitals are being populated. This requires analysis of the converged orbitals.

In situations that contain parallel potential energy curves, convergence to an excited state during a geometry optimization will not impact the optimized geometry. Not every system has parallel potential energy curves, however, and large deviations in the optimized geometries can be observed.

Even in cases of relatively small multireference character, such as for TiO, HF can have difficulty converging to a single state. For molecules with significant multireference character such as FeO, it is clearly more reasonable to use multireference methods of calculation. However, the SCF wave function provides a basis for a multireference calculation as well, and the convergence rate of the multireference calculation may depend on the quality of the SCF orbitals used. For this reason, it is of utmost importance to review the optimized wave function and ensure that the calculation has converged to the correct state.

It is notable that all molecules examined here possess a high degree of spatial symmetry. Issues with optimization to any of the multiple low-lying excited states may be less severe if less symmetry or no symmetry were present as this lifts many of the degeneracies that exasperate the problem of multiple stable solutions to the Hartree-Fock equations (i.e. Löwdin's symmetry dilemma) [41].

Acknowledgments This material is based on work supported by the National Science Foundation under grant numbers CHE-1213874 and instrument support was provided via CHE-0741936. RJW acknowledges support from the National Science Foundation GFRP under grant number DGE-1144248. Additional computing resources were provided by the Academic Computing Services at the University of North Texas. Support from the United States Department of Energy for the Center for Advanced Scientific Computing and Modeling (CASCaM) is acknowledged.

References

1. Stanton RE (1968) *J Chem Phys* 48:257
2. Gilbert ATB, Besley NA, Gill PMW (2008) *J Phys Chem A* 112:13164
3. Sears JC, Sherrill CD (2006) *J Chem Phys* 124:144314
4. Cramer CJ (2004) *Essentials of computational chemistry: theories and models*, 2nd edn. Wiley, West Sussex, p 182
5. Jensen F (2007) *Introduction to computational chemistry*, 2nd edn. Wiley, West Sussex
6. Plakhutin BN, Davidson ER (2009) *J Phys Chem A* 113:12386
7. Ghanty TK, Davidson ER (2000) *Int J Quantum Chem* 77:291
8. Lynch BJ, Truhlar DG (2002) *Chem Phys Lett* 361:251
9. Morokuma K, Iwata S (1972) *Chem Phys Lett* 16:192
10. Schoendorff G, South C, Wilson AK (2013) *J Phys Chem A* 117:42
11. Seeger R, Pople JA (1977) *J Chem Phys* 66:3045
12. Pulay P (1982) *J Comp Chem* 3:556
13. Schmidt MW, Baldridge KK, Boatz JA, Elbert ST, Gordon MS, Jensen JH, Koseki S, Matsunaga N, Nguyen KA, Su SJ, Windus TL, Dupuis M, Montgomery JT (1993) *J Comput Chem* R1:1347
14. Feller D, Peterson KA, Crawford TD (2006) *J Chem Phys* 124:054107
15. Piecuch P, Wloch M (2005) *J Chem Phys* 123:1–224105
16. Wloch M, Gour JR, Piecuch P (2007) *J Phys Chem A* 111:11359
17. Krylov AI (2001) *Chem Phys Lett* 338:375
18. Krylov AI, Slipchenko LV, Levchenko SV (2007) *ACS Symp Ser* 958:89
19. Szalay PG, Müller T, Gidofalvi G, Lischka H, Shepard R (2012) *Chem Rev* 112:108
20. Andersson K, Malmqvist P, Roos BO, Sadlej AJ, Wolinski K (1990) *J Phys Chem* 94:5483
21. Schmidt MW, Gordon MS (1998) *Annu Rev Phys Chem* 49:233
22. Pulay P (2011) *Int J Quantum Chem* 111:3273
23. Burke K (2012) *J Chem Phys* 136:150901
24. Huber KP, Herzberg G *Constants of diatomic molecules*. In: Linstrom PJ, Mallard WG (eds) NIST chemistry WebBook, NIST standard reference database, vol 69. National Institute of Standards and Technology, Gaithersburg, MD, 20899 <http://webbook.nist.gov>, (Retrieved 6 Sept 2014)
25. Lee TJ, Taylor PR (1989) *Int J Quantum Chem* 23:199
26. Janssen CL, Nielsen IMB (1998) *Chem Phys Lett* 290:423
27. Lee TJ (2003) *Chem Phys Lett* 372:362
28. Jiang W, DeYonker NJ, Determan JJ, Wilson AK (2012) *J Phys Chem A* 116:870

29. Noro T, Sekiya M, Koga T (2012) *Theor Chem Acc* 131:1124
30. Becke AD (1993) *J Chem Phys* 98:5648
31. Lee C, Yang W, Parr RG (1988) *Phys Rev B* 37:785
32. Perdew JP, Burke K, Ernzerhof M (1996) *Phys Rev Lett* 77:3865
33. Perdew JP, Burke K, Ernzerhof M (1997) *Phys Rev Lett* 78:1396
34. Zhao Y, Truhlar DG (2008) *Theor Chem Acc* 120:215
35. Peverati R, Truhlar DG (2011) *J Phys Chem Lett* 2:2810
36. Simons J (1991) *J Phys Chem* 95:1017
37. Velders GJM, Feil D (1992) *J Phys Chem* 96:10725
38. Pople JA, Nesbet RK (1954) *J Chem Phys* 22:571
39. Engelking PC, Lineberger WC (1977) *J Chem Phys* 6:5054
40. Bagus PS, Preston HJT (1973) *J Chem Phys* 59:2986
41. Lykos P, Pratt GW (1963) *Rev Mod Phys* 35:496

A General Geometric Representation of Sphere-Sphere Interactions

Ho-Kei Chan, Eric B. Lindgren, Anthony J. Stace
and Elena Bichoutskaia

Abstract A general geometric representation of sphere-sphere interactions is derived using the bispherical coordinate system. It presents a dimensionless, scaled surface-to-surface separation parameter s^* , which is valid for all possible combinations of sphere size and separation distance. The proposed geometric description is not limited to sphere-sphere interactions, but also describes interactions that involve a point particle or a plane. The surface-to-surface separation parameter approaches the limit of $s^* = 1$ if the radii of both spheres are much smaller than the actual surface-to-surface separation distance s , i.e. in the limit of two point particles. On the other hand, the geometric limit of $s^* = 0$ corresponds to two planes, namely when the radii of both spheres are much larger than s .

Keywords Sphere-sphere interactions · Bispherical coordinates · Geometric description · Surface-to-surface separation · Inverse points

1 Introduction

Much research has been carried out on pairwise interactions, notably in the area of classical electrostatics [1–7], in which each interacting body is geometrically described as a point particle, a sphere or a plane. As shown in Fig. 1, the geometries include the interaction between a pair of point particles (as described by Coulomb's law in the case of two point charges), the interaction between two spheres, as well

H.-K. Chan (✉) · E.B. Lindgren · A.J. Stace · E. Bichoutskaia (✉)
Department of Physical and Theoretical Chemistry, School of Chemistry,
University of Nottingham, University Park, Nottingham NG7 2RD, UK
e-mail: epkeiyeah@yahoo.com.hk

E. Bichoutskaia
e-mail: elena.bichoutskaia@nottingham.ac.uk

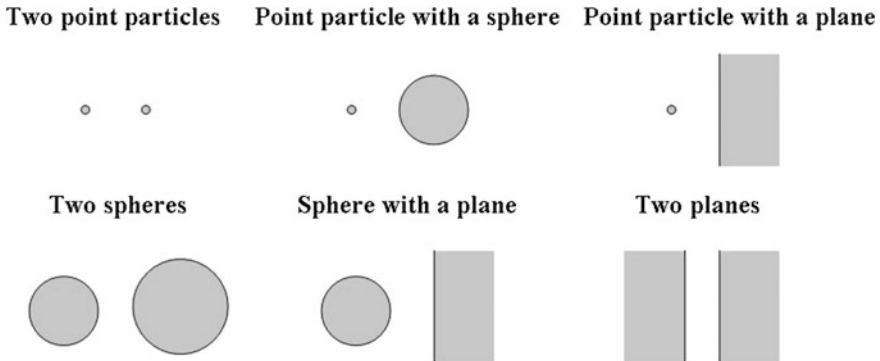


Fig. 1 Different geometric combinations for pairwise interactions involving point particles, spheres or planes

as four other geometric combinations drawn from the set of a point particle, a sphere and a plane. Note that a point particle and a plane are defined as a sphere of infinitely small and infinitely large radius, respectively.

While the *absolute* geometry of an individual point particle, sphere or plane is mathematically well defined, the geometry of a pair of interacting objects can only be described with respect to their surface-to-surface separation, which is denoted here as a distance s . Note that an alternative description based on the centre-to-centre separation distance would be ambiguous if one of the interacting objects is a plane. We therefore introduce a dimensionless, length-scale independent parameter s^* that describes all possible combinations of sphere size and surface-to-surface separation distance for a two-body system. Generally, a dimensionless separation distance s^* can be obtained by dividing the surface-to-surface separation s by a characteristic length, l , that depends on the sizes of the interacting bodies and their separation, i.e. $s^* = s/l$. For any given surface-to-surface separation s , a suitable choice of the length l will allow one to determine, from $s^* = s/l$, whether a pair of interacting objects is geometrically close to the limit of two point particles, the limit of two planes, or neither of these limits. For a_1 and a_2 being the radii of the interacting objects, any linear combination (or some other simple functions) of a_1a_2 or $(a_1 + a_2)$ is not a suitable form for the length l , because as a_i ($i = 1, 2$) approaches infinity (one of the interacting bodies approaches the planar limit) the value of s^* would approach zero if the value of the other a_i is non-zero. This implies that a system close to the geometric limit of two interacting planes ($a_1 \gg s$ and $a_2 \gg s$) cannot be distinguished from a system containing only one plane. In this paper, it is shown that a suitable choice of the length l can be derived from the bispherical coordinate system [8, 9], which has recently been employed for a study of electrostatic sphere-sphere [2, 10] and sphere-plane interactions [2].

2 Introduction to the Bispherical Coordinate System

In the bispherical coordinate system [8, 9] shown in Fig. 2 for a two-sphere system, the position of any point X in space is described with reference to a pair of foci, which are separated by a distance of $2a$. The foci are defined as inverse points of each other such that

$$d_1 c_1 = a_1^2 \quad (1)$$

and

$$d_2 c_2 = a_2^2. \quad (2)$$

The centre-to-centre separation $h > 0$ is given by

$$h = s + a_1 + a_2 = 2a + c_1 + c_2 \quad (3)$$

where $s \geq 0$ is the surface-to-surface separation. The bispherical coordinates are often denoted as (η, ξ, ϕ) , where

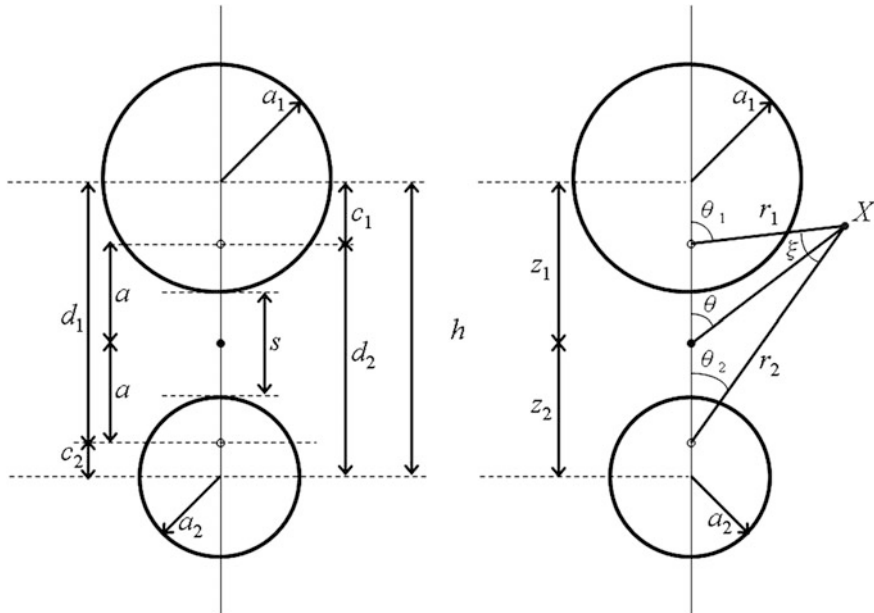


Fig. 2 Schematic diagrams of the bispherical coordinate system. The diagram on the left illustrates how the length quantities c_1 , c_2 , d_1 and d_2 are related to the inter-focal separation $2a$ and to the centre-to-centre separation h , and the diagram on the right illustrates how the position of an arbitrary point X in space is described with reference to the foci

$$\eta \equiv -\ln\left(\frac{r_1}{r_2}\right), \quad (4)$$

$$\xi \equiv \theta_1 - \theta_2 \quad (5)$$

and ϕ is an azimuthal angle about the axis that joins the centres of the spheres. They are related to the Cartesian coordinates (x, y, z) as follows

$$x = \frac{a \sin \xi \cos \phi}{\cosh \eta - \cos \xi}; y = \frac{a \sin \xi \sin \phi}{\cosh \eta - \cos \xi}; z = \frac{a \sinh \eta}{\cosh \eta - \cos \xi}. \quad (6)$$

The surface of each sphere is a surface of constant η , where the parameters

$$\eta = \eta_1 > 0 \quad (7)$$

and

$$\eta = -\eta_2 < 0 \quad (8)$$

represent the surfaces of sphere 1 and sphere 2, respectively. In general, η is positive for the upper half plane occupied by sphere 1 ($z \geq 0$ or $0 \leq \theta \leq \pi/2$) and negative for the lower half plane occupied by sphere 2 ($z \leq 0$ or $\pi/2 \leq \theta \leq \pi$).

3 Derivation of the Scaled Surface-to-Surface Separation

The interfocal separation $2a$ can be expressed as a function of h , a_1 and a_2 . Using Eqs. (1) and (2), together with

$$d_1 = c_1 + 2a \quad (9)$$

and

$$d_2 = c_2 + 2a, \quad (10)$$

two quadratic equations for $c_1 > 0$ and $c_2 > 0$, respectively, are obtained:

$$c_1^2 + 2ac_1 - a_1^2 = 0 \quad (11)$$

and

$$c_2^2 + 2ac_2 - a_2^2 = 0, \quad (12)$$

with solutions

$$c_1 = -a + \sqrt{a^2 + a_1^2} \geq 0 \quad (13)$$

and

$$c_2 = -a + \sqrt{a^2 + a_2^2} \geq 0, \quad (14)$$

respectively. Substituting Eqs. (13) and (14) into Eq. (3) yields

$$h = \sqrt{a^2 + a_1^2} + \sqrt{a^2 + a_2^2} \quad (15)$$

which implies

$$h^2 - 2a^2 - (a_1^2 + a_2^2) = 2\sqrt{a^4 + a^2(a_1^2 + a_2^2) + a_1^2a_2^2}. \quad (16)$$

A further rearrangement of terms leads to the arrival of an expression for the inter-focal separation:

$$\begin{aligned} 2a &= \frac{1}{h} \sqrt{h^4 + (a_1^2 - a_2^2)^2 - 2h^2(a_1^2 + a_2^2)} \\ &= \frac{1}{(s + a_1 + a_2)} \sqrt{(s + a_1 + a_2)^4 + (a_1^2 - a_2^2)^2 - 2(s + a_1 + a_2)^2(a_1^2 + a_2^2)} \end{aligned} \quad (17)$$

which leads to

$$\begin{aligned} \frac{2a}{s} &= \frac{1}{s(s + a_1 + a_2)} \sqrt{(s + a_1 + a_2)^4 + (a_1^2 - a_2^2)^2 - 2(s + a_1 + a_2)^2(a_1^2 + a_2^2)} \\ &= \frac{1}{(1 + a'_1 + a'_2)} \sqrt{(1 + a'_1 + a'_2)^4 + (a'^2_1 - a'^2_2)^2 - 2(1 + a'_1 + a'_2)^2(a'^2_1 + a'^2_2)} \end{aligned} \quad (18)$$

where $a'_1 \equiv a_1/s$ and $a'_2 \equiv a_2/s$ are relative measures of the radii of the interacting spheres with respect to their surface-to-surface separation s . Equation (18) can be written in the following form

$$\frac{2a}{s} = \frac{1}{\left(1 + \frac{1}{a'_1 + a'_2}\right)} \sqrt{\frac{1}{(a'_1 + a'_2)^2} + 4 \left[1 + \frac{\left(\frac{1}{a'_2} + 2a'_1\right)}{\left(1 + \frac{a'_1}{a'_2}\right)} + \frac{\left(\frac{a'_1}{a'_2}\right)}{\left(1 + \frac{a'_1}{a'_2}\right)^2}\right]} \quad (19)$$

which implies

$$\lim_{a'_2 \rightarrow \infty} \frac{2a}{s} = 2\sqrt{(1 + 2a'_1)}. \quad (20)$$

According to Eq. (20), the ratio $2a/s$ diverges only if both a'_1 and a'_2 approach infinity, which suggests that it can be used as a parameter to distinguish between geometries of sphere-plane and plane-plane interactions. If a scaled surface-to-surface separation $s^* \equiv s/2a$ is considered, a normalized parameter that applies to all possible combinations of sphere size and separation distance can be obtained, where it is

$$\lim_{\substack{a'_1 \rightarrow 0 \\ a'_2 \rightarrow 0}} s^* = 1 \quad (21)$$

for the interaction between two point particles, according to Eq. (18). Furthermore,

$$\lim_{\substack{a'_1 \rightarrow 0 \\ a'_2 \rightarrow \infty}} s^* = \frac{1}{2} \quad (22)$$

corresponds to the interaction of a point particle with a plane, according to Eq. (20); and

$$\lim_{\substack{a'_1 \rightarrow \infty \\ a'_2 \rightarrow \infty}} s^* = 0 \quad (23)$$

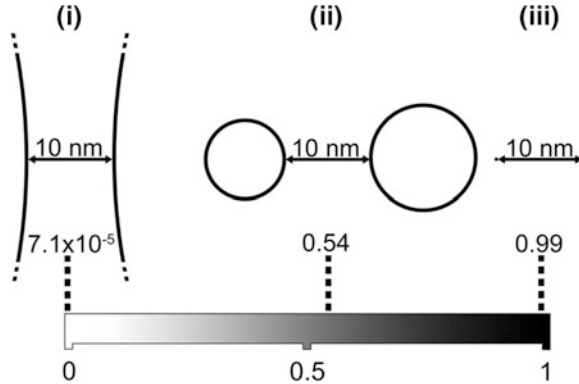


Fig. 3 Schematic illustration of various geometries between the limits $s^* = 0$ to $s^* = 1$, for $s^* \equiv s/2a$. The sphere radii in the given examples, which all correspond to a surface-to-surface separation of $s^* = 10$ nm, are: (i) $a_1 = a_2 = 0.5$ m, (ii) $a_1 = 5$ nm and $a_2 = 7.5$ nm, and (iii) $a_1 = a_2 = 0.05$ nm. At $s^* \rightarrow 0$, the interacting system is close to the geometric limit of two planes, and at $s^* \rightarrow 1$, the system is close to the geometric limit of two point particles. The range of values of s^* from 0 to 1 corresponds to a continuum of all possible combinations of sphere size and separation distance

corresponds to the interaction between two planes. As illustrated in Fig. 3, for any possible combination of sphere size and separation distance, the value of s^* lies within the range $[0, 1]$. A value of s^* close to unity indicates that the system is close to the geometric limit of two point particles, and a value of s^* close to zero indicates that it is close to the limit of two planes.

4 Graphical Representation of the Scaled Surface-to-Surface Separation

Figure 4 illustrates how the scaled surface-to-surface separation s^* depends on a_1' and a_2' . As shown in Fig. 4a, each value of s^* for $0 < s^* < 1$ does not correspond to a unique geometry, but rather to a range of possible combinations of a_1' and a_2' . If, for example, a_2' increases while a_1' remains unchanged, the value of s^* would decrease. To return to the original value of s^* , one can move in the direction of decreasing a_1' until the contour line of the original value of s^* is reached. Figure 4b is a ln-Ln plot of the same contour map, which illustrates a difference in the dependence of s^* on a_1' and a_2' between cases of $s^* < 0.5$ and cases of $s^* > 0.5$. Consider the regime of $s^* < 0.5$: At any given value of s^* , if a_1' increases indefinitely, a_2' will decrease towards a finite value. If a_2' decreases towards zero while a_1' increases indefinitely, the value of s^* will instead approach 0.5 which describes, among many others, a point-plane geometry. But if a_2' remains unchanged for increasing a_1' , the value of s^* will decrease towards a finite value, which describes a particular range of sphere-plane geometries.

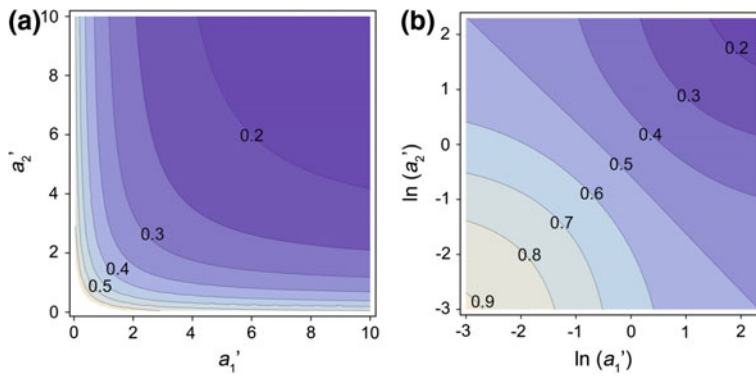


Fig. 4 Contour maps of the scaled surface-to-surface separation $s^* \equiv s/2a$, showing its dependence on a_1' and a_2' in (a), and on $\ln(a_1')$ and $\ln(a_2')$ in (b). The dimensionless parameter s^* approaches unity if the system is close to the geometric limit of two point particles at $a_1' = a_2' = 0$. The values of s^* ranging between 0 and 1 correspond to particular combinations of a_1' and a_2' . The ln-Ln plot in (b) illustrates a difference in the behaviour of s^* between cases of $s^* < 0.5$ and cases of $s^* > 0.5$.

Now consider the regime of $s^* > 0.5$. At any given value of s^* , if a_1' decreases towards zero, a_2' will increase towards a finite value. If a_2' increases indefinitely while a_1' decreases towards zero, the value of s^* will approach 0.5, again for a point-plane geometry. But if a_2' remains unchanged while a_1' decreases, the value of s^* will increase towards a limit which is less than unity, because in this case the parameter s^* describes only a particular range of point-sphere geometries but not the geometric limit of a pair of point particles.

5 Conclusions

A dimensionless, scaled surface-to-surface separation distance $s^* \in [0, 1]$ has been derived from the bispherical coordinate system to describe geometries of sphere-sphere interactions. It serves as a measure of how close a system of interacting spheres is to the geometric limit of two point particles or two planes. A value close to unity indicates that the system is close to the limit of two point particles, and a value close to zero indicates that the system is close to that of two planes. This approach applies to all possible combinations of sphere size and separation distance, including ambiguous cases where a description of the interacting bodies as spheres becomes questionable.

Acknowledgments EB gratefully acknowledges an ERC Consolidator Grant for financial support. EBL is supported by a PhD scholarship from the Brazilian Government's Science Without Borders programme (CAPES: 0702/13-7).

References

1. Bichoutskaia E, Boatwright AL, Khachatourian A, Stace AJ (2010) *J Chem Phys* 133:024105
2. Khachatourian A, Chan HK, Stace AJ, Bichoutskaia E (2014) *J Chem Phys* 140:074107
3. Ohshima H (1998) *J Colloid Interface Sci* 198:42
4. Matsuyama T, Yamamoto H, Washizu M (1995) *J Electrost* 36:195
5. Mahanty J, Michalewicz MT (1987) *Aust J Phys* 40:413
6. Raggi G, Stace AJ, Bichoutskaia E (2013) *Phys Chem Chem Phys* 15:20115
7. Messina R (2002) *J Chem Phys* 117:11062
8. Arfken G (1970) *Mathematical Methods for Physicists*, 2nd edn. Academic Press, Orlando, pp 115–117
9. Morse PM, Feshbach H (1953) *Methods of theoretical physics, part II*. McGraw-Hill, New York, p 1298
10. Munirov VR, Filippov AV (2013) *J Exp Theor Phys* 117:809

Understanding the Electronic Structure Properties of Bare Silver Clusters as Models for Plasmonic Excitation

Lindsey R. Madison, Mark A. Ratner and George C. Schatz

Abstract We present a detailed study of the optical properties of tetrahedral silver clusters ranging from Ag_{10} to Ag_{220} using frequency domain (FD) and real-time (RT) time-dependent density functional theory. We compare the electronic structure and optical properties of the clusters calculated with different exchange-correlation functionals, different basis sets, and different DFT software packages. We also present an analysis of the orbital contributions to the density of states, which for the larger clusters can be decomposed into surface and bulk contributions. We find that the description of optical properties is nearly insensitive to the choice of exchange-correlation functional and results are consistent for FD and RT implementations. Optical properties are sensitive to basis set selection however, and it is critical that the basis set correctly describes d-orbitals. We show that FD-TDDFT provides insights into the collective excitation nature of a plasmonic nanoparticle allowing us to investigate the hot electron distribution produced immediately after plasmonic excitation. This analysis shows that the electron distribution is largely a flat function of electron energy in the range between zero and the photon energy for a plasmonic transition whereas it is strongly peaked close to zero for an interband transition.

Keywords Nanoparticle · Optical Response · Intraband Transition · Time Dependent Density Functional Theory · Hot Electrons

L.R. Madison · M.A. Ratner · G.C. Schatz (✉)
Department of Chemistry, Northwestern University,
Evanston, IL 60208-3113, USA
e-mail: schatz@northwestern.edu

L.R. Madison
e-mail: madisonl@u.northwestern.edu

M.A. Ratner
e-mail: ratner@northwestern.edu

1 Introduction

Silver clusters having 20–220 silver atoms have recently played an important role as models for using electronic structure theory to understand the properties of plasmonic nanoparticles [1, 2]. It has been found that bare silver clusters in this size range have optical spectra that are related to what is found for much larger silver particles (10–20 nm) often having strong conduction band transitions in the 2.5–3.7 eV range that are related to the strong plasmon band seen in the extinction spectra of the larger nanoparticles. Significant size-dependent effects have been noted [3], such as strongly blue-shifted extinction bands in the smaller clusters, and by studying a range of cluster sizes, a linear variation of cluster excitation energies with inverse cluster size has been found [4]. Extrapolation of the cluster results to the large particle limit leads to spectra that are in reasonable agreement with the results of electrodynamics calculations for 20 nm clusters [4]. There have also been attempts to study other optical properties for these clusters, such as the Raman spectra of adsorbed molecules [5], and enhancement factors have been estimated [6]. However the intrinsic size-dependence of the cluster optical properties provides significant uncertainty in the connection of these results with surface enhanced Raman spectroscopy (SERS) measurements that are always done on much larger particles. There have been similar optical property studies for bare gold clusters that have been done for silver clusters, however 20 atom gold clusters do not show strong conduction band transitions that are as easily connected with the larger nanoparticle results as for silver [3], so gold clusters have been less popular for these studies. There have also been studies of bimetallic (silver-gold) clusters [7, 8].

The spectra of bare size-dependent silver clusters with about 20 atoms have rarely been studied experimentally, and only limited information is available for cluster sizes up to 22 atoms, in rare gas matrices where structures are unknown [9, 10]. There have also been theory studies using density functional theory [9], including a recent study of clusters sizes up to 75 atoms [11]. These studies show that the ground state of Ag_{20} has a low symmetry, compact structure rather than being a tetrahedron with the energy difference between the structures being 0.98 eV at the PW91 level of theory. Tetrahedral structures have usually been used for Ag_{20} , Ag_{84} , and Ag_{120} as these are closed shell structures that have especially simple spectra (typically dominated by one strong conduction band transition which is sometimes replaced by a clump of closely spaced lines due interaction between the bright state and background states) [4]. For compact clusters other than the tetrahedra [9], one still obtains spectra that are dominated by conduction band transitions, although the conduction band spectra are usually multipeaked. The latter property makes it harder to distinguish intrinsic contributions to the plasmon width from heterogeneous broadening effects. Also, in all spectra there are transitions that arise from D-band orbitals, the interband transitions. These are mostly important at higher energies, but they also define a broad background to the conduction band

structure. All of the discussion in this manuscript is focused on bare silver clusters, but there is also an extensive literature related to clusters with ligands, especially for gold clusters [1], but we will not consider this possibility.

In this paper we study the spectra of bare silver clusters in more detail than in past work, with the goal of determining sensitivity of the results to the electronic structure model used and to cluster structure. We also study the nature of the excited states that are produced in plasmon-like intraband excitation, and contrast that with results for interband excitation that is also found for the clusters we have studied. Much of our focus is on the tetrahedral structures of Ag_{20} and Ag_{84} , corresponding to particles between 0.9 and 1.5 nm in size, so that we can study trends in the results with cluster size. However we also consider a broader range of clusters going from Ag_{10} to Ag_{220} to establish trends in the results with cluster size. In all calculations we use time-dependent density functional theory (TDDFT), but here we consider both the frequency domain (FD) version that is contained in NWChem and Amsterdam Density functional theory (ADF) and the real-time (RT) version that is available in CP2K. These three codes provide access to a variety of density functionals and basis sets, so it is important to determine how the results differ as there have been many recent calculations based on these codes [1, 12–14], using the Ag_{20} cluster as a reference for understanding SERS. Both NWChem and CP2K rely on pseudopotentials for describing the core electrons, and we also investigate a jellium model for a pseudopotential and a dual-space separable model.

In a RT-TDDFT study, Chen et al. [12] developed a method for calculating absorption spectra of molecules interacting with metal particles by integrating the time-dependent Kohn-Sham equations subject to a short (1 fs) pulse of light that couples to the molecule and particle through the dipole $\mu \cdot E$ interaction. The field E is obtained either for the field in vacuum or from an electrodynamics calculation if one wants to include a nearby particle. In the latter case, this approach makes it possible to describe plasmon enhancement classically, and then the molecular response with RT-TDDFT (and thus the method is called QM/ED). In this procedure, the induced dipole resulting from the $\mu \cdot E$ perturbation is Fourier transformed to determine the polarizability. The absorption is proportional to the imaginary part of the polarizability. A key component of this approach is that the dipole is assumed to be damped in determining the Fourier transform, using a damping energy (0.1 eV) that is derived from the plasmon width for bulk silver. Except for the electrodynamics description of the metal particle, the theory is the time domain version of a frequency domain approach that included damping that was developed by Jensen et al. [15] and used with the ADF code. In either the frequency or time domain, the inclusion of a cluster of atoms from the particle in the TDDFT calculation makes it possible to describe chemical effects in SERS. However this procedure was not done in the past work, and no silver cluster extinction spectra were generated using TDDFT.

A similar QM/ED theory, but now in the frequency domain, was recently presented by Mullin and coworkers [13, 14], who used an approach similar to Jensen and coworkers, but with the NWChem code. In describing SERS, the particle is

treated with classical electrodynamics, and then the field is input to a TDDFT calculation for the particle.

In a later paper, this approach was extended to include a cluster of metal atoms to describe the chemical effect in SERS with a separate calculation where classical electrodynamics is used to describe electromagnetic enhancements, using what was termed an overlay theory [16].

What is still missing in this previous work is a unified calculation that includes both chemical and electromagnetic effects for large clusters. A reason for this is that realistic cluster models of plasmonics are still quite limited. The present study is therefore motivated by these earlier papers, as the ability of electronic structure codes to describe silver clusters is crucial to the ultimate goal of including a cluster of silver atoms in the QM/ED calculation.

Silverstein and Jensen have recently studied the effect of using long-range corrected density functionals on the spectra of Ag_n ($n = 4\text{--}20$) [17]. For the smaller clusters, coupled cluster calculations were also done to provide a higher level reference for comparison with the TDDFT results. Several functionals were considered, and in general it was found that the corrected functionals give more accurate ionization potentials. The influence of these functionals on the absorption spectra of Ag_{20} is more subtle, with only small improvements in the absorption spectra. This also provides motivation for the present study, where we examine very simple functionals to see if these might be adequate for the description of absorption spectra.

2 Methods

Time dependent density functional theory has been implemented in two different ways; in the time domain referred to as real-time TDDFT (RT-TDDFT) and in the frequency domain (FD-TDDFT). These two methods are equivalent in that they both solve the time-dependent Kohn-Sham equations using a scheme proposed by Runge and Gross [18]. However there are differences in their implementation in different codes, as we show below, such that even the same functional and basis set can give different results. Below we describe our implementation of these approaches where we have considered both calculations that make the different codes as close as possible, and where we also consider unique capabilities of each code.

2.1 RT-TDDFT

RT-TDDFT has been implemented using the CP2K molecular simulation software with pseudopotentials to simplify the electronic description [19]. These pseudopotentials account for 36 core electrons and the nuclear charge in each Ag atom, thus the potentials are optimized for eleven valence electrons [20]. Two different types of pseudopotentials were explored: a separable dual-space Gaussian

Pseudopotential and a Jellium model. Hybrid Gaussian and plane wave basis sets are used in these calculations [21]. These basis sets have been optimized for selected exchange-correlation (XC) functionals, namely the PBE and Pade XC functional, and as a result the PBE calculation based on CP2K is not rigorously the same as the PBE calculation with NWChem or ADF.

Geometry optimizations were performed on each initial silver cluster we considered and with each choice of functional and pseudopotential, using the conjugate gradient method. Following geometry optimization, RT-TDDFT was performed with CP2K, using a timestep of 1 atomic unit, 2.42×10^{-17} s, and each calculation has a total of 2,000 steps, or 48.4 fs duration. The RT-TDDFT calculations determine the time-dependent dipole moment of the molecule, which can be used to determine the optical spectra. This approach has been described by Chen [12] and will be briefly reviewed here.

To calculate spectra, the time-dependent dipole moment, $P_j(t)$ is used to calculate the induced time-dependent dipole $P_j^I(t)$ using:

$$P_j^I(t) = P_j(t) - P_j(0); \quad (1)$$

A damped dipole is then defined:

$$P_j^{I,D}(t) = P_j^I(t)e^{-\Gamma t} \quad (2)$$

to incorporate the effects of excited state damping due to dephasing and relaxation. The damping parameter Γ is chosen to be 0.10 eV, which is consistent with earlier work [12], and it leads to $e^{-\Gamma t}$ being 6.4×10^{-4} at the end of the time integration. Although this is an ad hoc method for incorporating the effect of a finite plasmon lifetime on optical response, it is consistent with the previous RT work [12] and is also related to earlier FD theory [4]. The main difference between the FD and RT approaches is that the FD evaluation is done in the linear response approximation while this is not required in RT. However the fields we impose in the RT calculations are sufficiently weak that the linear-response limit is satisfied.

The Fourier transform of the induced, damped dipole is defined in the usual way, and is approximated to be a sum over the simulation time (2,000 time-steps, 48 fs):

$$P_j^{I,D}(\omega) = \int e^{i\omega t} P_j^{I,D}(t) dt = \sum_{i=0}^T e^{i\omega t_i} P_j^{I,D}(t_i) \quad (3)$$

The polarizability associated with an induced dipole in the j direction that results from light polarized in the i direction is then given by:

$$\alpha_{ij}(\omega) = \frac{P_j^{I,D}(\omega)}{E_i(\omega)} = \frac{\sum_n e^{i\omega t_n} P_j^{I,D}(t_n)}{E_i(\omega)} \quad (4)$$

The absorption cross section is defined as proportional to the sum of the imaginary components of the polarizability:

$$\sigma(\omega) = \frac{4\pi\omega}{c} \left\langle \frac{1}{3} (\alpha_{xx} + \alpha_{yy} + \alpha_{zz}) \right\rangle_{\text{imaginary}} \quad (5)$$

2.2 FD-TDDFT

TDDFT is implemented in NWChem [22, 23] and ADF [24–26] in the frequency domain with the random phase approximation (RPA) to determine the frequency and intensities of single electron transitions. The PBE generalized gradient approximation [27] was employed for the ADF and NWChem calculations as it was for the CP2K calculations.

For NWChem, the CRENBS basis set, a Gaussian basis set, was used along with the accompanying effective core potential in NWChem [28]. The effective core potential is comparable in purpose to the pseudopotentials used in CP2K except that the CRENBS is of the form of a Gaussian expansion while the CP2K pseudopotentials are separated into local and nonlocal Gaussian functions with the use of error functions [19]. NWChem has the added capability of utilizing symmetry to simplify the geometry optimization. Unfortunately, because tetrahedral symmetry (Td) is a non-abelian symmetry group, this high symmetry cannot be utilized in the TDDFT calculations with NWChem. C2 symmetry, which is an abelian symmetry group, was employed during the TDDFT calculation instead.

For ADF, the TZP.4p basis set was used. This basis set is known as a large core basis set. Rather than representing the core electrons as a pseudopotential, the core states are kept frozen in their atomic orbital configuration. That is, the energy levels that make up the noble gas core (Kr) of each silver atom are still present but they are not perturbed by the existence of neighboring atoms while the valence $5s^2$ and $4d^9$ electrons are perturbed. This has the benefit of making TDDFT calculations of large clusters tractable. Furthermore, ADF takes advantage of tetrahedral symmetry and the abelian symmetry group, further reducing computational time and memory requirements.

For both ADF and NWChem, two methods are available to determine the optical spectra of the silver clusters: first, the calculation of the linear response at each frequency, and second, the calculation of the poles of the response function. The calculation of linear response is implemented in the AOResponse module [15, 29, 30] and a 0.1 eV energy discretization was used. The calculation of the poles of response function is implemented in the NWChem TDDFT module and the ADF Excitations module [31, 32]. The poles of the response function are broadened using a convolution of the poles of the response function with a Lorentzian function that has a full width at half maximum of 0.2 eV, consistent with previous work [4].

3 Results and Discussion

3.1 Comparison of RT-TDDFT and FD-TDDFT

3.1.1 Optical Properties

We first consider the absorption spectrum of Ag_{20} and Ag_{84} with the level of theory of ADF, NWChem and CP2K chosen to be as close to the same as possible. Thus we use PBE for all calculations, with the primary difference being in the pseudo-potential and basis set. Figure 1 presents the resulting spectra, including stick spectra derived from the FD calculations. For Ag_{84} we did not include NWChem results as the computational memory requirements needed to study this system are beyond our capabilities due to the lack of inclusion of tetrahedral symmetry in the calculations.

We see that the absorption spectra from the different codes are similar, but not the same. There is a strong intraband transition at 3.6 eV for Ag_{20} and 3.0 eV for Ag_{84} , with the differences between the three codes being less than 0.2 eV for each cluster. In addition, there are interband transitions at higher energies (4–6 eV). These correspond to transitions from filled the D-band to unoccupied SP-band, and we see that CP2K predicts a greater number of interband transitions and at greater intensity than the other codes.

A broader comparison between the optical properties from RT and FD calculations is presented in Fig. 2. Also included in this figure are results previously generated by Aikens [4] using ADF with the BP86 functional and a DZ basis set. The figure indicates that all methods show a nearly linear relationship between the

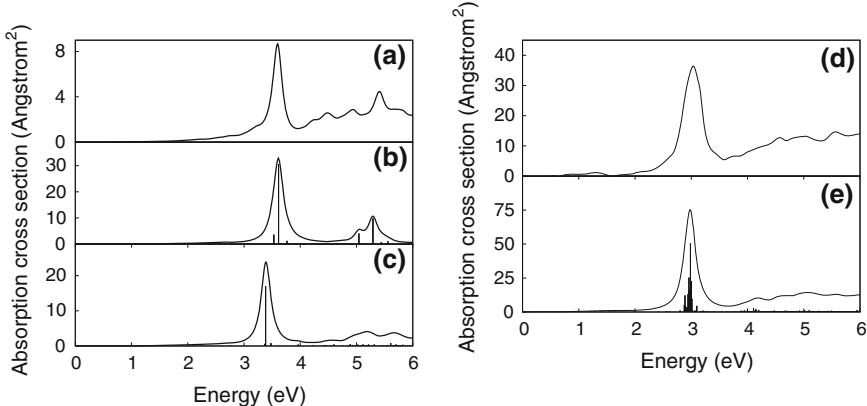


Fig. 1 Optical spectra of Ag_{20} (left) and Ag_{84} (right) calculated from the time domain implementation CP2K (XC:PBE) (top), a frequency domain implementation using NWChem (XC: PBE; Basis Set: CRENBS) (middle, left) and another frequency domain implementation using ADF (XC:PBE; Basis Set: TZVP.4P) (bottom). For Ag_{84} only the CP2K (top) and ADF (bottom) results are presented

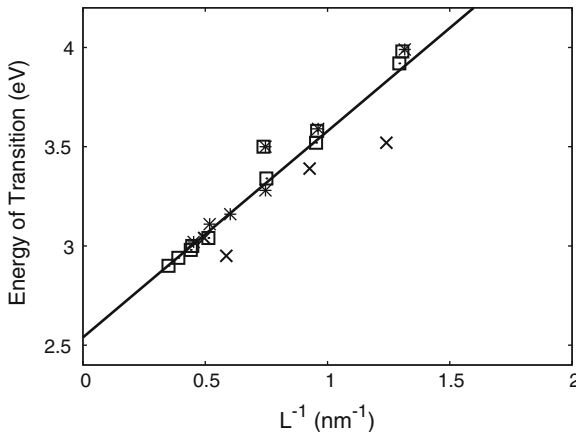


Fig. 2 Energy of the plasmon transition versus the inverse of edge length for clusters ranging in sizes from Ag_{10} to Ag_{220} calculated with RT-TDDFT results (squares) shows good agreement with the results from Aikens [4] using FD-TDDFT method with ADF and a DZ basis set with BP86 XC functional (stars). Also plotted are FD-TDDFT calculations using ADF and the TZP basis set with the PBE functional (X symbols). Line fit $E(\text{eV}) = 1.04 \pm 0.8 (\text{eV nm}) L^{-1} (\text{nm}^{-1}) + 2.54 \pm 0.06 (\text{eV})$

inverse of the edge length of the tetrahedral nanoparticles and the energy of the dominant transition. Our RT results compare well with previous work performed by Aikens et al., and we see that the linear relationship continues to larger particles, Ag_{165} and Ag_{220} than were considered in the FD studies. The linear relationship in Fig. 2 indicates asymptotic convergence (large particle limit) of the absorption peak at 2.54 eV.

3.1.2 Electronic State Density

Similarities in optical spectra are reflected in similarities in the electronic state density as seen in Fig. 3 where Ag_{20} and Ag_{84} are compared. For NWChem and ADF, only electronic states between approximately -10 and 10 eV are considered while CP2K includes much higher energy states, up to 70 eV. As particle size increases, predictably, the number of states increases as well. However the relative positions of the D-band and SP-band do not change, and in fact the results for the three codes for energies within a few eV of the Fermi energy are reasonably close.

The high density of states in the range -8 to -2 eV is due to the D-band. Notice that the D-orbitals are lower energy in the NWChem results than those calculated by CP2K and ADF in Fig. 3. This could make the interband transitions less accessible in the NWChem results, but the results in Fig. 1 show little difference with ADF. States higher than -2 eV are SP hybrid states with some D-orbital character included.

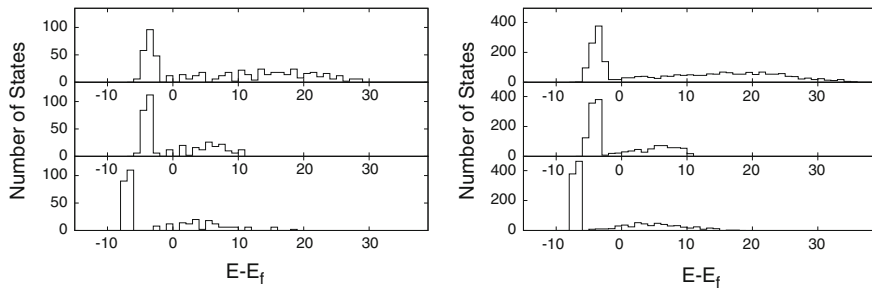


Fig. 3 The density of states as calculated by CP2K (top), ADF (middle), and NWChem (bottom) for Ag_{20} (left) and Ag_{84} (right)

3.1.3 Comparison of RT-TDDFT Results for Different Exchange-Correlation Functionals, Pseudopotentials, and Basis Set Descriptions

Two exchange-correlation functionals were used in CP2K, the PBE functional [27] and the Pade LDA functional [33]. Optical spectra (Fig. 4a, b) using these different methods are very comparable both in the location of the intraband transitions and the intensity of the transitions. The pseudopotential choice for the jellium model resulted in qualitatively different optical spectra (Fig. 4c), specifically in the energy location and predicted intensities of both the intra and interband transitions. The Pade LDA XC functional has two optimized basis sets, one with 11 valence electrons, and the other with 1 valence electron per silver atom. When the basis set

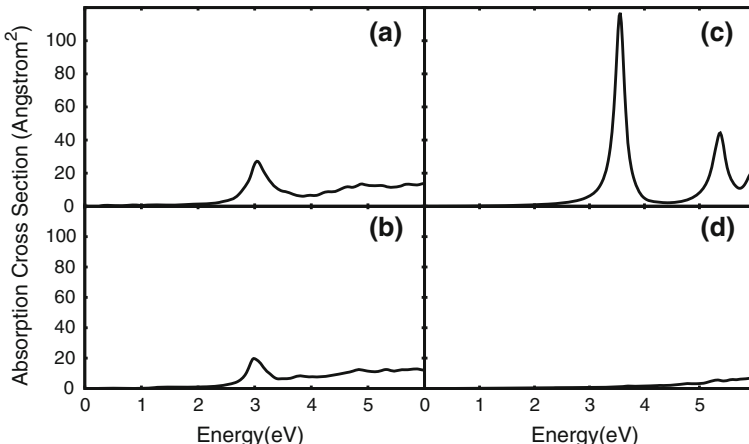


Fig. 4 Optical spectra of Ag_{84} tetrahedral clusters calculated with CP2K and different exchange-correlation functionals. **a** PBE; **b** Pade LDA with 11 valence electrons per silver atom; **c** Pade LDA with the jellium pseudopotential; **d** Pade LDA with 1 valence electron per silver atom

with only one valence electron is used, the electronic absorption spectrum shows no transitions in the energy range considered (Fig. 4d).

Some electronic understanding of these spectra can be obtained from the ground state electronic structure of the clusters. CP2K reports the decomposition of the states into their angular momentum contributions. This is presented in Fig. 5. The lowest energy states between -8 and -2 eV and the highest state density are mostly D in character. Between -2 and 25 eV the states are a mixture of P and D character, followed by an S-band at 30 eV, and a P-band at 37 eV. Regardless of the XC functional and corresponding optimized basis set used in CP2K, the density of states and contributions for S, P and D orbitals are qualitatively similar as can be seen when comparing Fig. 5a with Fig. 5b.

When using a Jellium model to describe the pseudopotential (Fig. 5c) there are no low energy states of D character observed. The differences between density of states of the Jellium model and the Pade LDA model seem to indicate that the D-band plays an important role in energy and intensity of both the interband and intraband transitions. For Ag_{84} the optical spectrum using the Jellium pseudopotential model and hybrid Gaussian separable dual-space pseudopotentials (Fig. 4b, c) have a similar dominant feature near 3 eV. However, the intensities of transitions are not comparable, the energies of the intraband transition disagree by about 0.5 eV, and the intraband transitions differ significantly qualitatively.

Figure 5d shows that a basis set describing only one valence electron modeled with S and P orbitals is insufficient at capturing the interband and intraband transitions in Fig. 4. The density of states profile is very dissimilar to the 11 valence

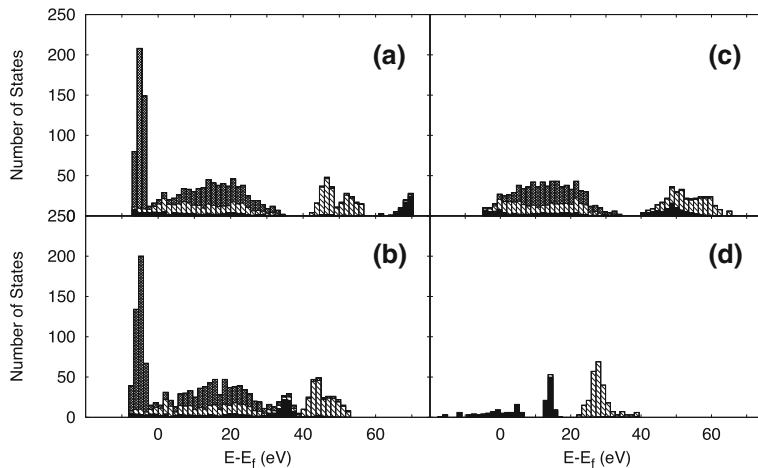


Fig. 5 The density of states for Ag_{84} decomposed into the contribution of silver's atomic orbitals: S (solid black), P (diagonal lines), and D (hatch marks) modeled with **a** the PBE XC functional and accompanying optimized basis set, **b** the Pade XC functional and the accompanying optimized basis set for 11 valence electrons, **c** the Pade XC functional and the Jellium pseudopotential for 11 valence electrons, and **d** the Pade XC functional with the optimized basis set for 1 valence electron per silver atom and the separable dual-space pseudopotential

electron models (Fig. 5a–c). The lack electronic transitions in Fig. 4 may be ascribed to the minimal number of electrons in this model and the complete lack of D orbitals in the basis set.

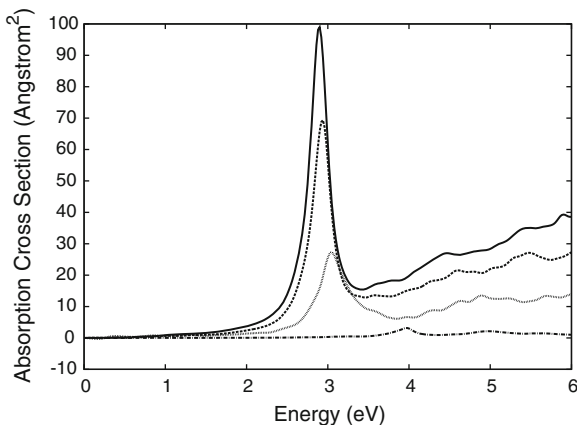
3.1.4 Size and Geometry of Clusters

We varied the tetrahedral cluster size from Ag_n from $n = 10, 20, 35, 56, 84, 120, 165$, and 220 . Figure 6 shows the resulting spectra from a subset of cluster sizes, based on CP2K and the PBE functional, with full geometry optimization performed on all clusters smaller than 165 atoms. A red shift in the plasmon-like intraband transition is seen as the cluster size goes from Ag_{10} (3.9 eV) to Ag_{220} (2.9 eV). There is only a small change of 0.1 eV between the energy of intraband transitions as the particles increase from Ag_{84} to Ag_{220} . Predictably, the intensities of both the intraband transition and the interband transitions increase as the cluster size increases.

Figure 7 demonstrates the difference in the optical spectra between an open shell Ag_{35}^{+1} and a closed shell Ag_{35}^{-5} . The optical spectrum of Ag_{35}^{+1} has two transitions of nearly equal intensity in the intraband region. Ag_{35}^{-5} , however has only one peak as is consistent with the other closed shell silver tetrahedral particles. This shows sensitivity of the results to shell closing, and it provides justification for considering a consistent series of closed shell structures in this study.

Figure 8 shows densities of states of the Ag_{120} cluster, here organized according to the orbitals that belong to atoms in the outer two layer shell of silver atoms, or atoms in the inner core of the cluster (see inset of figure). There are more shell states than core states because there are more shell atoms (100) than core atoms (20). The figure shows that the shell states are found throughout the energy range important to plasmonic transitions, so at least in this size range it is not useful to partition the atoms into shell and core atoms. This may be related to the fact that the even the core atoms are relatively close to the surface.

Fig. 6 Optical absorption spectra calculated with CP2K of four different size tetrahedral clusters, Ag_{220} (solid line), Ag_{165} (dashed line), Ag_{84} (dotted line), Ag_{10} (dashes and dots)



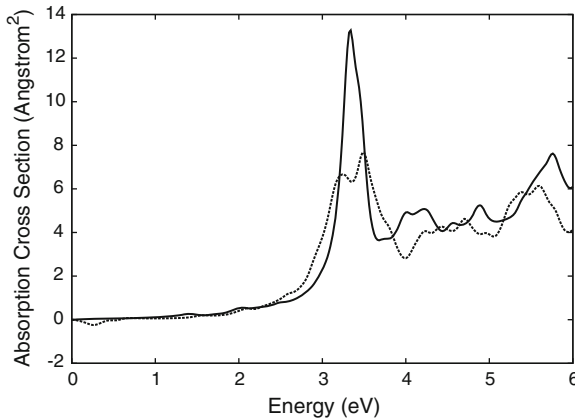


Fig. 7 Optical absorption spectra of Ag_{35}^{-5} (solid) and Ag_{35}^{+1} (dashed) using RT-TDDFT and the PBE XC functional and PBE optimized basis set. Ag_{35}^{-5} has a closed shell electronic structure Ag_{35}^{+1} does not

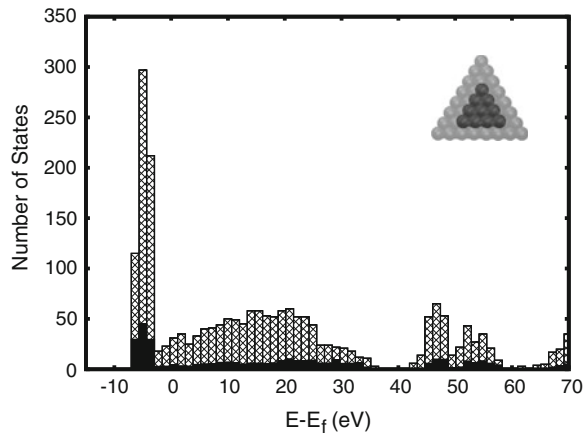


Fig. 8 Contribution of orbitals from the outer shell Ag atoms (solid black) and the inner core Ag atoms (hatch marks) for Ag_{120} . The shell atoms contribute most to the excited states closest to the fermi level. *Inset* The shell atoms (light gray) are distinguished from the inner core atoms (dark gray) in the Ag_{120} cluster in the *inset*

4 Insights into Hot Electron Properties

A significant benefit of the FD approach is the added chemical intuition derived from expressing the electronic excitation as a linear combination of orbital excitations in the silver atomic orbital basis. Figure 9 is an energy level diagram that shows that for the Ag_{84} cluster, the plasmon peak found at 2.98 eV is made up of 15

transitions from the occupied SP hybrid orbitals to the virtual SP hybrid orbitals. This can be characterized as an intraband transition and is consistent with a classical electrodynamic description. As seen on the right in Fig. 9, the single particle transitions of a high energy (4.11 eV) pole of the linear response function originate from occupied D atomic orbitals combined with some transitions that have SP character. This single particle transition diagram is typical of all of the higher energy poles of the linear response function between 3.5 and 6 eV and is consistent with the D character of interband transitions observed in bulk silver.

To gain insight into the hot electron population after plasmonic excitation, we sum over the weights of the single particle transitions that make up each electronic transition. This can be expressed as:

$$\Delta N(m) = \sum_i \sum_{j \in X} w_{ij}(m) f_j \quad (6)$$

where $\Delta N(m)$ is the change in occupancy of unoccupied state m due to single particle transitions i that comprise the electronic transitions j in the region of the spectrum X , where X is chosen to be either interband or intraband transitions. $\Delta N(m)$ is calculated from the weight, w_{ij} , of the single particle transition and oscillator strength f_j .

The change in hot electron population due to the intraband transition for Ag_{84} (between 2.5 and 3.5 eV) in Fig. 1e is shown in the top panel of Fig. 10. The plasmon transition produces hot electrons with a wide range of electron energies above the Fermi level, with the distribution being nearly a flat function of electron energy up to the maximum allowed by energy conservation. In contrast to this, the electron population for interband transitions in Ag_{84} (the bottom panel) is peaked near zero energy, indicating the dominance of transitions in which the final state is close to the Fermi energy.

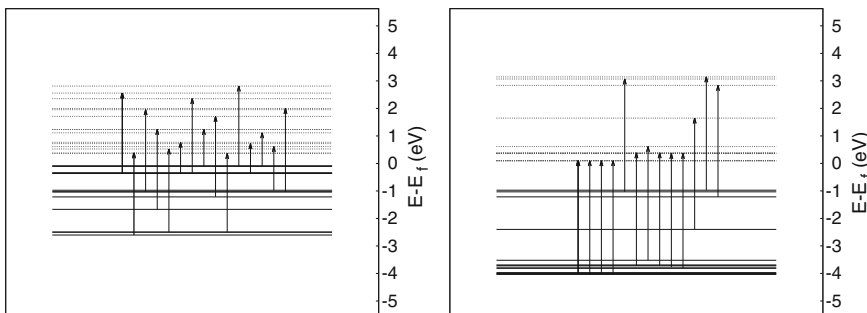


Fig. 9 This is an energy level diagram showing the single particle transitions that make up the dominant (plasmon-like) excitation at 2.98 eV in the absorption spectrum of Ag_{84} (left) and a higher, interband transition at 4.11 eV (right). The horizontal lines indicate the occupied (solid) and virtual (dashed) atomic orbitals of the system. The Y axis is the energy from the fermi energy. The vertical arrows indicate the single particle transitions that make up a single pole of the linear response function. The width of a vertical line reflects the weight or importance of that single particle transition in the overall excitation

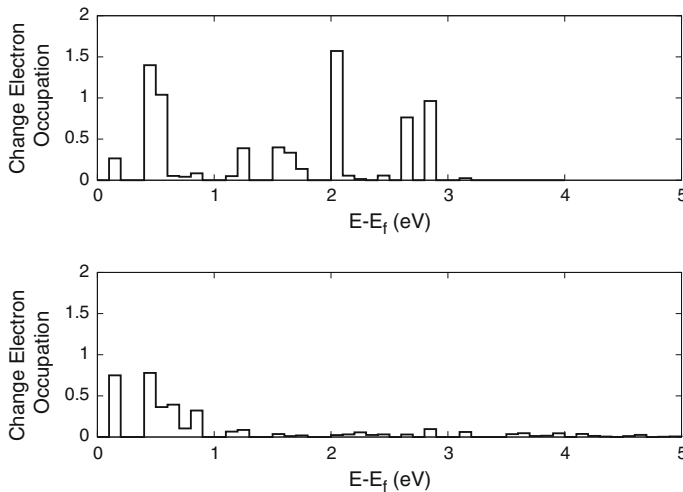


Fig. 10 The vertical axis refers to the change in electron occupation for the electronic states at energies above the Fermi energy, as indicated by the horizontal axis. Here we compare the population change from two regions of the Ag_{84} spectrum seen in Fig. 1, for the plasmon-like dominant transition at 3 eV (top), and for the interband transitions from 3.75 to 5 eV (bottom)

5 Conclusions

We have performed TDDFT calculations on a range of silver tetrahedral nanoparticle sizes using time domain and frequency domain methods. The optical response of the silver tetrahedral nanoparticles can be characterized as having a dominant intraband transition around 3 eV, with the smallest clusters being blue shifted relative to the larger clusters. The three codes we considered all give similar results for optical spectra and state densities when the functionals, basis sets and pseudopotentials are chosen to be as similar as possible. This is an encouraging result, as it means that we can use the different methods somewhat interchangeably. Using RT-TDDFT we have also determined that both GGA and LDA exchange-correlation functionals give similar optical response. It is important to use an appropriate basis set that includes 11 valence electrons for each silver atom and accurately describes the D orbitals. Using NWChem and ADF, both FD-TDDFT methods, we found that a smaller basis set is sufficient for determining linear response properties and the poles of the response function.

The electronic transitions can be described as a linear combination of single particle transitions from occupied atomic orbitals to unoccupied atomic orbitals. It was found that interband, plasmon-like transitions near 3 eV result in electron populations that are largely a flat function of electron energy. It has been found that states far above the Fermi level are excited with significant probability. However intraband transitions result in electrons close to the Fermi level.

Acknowledgments This research was supported by the Department of Energy, Basic Energy Sciences, under grant DOE DE-FG02-10ER16153. L.R.M. was supported by the National Science Foundation through a Graduate Research Fellowship under grant number DGE-1324585.

References

1. Jensen L, Aikens CM, Schatz GC (2008) *Chem Soc Rev* 37(5):1061
2. Morton SM, Silverstein DW, Jensen L (2011) *Chem Rev* 111(6):3962
3. Aikens CM, Schatz GC (2006) *J Phys Chem A* 110(49):13317
4. Aikens CM, Li S, Schatz GC (2008) *J Phys Chem C* 112(30):11272
5. Zhao L, Jensen L, Schatz GC (2006) *J Am Chem Soc* 128(9):2911
6. Zhao LL, Jensen L, Schatz GC (2006) *Nano Lett* 6(6):1229
7. Weissker HC, Mottet C (2011) *Phys Rev B* 84(16):165443
8. López Lozano X, Mottet C, Weissker HC (2013) *J Phys Chem C* 117(6):3062
9. Harb M, Rabilloud F, Simon D, Rydlo A, Lecoultr S, Conus F, Rodrigues V, Félix C (2008) *J Chem Phys* 129(19):194108
10. Fedrigo S, Harbich W, Buttet J (1993) *Phys Rev B* 47(16):10706
11. Itoh M, Kumar V, Adschari T, Kawazoe Y (2009) *J Chem Phys* 131(17):174510
12. Chen H, McMahon JM, Ratner MA, Schatz GC (2010) *J Phys Chem C* 114(34):14384
13. Mullin J, Schatz GC (2012) *J Phys Chem A* 116(8):1931
14. Mullin JM, Autschbach J, Schatz GC (2012) *Comput Theor Chem* 987(C):32
15. Jensen L, Autschbach J, Schatz GC (2005) *J Chem Phys* 122(22):224115
16. Mullin JJ, Valley NN, Blaber MG, Schatz GC (2012) *J Phys Chem A* 116(38):9574
17. Silverstein DW, Jensen L (2010) *J Chem Phys* 132(19):194302
18. Runge E, Gross EK (1984) *Phys Rev Lett* 52(12):997
19. Goedecker S, Teter M, Hutter J (1996) *Phys Rev B* 54(3):1703
20. Hartwigsen C, Goedecker S, Hutter J (1998) *Phys Rev B* 58(7):3641
21. Lippert G, Hutter J, Parrinello M (1999) *Theor Chem Acc: Theor Comput Model (Theoretica Chimica Acta)* 103(2):124
22. Valiev M, Bylaska EJ, Govind N, Kowalski K, Straatsma TP, Van Dam HJJ, Wang D, Nieplocha J, Apra E, Windus TL, de Jong WA (2010) *Comput Phys Commun* 181(9):1477
23. Windus T, Bylaska E, Dupuis M, Hirata S, Pollack L, Smith D, Straatsma T, Aprà E (2003) NWChem: new functionality computational science. In: Sloot P, Abramson D, Bogdanov A, Gorbachev Y, Dongarra J, Zomaya A (eds) *ICCS 2003*. Springer, Berlin, pp 168–177
24. Te Velde G, Bickelhaupt FM, Baerends EJ, Fonseca Guerra C, van Gisbergen SJ, Snijders JG, Ziegler T (2001) *J Comput Chem* 22(9):931
25. Guerra CF, Snijders JG, Te Velde G, Baerends EJ (1998) *Theor Chem Acc: Theory, Comput Model (Theoretica Chimica Acta)* 99(6):391
26. Baerends EJ, Ziegler T, Autschbach J, Bashford D, Bérces A, Bickelhaupt FM, Bo C, Boerrigter PM, Cavallo L, Chong DP, Deng L, Dickson RM, Ellis DE, van Faassen M, Fan L, Fischer TH, Guerra CF, Franchini M, Ghysels A, Giammona A, van Gisbergen SJA, Götz AW, Groeneveld JA, Gritsenko OV, Grüning M, Gusarov S, Harris FE, van den Hoek P, Jacob CR, Jacobsen H, Jensen L, Kaminski JW, van Kessel G, Kootstra F, Kovalenko A, Krykunov MV, van Lenthe E, McCormack DA, Michalak A, Mitoraj M, Morton SM, Neugebauer J, Nicu VP, Noddleman L, Osinga VP, Patchkovskii S, Pavanello M, Philipsen PHT, Post D, Pye CC, Ravenek W, Rodriguez JJ, Ros P, Schipper PRT, Schreckenbach G, Seldenthuis JS, Seth M, Snijders JG, Solà M, Swart M, Swerhone D, te Velde G, Vernooyjs P, Versluis L, Visscher L, Visser O, Wang F, Wesolowski TA, van Wezenbeek EM, Wiesenekker G, Wolff SK, Woo TK, Yakovlev AL ADF: density functional theory (DFT) software for chemists. URL <http://www.scm.com/>
27. Perdew JP, Burke K, Ernzerhof M (1996) *Phys Rev Lett* 77(18):3865

28. LaJohn LA, Christiansen PA, Ross RB, Atashroo T, Ermler WC (1987) *J Chem Phys* 87 (5):2812
29. Krykunov M, Autschbach J (2005) *J Chem Phys* 123(11):114103
30. Krykunov MM, Banerjee AA, Ziegler TT, Autschbach JJ (2005) *J Chem Phys* 122(7):074105
31. Kootstra F, de Boeij PL, Snijders JG (2000) *J Chem Phys* 112(15):6517
32. Romaniello P, de Boeij P (2005) *Phys Rev B* 71(15):155108
33. López-Boada R, Karasiev V, Liu S (1997) *Chem Phys Lett* 270(5–6):443

Part II

Structure and Properties

Optimized Perturbation Theory for Calculating the Hyperfine Line Shift and Broadening of Heavy Atoms in a Buffer Gas

Olga Yu. Khetselius

Abstract A consistent relativistic approach, based on the atomic gauge-invariant relativistic perturbation theory and the exchange perturbation theory, is presented and applied to calculating the interatomic potentials, van der Waals constants, hyperfine structure line collision shift and broadening for heavy atoms in an atmosphere of the buffer inert gas. The corresponding data on the collision hyperfine line shift and broadening for the thallium, alkali (Rb, Cs) and lanthanide (ytterbium) atoms in an atmosphere of the inert gas (He, Kr, Xe) are listed and compared with available alternative theoretical and experimental results.

Keywords Relativistic many-body perturbation theory • Exchange perturbation theory • Interatomic potentials and hyperfine line collision shifts • Alkali and lanthanide atoms in a buffer gas

1 Introduction

The broadening and shift of atomic spectral lines by collisions with neutral atoms has been studied extensively since the very beginning of atomic physics, physics of collisions etc. [1–12]. High precision data on the collisional shift and broadening of the hyperfine structure lines of heavy elements (alkali, alkali-earth, lanthanides, actinides and others) in an atmosphere of the buffer (for example, inert) gases are of a great interest for modern quantum chemistry, atomic and molecular spectroscopy, astrophysics and metrology as well as for studying a role of weak interactions in atomic optics and heavy-elements chemistry [1–24]. As a rule, the cited spectral lines shift and broadening due to a collision of the emitting atoms with the buffer atoms are very sensitive to a kind of the intermolecular interaction. It means that

O.Yu. Khetselius (✉)
Odessa State Environmental University (OSENU),
L'vovskaya Str., 15, Odessa-9 65016, Ukraine
e-mail: okhetsel@gmail.com

these studies provide insight into the nature of interatomic forces and, hence, they provide an excellent test of theory.

An accurate analysis of the spectral line profiles is a powerful technique for studying atomic and molecular interactions and is often necessary for probing matter in extreme conditions, such as in stellar atmospheres, ultracold traps and Bose–Einstein condensates [5–7, 13, 14]. Besides, calculation of the hyperfine structure line shift and broadening allows to check a quality of the wave functions (orbitals) and study a contribution of the relativistic and correlation effects to the energetic and spectral characteristics of the two-center (multi-center) atomic systems. From the applied point of view, the mentioned physical effects form a basis for creating an atomic quantum measure of frequency [22–29]. The corresponding phenomenon for the thallium atom has attracted a special attention because of the possibility to create the thallium quantum frequency measure. Alexandrov et al. [26] have realized the optical pumping thallium atoms on the line of 21 GHz, which corresponds to transition between the components of hyperfine structure for the Tl ground state. These authors have measured the collisional shift of this hyperfine line in the atmosphere of the He buffer gas.

The detailed non-relativistic theory of collisional shift and broadening the hyperfine structure lines for simple elements (such as light alkali elements etc.) was developed by many authors (see, for example, Refs. [1–35]). However, until now an accuracy of the corresponding available data has not been fully adequate to predict or identify transitions within accuracy as required for many applications. It is obvious that correct taking into account the relativistic and correlation effects is absolutely necessary in order to obtain sufficiently adequate description of spectroscopy of the heavy atoms in an atmosphere of the buffer gases. This stimulated our current investigation whose goals were to propose a new relativistic perturbation theory approach to calculating the interatomic potentials and hyperfine structure line collision shifts and broadening for the alkali and lanthanide atoms in an atmosphere of the inert gases. The basic expressions for the collision shift and broadening hyperfine structure spectral lines are taken from the kinetic theory of spectral lines [13, 14, 16, 17, 25–27, 30–32].

The exchange perturbation theory (the modified version EL-HAV) has been used to calculate the corresponding potentials (see details in [1–12]). Let us note that sufficiently detailed reviews of the different versions of exchange perturbation theory are presented, for example, in Refs. [1–21]. It is worth to remind about the known difficulties of the exchange perturbation theory, associated with complex structure series, which contain the overlap integrals and exchange integrals [1, 2]. Due to the ambiguity of the expansion in the antisymmetric functions it had been built a number of different formalisms of an exchange perturbation theory. Usually one could distinguish two groups in dependence on the zero-order approximation of the Hamiltonian. In the symmetry adapted theories the zeroth-approximation Hamiltonian is an asymmetric, but the zeroth-approximation functions have the correct symmetry. In symmetric formalisms there is constructed a symmetric zeroth-approximation Hamiltonian such as the antisymmetric function is its eigen function. Further formally standard Rayleigh–Schrodinger perturbation theory is

applied. However, this approach deals with the serious difficulties in switching to systems with a number of electrons, larger than two. In addition, the bare Hamiltonian is not hermitian.

So the symmetry adapted theories gain more spreading. In particular, speech is about versions as EL-HAV (Eisenschitz-London-Hirschfelder-van der Avoird), MS-MA (Murrel-Shaw-Musher-Amos) and others (see details in Refs. [8–12]). The detailed analysis of advantages and disadvantages of the exchange perturbation theory different versions had been performed by Batygin et al. (see, for example, [25–27, 30–32]) in studying the hyperfine structure line shift of the hydrogen atom in an atmosphere of an inert buffer gas. In our work the modified version of the EL-HAV exchange perturbation theory has been used to calculate the corresponding potentials (see details in [8–10]). On fact [8–10] this is the Schrödinger type perturbation theory for intermolecular or interatomic interactions, using the wave operator formalism. To include all exchange effects, wavefunctions are used whose symmetry with respect to permutations of both electronic and nuclear coordinates can be prescribed arbitrarily. The interaction energy is obtained as a series in ascending powers of the interaction operator. Further van der Avoird [8–10] has proved that every term in this series is real and that the terms of even order are negative definite for perturbation of the ground state. It has been also verified that up to and including third order the results of this theory, if they are restricted to electron exchange only, agree exactly with those of the Eisenschitz-London theory (see other details in Refs. [1–12]).

The next important point is choice of the most reliable version of calculation for multielectron atomic field and generating the basis of atomic orbitals. In Refs. [36–54] a consistent relativistic energy approach combined with the relativistic many-body perturbation theory has been developed and applied to calculation of the energy and spectroscopic characteristics of heavy atoms and multicharged ions. This is the relativistic many-body perturbation theory with the optimized Dirac-Fock (Dirac-Kohn-Sham) zeroth approximation and taking into account the nuclear, radiation, exchange-correlation corrections. It is worth to remind that this approach has been successfully used to calculate the β -decay parameters for a number of allowed (super allowed) transitions and study the chemical bond effect on β -decay parameters [53]. This approach has been used in our work to generate a basis of relativistic orbitals for heavy atoms. Besides, the correct procedures of accounting for the many-body exchange-correlation effects and relativistic orbital basis optimization (in order to provide a performance of the gauge-invariant principle) as well as accounting for the highly excited and continuum states have been used.

Earlier it was shown [40–54] that an adequate description of the energy and spectral characteristics of the multi-electron atomic systems requires using the optimized basis of wave functions. In Refs. [55, 56] a new ab initio optimization procedure for construction of the optimized basis had been proposed and based on the principle of minimization of the gauge dependent multielectron contribution $Im\delta E_{ninv}$ of the lowest QED perturbation theory corrections to the radiation widths of atomic levels. The minimization of the functional $Im\delta E_{ninv}$ leads to the Dirac-Kohn-Sham-like equations for the electron density that are numerically solved. This

procedure has been implemented into our approach. In result, the numerical data on the hyperfine line collision shifts and broadening for some alkali (Rb, Cs), thallium and ytterbium atoms in atmosphere of the inert gas (such as He, Kr, Xe) are presented and compared with available theoretical and experimental data (see, for example, [1–27, 30–32]). Besides, new data on the van der Waals constants and other parameters for the studied two-atomic systems are presented too.

2 Optimized Atomic Perturbation Theory and Advanced Kinetic Theory of Spectral Lines

In order to calculate a collision shift of the hyperfine structure spectral lines one can use the following expression known in the kinetic theory of spectral lines shape (see Refs. [13–17, 25–27, 30–32]):

$$f_p = \frac{D}{p} = \frac{4\pi w_0}{kT} \int_0^{\infty} [1 + g(R)] dw(R) \exp(-U(R)/kT) R^2 dR, \quad (1a)$$

$$g(R) = \begin{cases} \frac{2}{3\sqrt{\pi}} \left(-\frac{U(R)}{kT}\right)^{3/2}, & U < 0, \\ 0, & U > 0, \end{cases} \quad (1b)$$

Here $U(R)$ is an effective potential of interatomic interaction, which has the central symmetry in a case of the systems $A-B$ (in our case, for example, $A = \text{Rb, Cs}$; $B = \text{He}$); T is a temperature, w_0 is a frequency of the hyperfine structure transition in an isolated active atom; $d\omega(R) = Dw(R)/w_0$ is a relative local shift of the hyperfine structure line; $(1 + g(R))$ is a temperature form-factor.

The local shift is caused due to the disposition of the active atoms (say, the alkali atom and helium He) at the distance R . In order to calculate an effective potential of the interatomic interaction further we use the exchange perturbation theory formalism (the modified version EL-HAV) [20, 21].

Since we are interested by the alkali (this atom can be treated as a one-quasiparticle system, i.e. an atomic system with a single valence electron above a core of the closed shells) and the rare-earth atoms (here speech is about an one-, two- or even three-quasiparticle system), we use the classical model for their consideration. The interaction of alkali (A) atoms with a buffer (B) gas atom is treated in the adiabatic approximation and the approximation of the rigid cores. Here it is worth to remind very successful model potential simulations of the studied systems (see, for example, Refs. [27–29, 33–84]).

In the hyperfine interaction Hamiltonian one should formally consider as a magnetic dipole interaction of moments of the electron and the nucleus of an active atom as an electric quadrupole interaction (however, let us remind that, as a rule, the moments of nuclei of the most (buffer) inert gas isotopes equal to zero) [13, 14].

The necessity of the strict treating relativistic effects causes using the following expression for a hyperfine interaction operator H_{HF} (see, e.g., [1, 2, 11, 12]):

$$H_{HF} = a \sum_{i=1}^N I \frac{\alpha_i \times r_i}{r_i^3}, \quad (2)$$

$$a = -2\mu \frac{e^2 \hbar}{2m_p c},$$

where I —the operator of the nuclear spin active atom, α_i —Dirac matrices, m_p —proton mass, μ —moment of the nucleus of the active atom, expressed in the nuclear Bohr magnetons. Of course, the summation in (2) is over all states of the electrons of the system, not belonging to the cores. The introduced model of consideration of the active atoms is important to describe an effective interatomic interaction potential (an active atom—an passive atom), which is centrally symmetric ($J_A = 1/2$) in our case (the interaction of an alkali atom with an inert gas atom).

Let us underline that such an approximation is also acceptable in the case system “thallium atom—an inert gas atom” and some rare-earth atoms, in spite of the presence of p-electrons in the thallium (in the case of rare-earth atoms, the situation is more complicated).

Next, in order to determine a local shift within the consistent theory it should be used the expression obtained in one of versions of the exchange perturbation theory, in particular, EL-HAV version (see [1–12, 18–21]). The relative local shift of the hyperfine structure line is defined with up to the second order in the potential V of the Coulomb interaction of the valence electrons and the cores of atoms as follows:

$$\delta\omega(R) = \frac{S_0}{1 - S_0} + \Omega_1 + \Omega_2 - \frac{C_6}{R^6} \left(\frac{2}{\bar{E}_a} + \frac{1}{\bar{E}_a + \bar{E}_B} \right), \quad (3a)$$

$$\bar{E}_{a,b} = (I_{a,b} + E_{1a,b})/2. \quad (3b)$$

Here S_0 is the overlapping integral; C_6 is the van der Waals coefficient; I is the potential of ionization; $E_{1a,b}$ is the energy of excitation to the first (low-lying) level of the corresponding atom. The values Ω_1 , Ω_2 in Eq. (3a) are the first order non-exchange and exchange non-perturbation sums correspondingly. These values are defined as follows:

$$\Omega_1 = \frac{2}{N(1 - S_0)\rho_0} \sum_k' \frac{\langle \Phi'_0(1) | H'_{HF} | \Phi'_k(1) \rangle V_{k0}}{E_0 - E_k} \quad (4a)$$

$$\Omega_2 = \frac{2}{N(1 - S_0)\rho_0} \sum_k' \frac{\langle \Phi'_0(1) | H'_{HF} | \Phi'_k(1) \rangle U_{k0}}{E_0 - E_k} \quad (4b)$$

$$\rho_0 = \langle \Phi_0^1(1) | H'_{HF} | \Phi_0'(1) \rangle / \langle \Phi_0^1(1) | \Phi_0'(1) \rangle$$

where $H'_{HF} = \frac{[a \times r_1]_z}{r_1^3}$ is the transformed operator of the hyperfine interaction; $[a \times r_1]_z$ is Z component of the vector product; Z—quantization axis directed along the axis of the quasi-molecule; N is the total number of electrons, which are taken into account in the calculation; $E_k, \Phi'_k(1) = F'_{k_a}(1)\varphi_{k_b}(2 \dots N)$ are an energy and a non-symmetrized wave function of state $k = \{k_a, k_b\}$ for the isolated atoms A and B .

The non-exchange matrix element of the Coulomb interatomic interaction is as:

$$V_{k0} = \langle \Phi'_k(1) | V(1) | \Phi_0'(1) \rangle. \quad (5a)$$

Correspondingly the exchange matrix element is as follows:

$$U_{k0} = \sum_{i=2}^N \langle \Phi'_k(1) | V(i) | \Phi_0'(i) \rangle \quad (5b)$$

The operator $V(i)$ [for example, in a case of the system Rb(a)–He(b)] can be presented as follows:

$$V(i) = U_{SCF}(r_{a3}) + U_{SCF}(r_{a4}) - 2U_{SCF}(R) + \frac{1}{r_{bi}}, \quad (6)$$

where $U_{SCF}(r)$ is the self-conjunctive field, created by an active atom core.

The useful expressions for approximating the interaction potential and shift are presented in Refs. [25–27, 30–32]:

$$U_{A-B}(R) = U_{A-B}^{ex} - C_6/R^6, \quad (7)$$

$$\delta\omega_{A-B}^{(1)}(R) = \frac{2}{N\rho_0} (\chi^{1/2}(R) - \chi_{00}^{1/2}) U_{A-B}^{o\delta_M}(R) + (\Omega_1^{3/2} + \Omega_2^{3/2})_{A-He} \sqrt{\frac{S_{0A-B}}{S_{0A-He}}}, \quad (8)$$

where the overlap integrals S_{0A-B} are determined by the standard expressions, and the potential U_{A-B}^{ex} is calculated in the framework of the exchange perturbation theory [25–27]:

$$U^{ex} = (V_{00} - U_{00}) / (1 - S_0). \quad (9)$$

It should also be noted that as a rule, in the alternative non-relativistic theories of [13–21] the commutator technique [30–32] is used when calculating the sums of the type (4a, 4b). Earlier the reason of using actually approximate non-relativistic methods was the lack of reliable information on the wave functions of the excited states of the complex atoms. Starting approximations in alternative theories [25–27, 30–32] were rather simple approximations for the electronic wave functions of both active and passive atoms. In particular, in Refs. [30–32] the electronic wave functions were approximated by simple Slater expression (the approximation of the

effective charge = Z-approximation) or simple analytical approximation formulas by Löwdin (L-approximation) and Clementi-Roothaan (C-approximation) [85, 86] in studying the shift and broadening the hyperfine lines for such atoms as He, Rb, Cs etc. In Refs. [25–27] the wave functions had been determined within the Dirac-Fock approximation, however, these authors had used the approximate non-relativistic expressions to describe the interatomic interaction potential. Besides, determination of the polarizabilities and the van der Waals constants has been performed with using the following London's expressions [13, 14, 25–27]:

$$C_6^I = \frac{3}{2} \alpha_A \alpha_B \frac{I_A I_B}{I_A + I_B}, \quad (10a)$$

$$C_6^{II} = \frac{3}{2} \alpha_A \alpha_B \frac{1}{\sqrt{\frac{\alpha_A}{n_A}} + \sqrt{\frac{\alpha_B}{n_B}}}, \quad (10b)$$

$$C_6^{III} = \frac{3}{2} \alpha_B I_B \sum_k \frac{f_{ko}}{(E_o - E_k)(E_o - E_k + I_B)}. \quad (10c)$$

where f is the oscillator strength, other notations are the standard. However, sufficiently large error in definition of the van der Waals constants could provide a low accuracy of calculating the interatomic potentials. It is worth to note that the authors of the cited works indicate on the sufficiently large error ($\sim 50\%$) in the calculation of the collision shifts.

Let us return to consideration of the van der Waals coefficient C_6 for the interatomic A - B interaction. The van der Waals coefficient may be written as [33–35, 87–90]:

$$C_6(L, M) = C_{6,0}(L) - \frac{3M^2 - L(L+1)}{(2L-1)(2L+3)} \cdot C_{6,2}(l), \quad (11)$$

where $C_{6,0}(L)$ is the isotropic component of the interaction and $C_{6,2}(l)$ is the component corresponding to the $P_2(\cos\theta)$ term in the expansion of the interaction in Legendre polynomials, where the angle specifies the orientation in the space-fixed frame.

The dispersion coefficients $C_{6,0}(L)$ and $C_{6,2}(l)$ may be expressed in terms of the scalar and tensor polarizabilities $\alpha_0(L; iw)$ and $\alpha_2(L; iw)$ evaluated at imaginary frequencies [33–35]. In particular, one may write in the helium case as follows:

$$C_{6,0}(L) = \frac{3}{\pi} \cdot \int_0^\infty \alpha_0(L; iw) \bar{\alpha}_{He}(iw) dw, \quad (12)$$

where $\bar{\alpha}_{He}$ is the dynamic polarizability of He. The polarizabilities at imaginary frequencies are defined in atomic units by the following formula:

$$\alpha_{\parallel}(L, M; iw) = 2 \sum_{\gamma, M_{\gamma}} \frac{(E_{\gamma} - E_L) |\langle LM | \hat{z} | L_{\gamma} M_{\gamma} \rangle|^2}{(E_{\gamma} - E_L)^2 + w^2} \quad (13)$$

where E_{γ} is the energy of the electronically excited state $|L_{\gamma} M_{\gamma}\rangle$ and the z axis lies along the internuclear axis.

Obviously, generally speaking, the calculation of the dynamic polarizability and the resulting van der Waals constants is connected with a summation over infinite number of intermediate states (the states of the discrete spectrum and integrating over the states of the continuous spectrum). This is a known problem, which greatly complicates the computational procedure and significantly reduces an accuracy of the computing the atomic characteristics.

On the other hand, it is known that the space of functions of the atomic states can be stretched over the space of the Sturm orbitals, which is both discrete and countable [13, 14, 67–70, 87, 88]. Thus, it allows to eliminate a problem of accounting the continuous spectrum within the formally exact approach.

Naturally, the set of Sturm orbitals should be introduced with specially prescribed asymptotics that is crucial for the convergence of the spectral expansion, including a spectral expansion of the corresponding Green's functions.

3 Relativistic Many-Body Perturbation Theory with the Kohn-Sham Zeroth Approximation and the Dirac-Sturm Method

3.1 Relativistic Many-Body Perturbation Theory with the Kohn-Sham Zeroth Approximation

As it is well known (see also Refs. [1, 2, 15–17]), the non-relativistic Hartree-Fock method is mostly used for calculating the corresponding wave functions. More sophisticated approach is based on using the relativistic Dirac-Fock wave functions (first variant) [57–59]. Another variant is using the relativistic wave functions as the solutions of the Dirac equations with the corresponding density functional, i.e. within the Dirac-Kohn-Sham theory [91–96]. In fact, the theoretical models involved the use of different consistency level approximations led to results at quite considerable variance.

It is obvious that more sophisticated relativistic many-body methods should be used for correct treating relativistic, exchange-correlation and even nuclear effects in heavy atoms. (including the many-body correlation effects, intershell correlations, possibly the continuum pressure etc. [40–54]). In our calculation we have used the relativistic functions, which are generated by the Dirac-Kohn-Sham Hamiltonian [37, 48–54]. In a number of papers it has been rigorously shown that using the optimized basis in calculating the atomic electron density dependent

properties has a decisive role. This topic is in details discussed in many Refs. (see, for example, [13, 14, 51–58, 60–63, 97]).

As usual, a multielectron atom is described by the Dirac relativistic Hamiltonian (the atomic units are used):

$$H = \sum_i h(r_i) + \sum_{i>j} V(r_i r_j). \quad (14)$$

Here, $h(r)$ is one-particle Dirac Hamiltonian for electron in a field of the finite size nucleus and V is potential of the inter-electron interaction. In order to take into account the retarding effect and magnetic interaction in the lowest order on parameter α^2 (the fine structure constant) one could write [37]:

$$V(r_i r_j) = \exp(i\omega_{ij} r_{ij}) \cdot \frac{(1 - \alpha_i \alpha_j)}{r_{ij}}, \quad (15)$$

where ω_{ij} is the transition frequency; α_i , α_j are the Dirac matrices. The Dirac equation potential includes the electric potential of a nucleus and electron shells and the exchange-correlation potentials. The standard KS exchange potential is as follows [91, 92]:

$$V_X^{KS}(r) = -(1/\pi)[3\pi^2 \rho(r)]^{1/3}. \quad (16)$$

In the local density approximation the relativistic potential is [91, 92]:

$$V_X[\rho(r), r] = \frac{\delta E_X[\rho(r)]}{\delta \rho(r)}, \quad (17)$$

where $E_X[\rho(r)]$ is the exchange energy of the multielectron system corresponding to the homogeneous density $\rho(r)$. The corresponding correlation functional is [13, 14, 51, 52]:

$$V_C[\rho(r), r] = -0.0333 \cdot b \cdot \ln[1 + 18.3768 \cdot \rho(r)^{1/3}], \quad (18)$$

where b is the optimization parameter (for details see Refs. [13, 14, 55, 56, 60–63]).

As it has been underlined, an adequate description of the multielectron atom characteristics requires using the optimized basis of wave functions. In our work it has been used ab initio optimization procedure for construction of the optimized basis of the relativistic orbitals. It is reduced to minimization of the gauge dependent multielectron contribution $Im\delta E_{ninv}$ of the lowest QED perturbation theory corrections to the radiation widths of atomic levels.

The minimization of the functional $Im\delta E_{ninv}$ leads to the Dirac-Kohn Sham-like equations for the electron density that are numerically solved. According to Refs. [55, 56], the gauge dependent multielectron contribution can be expressed as functional, which contains the multi-electron exchange-correlation ones. From the

other side, using these functionals within relativistic many-body perturbation theory allows effectively to take into account the second –order atomic perturbation theory (fourth-order QED perturbation theory) corrections. In our work the corresponding functionals of Refs. [65, 66] have been used. As a result one can get the optimal perturbation theory one-electron basis. In concrete calculations it is sufficient to use more simplified procedure, which is reduced to the functional minimization using the variation of the correlation potential parameter b in Eq. (17).

The differential equations for the radial functions F and G (components of the Dirac spinor) are:

$$\begin{aligned} \frac{\partial F}{\partial r} + (1 + \chi) \frac{F}{r} - (\varepsilon + m - V)G = 0, \\ \frac{\partial G}{\partial r} + (1 - \chi) \frac{G}{r} + (\varepsilon - m - V)F = 0, \end{aligned} \quad (19)$$

where F , G are the large and small components respectively; χ is the quantum number.

At large χ , the functions F and G vary rapidly at the origin; we have

$$F(r), G(r) \approx r^{\gamma-1}, \gamma = \sqrt{\chi^2 - \alpha^2 z^2}.$$

This creates difficulties in numerical integration of the equations in the region $r \rightarrow 0$. To prevent the integration step from becoming too small it is usually convenient to turn to new functions isolating the main power dependence:

$$\begin{aligned} f &= Fr^{1-|\chi|}, \\ g &= Gr^{1-|\chi|}. \end{aligned}$$

The Dirac equations for F and G components are transformed as follows [37]:

$$\begin{aligned} f' &= -(\chi + |\chi|)f/r - \alpha ZVg - (\alpha ZE_{n\chi} + 2/\alpha Z)g, \\ g' &= (\chi - |\chi|)g/r - \alpha ZVf + \alpha ZE_{n\chi}f. \end{aligned} \quad (20)$$

Here $E_{n\chi}$ is one-electron energy without the rest energy. The boundary values are defined by the first terms of the Taylor expansion:

$$\begin{aligned} g &= (V(0) - E_{n\chi})r\alpha Z/(2\chi + 1); \quad f = 1 \text{ at } \chi < 0, \\ f &= (V(0) - E_{n\chi} - 2/\alpha^2 Z^2)\alpha Z; \quad g = 1 \text{ at } \chi > 0. \end{aligned} \quad (21)$$

The condition $f, g \rightarrow 0$ at $r \rightarrow \infty$ determines the quantified energies of the state $E_{n\chi}$. The system of Eq. (20) is numerically solved by the Runge-Kutta method ('Superatom' PC package is used [36–56, 60–75]). The other details can be found in Refs. [40–54].

3.2 The Dirac-Sturm Approach

The basic idea of the Dirac-Sturm approach is as follows [13, 14, 20, 21, 67–72]. In the usual formulation as basis functions used system of eigenfunctions of the generalized eigenvalue problem for the family of operators:

$$(H_0 - \varepsilon)\Phi_v = \Lambda_v \hat{g} \Phi_v, \quad (22)$$

where H_0 —unperturbed Hamiltonian of a system, \hat{g} is a weighting operator, generally speaking, do not commute with the operator H_0 ; Λ_v , Φ_v —eigenvalues and eigenfunctions of Eq. (22).

A weighting operator in Eq. (22) is usually chosen so that unlike a spectrum of H_0 , the spectrum of (22) is a purely discrete. Using the orthogonality and completeness conditions, it is easy to show that the Green operator of the unperturbed problem is diagonal in a representation, defined by a set of functions Φ_v and the corresponding expansion is as follows:

$$G_0(\varepsilon) = \sum_v |\Phi_v\rangle\langle\Phi_v|/\Lambda_v(\varepsilon) \quad (23)$$

and contains only a single summation over the quantum numbers $\{v\}$.

As the operator H_0 we use the Dirac-Kohn-Sham Hamiltonian. The corresponding Dirac-Kohn-Sham equation can be written in the next general form [20, 21]:

$$[h_{DKS}(x) - \varepsilon_n]u_n(x) = 0 \quad (24)$$

Along with discrete spectrum ($\varepsilon = \varepsilon_n \leq \varepsilon_F$) there is a continuous spectrum of the eigen-values ($\varepsilon > \varepsilon_F$), corresponding to the Dirac-Kohn-Sham virtual orbitals. In the Sturmian formulation of the problem one should search for the eigen-values and eigen-functions of the following equation:

$$[h_{DKS}(x) - \varepsilon]\varphi_v = \lambda_v \rho(x) \varphi_v \quad (25)$$

where

$$\varepsilon = E - \sum_{k=1}^{N-1} \varepsilon_{n_k} \quad (26)$$

when $\varepsilon < 0$ Eq. (25) has a purely discrete spectrum eigenvalues $\lambda_v = \lambda_v(\varepsilon)$.

As the weight of the operator there are commonly used operators, proportional to a part or even all potential energy in the Hamiltonian H_0 . Further, it is easily to understand that the Fourier-image of the one-particle Green's function in the Dirac-Kohn-Sham approximation can be represented as an expansion on the eigenfunctions of (25) [13, 14, 20, 21]:

$$G^{(+)} = (x, x'; \varepsilon) = \sum_v \frac{\tilde{\varphi}_v(x) \tilde{\varphi}_v^*(x')}{\lambda_v(\varepsilon) - 1}, \quad (27)$$

where $\tilde{\varphi}_v(x)$ is the Sturm designed function:

$$\tilde{\varphi}_v(x) = \varphi_v(x) - \sum_{k=1}^N u_{n_k}(x) \langle u_{n_k} | \varphi_v \rangle \quad (28)$$

In the case of the single-particle perturbed operator, say,

$$W(x) = \sum_{a=1}^N w_a(x) \quad (29)$$

the second-order correction to an energy of the atom is determined by the standard expression of the following type:

$$\begin{aligned} \delta E^{(2)} &= - \sum_{k=1}^N \left\langle u_{n_k} \left| w G^{(+)}(\varepsilon_{n_k}) w \right| u_{n_k} \right\rangle \\ &= - \sum_{k=1}^N \sum_v |\langle \tilde{\varphi}_v | w | u_{n_k} \rangle|^2 / [\lambda_v(\varepsilon_{n_k}) - 1] \end{aligned} \quad (30)$$

and it actually contains only the summation over the occupied states (core) and virtual orbitals of the Dirac-Kohn-Sham-Sturm type relating to a purely discrete spectrum.

If the operator $w_a(x)$ is an interaction with an external electric field, the expression (30) determines the many-electron atom polarizability in the relativistic Dirac-Kohn-Sham approximation.

Let us illustrate the specific numerical implementation of relativistic method of the Sturm expansions on the example of the rubidium atom. Calculation of the static polarizability is actually reduced to two stages. In the first stage one should solve the system of relativistic Dirac-Kohn-Sham equations with respect to the Dirac radial functions and the Lagrange diagonal parameters ε^{5s} , ε^{4p} , ε^{4s} etc.

In the second stage of the calculation procedure the system of equations equivalent to (25) is solved numerically:

$$(-i\alpha c \nabla + V_N(r) + \delta_i V_C(r) + V_X(r|b_i) - \varepsilon_i) \varphi_i = 0, \quad (31)$$

where, as above, V_N is the potential of the electron-nuclear interaction, V_C is a mean-field potential generated by the other electrons; V_X is the Kohn-Sham potential.

Two parameters ε_i , δ_i correspond to each orbital “i” of a real or Sturmian state. The parameter $\delta_i = 1$ for orbitals of the real states. It is also important to emphasize

that all orbitals of the Sturmian supplement of the Eq. (27) have an exponential asymptotic behavior as $r \rightarrow \infty$, which coincides with the asymptotic behavior of the last real state orbitals in the corresponding basis of the real state orbitals. In each case, the functions of the accounted real states represent a reduced spectral expansion of the Green's function G .

The residual part decreases as $\exp[-r(-2\varepsilon)^{1/2}]$ for $r \rightarrow \infty$ (here ε is the eigen energy of the explicitly accounted last real state). All orbitals of the Sturm supplement have absolutely the same asymptotic in the corresponding basis. This fact is very significant in terms of convergence of the method. As usually, the number of explicitly accounted real state functions is determined by the concrete numerical application of the method to computing the studied atomic characteristics. Other details can be found in Refs. [13, 14, 20, 21, 67–70].

4 Shift and Broadening of Hyperfine Spectral Lines for Multielectron Atoms in an Atmosphere of a Buffer Gas

4.1 Shift and Broadening of the Thallium and Ytterbium Hyperfine Lines in an Atmosphere of the Inert Gas

At first, let us consider the thallium atom in atmosphere of the inert gas. Its studying is of a great interest as this atom a sufficiently heavy. In contrast to more simple alkali atoms (look below) the thallium atom contains p-electrons outside closed shells and has a nuclear charge $Z = 81$. Obviously, a correct treating relativistic and exchange-correlation effects is critically important for accurate describing its energy and spectral characteristics.

In Table 1 the theoretical values of the van der Waals constants (in atomic units) respectively, for atom Tl (Tl-He, Kr, Xe) are listed. There are presented our results (*) obtained from our relativistic calculation by the optimized Dirac-Kohn-Sham method combined with the Dirac-Sturm approach, the calculation results by

Table 1 Theoretical values of the van der Waals constants (in atomic units) respectively, for atom Tl (Tl-He, Kr, Xe); see explanations in the text

	Tl-He	Tl-Ar	Tl-Kr	Tl-Xe
C_6^I (10a)	17.5	129	180	291
C_6^{II} (10b)	20.5	148	212	318
C_6^{III} (10c)	20.33	133	193	296
C_6 (Hartree-Fock)	6.59	48	71	111
C_6 (our data ^a)*	12.1	106	157	265
C_6 (our data ^b)*	14.5	119	173	289
C_6 (experiment)	–	100	150	260

Note ^a Calculation with optimization*

^b Calculation without optimization

Table 2 Local shift and interatomic interaction potential (in atomic units) for the pair Tl–He

R	Dirac-Fock method [25–27]		Our theory [18–21]	
	$\delta\omega(R) \times 10^2$	$U(R) \times 10^3$	$\delta\omega(R) \times 10^2$	$U(R) \times 10^3$
5	4.22	7.6	3.92	6.93
6	1.34	2.0	1.21	1.76
7	0.329	0.44	0.27	0.38
8	0.0788	0.099	0.070	0.085
9	0.0032	0.024	0.0025	0.020
10	−0.0145	−0.076	−0.0131	−0.067
11			−0.0119	−0.008

Batygin et al., based on the approximation formulas (10a)–(10c), the Hartree-Fock data by Penkin et al., as well as experimental data (from Refs. [18–27, 30–35]).

It is noteworthy sufficiently large error for values of the van der Waals constants, obtained during calculating on the basis of formula (11), as well as within the standard Hartree-Fock method.

The calculation shows the importance of the quality of the atomic wave functions (using an optimization and correct account for the exchange-correlation effects and continuum “pressure” etc.) for an adequate description of the corresponding constants.

In Table 2 there are listed the results of our calculation of the interatomic interaction potential $U(R)$ and the values of the local shift $\delta\omega(R)$ (all values are in atomic units) of the thallium hyperfine spectral line for different values of the internuclear distance in the system Tl–He. For comparison, similar results of the calculation of the potential $U(R)$ and the local shift $\delta\omega(R)$ with using the single-configuration Dirac-Fock method [25–27] are presented too.

In Table 3 we list the results of our calculation (as all values are given in atomic units) interatomic interaction potential $U(R)$ and the values of the local shift $\delta\omega(R)$ for pairs Tl–Kr, Tl–Xe.

Further in Table 4 we present our theoretical values (theory C) for the thallium atom hyperfine line collisional shift at the temperature $T = 700$ K for a number of

Table 3 Local shift and interatomic interaction potential (in atomic units) for the pair Tl–Kr, Xe (see text)

R	Tl–Kr (our theory)		Tl–Xe (our theory)	
	$\delta\omega(R) \times 10^2$	$U(R) \times 10^3$	$\delta\omega(R) \times 10^2$	$U(R) \times 10^3$
5	−14.30	13.24	−19.05	18.31
6	−2.88	6.10	−8.22	5.95
7	−1.44	1.72	−2.67	2.04
8	−0.67	0.49	−1.52	0.65
9	−0.48	0.06	−0.74	0.01
10	−0.35	−0.03	−0.48	−0.08
11	−0.24	−0.04	−0.37	−0.09

Table 4 The collisional shift f_p (in Hz/Torr) of the thallium hyperfine line for pairs Tl–He, Tl–Kr, Tl–Xe at $T = 700$ K

System	Tl–He	Tl–Kr	Tl–Xe
Experiment	130 ± 30	-490 ± 20	$-1,000 \pm 80$
Qualitative estimate	–	–	$-5,500$
Theory A	155.0	–850.0	–1,420.0
Theory B	139.0	–	–
Theory C	137.2	–504	–1,052

Experiment and the qualitative estimate by Choron-Scheps-Galagher (Virginia group); Theory: A—single-configuration Dirac-Fock method; B—the optimized Dirac-Fock method; C—our theory (see text)

Table 5 The temperature dependence of the collisional shift f_p (in Hz/Torr) for pairs Tl–He, Tl–Kr, Tl–Xe

Pair	Tl–He	Tl–He	Tl–Kr	Tl–Xe
T, K	Theory A	Theory C	Theory C	Theory C
700	155	137.2	–504	–1,052
750	153.0	135.3	–461	–964
800	151	134.1	–422	–899
850	149	133.3	–391	–841
900	147.5	131.4	–362	–794
950	146	129.1	–330	–751
1,000	143	126.2	–308	–713

Theory: A—single-configuration Dirac-Fock method; C—our theory

the diatomic systems, in particular, the pairs of Tl–He, Tl–Kr, Tl–Xe. For comparison, in this table there are also listed the results of calculation on the basis of the single-configuration Dirac-Fock method Batygina DF et al. [25–27] (theory A), the optimized DF-like method [18, 19] (theory B), as well as experimental data Choron-Scheps-Galagher (the Virginia group). The qualitative estimate from Refs. [22–24] has been listed as well.

In Table 5 we present the theoretical data on the collisional shift f_p (in Hz/Torr) of the thallium atom hyperfine line at different temperatures (TK) for the systems Tl–He, Tl–Kr, Tl–Xe: Theory A—the single-configuration Dirac-Fock method Batygina DF et al. [25–27]; C—our theory [18–21].

As can be seen from the presented data, our theory provides a physically reasonable agreement with experimental data on the hyperfine line collisional shifts for the pairs of Tl–He, Tl–Kr, Tl–Xe.

In Table 6 we present our calculated values for adiabatic broadening Γ_a/p (in Hz/Torr) of the thallium atom hyperfine line at different temperatures for the Tl–He pair: C—our theory; A theory [25–27]. In Table 7 we list the similar our theoretical data on the thallium atom hyperfine line adiabatic broadening of Γ_a/p (in Hz/Torr) for the pairs Tl–Kr, Tl–Xe.

Table 6 Adiabatic broadening Γ_a/p (in Hz/Torr) for the Tl–He: Theory A—single-configuration Dirac–Fock method; C—our theory

T, K	Tl–He	Tl–He
	Theory A	Theory C
700	2.83	2.51
800	2.86	2.54
900	2.90	2.58
1,000	2.89	2.56

Table 7 Adiabatic broadening Γ_a/p (in Hz/Torr) for the Tl–Kr, Yl–Xe (our theory)

T, K	Tl–Kr	Tl–Xe
700	6.81	17.3
800	5.89	14.6
900	5.26	12.9
1,000	5.24	11.5

It is easily to estimate that the ratio values $(\Gamma_a/p)/f_p \sim 1/50$ for the system Tl–He, $(\Gamma_a/p)/f_p \sim 1/70$ for the system Tl–Kr and $(\Gamma_a/p)/f_p \sim 1/60$ for the Tl–Xe. These estimates (at first it had been noted in Refs. [25–27]) show that well-known in the theory of optical range spectral line broadening Foley law $\Gamma_a \sim |\Delta|$ (see, for example, [13, 14]) is incorrect for the spectral lines of transitions between components of the hyperfine structure. At least this fact is absolutely obvious for the thallium atom.

In any case we suppose that more detailed experimental studying are to be very actual and important especially a light of availability of the theoretical data on temperature dependences of the thallium hyperfine line collisional shift and broadening. Obviously, this is also very actual from the point of view of the construction the thallium quantum frequency measure, as well as studying a role of the weak interactions in atomic physics and physics of collisions (see, for example, [13, 14, 22–24]).

Now let us consider the pair “Yb–He”. The ground configuration for the ytterbium atom is: $[\text{Xe}]4f^46s^2$ (term: 1S). Further we present our results for the scalar static polarizability α_0 (in units of a_0^3 , a_0 is the Bohr radius) and isotropic dispersion coefficient $C_{6,0}$ (in units of $E_H a_0^6$, E_H is the Hartree unit of energy). Our data are as follows [20, 21]: $C_{6,0} = 45.2$ and $\alpha_0 = 169.3$. For comparison let us present the corresponding data by Dalgarno et al. [33–35]: $C_{6,0} = 39.4$, $\alpha_0 = 157.3$ and by Buchachenko et al. [89, 90]: $C_{6,0} = 44.5$.

In Table 8 we present our calculation results for the observed f_p (in Hz/Torr) shift for the system of Yb–He.

It is obvious that the pair Yb–He is more complicated system in comparison with the pair of Tl–He or “alkali atom–He”. Until now there are no any experimental or theoretical data for this system. So, we believe that our data may be considered as the first useful reference.

Table 8 The observed f_p (in, Hz/Torr) shift for the system Yb–He (see text)

T, K	f_p
700	148.1
750	146.0
800	143.8
850	141.5
900	138.9

4.2 Shift and Broadening of the Alkali Atom Hyperfine Lines in an Atmosphere of the Inert Gas

Here we present the results of our studying hyperfine line collisional shift for alkali atoms (rubidium and cesium) in the atmosphere of the helium gas. In Table 9 we present our data on the van der Waals constants in the interaction potential for alkali Rb, Cs atoms with inert gas atoms Ne, Kr, Xe, and also available in the literature experimental data [22–24, 30–32].

In Table 10 we list the results of our calculating (in atomic units) interatomic potentials, local shifts $\delta\omega(R)$ for the pair Cs–He. Noteworthy is the fact that an accuracy of the experimental data for the van der Waals constants does not exceed 10 % for heavy alkali atoms. Calculation has shown that the optimization of the relativistic orbitals basis and accounting for the exchange-correlation effects seem to be very important for obtaining adequate accuracy of the description of the constants.

In Tables 11 and 12 we present our theoretical results for the hyperfine line observed shift f_p (1/Torr) in a case of the Rb–He and Cs–He pairs. The experimental and alternative theoretical results by Batygin et al. [30–32] for f_p are listed too. At present time there are no precise experimental data for a wide interval of temperatures in the literature.

The theoretical data from Refs. [30–32] are obtained on the basis of calculation within the exchange perturbation theory with using the He wave functions in the Clementi-Rothaane approximation [85, 86] (column: Theory^a), and in the Z-approximation (column: Theory^b), and in the Löwdin approximation (column: Theory^c).

The important feature of the developed optimized perturbation theory approach is using the optimized relativistic orbitals basis, an accurate accounting for the

Table 9 The van der Waals constants (in atomic units.) for alkali atoms, interacting with inert gas atoms Ne, Kr, Xe (see text)

Pair of atoms	Our theory	Experiment
Rb–He	42	41
Rb–Kr	484	470
Rb–Xe	758	–
Cs–He	52	50
Cs–Kr	582	570
Cs–Xe	905	–

Table 10 The interatomic potential (10^5) and local $\delta\omega(R)$ shift (10^5) for Cs–He pair (in atomic units; see text)

R	$\delta\omega(R)$	$U(R)$
8	4,280	610
9	2,845	336
10	1,890	169
11	955	77
12	482	32
13	251	12.8
14	113	4.1
15	59	1.9

Table 11 The observed f_p (10^{-9} 1/Torr) shifts for the systems of the Cs–He and corresponding theoretical data (see text)

T, K	Experiment	Our theory	Theory ^a [30–32]	Theory ^b [30–32]	Theory ^c [30–32]
223	–	178	164	142	169
323	135	137	126	109	129
423	–	123	111	96	114
523	–	112	100	85	103
623	–	105	94	78	96
723	–	98	–	–	–
823	–	92	–	–	–

Note ^a Calculation with using the He wave functions in the Clementi–Rothaane approximation

^b Calculation with using the He wave functions in the Z-approximation

^c Calculation with using the He wave functions in the Löwdin approximation

Table 12 The observed f_p (10^{-9} 1/Torr) shifts for the systems of Rb–He and corresponding theoretical data (see text)

T, K	Experiment	Our theory	Theory ^a [30–32]	Theory ^b [30–32]	Theory ^c [30–32]
223	–	113	79	67	81
323	105	101	73	56	75
423	–	89	62	48	64
523	–	80	55	43	56
623	–	73	50	38	50
723	–	71	47	36	47
823	–	69	–	–	–

Note ^a Calculation with using the He wave functions in the Clementi–Rothaane approximation

^b Calculation with using the He wave functions in the Z-approximation

^c Calculation with using the He wave functions in the Löwdin approximation

exchange-correlation and continuum pressure effects with using the effective functionals [37, 65, 66].

The difference between the obtained theoretical data and other alternative calculation results can be explained by using different perturbation theory schemes and different approximations for calculating the electron wave functions of heavy atoms. It is obvious that the correct account for the relativistic and exchange-correlation and continuum pressure effects will be necessary for an adequate description of the energetic and spectral properties of the heavy atoms in an atmosphere of the heavy inert gases (for example, such as Xe).

5 Conclusion

In this chapter a brief review of the experimental and theoretical works on the hyperfine structure line collision shifts for heavy atoms in an atmosphere of the buffer inert gases is given. A new, consistent relativistic perturbation theory combined with the exchange perturbation theory, is presented and applied to calculating the interatomic potentials, van der Waals constants, hyperfine line collision shift and broadening for some heavy atoms in an atmosphere of the buffer inert gases. It should be noted that the presented approach can be naturally generalized in order to describe the energy and spectral characteristics of other atomic systems and buffer mediums.

The calculation results on the hyperfine line collision shift and broadening for the alkali (Rb, Cs), thallium, and ytterbium atoms in an atmosphere of the inert gas (He, Kr, Xe) are listed and compared with available alternative theoretical and experimental results. The obtained data for the $(\Gamma_a/p)/f_p$ ratio allowed to confirm that the well-known Foley law $\Gamma_a \sim f_p$ in the theory of optical range spectral line broadening is incorrect for the spectral lines of transitions between components of the hyperfine structure of the heavy multielectron atoms.

The studying hyperfine structure line collision shifts and widths for different heavy atomic systems in the buffer gases opens new prospects in the bridging of quantum chemistry and atomic and molecular spectroscopy and physics of collisions. These possibilities are significantly strengthened by a modern experimental laser and other technologies [22–24, 98–106]. Really, new experimental technologies in physics of collisions may provide a measurement of the atomic and molecular collision spectral parameters with very high accuracy.

Acknowledgments The support of the Odessa State University—OSENUR as well as of the Ministry of Education and Science of Ukraine (2013) is acknowledged. The author would like to thank Prof. Marco Nascimento for his invitation to present this contribution at QSCP-XVIII (Paraty, Rio de Janeiro, Brazil), and Prof. Andrey N. Starostin (Centre for Theoretical Physics and Computational Mathematics, Research State Center of the Russian Federation “Troitsk Institute for Innovation and Fusion Research”, Troitsk, Russian Federation) and Vladimir G. Shevchuk (Department of Chemical Physics, Odessa National University, Odessa, Ukraine) for useful comments.

References

1. Kaplan IG (1985) Theory of intermolecular interactions. Nauka, Moscow, pp 1–380
2. Kaplan IG, Rodimova OB (1987) *Phys Usp* 126:403
3. Nikitin EE (1980) In: Nikitin EE, Umansky SYa (eds) Semiempirical methods of calculation of interatomic interaction potentials. Series: Structure of molecules and chemical bond, vol 4. VINITI, Moscow, pp 1–220
4. Devdariani AL (1989) In: Smirnov BM, Devdariani AL, Zagrebin AL (eds) Chemistry of plasma, vol 15. Nauka, Moscow, p 44
5. Torrens IM (1972) Interatomic potentials. Academic Press, New York, pp 1–390
6. Freeman AJ, Frankel RH (1987) Hyperfine interactions. Plenum, New York, pp 1–360
7. Weiner J, Bagnato VS, Zilio S, Julianne PS (1999) *Rev Mod Phys* 71:1
8. Eisenschitz R, London F (1930) *Zs Phys* 60:491
9. Hirschfelder JO (1967) *Chem Phys Lett* 1:325, 363
10. van der Avoird Ad (1967) *J Chem Phys* 47:3649
11. Murrell JN, Shaw G (1967) *J Chem Phys* 46:1768
12. Musher JI, Amos AT (1967) *Phys Rev* 164:31
13. Sobel'man II (1977) Introduction to theory of atomic spectra. Nauka, Moscow, pp 1–380
14. Glushkov AV (2006) Relativistic and correlation effects in theory of atomic spectra. Astroprint, Odessa, pp 1–450
15. Grim G (1974) Broadening spectral lines in plasmas. Academic Press, New York, pp 1–480
16. Oks E (2010) *Int J Spectrosc* 10:852581
17. Unsöld A (1977) The new cosmos. Springer, Berlin, p 169
18. Khetselius OYu, Glushkov AV, Loboda AV, Gurnitskaya EP, Mischenko EV, Florko TA, Sukharev DE (2008) Spectral line shapes 15:231
19. Glushkov AV, Khetselius OYu, Loboda AV, Gurnitskaya EP, Mischenko EV (2009) Theory and applications of computational chemistry (AIP) 1113:131
20. Malinovskaya SV, Glushkov AV, Khetselius OYu, Svinarenko AA, Mischenko EV, Florko TA (2009) *Int J Quant Chem* 109:3325
21. Khetselius OYu, Florko TA, Svinarenko AA, Tkach TB (2013) *Phys Scr* T153:014037
22. Cheron B, Scheps R, Gallagher A (1976) *J Chem Phys* 65:326
23. Aumar F, Winter H (eds) (1997) Photonic, electronic, atomic collisions. World Scientific, Singapore, pp 1–630
24. Turner D, Baker C, Baker A, Brunrile C (1997) Molecular photoelectron spectroscopy. Wiley, New York, pp 1–540
25. Batygin VV, Matisov BG (1976) *J Techn Phys* 46:221
26. Alexandrov EB, Popov VI, Yakobson NN (1979) *Opt Spectrosc* 46:404
27. Batygin VV, Sokolov IM (1983) *Opt Spectrosc* 55:30
28. Glushkov AV (2008) Relativistic quantum theory. Quantum mechanics of atomic systems. Astroprint, Odessa, pp 1–900
29. Khetselius OYu (2008) Hyperfine structure of atomic spectra: new methods and applications. Astroprint, Odessa, pp 1–240
30. Batygin VV, Guzhva YuV, Matisov BG, Toptygin IN (1977) *JETP* 47:2414
31. Batygin VV, Gorny MB, Ivanov AN, Matisov BG (1977) *J Techn Phys* 47:2414
32. Batygin VV, Gorny MB, Gurevich BM (1978) *J Techn Phys* 48:1097
33. Penkin NP, Ruzov VP, Shabanova LN (1973) *Opt Spectrosc* 35:601
34. Chi X, Dalgarno A, Groenenborn GC (2007) *Phys Rev A* 75:032723
35. Jamieson MJ, Drake GWF, Dalgarno A (1995) *Phys Rev A* 51:3358
36. Glushkov AV, Ambrosov SV, Khetselius OYu, Loboda AV, Gurnitskaya EP (2006) In: Julien J-P, Maruani J, Mayou D, Wilson S, Delgado-Barrio G (eds) Recent advances in the theory of chemical and physical systems. Series: progress in theoretical chemistry and physics, vol 15. Springer, Berlin, p 285

37. Glushkov AV, Khetselius OYu, Gurnitskaya EP, Loboda AV, Florko TA, Sukharev DE, Lovett L (2008) In: Wilson S, Grout PJ, Maruani J, Delgado-Barrio G, Piecuch P (eds) *Frontiers in quantum systems in chemistry and physics*. Series: *progress in theoretical chemistry and physics*, vol 18. Springer, Berlin, p 505
38. Glushkov AV, Malinovskaya SV, Svinarenko AA, Chernyakova YuG (2004) *Int J Quant Chem* 99:889
39. Glushkov AV, Ambrosov SV, Loboda AV, Gurnitskaya EP, Prepelitsa GP (2005) *Int J QuantChem* 104:562
40. Glushkov AV, Ambrosov SV, Khetselius OYu, Loboda AV, Chernyakova YuG, Svinarenko AA (2004) *Nucl Phys A* 734S:21
41. Glushkov AV, Khetselius OYu, Lovett L, Gurnitskaya EP, Dubrovskaya YuV, Loboda AV (2009) *Int J Mod Phys A: Part Fields Nucl Phys* 24:611
42. Khetselius OYu (2009) *Int J Quant Chem* 109:3330
43. Khetselius OYu (2009) *Phys Scr* T135:014023
44. Khetselius OYu (2012) *J Phys C Ser* 397:012012
45. Glushkov AV, Ambrosov SV, Loboda AV, Prepelitsa GP, Gurnitskaya EP (2005) *Int J Quant Chem* 104:562
46. Glushkov AV, Malinovskaya SV, Khetselius OYu, Dubrovskaya YuV, Gurnitskaya EP (2006) *J Phys CS* 35:425
47. Malinovskaya SV, Glushkov AV, Khetselius OYu, Svinarenko AA, Loboda AV, Lopatkin YuM, Nikola LV (2011) *Int J Quant Chem* 111:288
48. Glushkov AV, Khetselius OYu, Malinovskaya SV (2008) In: Wilson S, Grout PJ, Maruani J, Delgado-Barrio G, Piecuch P (eds) *Frontiers in quantum systems in chemistry and physics*. Series: *progress in theoretical chemistry and physics*, vol 18. Springer, Berlin, p 523
49. Glushkov AV, Khetselius OYu, Malinovskaya SV (2008) *Eur Phys J ST* 160:195 (2008)
50. Glushkov AV, Khetselius OYu, Malinovskaya SV (2008) *Mol Phys* 106:1257
51. Glushkov AV, Khetselius OYu, Loboda AV, Svinarenko AA (2008) In: Wilson S, Grout PJ, Maruani J, Delgado-Barrio G, Piecuch P (eds) *Frontiers in quantum systems in chemistry and physics. Progress in theoretical chemistry and physics*, vol 18. Springer, Berlin, p 541
52. Glushkov AV, Loboda AV, Gurnitskaya EP, Svinarenko AA (2009) *Phys Scr T* 135:014022
53. Glushkov AV, Khetselius OYu, Lovett L (2009) In: Piecuch P, Maruani J, Delgado-Barrio G, Wilson S (eds) *Advances in the theory of atomic and molecular systems dynamics, spectroscopy, clusters, and nanostructures*. Series: *progress in theoretical chemistry and physics*, vol 20. Springer, Berlin, pp 125–172
54. Glushkov AV, Khetselius OYu, Svinarenko AA (2012) In: Hoggan P, Brändas E, Delgado-Barrio G, Piecuch P (eds) *Advances in the theory of quantum systems in chemistry and physics*. Series: *progress in theoretical chemistry and physics*, vol 22. Springer, Berlin, pp 51–70
55. Glushkov AV, Ivanov LN, Ivanova EP (1986) *Autoionization phenomena in atoms*. Moscow University Press, Moscow, p 58
56. Glushkov AV, Ivanov LN (1992) *Phys Lett A* 170:33
57. Grant IP (2007) *Relativistic quantum theory of atoms and molecules, theory and computation*. Springer series on atomic, optical, and plasma physics, vol 40. Springer, Berlin, pp 1–587
58. Grant IP, Quiney HM (2000) *Int J Quant Chem* 80:283
59. Wilson S (2007) In: Maruani J, Lahmar S, Wilson S, Delgado-Barrio G (eds) *Recent advances in theoretical physics and chemistry systems*. Series: *progress in theoretical chemistry and physics*, vol 16. Springer, Berlin, p 11
60. Glushkov AV (1992) *JETP Lett* 55:97
61. A.V. Glushkov (1998) *Opt Spectrosc* 84:670
62. Glushkov AV (1998) *Russ J Struct Chem* 39:220
63. Glushkov AV, Malinovskaya SV (1988) *Russ J Phys Chem* 62:100
64. Ivanov LN, Ivanova EP (1979) *Atom Data Nucl Data Tabl* 24:95
65. Ivanova EP, Ivanov LN, Glushkov AV, Kramida A (1985) *Phys Scr* 32:512

66. Glushkov AV, Ivanova EP (1986) *J Quant Spectrosc Radiat Transfer* 36:127
67. Ivanov LN, Ivanova EP, Knight L (1993) *Phys Rev A* 48:4365
68. Ivanova EP, Ivanov LN, Aglitsky EV (1988) *Phys Rep* 166:315
69. Ivanova EP, Ivanov LN (1996) *JETP* 83:258
70. Ivanova EP, Grant IP (1998) *J Phys B* 31:2871
71. Ivanov LN, Letokhov VS (1985) *Com Mod Phys D* 4:169
72. Glushkov AV, Ivanov LN, Letokhov VS (1991) Preprint of institute for spectroscopy of USSR Academy of Sciences (ISAN), N AS-5, Troitsk
73. Vidolova-Angelova E, Ivanov LN, Angelov DA (1988) *J Phys B: At Mol Opt Phys* 21:3877
74. Vidolova-Angelova E, Ivanova EP, Ivanov LN (1981) *Opt Spectrosc* 50:243
75. Bekov GI, Vidolova-Angelova E, Ivanov LN, Letokhov VS, Mishin VI (1981) *Soviet-JETP* 80:866
76. Nemukhin AB, Stepanov NF (1984) *Herald of Moscow State Univ Ser Chem* 18:282
77. Kupriyanov D, Sokolov S (1986) *Sov Chem Phys* 5:1160
78. Aubert M, Bessis M, Bessis G (1974) *Phys Rev A* 10:51
79. Aubert M, Bessis M, Bessis G (1974) *Phys Rev A* 10:61
80. Bellomonte L, Cavaliere P, Ferrante G (1974) *J Chem Phys* 61:3225
81. Aguilar J, Nakamura H (1976) *Chem Phys* 32:115
82. Masnou F, Philips N, Valiron P (1978) *Phys Chem Lett* 41:395
83. Luh W-T, Bahns JT (1988) *J Chem Phys* 88:2235
84. Frauss M, Stevens WJ (1990) *J Chem Phys* 93:4236
85. Clementi E, Roothaan CCJ, Yoshimine M (1962) *Phys Rev* 127:1618
86. Löwdin PO (1953) *Phys Rev* 30:120
87. Gruzdev PF, Solov'eva SG, Sherstyuk AI (1988) *Russ Phys J* 29(N1):73
88. Glushkov AV, Polischuk VP, Kivganov AF, Khokhlov VN, Buyadzhi TV, Vitavetskaya LA, Borovskaya GA (1998) *Russ Phys J* 41(N3):36
89. Buchachenko AA, Szczesniak MM, Chalazinski G (2006) *J Chem Phys* 124:114301
90. Jamieson MJ, Dalgarno A, Aymar M, Tharamel J (2009) *J Phys B: At Mol Opt Phys* 42:095203
91. Kohn W, Sham LJ (1964) *Phys Rev A* 140:1133
92. Hohenberg P, Kohn W (1964) *Phys Rev B* 136:864
93. Chu X, Chu S-I (2000) *Phys Rev A* 63:013414
94. Chu X, Chu S-I (2001) *Phys Rev A* 63:023411
95. Gross EG, Kohn W (2005) Exchange-correlation functionals in density functional theory. Plenum, New York
96. Gidopoulos N, Wilson S (eds) The fundamentals of electron density, density matrix and density functional theory in atoms, molecules and the solid state. Series: progress in theoretical chemistry and physics, vol 14. Springer, Berlin, p 1
97. Kunisz MD (1982) *Acta Phys Pol A* 62:285
98. Glushkov AV, Khetselius OYu, Svinarenko AA (2013) *Phys Scr* T153:014029
99. Vadla C, Horvatic V, Niemax K (2001) *Eur Phys J D* 14:23
100. Horvatic V, Veza D, Movre M, Niemax K, Vadla C (2008) *Spectrochim Acta B* 63:652
101. Kötteritzsch M, Gries W, Hese A (1992) *J Phys B: At Mol Opt Phys* 25:913
102. Ehrlacher E, Huennekens J (1992) *Phys Rev A* 46:2642
103. Singer K, Reetz-Lamour M, Amthor T, Marcassa L, Weidemuller M (2004) *Phys Rev Lett* 93:163001
104. Hancox CI, Doret SC, Hummon MT, Luo L, Doyle JM (2004) *Nature (London)* 431:281
105. Hancox CI, Doret SC, Hummon MT, Krems RV, Doyle JM (2005) *Phys Rev Lett* 94:013201
106. Khetselius OYu (2012) In: Nishikawa K, Maruani J, Brändas E, Delgado-Barrio G, Piecuch P (eds) Quantum systems in chemistry and physics: progress in methods and applications. Series: progress in theoretical chemistry and physics, vol 26. Springer, Berlin, pp 217–230

Proton Quantum Confinement on Symmetric Dimers of Ammonia and Lower Amine Homologs

Jake A. Tan, Jheng-Wei Li and Jer-Lai Kuo

Abstract Behavior of shared proton in symmetric dimers of ammonia and lower amine homologs were studied by several theoretical methods. Corresponding optimized structures by density functional theory show an intuitive hypsochromic shift as the degree of methylation is enhanced. Inclusion of nuclear quantum effect, however, changes the whole picture. It was found out that the fundamental vibrational transition corresponding to the shared proton's stretching motion, ν_{sp} is counter intuitive. Based from these calculations, there is a bathochromic shift from ammonia to trimethylamine. These ramifications do clearly indicate that proton is a quantum object. Furthermore, spectroscopic features for the stretching modes of the shared proton and H-bond donor-acceptor atoms were proposed.

Keywords Ionic hydrogen bond · Infrared spectroscopy · Quantum confinement

1 Introduction

The importance of hydrogen bonded systems can be seen in a plethora of systems. Acid-base chemistry, protein folding, biocatalysis and molecular recognition are just to name some. This type of non-covalent interaction is considered to be the

J.A. Tan · J.-L. Kuo (✉)

Institute of Atomic and Molecular Sciences, Academia Sinica,
P.O. Box 23-166, Taipei 10617, Taiwan, ROC
e-mail: jlkuo@pub.ams.sinica.edu.tw

J.A. Tan · J.-L. Kuo

Molecular Science and Technology Program, Taiwan International Graduate Program,
Academia Sinica, 128 Academia Road, Sec. 2, Nangang, Taipei 115, Taiwan, ROC

J.A. Tan

Department of Chemistry, National Tsing Hua University, 101 Kuang-Fu Road,
Sec. 2, Hsinchu 30013, Taiwan, ROC

J.-W. Li

Department of Physics, National Taiwan University, No. 1, Sec. 4, Roosevelt Rd.,
Taipei 10617, Taiwan, ROC

heart of biochemistry. This is due to the fact that, the secondary, tertiary and quaternary structure of a protein involves hydrogen bonds. In addition to this, the double helical nature of DNA is sustained by the hydrogen bonds between adenine and thymine; cytosine and guanine. Also, the recognition scheme between an enzyme and substrate usually involves hydrogen bonding between the active site and the substrate [1–4].

Under suitable conditions, proton transfer processes can be mediated by hydrogen bonds and the nature of proton hopping had been a subject of interest. Significant studies can be seen in a review of DeCoursey [5] and the nature of intraprotein proton transfer [6] and the recent proton's active role in Excited State Intramolecular Proton Transfer (ESIPT) [7].

One of the most conventional methods in studying hydrogen bonding is by means of infrared spectroscopy. Since 1930s, vibrational signature due to hydrogen bond has been identified, such observations reveals that there is an associated bathochromic shift on the stretching frequency of a typical A–H bond when hydrogen bonding is present [8–10]. However, the study of such systems in condense phase poses some complications, due to the fact that solvation phenomena can obscure the important peaks of shared proton motion. As a result, gas phase studies are more favored and do have promising insights.

Experimental studies on the infrared spectra of $[\text{NH}_3]_{n-1}\text{H}^+$, $n = 1–5$ was pioneered by Schwarz with the interest of obtaining the spectrum of free NH_4^+ and the effects of hydrogen bonding on it [11]. Unfortunately, the details of the N–N stretching together with the N–H_{sp} (shared proton) modes were not studied. The main focus of their study was on the $\sim 2,000$ – $4,000\text{ cm}^{-1}$. Later, Lee and coworkers reported the first observed internal rotation in ionic cluster of $\text{NH}_4^+(\text{NH}_3)_4$ [12]. Furthermore, the same group had proposed that the structure of NH_4^+NH_3 has a D_{3h} geometry, which implies that the shared proton is midway between the two nitrogen atoms and that it adopts an eclipsed conformation [13]. However, they have speculated that D_{3d} might be a more stable structure with approximately 10 cm^{-1} lower than the D_{3h} geometry.

Meanwhile, in terms of the stretching modes of the shared proton, Johnson's group performed vibrational predissociation experiments for selected proton bound symmetric and asymmetric dimers. Based from their results, it was found out that there is a correlation between the stretching modes of the shared proton with respect to the differences in the proton affinity, ΔPA of the vicinal Lewis bases [14]. Although stretching modes of the shared proton for symmetric cases were reported; a correlation between, ΔPA and ν_{sp} is not possible. Moreover, for the case of symmetric dimers, ν_{sp} depends on the nature of the monomers. This in turn suggests that aside from proton affinities, there are other factors contributing to ν_{sp} .

Theoretical studies on proton bound ammonia dimer were also reported in the literature. One of the earliest works was done by Scheiner [15] using HF level of theory with the minimal basis set; the results had shown that the shared proton is

located closer to one of the NH_3 moiety with a C_{3v} geometry. Furthermore, the proton transfer coordinate is described by a double well potential as it traverses between two nitrogen atoms.

On the other hand, classical Monte Carlo approach and wavepacket dynamics under MP2/6-31+G* simulations were reported by Asada et al. [16]. Optimized structures and transition state geometries were found to be C_{3v} and D_{3d} respectively. Classical ab initio Monte Carlo reveals that the C_{3v} structure is a consequence of classical considerations. However, once quantum effects on the proton kinetics had been accounted, the structure was found to be D_{3d} .

Variational calculations were done by Yang [17–19] on protonated ammonia cluster, $\text{NH}_4^+(\text{NH}_3)_n$ for $n = 1–4$ under MP2 level of theory. For $\text{NH}_4^+(\text{NH}_3)$, local mode calculations were reported up to six degrees of freedom. Isotope studies were also performed. Based from their results, six dimensional treatment is sufficient to describe the experimental IR spectrum, which previous theoretical treatments failed to account.

One straightforward quantum treatment of all nuclear degree of freedom is using Path Integral Molecular Dynamics, PIMD. The study of protonated ammonia dimer $(\text{NH}_3)_2\text{H}^+$ has been done by Ishibashi et al. [20]. Geometric isotope effect is discussed at 300 K with imaginary time slice $P = 16$. Propagation along Born–Oppenheimer surface is at MP2 level with 6-31++G** basis set during the MD sampling. Statistical properties depending only on $3N$ coordinate space could be directly estimated. Two internal coordinates, N–N bond distance and antisymmetric N–H bond stretching, are found essential for nuclear quantum effect to illustrate the geometric difference between H and D.

The aim of this study is to consider the behavior of the shared proton sandwiched between amines with varying degrees of methylation. The stratagem was by means of changing the degree of methylation, the potential energy surface can be tuned as well as the corresponding vibrational frequencies. This in turn can help in understanding and interpreting the spectrum where the shared proton is under a tug of war between molecules with the same proton affinities.

2 Calculation Methods

In this work, we use a combination of several theoretical methods to account for the quantum nature of the shared proton. First, the interactions among the nuclei are described by ab initio methods. Second, full dimensional quantum treatment of nuclear degrees of freedom using Path Integral Molecular Dynamics (PIMD) method were carried out to extract key degrees of freedom associated with proton motion. Vibrational Hamiltonian on selected dimensions were constructed to compute spectroscopic features.

2.1 Density Functional Methods

All static ab initio calculations (geometry optimizations, transition state locations and potential energy surface (PES) scan) were done using Gaussian 09 [21] under B3LYP level of theory with 6-311+G(d,p) taken as the basis set. The definition of coordinates used in this study is shown in Fig. 1. The proton's coordinate along hydrogen bond is designated as z , whose origin is the midpoint between the inter-nitrogen distance designated as R , while ϕ_1 and ϕ_2 refers to the umbrella type motion.

The significant structural parameters for the minimum and transition state structures are compiled and compared in Table 1. The following results were benchmarked against MP2/aug-cc-pVTZ reported by Yang [19]. Based from their little differences, it follows that B3LYP/6-311+G(d,p) yields results comparable to MP2/aug-cc-pVTZ. This in turn justifies the use of a more economical calculation method for the sake of speed and efficiency.

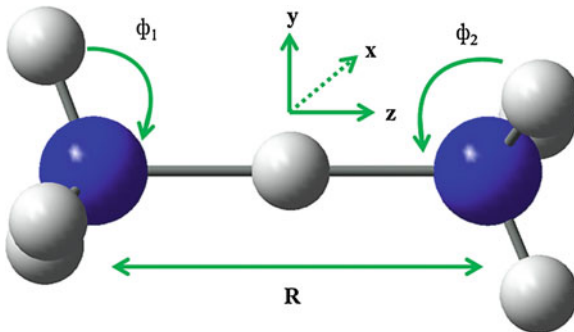


Fig. 1 Structure of $(\text{NH}_3)_2\text{H}^+$ and definition of six molecular coordinates used by Yang [19]; blue and gray represents nitrogen and hydrogen atoms respectively

Table 1 Comparison of calculated N–N and N–H_{sp} (SP = shared proton) distance for protonated dimers of ammonia using B3LYP/6-311+G(d,p) and MP2/aug-cc-pVTZ

Structural parameter	Minimum (Å)	Transition state (Å)	Level of theory
N–N	2.699	2.599	MP2/aug-cc-pVTZ
	2.692	2.618	B3LYP/6-311+G(d,p)
N–H _{sp}	1.116	1.300	MP2/aug-cc-pVTZ
	1.143	1.309	B3LYP/6-311+G(d,p)

2.2 *Ab Initio Path Integral Molecular Dynamics (PIMD)*

The full dimensional treatment of nuclear degrees of freedom using PIMD could be achieved via an efficient Car-Parrinello PIMD algorithm [22]. Owing to the inefficiency of plane-wave pseudopotential (PWP) method for exact exchange calculation, electronic ground energy in current work is carried out on the fly using Becke-Lee-Yang-Parr (BLYP) exchange-correlation functional and Martins-Trouiller (MT) normconserving pseudopotentials. Effectiveness of this standard method has been well documented [23]. In our PIMD calculations, the number of Trotter slices (P) was set to 32 or 16 in order to obtain sufficient convergence at temperatures 100 and 300 K. In addition, classical CPMD (that is $P = 1$) calculations were also performed in the same protocol for comparisons. Statistical properties are collected from six independent trajectories starting from uncorrelated structures.

In the case of protonated ammonia dimer ($(\text{NH}_3)_2\text{H}^+$), classical CPMD simulations show significant coupling between z and R and giving rise to the necessity of study beyond normal mode analysis [19]. Furthermore, it is clear from Fig. 2 that the distinction between classical and quantum simulations indicates the non-negligible nuclear quantum effect. The reduced probability distribution over z and R integrating over the other degree of freedom shows characteristic quantum nature of proton motion.

As the degree of methylation increases, the barrier for proton transfer will increase. To reassure that z and R coordinates do account for the important quantum features in high barrier circumstances, we have also carried out simulations on proton bound trimethylamine dimer. The two dimensional probability distribution

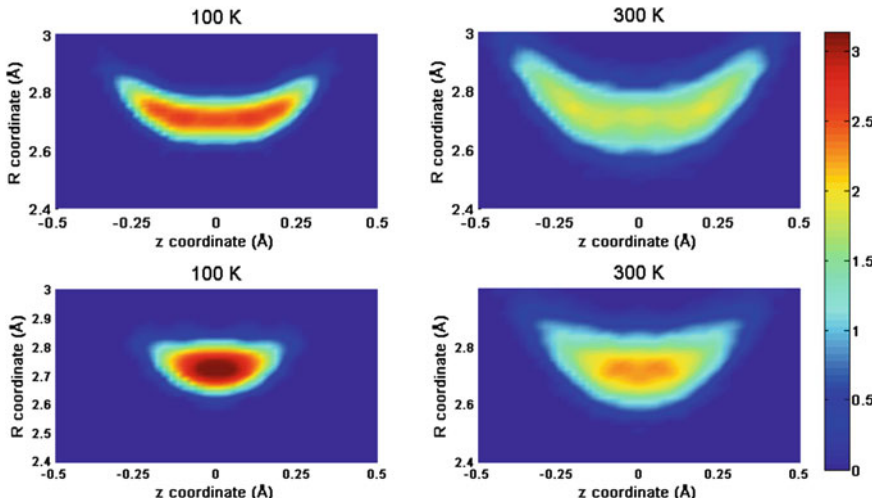


Fig. 2 Reduced probability distribution (z , R) for $(\text{NH}_3)_2\text{H}^+$. Classical simulations (top row) 100 K (left) and 300 K (right); Quantum simulations (bottom row) 100 K (left) and 300 K (right)

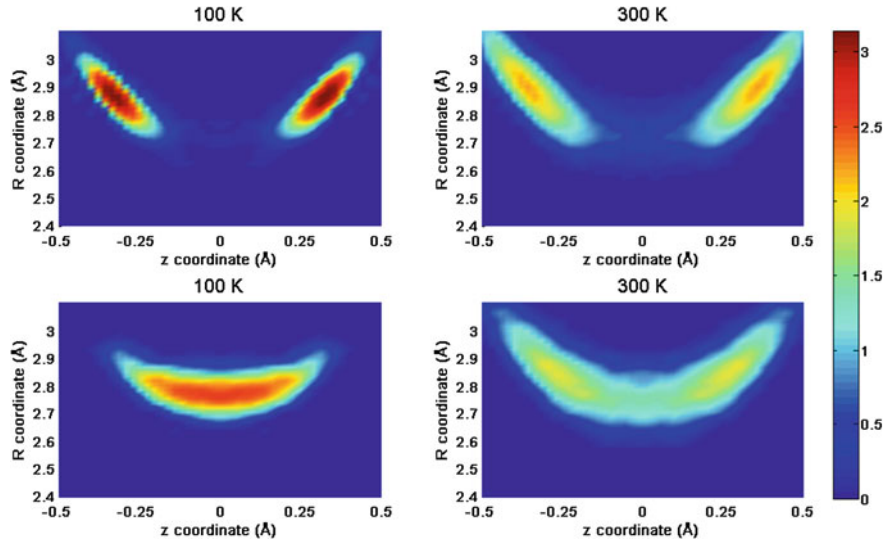


Fig. 3 Reduced probability distribution (z , R) for $(\text{Me}_3\text{N})_2\text{H}^+$. Classical simulations (top row) 100 K (left) and 300 K (right); Quantum simulations (bottom row) 100 K (left) and 300 K (right)

of $(\text{Me}_3\text{N})_2\text{H}^+$ is shown in Fig. 3. It is clear to see a very significant nuclear quantum effect at 100 K. In classical CPMD, proton is localized on either of Me_3N , but in PIMD a clear delocalization of proton shared by both Me_3N is evident.

One of the advantages of PIMD over vibrational variational approach is to obtain finite-temperature behaviors. It is worth mentioning that in these two cases, temperature dependency could be rationalized in the basis of quantum statistical mechanics [24]. In path integral simulation, the partition function is represented in coordinate space; still, the representation in Hilbert space through eigenfunctions is equivalent. Viewing the results in $(\text{NH}_3)_2\text{H}^+$ and $(\text{Me}_3\text{N})_2\text{H}^+$ at 100 K, it is certain that at low temperature the predominant ground state wavefunctions are delocalized which cannot be described by equilibrium structure of MD or stationary point analysis of potential energy surface. At 300 K, the change in distribution is lying upon the variational weighting of eigenstates $\exp(-\beta E)$, where $\beta = 1/kT$ is different from one at 100 K. PIMD simulations, herein, indicate that proton whether symmetrically or asymmetrically hydrogen bonded Fig. 3 is affected by excited states along z direction which are strongly coupled to the N–N stretching, R . Therefore, an investigation of wavefunctions in these two degrees of freedom is important and should qualitatively describe the nature of quantum nature of proton.

2.3 Vibrational Hamiltonian at Reduced Dimensions

To account for the quantum effect of the nuclei and to compute spectra, one of the most powerful approaches is to construct a vibrational Hamiltonian and solve the corresponding Schrödinger equation. However, a full dimensional treatment is not feasible for the systems we are interested in. In this work, we use a simple finite difference method to treat the relevant degrees of freedom. The one-dimensional vibrational Schrödinger equation is written as

$$\hat{H}\Psi = -\frac{\hbar^2}{2\mu_z} \left[\frac{d^2\Psi}{dz^2} \right] + \hat{U}(z)\Psi = E\Psi$$

Within finite difference methods, the kinetic (\hat{T}_z) and potential ($\hat{U}(z)$) energy operators can be discretized as follows:

$$\hat{T}_z = -\frac{\hbar^2}{2\mu_p(\Delta z)^2} \begin{pmatrix} -2 & 1 & & 0 \\ 1 & \ddots & \ddots & \\ & \ddots & \ddots & 1 \\ 0 & & 1 & -2 \end{pmatrix}$$

$$\hat{U}(z) = \begin{pmatrix} U(z_1) & & 0 \\ & \ddots & \\ 0 & & U(z_n) \end{pmatrix}$$

To extend the method of finite difference for solving higher dimensional Schrödinger equations, one has to map a one-dimensional Hamiltonian to the other dimension. For the sake of illustration purposes, for the z and R degrees of freedom, the Hamiltonian can be written as follows:

$$H = I_R \otimes T_z + T_R \otimes I_z + V(z, R),$$

where I_z and I_R represents the identity matrix along z and R and kinetic energies along z and R has the following forms:

$$T_z = -\frac{\hbar^2}{2\mu_z(\Delta z)^2} \begin{pmatrix} -2 & 1 & & 0 \\ 1 & \ddots & \ddots & \\ & \ddots & \ddots & 1 \\ 0 & & 1 & -2 \end{pmatrix}$$

$$T_R = -\frac{\hbar^2}{2\mu_R(\Delta R)^2} \begin{pmatrix} -2 & 1 & & 0 \\ 1 & \ddots & \ddots & \\ & \ddots & \ddots & 1 \\ 0 & & 1 & -2 \end{pmatrix}$$

In the systems we considered, the reduced masses along z and R are defined as $\mu_z = \frac{2m_{Nq_3}m_H}{2m_{Nq_3}+m_H}$ and $\mu_R = \frac{1}{2}m_{Nq_3}$, where q in Nq_3 can either be $-H$, or $-CH_3$.

Table 2 Vibrational transition energies in cm^{-1} for $(\text{NH}_3)_2\text{H}^+$; results were from a $|\text{z}, \text{R}, \phi_1, \phi_2>$ (4D) and $|\text{z}, \text{R}, \phi_1, \phi_2, \text{x}, \text{y}>$ (6D)

	B3LYP	MP2	MP2	MP2	Experiment
$ \text{z}, \text{R}, \phi_1, \phi_2, \text{x}, \text{y}>$	2D	2D	4D	6D	Full-dimension
$ \text{0}, \text{1}, \text{0}, \text{0}, \text{0}, \text{0}>$	462.98	469	421	403	–
$ \text{1}, \text{0}, \text{0}, \text{0}, \text{0}, \text{0}>$	613.49	594	460	409	374
$ \text{0}, \text{2}, \text{0}, \text{0}, \text{0}, \text{0}>$	888.20	893	729	701	–
$ \text{1}, \text{1}, \text{0}, \text{0}, \text{0}, \text{0}>$	1,016.45	997	760	713	743

The experimental values are also tabulated for reference

All of the coordinates mentioned are the same as were defined in Fig. 1

To assess the validity of using two-dimensional approach, we compare the 2D calculations using B3LYP/6-311+G(d,p) and MP2/aug-cc-pVTZ with the 4D and 6D calculations by Yang [19]. In Table 2, it is clear that our results using B3LYP/6-311+G(d,p) does not differ significantly with MP2/aug-cc-pVTZ. This in turn justifies the use of B3LYP in this study. Moreover, vibrational variational calculations in this study will be limited to two degrees of freedom, z and R . The researchers feel that two-dimensional treatment is sufficient for our purposes due to the fact that: (1) An assignment of the peak is not a major concern in this study. Instead, only a qualitative picture is sought which demonstrates quantum confinement. (2) Based from Yang's dissertation [19], two-dimensional treatment gives frequencies close within 250 cm^{-1} .

3 Results and Discussion

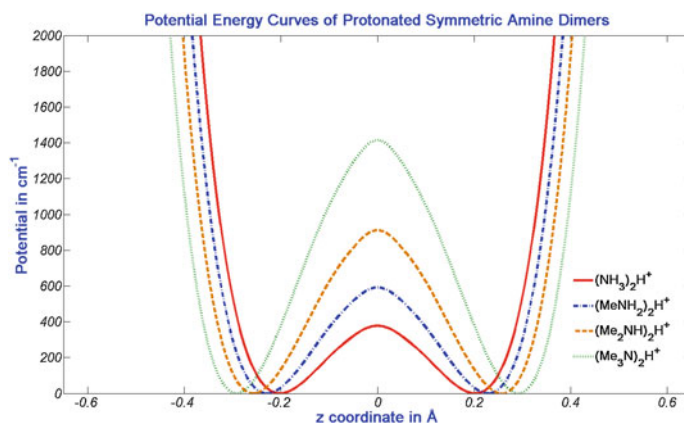
Standard static quantum chemistry calculations yield an intuitive hypsochromic shift as the degree of methylation is enhanced. Given the delocalization of the shared proton due to its quantum nature, we carried out vibrational variational calculations and our results show a counter intuitive bathochromic shift. The physical origin of this counter intuitive picture is analyzed and possible experimental observables were proposed.

3.1 An Intuitive Trend Based on a Static Picture

Key structural parameters for the other amines calculated by B3LYP/6-311+G(d,p) are tabulated in Table 3. The results show consistency with usual chemical wisdom. Across the series, N–N distance increases due to steric strain from ammonia to trimethylamine. On the other hand, the N–H distance decreases across the series

Table 3 Calculated N–N and N–H_{sp} (SP = shared proton) distance for protonated dimers of ammonia and lower homolog amines under B3LYP/6-311+G(d,p)

System	N–N (Å)	N–H _{sp} (Å)
(NH ₃) ₂ H ⁺	2.692	1.143
(MeNH ₂) ₂ H ⁺	2.715	1.129
(Me ₂ NH) ₂ H ⁺	2.742	1.114
(Me ₃ N) ₂ H ⁺	2.781	1.098

**Fig. 4** One-dimensional (z-coordinate) potential energy curve of the protonated symmetric amine dimers in this study. Red (NH₃)₂H⁺, blue (MeNH₂)₂H⁺, brown (Me₂NH)₂H⁺ and green (Me₃N)₂H⁺

due to the fact that the basicity of the amine is enhanced upon increasing methylation.

The potential energy curves along the z coordinates are shown in Fig. 4 using the minimum as the reference geometry. Based from the potential energy curves, the energy barrier increases with increasing degree of methylation; this implies that it is harder for the shared proton to move between two minima from (NH₃)₂H⁺ to (Me₃N)₂H⁺. This conclusion agrees well with conventional chemical wisdom, where methyl substituents are known to be electron donating moieties and do indeed enhance the basicity of an amine. From here, it can be predicted that the fundamental transition corresponding to the z degree of freedom will undergo a hypsochromic shift as the degree of methylation is enhanced.

3.2 A Counter Intuitive Trend Arose from Quantum Nature

To assess the fidelity of the quantum behavior of proton with conventional chemical wisdom; we solve both one- (z-coordinate) and two-dimensional (z and R-coordinate) vibrational Schrödinger equation using the method of finite difference discussed in previous section.

The results of one-dimensional calculations we obtained show a counter intuitive from our conventional wisdom. One-dimensional probability densities for the lowest four states of each amine dimer are shown in Fig. 5. Instead of observing a hypsochromic shift with increasing degree of methylation, a bathochromic shift was obtained.

In order to account for this disparity between the vibrational calculations and chemical intuition, the concept of quantum confinement needs to be invoked. Perhaps the best model to relate with this is the particle in a line model. Based from standard quantum mechanics text [25, 26], as the length of the line is decreased, the corresponding eigenenergies increases. From this line of thinking and based from the potential energy curves in Fig. 4, the potential energy curve becomes wider from ammonia to trimethylamine and as a consequence, there is a lowering of energy in the first excited state. On the other hand, the presence of a barrier in the potential causes the ground state energy to be higher. The combination of these two purely quantum effects do account for the observed bathochromic shift in the fundamental transitions of the proton bound dimers.

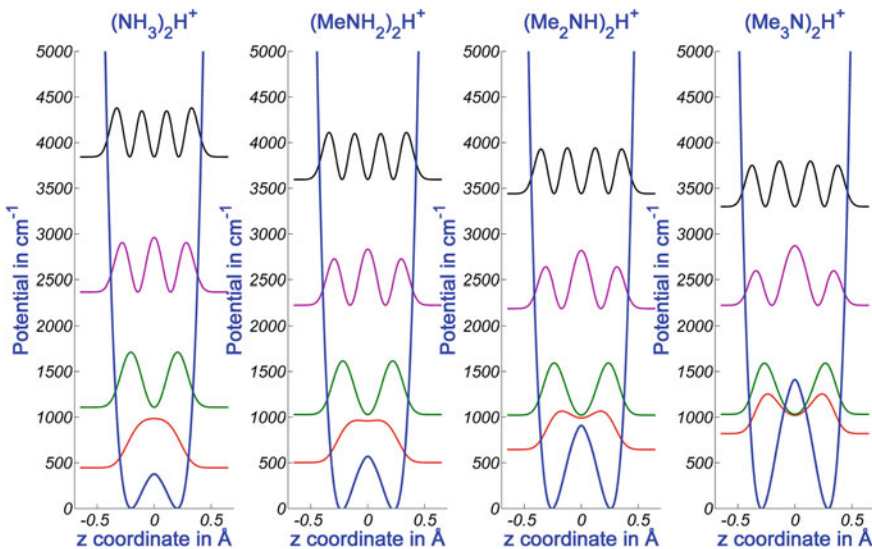


Fig. 5 Probability densities corresponding to the four lowest states of protonated amine dimers. From left to right, ammonia, methylamine, dimethylamine and trimethylamine

Table 4 Transition wavenumbers (ν) relative to the ground state for protonated symmetric dimers of ammonia and amines under two-dimensional (z and R) treatment

	(NH ₃) ₂ H ⁺	(MeNH ₂) ₂ H ⁺	(Me ₂ NH) ₂ H ⁺	(Me ₃ N) ₂ H ⁺
z, R>	ν (cm ⁻¹)	ν (cm ⁻¹)	ν (cm ⁻¹)	ν (cm ⁻¹)
0, 0>	0.00	0.00	0.00	0.00
0, 1>	462.98	334.91	266.02	213.98
1, 0>	613.49	546.32	462.54	345.65
0, 2>	888.20	647.23	512.94	410.75
1, 1>	1,016.45	837.22	694.62	536.95

To further check if the same trend is observed in higher dimension, two-dimensional calculations were performed. The chosen internal coordinates are z and R. A two dimensional potential energy surface was calculated and its corresponding vibrational Schrödinger equation was numerically solved using eleven-point finite difference. The results are shown in Table 4. Based from the results, the same trend was found to that of the one-dimensional treatment.

3.3 Possible Experimental Observables

To link this counter intuitive bathochromic shift to possible experimental observables. We compute IR spectra associated from transition from ground vibrational state from the two-dimensional PES. The integrated absorption coefficient is calculated by integrating over the dipole surface computed by the same level of DFT method. In Fig. 6, the stick spectra are shown, note that the most intense transitions ($|0, 0>$ to $|1, 0>$) associated with ν_{sp} can be found within 300–650 cm⁻¹. From ammonia to trimethylamine these intense peaks show a low-frequency shift—a clear demonstration of the bathochromic shift we proposed.

Vibrational signature of ν_{NN} is normally forbidden in IR, but in these systems we can observe strong combination bands due to the strong coupling between z- and R-motion. ν_{NN} can be found within 200–500 cm⁻¹ and the decrease of the gaps associated with ν_{NN} is mainly due to the increase of mass from ammonia to trimethylamine.

So far experimental vibrational spectra for proton bound dimers of methylamine, dimethylamine and trimethylamine are not yet available in the literature. We hope that our calculated IR spectra can stimulate further experimental work along this direction.

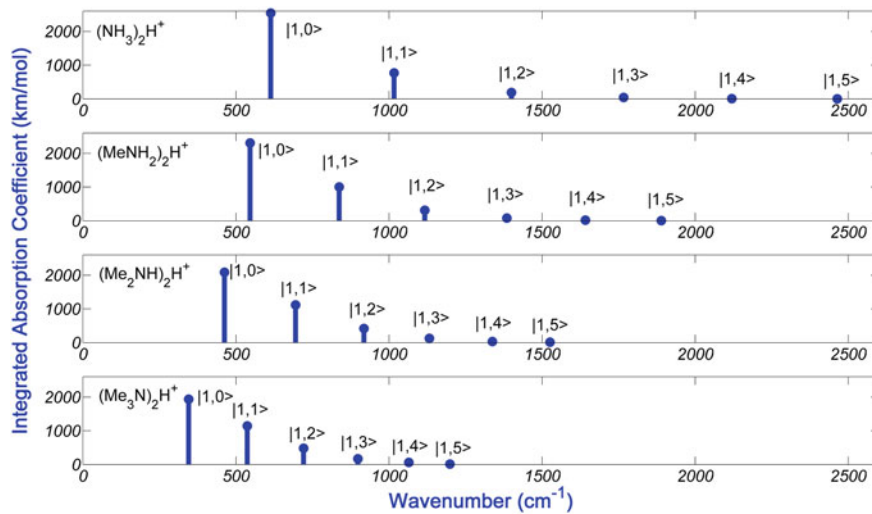


Fig. 6 Stick spectra of proton bound ammonia and other homologs. The gap between the fundamental band and $|1, 1\rangle$ combination band agrees with the one-dimensional treatment

4 Conclusion

The results obtained in this study shed light on the quantum behavior of the shared proton between two identical amines. The major features of the shared proton's nature includes: (1) The excited vibrational states do exhibit quantum confinement and (2) The ground vibrational state energy level upon enhancement of the proton transfer barrier. These two quantum effects, which happened to be innate for the shared proton clearly indicates that proton is a quantum object. Furthermore, the same trend was observed in the two-dimensional treatment (z and R coordinates). The combination of these two effects do account for the observed bathochromic shift in the fundamental transitions from ammonia to trimethylamine. IR spectra were computed and spectral features associated with the bathochromic shift is proposed for future experimental realizations.

Acknowledgments This work was financially supported by the Academia Sinica and the National Science Council (NSC101-2113-M-001-023-MY3) of Taiwan. Computational resources are supported in part by the National Center for High Performance Computing. We wish to thank contributions from Linda Shen and Tzu-Chien Wang at the early stage of this project. Fruitful discussions with Prof. Yonggang Yang and Prof. Masanori Tachikawa are also acknowledged.

References

1. Cleland WW, Kreevoy MM (1994) *Science* 264:1887
2. Voet D, Voet J (2004) *Biochemistry*, 3rd edn. Wiley, New York
3. Baker EN (2006) *Int Tables Crystallogr F*:546–552
4. Graham JD, Buytendyk AM, Wang D, Bowen KH, Collins KD (2013) *Biochemistry* 53:344
5. DeCoursey TE (2003) *Physiol Rev* 83:475
6. Garczarek F, Gerwert K (2006) *Nature* 439:109
7. Lee J, Kim CH, Joo T (2013) *J Phys Chem A* 117:1400–1405
8. Pimentel GC, McClellan AL (1960) *The hydrogen bond*. Freeman and Company, San Francisco
9. Hilbert GE, Wulf OR, Hendricks SB, Liddel U (1936) *J Am Chem Soc* 58:548–555
10. Ellis JW (1939) *J Am Chem Soc* 51:1384
11. Schwarz HA (1980) *J Chem Phys* 72:284–287
12. Price JM, Crofton MW, Lee YT (1989) *J Chem Phys* 91:2749–2751
13. Price JM, Crofton MW, Lee YT (1989) *J Chem Phys* 95:2182–2195
14. Roscioli JR, McCunn LR, Johnson MA (2007) *Science* 316:249–254
15. Scheiner S, Harding LB (1981) *J Am Chem Soc* 103:2169–2173
16. Asada T, Haraguchi H, Kitaura K (2001) *J Phys Chem A* 105:7423–7428
17. Yang Y, Kühn O (2011) *Chem Phys Lett* 505:1–4
18. Asmis KR, Yang Y, Santambrogio G, Brümmer M, Roscioli JR, McCunn LR, Johnson MA, Kühn O (2007) *Angew Chem Int Ed* 46:8691–9694
19. Yang Y (2008) PhD Dissertation, Freie Universität Berlin
20. Ishibashi H et al (2008) *Chem Phys Chem* 9:383
21. Frisch MJ, Trucks GW, Schlegel HB, Scuseria GE, Robb MA, Cheeseman JR, Scalmani G, Barone V, Mennucci B, Petersson GA, Nakatsuji H, Caricato M, Li X, Hratchian HP, Izmaylov AF, Bloino J, Zheng G, Sonnenberg JL, Hada M, Ehara M, Toyota K, Fukuda R, Hasegawa J, Ishida M, Nakajima T, Honda Y, Kitao O, Nakai H, Vreven T, Montgomery JA, Jr., Peralta JE, Ogliaro F, Bearpark M, Heyd JJ, Brothers E, Kudin KN, Staroverov VN, Kobayashi R, Normand J, Raghavachari K, Rendell A, Burant JC, Iyengar SS, Tomasi J, Cossi M, Rega N, Millam JM, Klene M, Knox JE, Cross JB, Bakken V, Adamo C, Jaramillo J, Gomperts R, Stratmann RE, Yazyev O, Austin AJ, Cammi R, Pomelli C, Ochterski JW, Martin RL, Morokuma K, Zakrzewski VG, Voth GA, Salvador P, Dannenberg JJ, Dapprich S, Daniels AD, Farkas O, Foresman JB, Ortiz JV, Cioslowski J, Fox DJ (2009) Gaussian, Inc., Wallingford. Gaussian 09, Revision A.02
22. Tuckerman ME, Marx D, Klein ML, Parrinello (1996) *J Chem Phys* 104:5579
23. Marx D, Tuckerman ME, Hutter J, Parrinello M (1999) *Nature* 397:601
24. Grotendorst J, Marx D, Muramatsu A (2002) Path integration via molecular dynamics. In: Von Neumann J (ed) *Quantum simulations of complex many-body systems: from theory to algorithms*, vol 10. Institute for Computing, Julich, p 269
25. Simons J, Nichols J (1997) *Quantum mechanics in chemistry*. Oxford University Press, New York
26. Ratner MA, Schatz GC (2000) *Introduction to quantum mechanics in chemistry*. Prentice Hall, Englewood Cliffs

Ab-Initio and DFT Study of the Muchimangin-B Molecule

Liliana Mammino, Mireille K. Bilonda
and Tendamudzimu Tshiwawa

Abstract Muchimangin B is a xanthone derivative isolated from the root of *Securidaca longepedunculata* and exhibiting activity against pancreatic cancer. Detailed information about the molecular properties of a biologically active compound is important for the design of compounds with more potent activities. This work presents the results of an ab initio and DFT study of the muchimangin B molecule. HF/6-31G(d,p) and DFT/B3LYP/6-31+G(d,p) calculations were performed in vacuo with fully relaxed geometry, to identify conformational preferences. These preferences are dominantly determined by different intramolecular hydrogen bonding patterns, although the orientation of the rings with respect to the xanthone moiety also has significant influence. Frequency calculations were performed to verify that identified stationary points are true minima. Calculations in solution were performed on the in vacuo optimized geometries, as single point calculations at the DFT/B3LYP/6-31+G(d,p) level, considering three solvents with different polarity and H-bonding ability—chloroform, acetonitrile and water. Selected adducts with explicit water molecules were calculated, for their informative roles in view of the presence, in the muchimangin B molecule, of a high number of sites that can act as donors or acceptors of intermolecular hydrogen bonds with water molecules.

Keywords Anticancer · Muchimangin B · Solute-solvent interactions · Xanthone derivatives

L. Mammino (✉) · M. K. Bilonda · T. Tshiwawa
Department of Chemistry, University of Venda, Thohoyandou, South Africa
e-mail: sasdestria@yahoo.com

M. K. Bilonda
e-mail: mireillebilonda@yahoo.fr

T. Tshiwawa
e-mail: ttshiwawa@yahoo.com

1 Introduction

Muchimangin B ($C_{31}H_{28}O_{11}$, Fig. 1) is a xanthone derivative isolated from the root of *Securidaca longepedunculata*, a plant utilised in traditional medicine in the DR Congo [1]. It exhibits activity against pancreatic cancer [1], a type of cancer largely resistant to most anticancer drugs currently in clinical use.

Biologically active compounds of natural origin are important sources of new active molecular structures, because they are already known to possess a certain type of desired activity and already known to be compatible with a living organism and to be able to reach their targets within the organism. Detailed information about the molecular properties of a biologically active compound is important for the design of compounds with more potent activities [2]. It is important to know as many details of the molecular properties as possible, as the biological activity may be related to the finest details of these properties [3]. This motivates detailed computational studies of biologically active molecules.

The current study investigates the conformational preferences of muchimangin B (concisely denoted by the acronym MUCH-B in the rest of the text) in vacuo and in three solvents with different polarities and different hydrogen-bonding abilities—chloroform, acetonitrile and water. Considering solvents with different polarities is important to take into account the possible environments in which a molecule may be present within a living organism. The octanol/water partition coefficient of MUCH-B (4.23138, estimated with [4]) suggests that it is mostly present in non-polar media. However, the dominant presence of water in living organisms recommends its inclusion in the range of solvents considered for a biologically active molecule. Chloroform is a good model for non-polar media, and acetonitrile has intermediate polarity and is also a suitable model for the medium in cellular membranes. Considering solvents with different H-bonding abilities is important for molecules containing H-bond donor or acceptor sites.

The results show the dominant role of intramolecular hydrogen bonds (IHB) in determining the conformational preferences and relative energies of MUCH-B, followed by the orientation of the two rings with respect to the xanthone moiety. The results in solution show the changes of the molecular properties with increasing solvent polarity. The solvent-stabilising effect is greater for water.

2 Computational Details

Calculations in vacuo with full geometry optimization (fully relaxed geometry) were performed at two levels of theory: Hartree-Fock (HF/6-31G(d,p)) and density functional theory with the B3LYP functional (DFT/B3LYP/6-31+G(d,p)). In addition, Møller-Plesset perturbation theory (MP2/6-31G(d,p)) calculations were performed as single point (SP) calculations on the HF-optimized results.

HF can be expected to give reasonable information for conformational aspects, including the identification of trends. It can also be considered interesting for

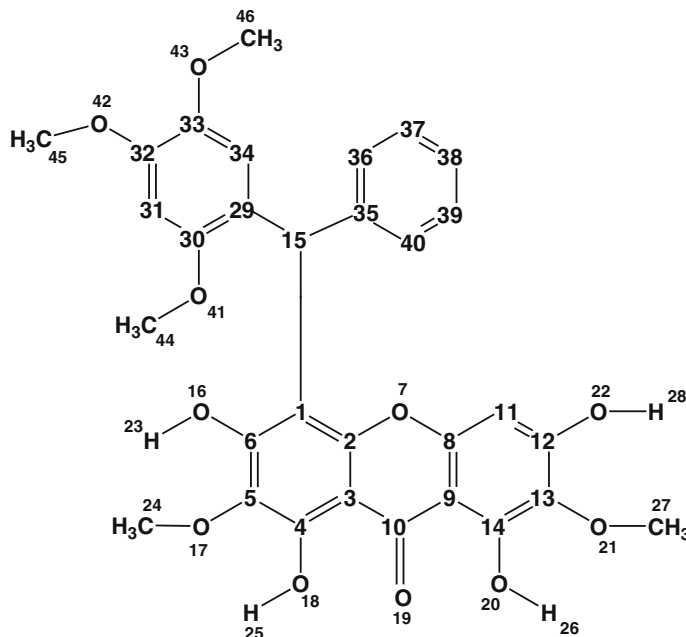


Fig. 1 Structure of the muchimangin B molecule and atom numbering utilised in this work

molecules having the possibility of forming IHBs, because it proved to yield better results (results closer to experimental values, when available, or closer to MP2 results) for IHB parameters and for the effects of IHB removal, for some classes of molecules, including the large class of acylphloroglucinols [5–10]. It also provides HOMO-LUMO energy differences closer to experimental values. Furthermore, HF constitutes the first (unperturbed) step for MP2 calculations.

DFT calculations are popular because of their ability to take into account part of the correlation effects at a not-too-high cost, and B3LYP [11–13] is the most commonly used functional. The presence of diffuse functions in the basis set for DFT/B3LYP calculations proved important for better-quality results with molecules containing IHBs [5].

MP2 calculations are important for their ability to take into account both correlation and dispersion effects. They were performed as SP calculations because full-optimization MP2 calculations would be unaffordable for a molecule of this size. On the other hand, SP calculations provide valuable information on features like conformers' energetics.

Calculations in solution utilized the Polarisable Continuum Model (PCM [14, 15]), which considers the solute molecule as embedded in a cavity in the continuum solvent, which is characterised by its dielectric constant. The default settings of Gaussian03 [16] were utilised, i.e., Integral Equation Formalism model, IEF [17–20], Gepol model for building the cavity around the solute molecule

[21–23], with simple United Atom Topological Model (UAO) for the atomic radii (default values) and average tesserae area 0.200 Å². The SCFVAC option was selected to obtain thermodynamic data. Calculations in solution were performed as SP calculations because of the high costs of PCM re-optimization in solution for a molecule of this size. Although the SP option does not enable the identification of geometry changes caused by the solvent, it can be expected to provide reasonable information for the energetics [5], both in terms of relative energies of the conformers in different media and in terms of energy aspects of the solution process (the free energy of solvation, ΔG_{solv}, and its components).

Harmonic vibrational frequencies were calculated at the DFT/B3LYP/6-31+G(d,p), level, to verify that identified stationary points correspond to actual minima and to obtain the zero-point energy (ZPE) corrections. The frequency values were scaled by 0.964, the factor recommended for DFT/B3LYP/6-31+G(d,p) calculations [24].

Three adducts with explicit water molecules were calculated for one of the low energy conformers, because of their information-ability in view of the presence of several H-bond donor/acceptor sites in the MUCH-B molecule [10]. They were calculated at the HF/6-31G(d,p) level because of the high computational costs of the supermolecular structure. The interaction energy (ΔE_{mol-n aq}) between the MUCH-B molecule and the water molecules H-bonded to it in the adduct is calculated as:

$$\Delta E_{\text{mol}-n \text{ aq}} = E_{\text{adduct}} - (E_{\text{mol}} + n E_{\text{aq}}) - \Delta E_{\text{aq-aq}} \quad (1)$$

where E_{adduct} is the energy of the adduct, n is the number of water molecules in the adduct, E_{mol} is the energy of an isolated MUCH-B molecule, E_{aq} is the energy of an isolated water molecule and ΔE_{aq-aq} is the overall interaction energy between water molecules, due to water-water H-bonds. ΔE_{aq-aq} is evaluated as

$$\Delta E_{\text{aq-aq}} = E_{\text{water-adduct}} - n E_{\text{aq}} \quad (2)$$

where E_{water-adduct} is the energy of a group of water molecules arranged exactly as in the adduct, but without the MUCH-B molecule [25], and is obtained from an SP calculation at the same level at which the adduct is calculated. Comparison of Eqs. (1) and (2) leads to

$$\Delta E_{\text{mol-n aq}} = E_{\text{adduct}} - E_{\text{mol}} - E_{\text{water-adduct}} \quad (3)$$

Both E_{adduct} and E_{water-adduct} were corrected for BSSE using the counterpoise method [26]. All the calculations were performed using GAUSSIAN 03, Revision D 01 [16]. All the energy values reported are in kcal/mol and all the distances are in Å.

Acronyms are utilized for conciseness sake on reporting values: HF for HF/6-31G(d,p), DF+ for DFT/B3LYP/6-31+G(d,p) and MP for MP2/6-31G(d,p).

Table 1 Combinations of intramolecular hydrogen bonds (IHB) in the conformers of muchimangin B and numbers utilised to denote them in the conformers' names

Conformer number	IHB present						
	H23···O17	H25···O17	H25···O19	H26···O19	H23···O41	H26···O21	H28···O21
1	x		x	x			x
2			x	x	x		x
3	x		x	x			
4		x		x	x		x
5	x		x			x	x
6	x	x		x			x
7		x		x	x		
8			x		x	x	x
9	x	x		x			
10		x			x	x	x
11	x	x				x	x

3 Results

3.1 Results in Vacuo

The major factors influencing the conformational preferences of MUCH-B are the IHB patterns, i.e. the number and types of IHBs present in the conformer, and the orientations of the two benzene rings, both mutually and with respect to the xanthone moiety. Seven IHBs are possible (not all simultaneously, but up to four simultaneously): H23···O17, H25···O17, H25···O19, H26···O19, H26···O21, H28···O21 and H23···O41 (the atom numbering utilised in this work is shown in Fig. 1). H23···O41 is the only possible IHB between the two moieties, as only O41, being in ortho to C15, can come close enough to the xanthone moiety to engage in an IHB.

Because of the importance of the IHBs, the IHB pattern is selected as the first criterion to classify the conformers. Therefore, conformers are denoted with a number referred to their IHB pattern, as shown in Table 1 and illustrated in Fig. 2, followed by a letter. The letter is progressive according to the relative energy of the 1-type conformers and remains associated with similar orientation of the A and B rings with respect to the xanthone moiety for the 3-, 5-, 6-, 9- and 11-type conformers (conformers not having the H23···O41 IHB). For the conformers with the H23···O41 IHB (2-, 4-, 7-, 8- and 10-type), two orientations of the A and B rings are possible without disrupting this IHB, and they are denoted with the letters a and b, independently of the use of these letters for the conformers not having the H23···O41 IHB. Table 2 shows the relative energies of the calculated conformers in the results of all the methods utilised in vacuo and, for the DFT/B3LYP/6-31+G(d, p) level, also in all the solvent considered. Figure 3 shows the geometries of most of the conformers.

The mutual orientation of the three moieties can remarkably influence the conformers' energy. For instance, among the conformers with the most favourable

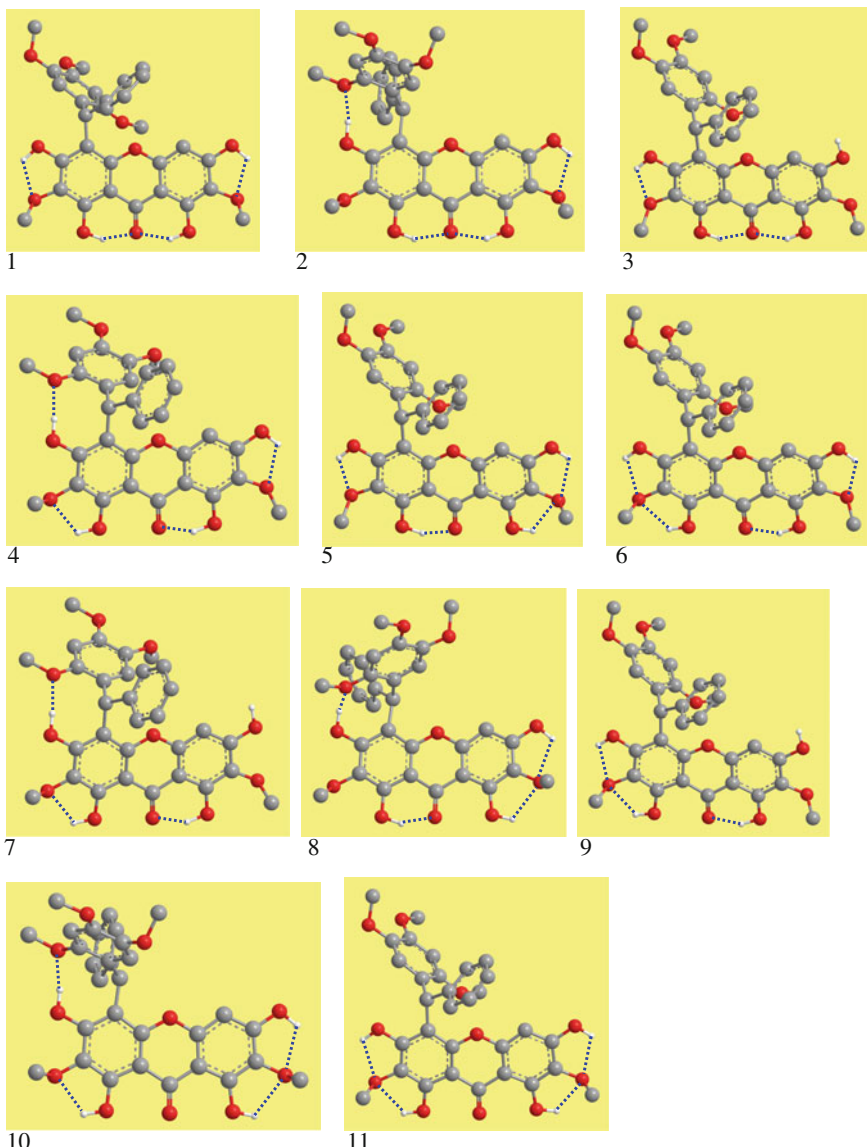


Fig. 2 Intramolecular hydrogen bond patterns in the conformers of muchimangin B. The intramolecular hydrogen bonds are denoted by *dotted segments*. The conformer/s in which each pattern is present are indicated under each image. The H atoms attached to C atoms are not shown, to increase the readability of the images

IHB pattern, the relative energy of conformer 1-i is 4.3222 kcal/mol higher than the relative energy of the conformer with the same IHB pattern and most favourable mutual orientation of the moieties (1-a). While many different orientations of the

Table 2 Relative energies of the calculated conformers of muchimangin B from the results of different calculation methods in vacuo, and from PCM DFT/B3LYP/6-31+G(d,p) results in solution

Conformer	Relative energy (kcal/mol)			Results in solution		
	Results in vacuo		DFT/B3LYP/ 6-31+G(d,p)	Single point PCM DFT/B3LYP/ 6-31+G(d,p)		
	HF /6-31G(d,p)	MP2/6-31 G(d,p)/ HF 6-31G(d,p)		In chloroform	In acetonitrile	In water
1-a	0.0000	0.5982	0.0000	0.0000	0.0000	0.0000
1-b	0.3343	0.0000	0.2140	0.2789	0.3582	0.5897
1-c	2.4190	1.7529	2.5401	2.5649	2.6450	2.6953
1-d	2.4558	1.7070	2.5747	2.5973	2.6781	2.5461
1-e	2.4874	1.8227	2.6084	2.5971	2.5151	2.5647
1-f	3.0172	1.4935	2.7248	3.1242	3.3410	3.3195
2-a	3.3325	4.1170	3.2298	2.3954	2.1274	2.5658
1-g	4.1060	4.5032	3.9878	3.9250	3.9809	3.1990
1-h	3.4252	2.6130	4.1677	4.4261	4.5547	4.7132
1-i	4.8767	6.2248	4.3222	— ^a	4.6177	4.4089
2-b	3.4452	3.2651	4.4005	3.6109	3.3168	2.2662
3-a	4.8394	6.3072	5.5822	4.1419	3.2705	1.1222
3-b	5.2861	5.6544	6.1847	5.4740	5.1303	4.0781
3-c	7.2460	7.4161	8.1035	6.7170	6.0750	3.8554
4	10.0476	8.8642	10.7170	8.8718	8.2724	6.7211
5-a	9.8454	10.7076	11.9078	9.7970	8.9512	6.4816
5-b	10.4446	10.3351	12.4754	10.3284	9.5053	7.1355
6-b	10.4990	10.2458	12.5153	10.3284	9.5053	7.1355
6-a	10.4921	11.2258	12.6213	10.3306	9.4168	6.9981
5-c	12.6057	12.2092	14.7312	12.5653	11.7334	9.3089
6-c	12.7889	12.2429	15.0566	12.9609	12.2222	9.7075
7	15.0441	14.6959	16.4368	12.9303	11.5555	7.8820
8	13.7769	13.8853	16.7844	13.6567	12.4045	9.0351
9-a	15.4831	17.1122	18.2963	14.4347	12.7259	8.2238
9-b	16.2296	16.6169	18.7053	15.7674	14.4449	11.2084
9-c	17.7476	18.0487	20.7192	17.1660	15.8641	10.9043
10	21.9005	22.6201	25.5025	20.9490	19.1335	15.7362
11-a	22.0281	23.1336	27.0336	22.3711	20.5083	15.4427
11-b	22.5293	22.3876	27.1816	22.6862	20.9011	15.9954
11-c	24.6747	24.4410	29.7708	25.2173	23.4325	18.3900

The conformers are listed in order of increasing energy referred to the DFT/B3LYP/6-31+G(d,p) results in vacuo. The DFT/B3LYP/6-31+G(d,p) results in vacuo are reported in the third column to facilitate comparisons with the results in solution, that appear in the subsequent columns

^a The calculation in chloroform solution does not converge for this conformer

three moieties were considered for the lowest-energy IHB pattern, only some of them were considered—with a representative role—for the other IHB patterns. It is important to note that the conformers which may be responsible for the biological activity are those with comparatively low relative energy (a sufficiently cautious threshold value considering those with relative energy ≤ 3.5 kcal/mol). Conformers

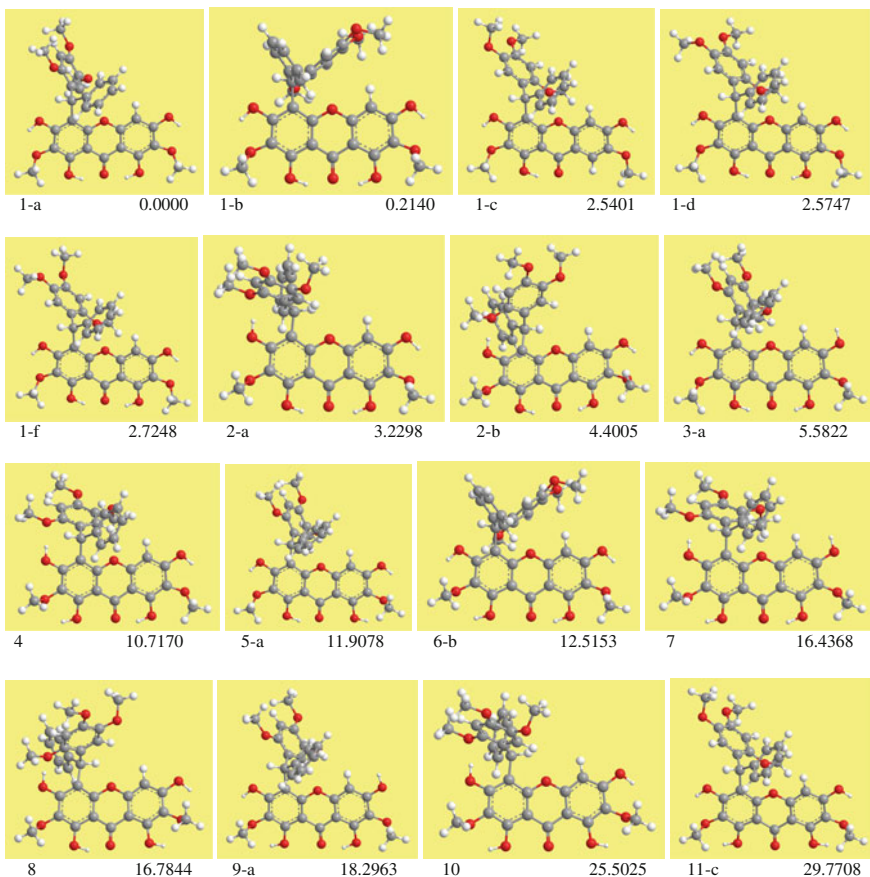


Fig. 3 Representative conformers of muchimangin B. The selected conformers are shown in order of increasing relative energy, whose values (kcal/mol) are reported under each image

with high relative energy are not sufficiently populated to have a role in the biological activity. The only reason for considering them in the computational study of a molecule is their utilisation as references to estimate the influence of the various factors determining conformational preferences and the conformers' energetics. For instance, a conformer in which a certain IHB is removed can help assess the stabilising influence of that IHB, by comparison with the conformer in which it is present.

The orientation of the methyls of the ether groups does not have significant influence on the conformers' energy. For instance, conformers 1-c, 1-d, 1-e and 1-f have all the same IHBs and similar orientations of the A and B rings, and differ only by the orientations of the ether groups: the ether at O42 is perpendicular to the plane and on opposite sides of the plane in 1-c and 1-d, while it is coplanar to the benzene ring in 1-f; the ethers at O17 and O21 are on the opposite side of the plane in 1-e with respect to 1-c. The energy difference between these conformers is negligible.

Table 3 Parameters of the intramolecular hydrogen bonds in the calculated conformers of muchimangin B, in vacuo

Conformer	IHB considered	Parameters of the IHB					
		HF/6-31G(d,p) results			DFT/B3LYP/6-31+G(d,p) results		
		H···O (Å)	O···O (Å)	O $\ddot{\text{O}}$	H···O (Å)	O···O (Å)	O $\ddot{\text{O}}$
1-a	H23···O17	2.087	2.636	115.3	2.034	2.633	117.8
	H25···O19	1.787	2.617	143.5	1.673	2.576	148.7
	H26···O19	1.805	2.635	143.5	1.692	2.592	148.5
	H28···O21	2.139	2.669	114.0	2.082	2.663	116.4
1-b	H23···O17	2.083	2.633	115.5	2.036	2.634	117.7
	H25···O19	1.791	2.620	143.4	1.675	2.576	148.6
	H26···O19	1.801	2.632	143.6	1.685	2.587	148.7
	H28···O21	2.141	2.670	114.0	2.082	2.663	116.4
1-c	H23···O17	2.093	2.637	115.0	2.036	2.633	117.6
	H25···O19	1.781	2.612	143.6	1.667	2.571	148.9
	H26···O19	1.802	2.633	143.6	1.688	2.590	148.7
	H28···O21	2.135	2.667	114.2	2.079	2.661	116.6
1-d	H23···O17	2.084	2.634	115.4	2.030	2.631	117.9
	H25···O19	1.780	2.612	143.6	1.666	2.570	148.9
	H26···O19	1.803	2.634	143.6	1.688	2.590	148.7
	H28···O21	2.136	2.668	114.2	2.078	2.660	116.6
1-e	H23···O17	2.088	2.636	115.3	2.036	2.634	117.6
	H25···O19	1.781	2.612	143.6	1.669	2.572	148.7
	H26···O19	1.802	2.633	143.6	1.688	2.589	148.7
	H28···O21	2.136	2.667	114.1	2.079	2.661	116.5
1-f	H23···O17	2.084	2.634	115.4	2.027	2.629	118.0
	H25···O19	1.780	2.611	143.6	1.666	2.570	148.9
	H26···O19	1.803	2.634	143.6	1.690	2.591	148.6
	H28···O21	2.137	2.667	114.2	2.080	2.662	116.5
2-a	H23···O41	1.807	2.726	162.0	1.736	2.688	162.9
	H25···O19	1.801	2.629	143.4	1.699	2.594	148.1
	H26···O19	1.799	2.630	143.6	1.681	2.584	148.8
	H28···O21	2.140	2.669	113.9	2.082	2.662	116.4
1-g	H23···O17	2.062	2.617	115.8	2.006	2.616	118.6
	H25···O19	1.794	2.624	143.5	1.682	2.583	148.6
	H26···O19	1.802	2.633	143.6	1.688	2.590	148.7
	H28···O21	2.140	2.669	114.0	2.083	2.663	116.4
1-h	H23···O17	2.081	2.632	115.5	2.032	2.632	117.8
	H25···O19	1.787	2.617	143.5	1.675	2.577	148.6
	H26···O19	1.805	2.635	143.5	1.689	2.590	148.6
	H28···O21	2.135	2.667	114.2	2.080	2.661	116.5

(continued)

Table 3 (continued)

Conformer	IHB considered	Parameters of the IHB					
		HF/6-31G(d,p) results			DFT/B3LYP/6-31+G(d,p) results		
		H···O (Å)	O···O (Å)	O \cdots O	H···O (Å)	O···O (Å)	O \cdots O
1-i	H23···O17	2.072	2.626	115.8	2.012	2.621	118.5
	H25···O19	1.794	2.623	143.3	1.681	2.581	148.5
	H26···O19	1.804	2.634	143.5	1.688	2.589	148.6
	H28···O21	2.141	2.669	113.9	2.082	2.662	116.4
2-b	H23···O41	2.167	2.777	121.7	1.969	2.729	133.3
	H25···O19	1.803	2.630	143.4	1.697	2.593	148.2
	H26···O19	1.798	2.630	143.6	1.682	2.586	148.8
	H28···O21	2.141	2.669	114.0	2.083	2.663	116.4
3-a	H23···O17	2.088	2.636	115.3	2.035	2.634	117.7
	H25···O19	1.786	2.617	143.5	1.672	2.575	148.7
	H26···O19	1.819	2.646	143.3	1.712	2.607	149.1
3-b	H23···O17	2.082	2.633	115.5	2.036	2.634	117.7
	H25···O19	1.791	2.621	143.4	1.671	2.574	148.7
	H26···O19	1.815	2.643	143.4	1.705	2.602	148.2
3-c	H23···O17	2.094	2.637	114.9	2.037	2.633	117.5
	H25···O19	1.781	2.613	143.6	1.666	2.570	148.9
	H26···O19	1.817	2.645	143.5	1.709	2.650	148.2
4	H23···O41	1.935	2.881	174.4	1.833	2.807	173.2
	H25···O17	2.102	2.647	115.2	2.048	2.647	117.8
	H26···O19	1.774	2.612	144.2	1.616	2.542	150.8
	H28···O21	2.140	2.670	114.1	2.083	2.665	116.6
5-a	H23···O17	2.089	2.638	115.4	2.037	2.636	117.8
	H25···O19	1.760	2.597	144.1	1.609	2.534	150.6
	H26···O21	2.199	2.707	112.7	2.185	2.736	114.6
	H28···O21	2.247	2.734	111.1	2.243	2.766	112.7
5-b	H23···O17	2.084	2.635	115.5	2.036	2.636	117.8
	H25···O19	1.763	2.599	144.1	1.611	2.535	150.6
	H26···O21	2.199	2.708	112.7	2.186	2.737	114.5
	H28···O21	2.247	2.736	111.2	2.242	2.767	112.8
6-b	H23···O17	2.184	2.692	112.5	2.182	2.729	114.3
	H25···O17	2.199	2.708	112.6	2.189	2.739	114.6
	H26···O19	1.774	2.611	144.2	1.620	2.545	150.7
	H28···O21	2.141	2.671	114.1	2.081	2.663	116.6
6-a	H23···O17	2.188	2.697	112.6	2.183	2.731	114.4
	H25···O17	2.201	2.708	112.5	2.192	2.740	114.4
	H26···O19	1.779	2.615	144.1	1.627	2.550	150.5
	H28···O21	2.140	2.671	114.1	2.084	2.665	116.5
5-c	H23···O17	2.095	2.639	115.0	2.038	2.635	117.6

(continued)

Table 3 (continued)

Conformer	IHB considered	Parameters of the IHB					
		HF/6-31G(d,p) results			DFT/B3LYP/6-31+G(d,p) results		
		H···O (Å)	O···O (Å)	O \hat{O}	H···O (Å)	O···O (Å)	O \hat{O}
	H25···O19	1.753	2.592	142.2	1.601	2.529	150.8
	H26···O21	2.199	2.709	112.7	2.186	2.737	114.6
	H28···O21	2.141	2.733	111.5	2.238	2.765	113.0
6-c	H23···O17	2.198	2.698	111.9	2.190	2.732	114.0
	H25···O17	2.200	2.709	112.7	2.191	2.740	114.5
	H26···O19	1.775	2.613	144.3	1.621	2.540	150.8
	H28···O21	2.136	2.669	114.3	2.079	2.662	116.7
7	H23···O41	1.939	2.884	174.3	1.838	2.812	173.3
	H25···O17	2.103	2.647	115.1	2.049	2.647	117.7
	H26···O19	1.789	2.624	144.0	1.638	2.558	150.3
8	H23···O41	2.159	2.778	122.1	1.973	2.735	133.6
	H25···O19	1.776	2.610	144.0	1.634	2.551	150.1
	H26···O21	2.198	2.707	112.6	2.185	2.736	114.6
	H28···O21	2.246	2.735	111.2	2.245	2.768	112.7
9-a	H23···O17	2.188	2.697	112.6	2.183	2.731	114.4
	H25···O17	2.202	2.704	112.5	2.193	2.740	114.3
	H26···O19	1.793	2.627	143.9	1.647	2.563	150.0
9-b	H23···O17	2.187	2.695	112.6	2.184	2.730	114.2
	H25···O17	2.200	2.708	112.6	2.189	2.739	114.5
	H26···O19	1.789	2.623	144.0	1.641	2.559	150.2
9-c	H23···O17	2.199	2.698	111.9	2.190	2.732	113.9
	H25···O17	2.201	2.709	112.6	2.192	2.741	114.4
	H26···O19	1.791	2.626	144.1	1.643	2.561	150.3
10	H23···O41	1.808	2.628	162.1	1.740	2.696	164.2
	H25···O17	2.091	2.641	115.6	2.039	2.643	118.2
	H26···O21	2.194	2.705	112.8	2.177	2.732	114.9
	H28···O21	2.245	2.735	111.3	2.241	2.766	112.9
11-a	H23···O17	2.187	2.697	112.7	2.182	2.731	114.5
	H25···O17	2.194	2.704	112.8	2.182	2.735	114.8
	H26···O21	2.191	2.704	112.9	2.175	2.731	114.9
	H28···O21	2.246	2.735	111.2	2.243	2.767	112.8
11-b	H23···O17	2.186	2.695	112.7	2.181	2.729	114.4
	H25···O17	2.193	2.705	112.9	2.179	2.734	114.9
	H26···O21	2.195	2.706	112.8	2.178	2.733	114.9
	H28···O21	2.245	2.736	111.4	2.240	2.766	112.9
11-c	H23···O17	2.198	2.699	112.0	2.189	2.732	114.0
	H25···O17	2.193	2.705	112.9	2.180	2.735	114.9
	H26···O21	2.193	2.706	113.0	2.175	2.732	115.0
	H28···O21	2.239	2.733	111.6	2.238	2.766	113.1

Table 4 Vibrational frequencies (harmonic approximation) of the O–H bonds in the muchimanganin B molecule

Conformer	Vibrational frequencies			
	O16–H23	O18–H25	O20–H26	O22–H28
1-a	3,563.57	3,178.20 ^a	3,178.20 ^a	3,575.97
		3,125.44 ^b	3,125.44 ^b	
1-b	3,565.50	3,171.05 ^a	3,171.05 ^a	3,575.13
		3,126.40 ^b	3,126.40 ^b	
1-c	3,565.60	3,166.40 ^a	3,166.40 ^a	3,574.76
		3,116.98 ^b	3,116.98 ^b	
1-e	3,563.93	3,167.91 ^a	3,167.91 ^a	3,574.50
		3,120.28 ^b	3,120.28 ^b	
1-f	3,560.61	3,170.09 ^a	3,170.09 ^a	3,574.93
		3,116.91 ^b	3,116.91 ^b	
2-a	3,400.16	3,218.00 ^a	3,218.00 ^a	3,574.73
		3,128.23 ^b	3,128.23 ^b	
1-g	3,555.22	3,176.18 ^a	3,176.18 ^a	3,576.02
		3,132.22 ^b	3,132.22 ^b	
1-h	3,562.12	3,173.64 ^a	3,173.64 ^a	3,573.5
		3,128.04 ^b	3,128.04 ^b	
1-i	3,552.34	3,176.70 ^a	3,176.70 ^a	3,574.13
		3,133.32 ^b	3,133.32 ^b	
2-b	3,588.72	3,209.91 ^a	3,209.91	3,575.37
		3,131.56 ^b	3,131.56 ^b	
3-a	3,563.20	3,219.62 ^a	3,219.62 ^a	3,687.05
		3,126.31 ^b	3,126.31 ^b	
3-b	3,564.80	3,207.07 ^a	3,207.07 ^a	3,687.56
		3,130.72 ^b	3,130.72 ^b	
3-c	3,565.28	3,209.29 ^a	3,209.29 ^a	3,686.23
		3,120.08 ^b	3,120.08 ^b	
5-a	3,565.53	2,942.08	3,606.83	3,626.37
5-b	3,566.92	2,954.10	3,606.27	3,625.38
6-b	3,619.97	3,607.98	2,950.89	3,576.63
6-a	3,620.62	3,607.65	2,973.13	3,577.79
5-c	3,567.63	2,930.72	3,607.10	3,625.30
6-c	3,621.91	3,607.44	2,949.33	3,575.95
8	3,589.34	3,027.12	3,605.79	3,626.07
9-b	3,618.82	3,608.18	3,019.10	3,688.67
10	3,406.23	3,561.38	3,604.93	3,626.06
11-a	3,621.74	3,605.86	3,604.63	3,627.26
11-b	3,620.54	3,605.91	3,604.41	3,626.48
11-c	3,623.20	3,605.11 ^c	3,605.11 ^c	3,626.62
		3,604.92 ^d	3,604.92 ^d	

DFT/B3LYP/6-31+G(d,p) results in vacuo. The frequency values have been scaled by the factor 0.964, recommended for DFT/B3LYP/6-31+G(d,p) calculations [24]

^a H25 and H26 moving symmetrically toward O19 and away from it

^b H25 and H26 moving asymmetrically toward O19 and away from it (when one approaches, the other moves away)

^c H25 and H26 moving symmetrically toward O17 and O21 respectively

^d H25 and H26 moving asymmetrically toward O17 and O21 respectively

Table 5 Relative energies (ΔE) corrected for ZPE, and ZPE corrections, for the conformers of muchimangin B in vacuo

Conformer	ΔE corrected for ZPE (kcal/mol)	ZPE correction (kcal/mol)	Conformer	ΔE corrected for ZPE (kcal/mol)	ZPE correction (kcal/mol)
1-a	0.0000	341.6328	5-a	11.4508	341.1760
1-b	0.3558	341.7740	5-b	12.0469	341.2043
1-c	2.6299	341.7219	6-b	12.1561	341.2733
1-e	2.6707	341.6950	6-a	12.0632	341.0750
1-f	2.8778	341.7853	5-c	14.3361	341.2375
2-a	3.3553	341.7577	6-b	14.5927	341.1685
1-g	3.9477	341.5927	8	16.2211	341.0693
1-h	4.0085	341.4735	9-b	17.7980	340.7248
1-i	4.3505	341.6611	10	25.0960	341.2262
2-b	4.3035	341.5356	11-a	26.1276	340.7267
3-a	5.2115	341.2620	11-b	26.4200	340.8710
3-b	5.8954	341.3436	11-c	28.8993	340.7612
3-c	7.8106	341.3392			

From DFT/B3LYP/6-31+G(d,p) frequency calculations

Detailed information on the relevant molecular properties of MUCH-B is given in tables. Table 3 reports the parameters of the IHBs; Table 4 reports the calculated harmonic vibrational frequencies for the O–H bonds of the OH groups; Table 5 reports the relative energies (ΔE) corrected for ZPE, and the ZPE corrections, for most conformers; Table 6 reports the dipole moments, and Table 7 reports the HOMO-LUMO energy gaps.

The consideration of IHBs requires simultaneous consideration of the conformers' relative energies, of the IHBs' parameters, and of the vibrational frequencies. H25···O19 and H26···O19 are the strongest IHBs. Their simultaneous presence is typical of the lower energy conformers' types (1, 2 and 3). Their H-bond length is considerably shorter than that of the other IHBs, being 1.666–1.699/DF+ and 1.787–1.807/HF. Their O–H bond angle ($\approx 145.5^\circ$) is more favourable than that of the other IHBs (which remains below 120°). Their red shift (lowering of the IR vibrational frequency with respect to when the same OH is not engaged in an IHB) is considerably greater than for the other IHB: from 3,605–3,607 for free O18–H25 or O20–H26 to 3,166–3,178 for the symmetric vibration and 3,116–3,133 for the asymmetric vibration when they are present simultaneously, and to 2,930–2,942 for H25–O19 and 2,949–3,019 for H26–O19 when each of them is present alone. Their greater strength is to be expected, as they involve an sp^2 O (O19).

The IHBs in which the acceptor is an ether O are considerably weaker. Their bond length is considerably longer than for H25···O19 or H26···O19, and also depends on the types of other IHBs present. H23···O41 is the strongest IHB engaging an ether O, with 1.736/DF+ and 1.807/HF bond length in 2-a, the lowest

Table 6 Dipole moment of the conformers of muchimangin B in the media considered

Conformer	Dipole moment (debye)				
	In vacuo		In solution		
	HF	DF+	In chloroform	In acetonitrile	In water
1-a	4.1662	3.9885	4.7594	5.1087	5.4182
1-b	1.7091	1.3588	1.5993	1.7075	1.7913
1-c	1.9821	1.8086	2.2881	2.5723	2.8092
1-d	1.2802	1.4782	1.7053	1.8188	1.8696
1-e	5.4458	5.4539	6.3211	6.7522	7.0890
1-f	3.1875	2.9062	3.4974	3.8409	4.3157
2-a	7.8440	7.8414	9.1170	9.6765	10.1632
1-g	5.8225	5.5955	6.4401	6.7994	7.0356
1-h	4.4311	5.8656	6.7562	7.1279	7.3608
1-i	3.9327	4.0896	— ^a	5.1223	5.4417
2-b	7.2060	7.4112	8.5433	9.0041	9.3447
3-a	7.1609	6.8873	8.1754	8.7262	9.3896
3-b	3.5714	2.8503	3.2916	3.3307	3.5051
3-c	3.5924	3.3345	4.0677	4.4421	4.8917
4	6.8559	7.3908	8.7117	9.1853	9.7601
5-a	3.2392	3.1910	4.0539	4.4051	4.7842
5-b	2.6990	3.7297	4.3824	4.6768	4.9450
6-b	4.7504	3.7297	4.3824	4.6768	4.9450
6-a	7.0239	7.0554	8.4389	9.0318	9.5749
5-c	5.4365	5.2699	6.4487	7.0350	7.5681
6-c	2.0224	2.2156	2.6125	2.7015	2.7775
7	9.8406	10.2365	12.0693	12.7602	13.6835
8	7.5252	7.8278	9.2467	9.8144	10.3495
9-a	9.8322	9.6991	11.5354	12.2909	13.1572
9-b	5.3468	5.4582	6.4969	6.8280	7.2309
9-c	5.0431	5.0250	5.9585	6.2923	6.7949
10	7.8202	8.1286	9.8208	10.5829	11.2538
11-a	4.1903	4.2402	5.3132	5.7960	6.2369
11-b	1.7791	1.4909	1.8078	1.9832	2.1970
11-c	2.4432	2.2783	3.0073	3.4131	3.7158

The results in vacuo are from full optimization HF/6-31G(d,p) calculations and DFT/B3LYP/6-31+G(d,p) calculations (respectively denoted as HF and DF+ in the column headings). The results in solution are from PCM DFT/B3LYP/6-31+G(d,p) single point calculations on the in-vacuo-optimised DFT/B3LYP/6-31+G(d,p) results

^a The calculation in chloroform solution does not converge for this conformer

energy conformer containing it. The vibrational frequency of O16–H23 decreases from 3,619–3,623 when it is free to 3,400 in conformer 2-a. The other IHBs engaging an ether O are considerably weaker. For instance, the length of H23···O17 is 2.006–2.037/DF+, 2.083–2.095/HF when H25···O19 is also present,

Table 7 HOMO-LUMO energy difference for the conformers of muchimangin B

Conformer	HOMO-LUMO energy difference (kcal/mol)				
	In vacuo		In solution/DF+		
	HF	DF+	In chloroform	In acetonitrile	In water
1-a	225.0	83.1	81.8	81.8	83.7
1-b	222.5	81.0	80.9	81.4	82.6
1-c	226.4	84.1	83.4	83.5	84.2
1-d	226.2	84.0	83.4	83.7	84.3
1-e	227.3	85.0	83.7	83.5	84.3
1-f	225.1	82.2	81.4	81.5	82.1
2-a	234.7	90.3	88.8	87.9	87.8
1-g	227.6	85.1	82.3	82.3	83.2
1-h	229.9	82.8	82.3	82.3	83.2
1-i	222.6	80.8	– ^a	79.6	81.2
2-b	232.6	89.5	87.3	86.2	86.1
3-a	226.8	84.3	82.4	82.2	84.0
3-b	225.0	83.9	81.8	81.7	82.5
3-c	227.9	85.2	83.7	83.6	84.4
4	240.2	95.0	92.7	91.5	90.6
5-a	231.6	87.9	86.3	86.0	87.2
5-b	228.9	85.9	85.4	85.5	85.4
6-b	231.1	87.6	85.4	85.5	86.1
6-a	233.8	90.3	87.3	86.6	87.6
5-c	232.1	88.1	87.6	87.4	87.5
6-c	235.3	91.4	88.9	88.2	88.1
7	240.5	94.5	92.9	91.7	90.8
8	237.5	92.3	91.1	90.0	89.5
9-a	235.6	91.6	88.0	86.9	88.0
9-b	235.4	90.8	87.4	86.7	86.5
9-c	236.7	92.3	89.3	88.3	88.3
10	249.2	102.6	99.6	97.9	96.5
11-a	241.1	96.9	93.4	92.2	92.5
11-b	239.1	94.4	92.3	91.7	91.2
11-c	242.3	97.5	94.7	93.6	92.8

The results in vacuo are from full optimization HF/6-31G(d,p) calculations and DFT/B3LYP/6-31+G(d,p) calculations (respectively denoted as HF and DF+ in the column headings). The results in solution are from PCM DFT/B3LYP/6-31+G(d,p) single point calculations on the in-vacuo-optimised DFT/B3LYP/6-31+G(d,p) results

^a The calculation in chloroform solution does not converge for this conformer

and 2.182–2.190/DF+, 2.184–2.199/HF when (engaging the same acceptor) H25···O17 is also present. Its red shift for the vibrational frequency of O16–H23 implies a decrease from 3,619–3,623, when it is free, to 3,562–3,568; this decrease

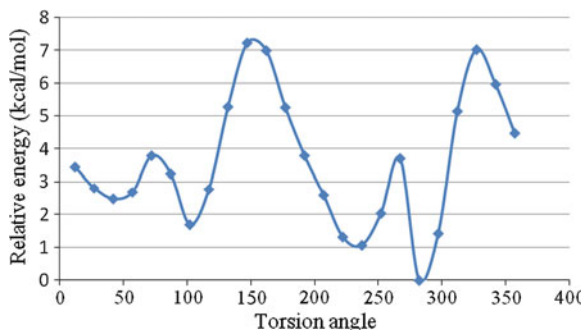


Fig. 4 Scan of the rotation of the C1–C15 bond (C29–C15–C1–C6 torsion angle) highlighting the influence of the orientation of the xanthone moiety with respect to the system of the A and B rings

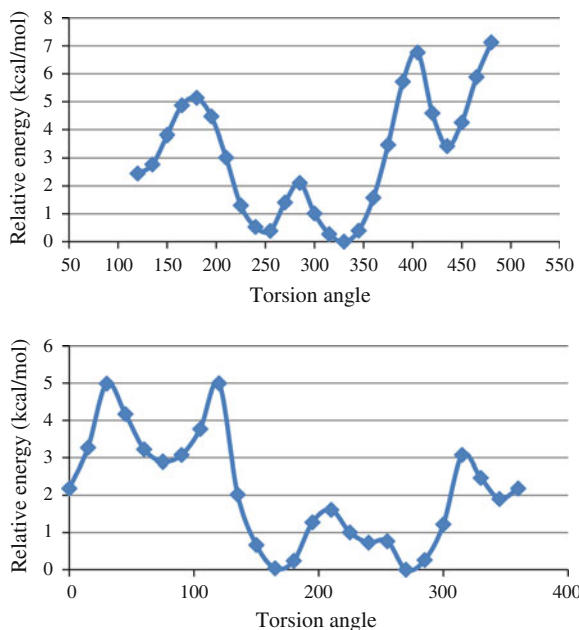
is considerably smaller than that caused by H23···O41. An analysis of Tables 2, 3 and 4 highlights similar trends for the other IHBs involving ether O atoms.

Estimating the energy of IHBs is not easy. In principle, the removal of the IHB by 180° rotation of the donor OH should enable an estimation by comparison of the conformers with and without the IHB. In practice, if the molecule is flexible, the IHB removal may cause substantial geometry changes, so that the two conformers do not differ only by the presence or absence of the IHB. When the donor and the acceptor are attached to an aromatic ring, the geometry of the molecule does not change significantly, but the ensuing O↔O repulsion contributes remarkably to the energy increase on IHB removal. In the case of the MUCH-B molecule, the situation is further complicated by the fact that, in most cases, the rotation of a donor OH removes one IHB but brings the formation of another. The only IHB that is removed without bringing about the formation of another is H28···O21. Comparison of relevant pairs of conformers (1-a and 3-a, 1-b and 3-b, 1-c and 3-c, 4 and 7, 6-a and 9-a, 6-c and 9-c) yields 4.83–4.99/HF, 5.65–5.89/MP, 5.56–5.97/DF+. The comparison of 6-b and 9-b yields 5.73/HF, 6.37/MP and 6.19/DF+.

The mutual orientation of the three moieties has relevant influence on the conformers' energetics. It was investigated through scans of the rotation of the C1–H15 (Fig. 4), C15–C29 (Fig. 5) and C15–C35 (Fig. 5) bonds. This orientation markedly influences the dipole moment (Table 6). For instance, the dipole moments of the 1-type conformers, having the best IHB pattern, range from 1.3 to 5.8, and these differences are due totally to the orientation of the A and B rings with respect to the xanthone moiety. This suggests that the orientation of the A and B rings may be relevant for the biological activity, since it influences properties that are Quantitative Structure Activity Relationship (QSAR) descriptors, such as the dipole moment. On the average, the highest dipole moments correspond to conformers with the H23···O41 IHB, which implies constraints on the orientation of ring A.

The ZPE correction (Table 5) is very close for all the conformers, differing by less than 1 kcal/mol.

Fig. 5 **a** Scan of the rotation of the C1–C29 bond (C34–C29–C15–C1 torsion angle), highlighting the influence of the orientation of the rest of the molecule with respect to the A ring. **b** Scan of the rotation of the C15–C29 bond (C34–C29–C15–C1 torsion angle), highlighting the influence of the orientation of the B ring with respect to the A ring



The HOMO-LUMO energy gaps (Table 7) are in line with the known huge difference between HF and DFT estimations, with the DFT estimations being the less reliable [27]. Studies on a high number of other molecules of the same class (acylphloroglucinols, [28]) have highlighted that, although the DFT values for the energy gap are not realistic, the trends that can be identified on the basis of those values are realistic. For the results in vacuo, the trends are similar in the HF and DFT results. The HOMO-LUMO gap does not vary considerably for different conformers, and it has slightly higher values for the conformers containing the H23···O41 IHB.

Figure 6 shows representative shapes of the HOMO and LUMO frontier orbitals. The shapes are largely similar in the HF and DFT results. For the conformers of types 1, 3, 5, 6, 9 and 11, the HOMO is mostly located on the A ring, whereas it extends also to the xanthone moiety for conformers containing the H23···O41 IHB. The LUMO is located on the xanthone moiety for all the conformers.

3.2 Results in Solution

Since calculations in solution were performed only at the DFT/B3LYP/6-31+G(d,p) level, the comparison of relevant quantities in different media is based only on the DFT/B3LYP/6-31+G(d,p) results.

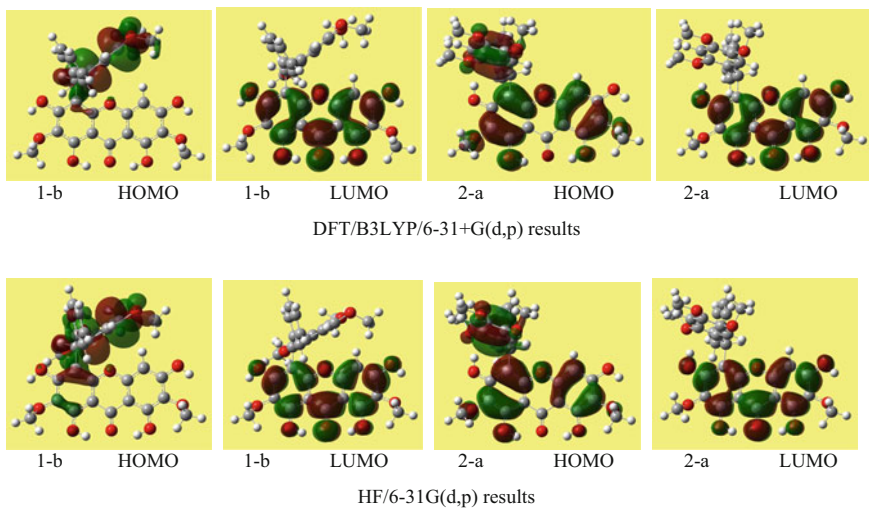


Fig. 6 Typical shapes of the HOMO and LUMO frontier orbitals when the H23···O41 intramolecular hydrogen bond is not present (conformer 1-b) and when it is present (conformer 2-a). Results in vacuo from the methods for which calculations were made with fully relaxed geometry

The results in solution show trends consistent with many other observations in solution, above all for molecules containing OH groups. For conformers with the most stable IHB pattern (1-type conformers), the energy in solution does not decrease significantly and may increase. This is likely related to the mainly hydrophobic character of the IHB regions and to the greater stability of this IHB pattern. For the other conformers, the relative energy decreases as the solvent polarity increases. The decrease is sharper—above all in water solution—for conformers having an OH not engaged in an IHB (3, 7, 9), as this OH is available to form intermolecular H-bonds with the water molecules. Although PCM does not explicitly take into account directional solute-solvent interactions such as H-bonds, its results are often attuned to the expected stronger solute-solvent interactions when H-bonds are possible [8]. The relative energies in water suggest that even conformers such as 2-a, 2-b or 3-a may be somewhat responsible for the molecule's biological activity (although these conformers would be excluded on the sole basis of the results in vacuo).

Table 8 reports the solvent effect (free energy of solvation, ΔG_{solv}) and its electrostatic component (G_{el}) for the three solvents considered. The ΔG_{solv} values would suggest greater solubility in water than in the other two solvents. The magnitude of ΔG_{solv} in water increases for higher energy conformers, in correspondence with weaker IHB patterns or the absence of one IHB in the conformer (both these factors facilitate stronger solute-water interactions, with consequent greater stabilising effect by the solvent).

The dipole moment (Table 6) increases slightly as the solvent polarity increases.

Table 8 Solvent effect (free energy of solvation, ΔG_{solv}) and its electrostatic component (G_{el}) for the conformers of muchimangin B in the three solvents considered

Conformer	ΔG_{solv} (kcal/mol)			G_{el} (kcal/mol)		
	In chloroform	In acetonitrile	In water	In chloroform	In acetonitrile	In water
1-a	7.64	15.44	0.59	-5.04	-7.35	-17.48
1-b	8.19	16.17	1.87	-4.97	-7.20	-17.10
1-c	7.43	15.47	0.90	-5.01	-7.24	-17.32
1-d	7.45	15.49	0.75	-5.01	-7.24	-17.51
1-e	7.56	15.38	0.81	-5.05	-7.44	-17.52
1-f	7.83	15.97	1.32	-4.64	-6.73	-16.88
2-a	5.84	13.43	-1.17	-5.87	-8.45	-18.14
1-g	6.86	14.86	-0.73	-5.10	-7.35	-18.27
1-h	7.91	15.98	1.51	-4.78	-6.96	-16.93
1-i	- ^a	14.76	-0.46	- ^a	-7.05	-17.39
2-b	6.00	13.64	-2.27	-5.83	-8.43	-19.61
3-a	6.57	13.58	-3.30	-6.48	-9.66	-21.94
3-b	7.53	15.08	-0.47	-5.75	-8.40	-19.59
3-c	6.16	13.51	-3.25	-6.42	-9.38	-21.73
4	5.56	12.75	-3.58	-6.88	-9.79	-21.47
5-a	5.89	12.89	-4.33	-7.15	-10.30	-22.90
5-b	6.31	13.44	-3.35	-7.18	-10.32	-22.82
6-a	5.76	12.69	-4.45	-7.33	-10.55	-23.10
6-b	6.31	13.44	-3.35	-7.18	-10.32	-22.82
5-c	5.59	12.77	-4.18	-7.20	-10.34	-22.90
6-c	5.69	12.95	-4.07	-7.13	-10.18	-22.83
7	4.02	10.45	-7.93	-8.54	-12.23	-26.03
8	4.00	10.73	-7.41	-8.16	-11.73	-25.23
9-a	4.29	10.45	-8.71	-8.90	-12.92	-27.55
9-b	5.80	12.40	-5.17	-7.98	-11.61	-24.98
9-c	4.34	11.07	-8.32	-8.59	-12.20	-27.29
10	2.68	8.79	-9.47	-9.59	-13.72	-27.25
11-a	3.80	9.83	-9.85	-9.70	-13.87	-29.07
11-b	4.49	10.71	-8.45	-9.53	-13.63	-28.66
11-c	3.64	9.91	-9.52	-9.59	-13.69	-28.86

Results from PCM DFT/B3LYP/6-31+G(d,p) single point calculations on the in-vacuo-optimised DFT/B3LYP/6-31+G(d,p) results

^a The calculation in chloroform solution does not converge for this conformer

Although the comparison of the HOMO-LUMO energy gap in different media is based only on the DFT results (Table 7), the trend-identification has proved reliable for other molecules [28] and is, therefore, considered realistic. For conformers not containing the H23···O41 IHB, the gap decreases slightly for chloroform and acetonitrile, with respect to *in vacuo*, and increase slightly in water. For conformers containing the H23···O41 IHB, the slight decrease in solution is steady with increasing solvent polarity and water solution corresponds to the smallest value.

3.3 Adducts with Explicit Water Molecules

Three adducts with explicit water molecules were calculated for conformer 1-c: an adduct with six water molecules (1-c-6aq), an adduct with nine water molecules (1-c-9aq), and an adduct with 13 water molecules (1-c-13aq). Figure 7 shows their geometries and their molecule-water interaction energies and Table 9 shows the lengths of the H-bonds between water molecules and the MUCH-B molecule and between different water molecules. The shorter solute-water distances correspond to the cases when an OH of the xanthone moiety is donor to a water molecule, which is made possible because the H23···O17 IHB weakens, and H23 bonds simultaneously to a water molecule.

For both 1-c-6aq and 1-c-9aq, no water molecules were placed in the region of the cooperative H25···O19 and H26···O19 IHB in the inputs. The increase in the solute-water interaction energy from 1-c-6aq to 1-c-9aq is consistent with the greater stabilization of an adduct when two water molecules directly H-bonded to the solute molecule are bridged by a third water molecule.

Water molecules forming pentagonal rings of O atoms [10] around the H25···O19 and around the H25···O19 IHBs were placed in the input of 1-c-13aq adding them to the optimised geometry of 1-c-9aq (the pentagonal rings including O18, O19 and three water molecules, or O18, O20 and three water molecules). The optimisation confirms the hydrophobic character of the IHBs. Although one water molecule remains bonded to O19, no water molecule remains bonded to O18 or O20: water molecules bonded to each other “keep away” from the two IHBs, and one water molecule bonds to O17 or O21, on either side of the two strong IHBs. This is consistent with the results obtained for other molecules in which an sp^2 O forms an IHB with an OH attached to an aromatic ring [10].

Table 10 compares the parameters of the IHBs in the isolated MUCH-B molecule and in the three adducts. Remarkable changes occur for the H23···O17 IHB, as H23 rotates off plane enough to be able to simultaneously H-bond a water molecule: the length of H23···O17 increases, and the O-H-O angle decreases.

The counterpoise BSSE corrections (kcal/mol) were 12.43 for 1-c-6aq, 19.15 for 1-c-9aq and 25.07 for 1-c-13aq.

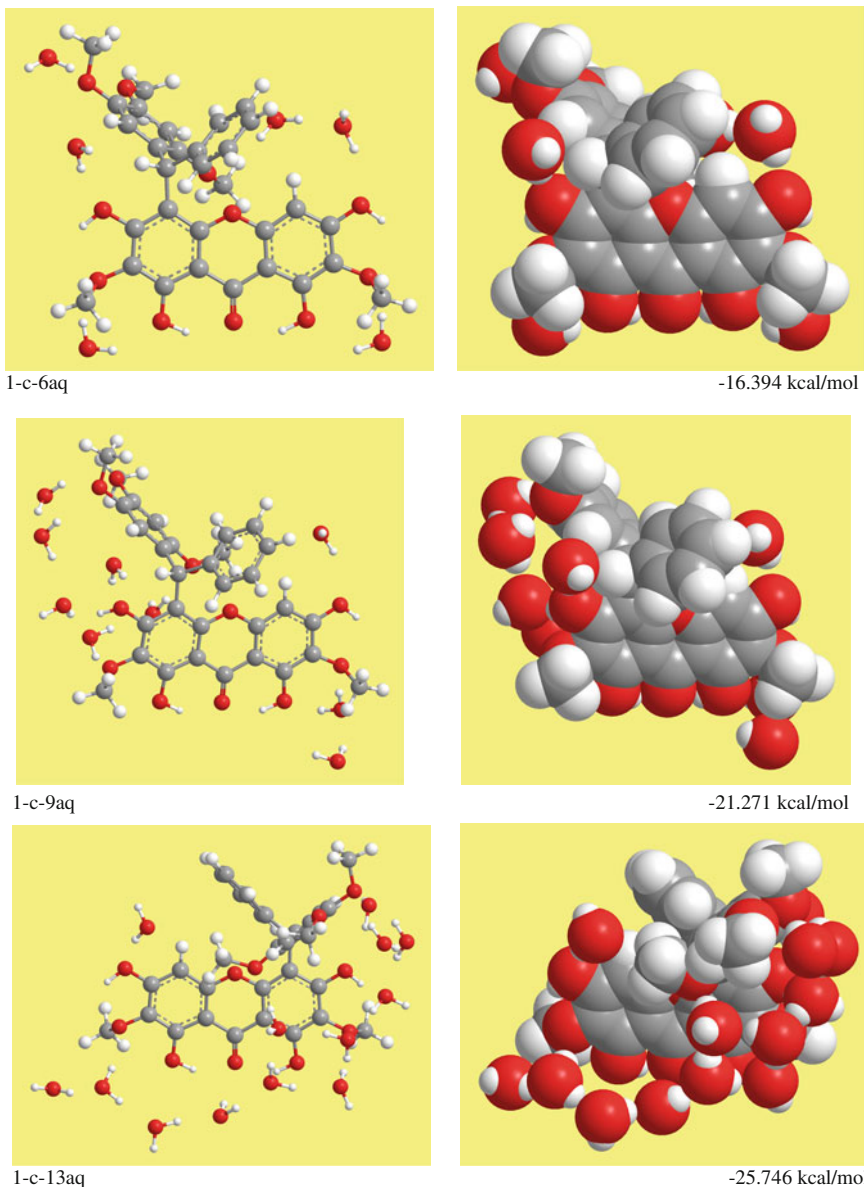


Fig. 7 Calculated adducts of conformer 1-c with explicit water molecules. Both ball-and-sticks and space-filling models are shown, to better highlight the adducts' geometries. The name of the adduct is reported on the *left*, and the molecule-water interaction energy on the *right*

Table 9 Length of water-molecule and water-water hydrogen bonds in the calculated adducts of the 1-c conformer of muchimangin B

Adduct	Water-water hydrogen bonds		Water-molecule hydrogen bonds	
	Distance considered ^a	Length (Å)	Distance considered ^a	Length (Å)
1-c-6aq	$H_F \cdots O_E$	2.068	$H_A \cdots O43$	2.457
			$H_B \cdots O16$	2.211
			$H_C \cdots O17$	2.363
			$H_D \cdots O20$	2.529
			$H_D \cdots O21$	2.250
			$H_E \cdots O22$	2.137
			$H_F \cdots O41$	2.394
1-c-9aq	$H_A \cdots O_B$	2.064	$H_A \cdots O42$	2.279
	$H_B \cdots O_C$	2.079	$H_B \cdots O43$	2.272
	$H_D \cdots O_F$	1.960	$H_{23} \cdots O_C$	1.855
	$H_G \cdots O_H$	2.079	$H_D \cdots O17$	2.272
			$H_E \cdots O16$	2.143
			$H_F \cdots O41$	2.058
			$H_G \cdots O20$	2.597
			$H_H \cdots O21$	2.110
			$H_I \cdots O22$	2.271
1-c-13aq	$H_A \cdots O_B$	2.075	$H_A \cdots O42$	2.285
	$H_B \cdots O_C$	2.098	$H_B \cdots O43$	2.256
	$H_C \cdots O_F$	1.805	$H_{23} \cdots O_C$	1.817
	$H_F \cdots O_E$	2.047	$H_D \cdots O16$	2.143
	$H_F \cdots O_G$	2.101	$H_E \cdots O41$	1.962
	$H_H \cdots O_E$	2.012	$H_G \cdots O16$	2.057
	$H_H \cdots O_g$	2.063	$H_I \cdots O19$	2.236
	$H_I \cdots O_H$	1.942	$H_M \cdots O22$	2.240
	$H_J \cdots O_I$	1.912		
	$H_K \cdots O_J$	1.954		
	$H_L \cdots O_K$	1.926		

^a The geometries of the adducts are shown in Fig. 7. The water molecules are denoted by uppercase letters, in the following way:

For adduct 1-c-6aq: A is the water molecule bonded to O43; B is the water molecule bonded to O16; C is the water molecule bonded to O17; D is the water molecule bonded to O20 and O21; E is the water molecule bonded to O22; F is the water molecule bonded to O41. For adduct 1-c-9aq: A is the water molecule bonded to O42; B is the water molecule bonded to O43; C is the water molecule bonded to H23; D is the water molecule bonded to O17; E is the water molecule bonded to O16; F is the water molecule bonded to O41; G is the water molecule bonded to O20; H is the water molecule bonded to O21; I is the water molecule bonded to O22. For adduct 1-c-13aq: A is the water molecule bonded to O42; B is the water molecule bonded to O43; C is the water molecule bonded to H23; D is the water molecule bonded to O16; E is the water molecule bonded to O41; F is the water molecule bonded to C, E and G; G is the water molecule bonded to O16; H is the water molecule bonded to E, H and I; I is the water molecule bonded to O19; J is the water molecule bonded to I and K; K is the water molecule bonded to O21; L is the water molecule bonded to K; M is the water molecule bonded to O22

Table 10 Comparison of the parameters of the intramolecular hydrogen bonds in the isolated 1-c conformer of muchimangin B and in its adducts with explicit water molecules

Conformer or adduct	H-bond	Parameters of the H-bond		
		H–O (Å)	O–O (Å)	O $\ddot{\text{O}}$
1-c isolated	H23···O17	2.093	2.637	115.0
	H25···O19	1.781	2.612	143.6
	H26···O19	1.802	2.633	143.6
	H28···O21	2.135	2.667	114.2
1-c-6aq	H23···O17	2.092	2.633	114.6
	H25···O19	1.777	2.609	143.6
	H26···O19	1.799	2.631	143.6
	H28···O21	2.145	2.670	113.6
1-c-9aq	H23···O17	2.370 ^a	2.699	99.4
	H25···O19	1.804	2.627	142.7
	H26···O19	1.784	2.624	144.6
	H28···O21	2.161	2.679	113.2
1-c-13aq	H23···O17	2.442 ^a	2.716	96.0
	H25···O19	1.803	2.628	142.8
	H26···O19	1.832	2.651	142.4
	H28···O21	2.146	2.675	113.9

^a H23 is simultaneously engaged in intramolecular and intermolecular H-bonds

4 Discussion and Conclusions

The computational study has highlighted the main properties of the MUCH-B molecule in vacuo and in the three solvents considered. The IHB pattern has the dominant role in determining conformational preferences, and the mutual orientation of the three moieties also plays a significant role. The results from the different calculation methods utilised are consistent. They are also consistent with the findings for other molecules, as far as individual common features—such as the behaviour of and around a certain type of IHB—is concerned.

References

1. Dibwe DF, Awale S, Kadota S, Tezuka Y (2012) Tetrahedron Lett 53(46):6186–6290
2. Alagona G, Ghio C (2009) Phys Chem Chem Phys 11:776–790
3. Bushelyev SN, Stepanov NF (1989) Elektronnaya Struktura y Biologicheskaya Aktivnost Molekul. Khimiya, Snanye, Moscow
4. ChemOfficeem Cambridge Software
5. Kabanda MM, Mammino L (2012) Int J Quantum Chem 112:3691–3702
6. Mammino L, Kabanda MM (2009) J Mol Struct (Theochem) 901:210–219
7. Mammino L, Kabanda MM (2009) J Phys Chem A 113:15064–15077
8. Mammino L, Kabanda MM (2012) Int J Quantum Chem 112:2650–2658
9. Mammino L, Kabanda MM (2013) Molec Simul 39(1):1–13

10. Mammino L, Kabanda MM (2010) *Int J Quantum Chem* 110:2378–2390
11. Lee C, Yang W, Parr RG (1998) *Phys Rev B* 37(2):785–789
12. Becke AD (1993) 98(2):1372–1377
13. Becke AD (1993) *J Chem Phys* 98(7):5648–5652
14. Tomasi J, Persico M (1994) *Chem Rev* 94:2027–2094
15. Tomasi J, Mennucci B, Cammi R (2005) *Chem Rev* 105:2999–3094
16. Frisch MJ, Trucks GW, Schlegel HB, Scuseria GE, Robb MA, Cheeseman JR, Montgomery JA, Vreven T, Kudin KN, Burant JC, Millam JM, Iyengar SS, Tomasi J, Barone V, Mennucci B, Cossi M, Scalmani G, Rega N, Petersson GA, Nakatsuji H, Hada M, Ehara M, Toyota K, Fukuda R, Hasegawa J, Ishida M, Nakajima T, Honda Y, Kitao O, Nakai H, Klene M, Li X, Knox JE, Hratchian HP, Cross JB, Adamo C, Jaramillo J, Gomperts R, Stratmann RE, Yazyev O, Austin AJ, Cammi R, Pomelli C, Ochterski JW, Ayala PY, Morokuma K, Voth GA, Salvador P, Dannenberg JJ, Zakrzewski VG, Dapprich S, Daniels AD, Strain MC, Farkas O, Malick DK, Rabuck AD, Raghavachari K, Foresman JB, Ortiz JV, Cui Q, Baboul AG, Clifford S, Cioslowski J, Stefanov BB, Liu G, Liashenko A, Piskorz P, Komaromi I, Martin RL, Fox DJ, Keith T, Al-Laham MA, Peng CY, Nanayakkara A, Challacombe M, Gill PMW, Johnson B, Chen W, Wong MW, Gonzalez C, Pople JA (2003) Gaussian 03. Gaussian Inc, Pittsburgh
17. Mennucci B, Tomasi J (1997) *J Chem Phys* 106:5151
18. Mennucci B, Cancès E, Tomasi J (1997) *J Phys Chem B* 101:10506
19. Cancès E, Mennucci B, Tomasi J (1997) *J Chem Phys* 107:3032
20. Barone V, Cossi M, Tomasi J (1998) *J Comput Chem* 19:404
21. Pascual-Ahuir JL, Silla E (1990) *J Comput Chem* 11:1047
22. Silla E, Villar F, Nilsson O, Pascual-Ahuir JL, Tapia O (1990) *J Mol Graph* 8:168
23. Silla E, Tunon I, Pascual-Ahuir JL (1991) *Comput Chem* 12:1077
24. <http://cccbdb.nist.gov/vibscalejust.asp>
25. Alagona G, Ghio C (2006) *J Phys Chem A* 110:647
26. Boys SF, Bernardi F (1970) *Molec Phys* 19:553
27. <https://www.wiki.ed.ac.uk/display/EaStCHEMresearchwiki/How+to+analyse+the+orbitals+from+a+Gaussian+calculation>
28. Mammino L, Tshiwawa T (2013) In: 44th IUPAC congress, Istanbul, 11–16 August 2013

Molecular Dynamics Analysis of FAAH Complexed with Anandamide

Sérgio F. Sousa, João T.S. Coimbra, Pedro A. Fernandes,
Tiziana Marino, Maria J. Ramos and Nino Russo

Abstract Fatty Acid Amide Hydrolase (FAAH) is a very interesting serine hydrolase that promotes the hydrolysis of both amides and esters, such as the endogenous cannabinoid anandamide or N-arachidonoyl ethanolamine (AEA), and the sleep-inducing lipid oleamide. The therapeutic potential from the pharmacological modulation of this enzyme is vast, including relevant neurological and inflammatory disorders. Different computational approaches have fallen upon the characterization of the oleamide-FAAH monomer complex. With this study, we propose a description of both the dimeric and monomeric FAAH complexes with the substrate anandamide, in order to look for relevant interactions in the active-site and differences in the monomer and dimer incorporation approaches. The study involves a comparative analysis of several important molecular aspects for which are vital not only motion but also the conformational sampling of both enzyme and substrate as well as their interaction, with the inclusion of solvent. This work comprises a flexibility analysis of FAAH through Root Mean Square Fluctuation (RMSF), Solvent Accessible Surface Accessible Area (SASA) measurements on the substrate and enzyme, Radial Distribution Functions (RDFs) of the water molecules hydrating anandamide, as well as a study on significant hydrogen bonds between the active-site residues and the substrate. The results highlight meaningful interacting residues of the FAAH active-site with the AEA substrate, and the importance of considering the dimeric complex when flexibility effects are relevant.

Keywords Fatty acid amide hydrolase • Anandamide • Molecular dynamics

S.F. Sousa · J.T.S. Coimbra · P.A. Fernandes · M.J. Ramos (✉)
REQUIMTE, Departamento de Química e Bioquímica, Faculdade de Ciências,
Universidade do Porto, Rua do Campo Alegre s/n, 4169-007 Porto, Portugal
e-mail: mjramos@fc.up.pt

T. Marino (✉) · N. Russo
Dipartimento di Chimica and Centro di Calcolo ad Alte Prestazioni per
Elaborazioni Parallele e Distribuite-Centro d'Eccellenza MIUR,
Università della Calabria, 87030 Arcavacata di Rende, CS, Italy
e-mail: tmarino@unical.it

1 Introduction

Fatty Acid Amide Hydrolase (FAAH) [1], first isolated from rat liver [2] is a mammalian membrane-associated enzyme that belongs to the amidase signature (AS) family, a class of serine hydrolases with a unique catalytic triad of Ser-Ser-Lys [3–7]. FAAH catalyzes the hydrolysis of both amides and esters [8]. Known substrates include anandamide (Fig. 1), an endogenous cannabinoid ligand for both cannabinoid receptors [9] and non-cannabinoid receptors [10], and oleamide, a sleep-inducing lipid originally isolated from the cerebrospinal fluid of sleep-deprived cats [11–14].

The role of FAAH in the inactivation of neuromodulatory lipid amides as well as several other experimental studies, including knockout models for the enzyme [15–28], inhibition studies [29–34], and immunohistochemical evaluations [35, 36], have confirmed FAAH as a potent potential pharmacological target to treat numerous pathophysiological conditions, such as sleep disorders, neuropathic and inflammatory pain, neurological conditions, inflammatory disorders, hypertension and even cancer [17, 37–42]. Furthermore, associations were made between polymorphisms of the *Faah* gene and disorders such as obesity [43] and drug-addiction [44]. A potential neuroprotective therapeutic profile for FAAH inhibitors has also been characterized, revealing potential against relevant neuropathological states including traumatic brain injury, Alzheimer's disease, Huntington's Disease, Parkinson's Disease, and stroke [38].

The pharmacological inhibition of FAAH has attracted great attention in recent literature, mainly due to the avoidance of unwanted side effects of the conventional cannabinoid receptors agonist's based therapy [17, 38, 45, 46]. Several classes of inhibitors for the FAAH enzyme have been described in the literature [42, 45, 47–49] and patents have been applied for, describing FAAH inhibitors [45, 46]. Several of these inhibitors are now moving, or have moved into clinical trials mainly focused on pain and inflammatory disorders. Promising results for human efficacy have been observed [45, 46, 50], with some of the inhibitors moving into clinical trials to treat anxiety and depression as a consequence [45].

FAAH is a homodimeric enzyme that exhibits a series of channels and cavities involved in the substrate binding and recognition [3, 42]. The catalytic mechanism of this enzyme involves a nucleophilic attack from the catalytic Ser241 on the carbonyl group of the substrate, forming a tetrahedral intermediate, which then

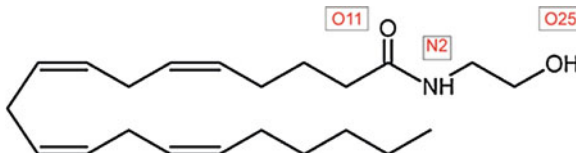


Fig. 1 The anandamide substrate: structure of the molecule with the indication of the nomenclature used to describe the oxygen and nitrogen atoms present throughout the manuscript

collapses to release the amine and the enzyme-bound acyl intermediate. Lys142 acts as a general base-general acid, mediating both the deprotonation of Ser241 and subsequent protonation of the leaving group, shuttled through Ser217. The reaction terminates with a water-mediated deacylation of the acyl enzyme-bound intermediate [4, 7, 8, 51]. The mechanistic characterization of the hydrolysis of oleamide and similar compounds has been computationally carried out with QM/MM calculations [52–56]. Furthermore, studies on drug-design computational perspectives for inhibitors of FAAH have appeared to [57–59].

The present study provides an extensive atomic-level molecular dynamics structural analysis for the FAAH-anandamide complex, of both monomer and dimerized structures of the enzyme. The intent was also to discover key players at the active site complexed with anandamide. An extensive analysis was performed on the protein stability during MD, residue flexibility, and analysis of the SASA, for both monomer and dimer complexes of FAAH-anandamide. Additionally, the water distribution around anandamide and a hydrogen bond analysis for the substrate inserted in the active site were considered.

In sum, the results provide detailed atomistic insights that include the dynamic effect of the systems and the effect of the solvent, complementing the static view that could be obtained from the X-ray structures available for this enzyme, and contributing with important indications for future mechanistic and drug-design studies on this important enzyme, allowing a better understanding of FAAH.

2 Methodology

The AMBER 10 [60] molecular dynamics package was used in all the molecular dynamics simulations performed. The monomer and dimer systems were prepared from the 1MT5 X-ray crystallographic structure of FAAH complexed with an arachidonyl inhibitor (methoxy arachidonyl fluorophosphonate) [3]. The full X-ray structure contains a total of 32 subunits, each one with 572 amino acids. A monomer and a dimer were prepared from this structure and considered for the MD study. In both systems, the substrate analogue methoxy arachidonyl fluorophosphonate was modelled into the endogenous cannabinoid substrate anandamide. The Duan et al. 2002 [61] parameters were employed to describe the protein, while the ANTECHAMBER module [62] of AMBER and the General AMBER Force Field (GAFF) [63] were used to parameterize the anandamide substrate (Fig. 1), with charges derived with RESP at the HF/6-31G(d) level of theory, to be coherent with all other parameters used.

Conventional protonation states for all amino acids at pH 7 were considered. All the hydrogen atoms were added and counter-ions (Cl^-) were employed to neutralize the positive charge of the system (ranging from -3 to -6 , in the monomer and dimer studies, respectively). The Leap program was used in this regard. Each system was placed in its own rectangular box containing a minimum distance of 12 Å of TIP3P water molecules between the enzyme and the box side. The size of

these systems was of ca. 75,000 and 150,000 atoms, respectively for the monomer and dimer.

Each of the two systems was subjected to a 4-stages refinement protocol using the SANDER module of AMBER 10, in which the constraints on the enzyme were gradually removed. In the first stage (10,000 steps), 50 kcal/mol/Å² harmonic forces were used to restrain the positions of all atoms in the systems except those from the water molecules. In the second stage (10,000 steps) these constraints were applied only to the heavy atoms, and in the third stage (30,000 steps), they were limited to the CA and N atom-type atoms (backbone alfa carbon atoms and nitrogen atoms). This process ended with a full energy minimization (4th stage, maximum 80,000 steps) until the rms gradient was smaller than 0.02 kcal/mol/Å².

MD simulations were carried out using the PMEMD module of AMBER 10, and considering periodic boundary conditions to simulate a continuous system. The SHAKE algorithm [64] was applied to fix all bond lengths involving a hydrogen bond, permitting a 2 fs time step. The Particle-Mesh Ewald (PME) method [65] was used to include the long-range interactions, and a non-bond interaction cut-off radius of 10 Å was considered. Following a 40 ps equilibration procedure, 10 ns MD simulations were carried out at 310 K for each of the 2 systems (a total of 20 ns), using Langevin temperature coupling and constant pressure (1 atm) with isotropic molecule-based scaling. The MD trajectory was sampled every 2 ps. All of the MD results were analyzed with the PTRAJ module of AMBER 10.

The ConSurf server [66] was used to obtain estimated conservation grades for each amino acid position along the FAAH sequence. This server uses the initial 3-D structure of a given protein or domain (in this case the chain A in the 1MT5 PDB structure [3]) and carries out a search for close homologous sequences using the PSI-Blast [67] heuristic algorithm, with default parameters, to collect homologous sequences of a single polypeptide chain of known 3D-structure from the SWISS-PROT database [68]. These sequences are then aligned against the sequence of the initial protein with the MUSCLE algorithm [69]. A conservation score is calculated along each amino acid position using an empirical Bayesian [70] approach. The ConSurf-HSSP database may be accessed at <http://consurf-hssp.tau.ac.il>.

3 Results and Discussion

This section describes the broad analysis on the FAAH-anandamide complex of both monomer and dimer complexes. First, a description of the stability of both systems is shown through a Root Mean Square Displacement analysis (RMSD). Root Mean Square Fluctuation (RMSF) values on both monomer and dimer complexes are also presented, allowing an analysis on the flexibility patterns of both systems. Finally, and in order to characterize the interaction of FAAH and the anandamide substrate, SASA analysis, Radial Distribution Functions (RDFs) of the water around the substrate, and hydrogen bond analysis on the active-site are additionally conducted.

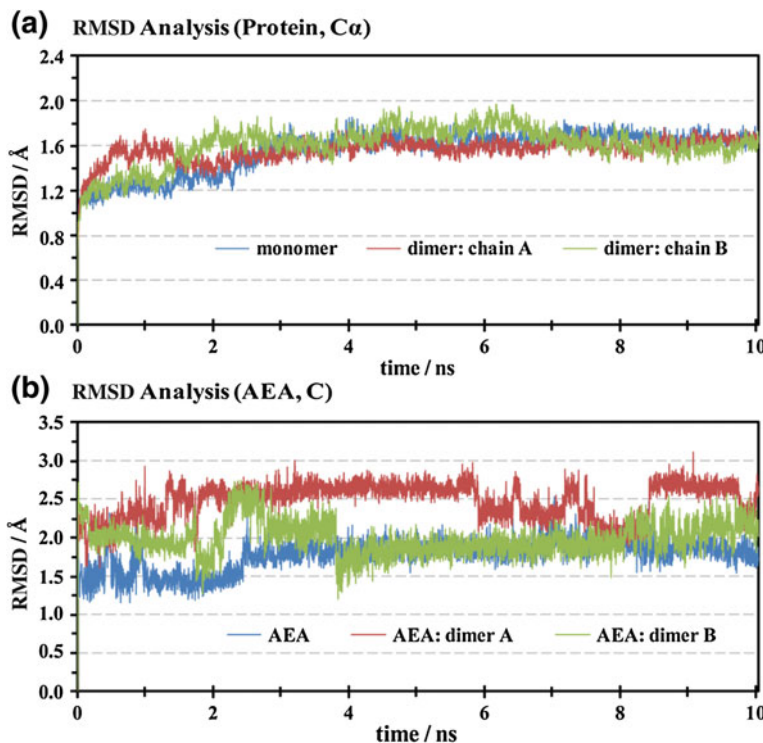


Fig. 2 **a** RMSD representation of the protein C_α atoms as a function of time for the monomer and dimer MD simulations; **b** RMSD representation of the anandamide (AEA) carbon atoms (C) as a function of time for the monomer and dimer MD simulations

3.1 Root Mean Square Deviation (RMSD) Analysis

Figure 2a shows the RMSD values for the backbone carbon atoms in the monomer and dimer MD simulations, while Fig. 2b presents the same values but for the framework of carbon atoms in the anandamide substrate in the two simulations. The results show that both the protein and the substrate molecule are well equilibrated after the initial 4 ns in both simulations. In agreement with this observation only the remaining 6 ns on both simulations were taken into consideration for the calculation of the values in the subsequent sections.

3.2 Root Mean Square Fluctuation (RMSF) Analysis

The Root mean square fluctuation values illustrate the average displacement (i.e. the positional variation) of each structural element considered in relation to their average structure over the last 6 ns of simulation, thereby giving an indication of the

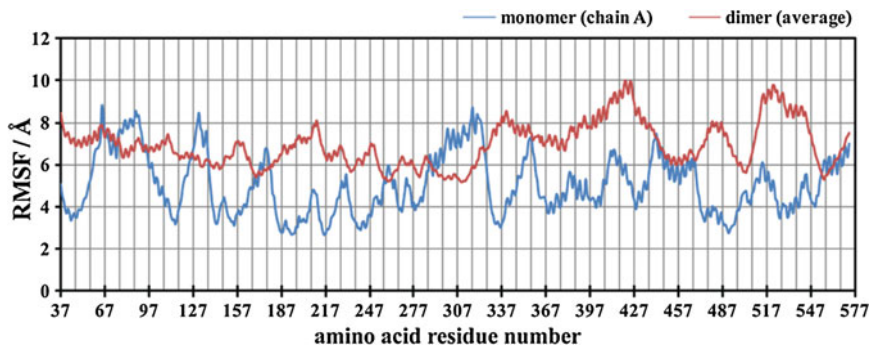


Fig. 3 RMSF analysis for all the amino acid residues along the FAAH sequence calculated for the last 6 ns of the MD simulation performed for the monomer and dimer simulation. The values for the dimer refer to the average values calculated for each residue in the two chains

relative flexibility that characterizes each of these components. In this study such analysis was performed for each amino acid residue, considering the C_α carbon atoms. Figure 3 presents the RMSF values calculated for all the amino acid residues from the MD simulation on the monomer and dimer FAAH structure.

The results highlight the existence of intrinsic differences in terms of flexibility between the several amino acid positions when treating the FAAH monomer and dimer structures. While in the monomer simulation the RMSF differences between the more flexible and the less flexible regions of the enzyme are very pronounced, in the dimer simulation there is a much higher homogeneity in terms of RMSF values along the FAAH amino acid sequence.

In the monomer structure there are 4 main flexible regions. Region 1 comprises the moderately conserved amino acids residues Gln65, Asn66 and Pro67 (with conservation scores between 6 and 8). Region 2 is defined by a stretch of 11 amino acid residue between Gln81 and Leu91. Residues in this region are in general poorly or moderately conserved, with conservation scores between 1 and 5. The only exceptions are Leu82 and Leu86 with amino acid conservation scores of 7 and 6, respectively. Region 3 is comprised by the amino acid residues Pro129, Arg130, Gln131, and Gly132. Arg130 is highly conserved (conservation score 9), while the remaining 3 residues are very poorly conserved among related sequences. Finally, region 4 is defined by a set of 9 amino acid residues, located between Arg315 and Arg323. All the residues are poorly conserved (conservation score lower than 4).

Interestingly, all these 4 regions are only moderately or poorly flexible in the RMSF analysis for the dimer. In this case, the more flexible regions are located between the amino acid residues Gly402-Ala431, and Val512-Gly544. While the more flexible regions identified in the monomer simulation refer to amino acid residues that in the functional FAAH dimer in the cell would be located opposite to the protein-membrane surface, i.e. in contact with the solvent, the more flexible regions identified in the dimer simulation refer to amino acid residues that are located in the portion of the enzyme that would interact with the cellular membrane (Fig. 4).

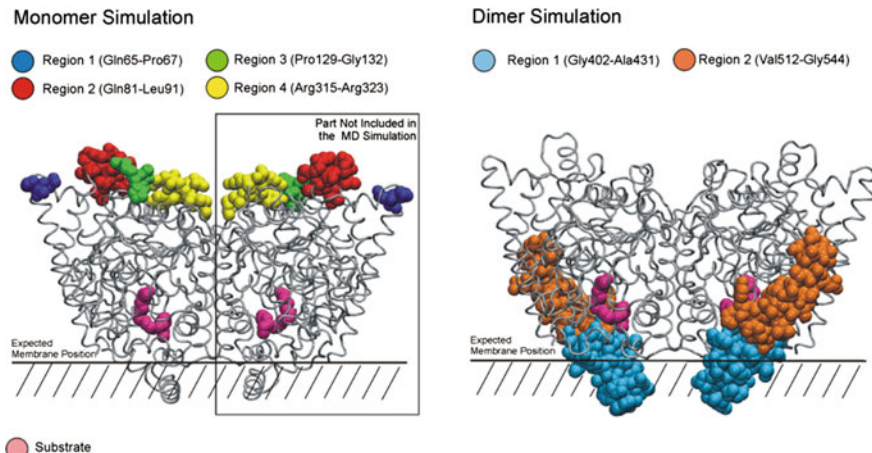


Fig. 4 Schematic representation of the most flexible regions (in terms of RMSF) identified in the monomer and dimer FAAH simulations, highlighting the differences observed for the two levels of structure considered

These observations highlight the global differences, in terms of flexibility, that exist between simulations performed on both structural elements—the FAAH monomer and the dimer. While for some more localized properties, the MD simulations performed in the monomer may be taken as a safe approximation to a more computational expensive simulation performed on the dimer, for other more global dynamic properties, such as flexibility, the inclusion of a second chain is required.

3.3 SASA Analysis

Anandamide accessible surface. SASA analysis allows an examination of the part of a given molecule that is exposed to molecules from the solvent, calculated from a probe radius that is characteristic of the solvent considered. With water, the probe radius normally considered is 1.4 Å.

The analysis performed for the anandamide substrate in the MD simulations demonstrates that this molecule is almost fully shielded from the solvent by the protein. In fact, the MD simulations performed with the monomer structure demonstrate an average SASA of only 19.2 \AA^2 for the ligand molecule, a value that represents only 2.8 % of the total surface area of the anandamide molecule free in solution ($687 \pm 10 \text{ \AA}^2$). Throughout the full MD simulation analyzed (3,000 configurations at 2 ps intervals), a maximum percentage of SASA of 6.2 % (44.2 \AA^2) was observed for this molecule, while a minimum value of 0.5 % (3.5 \AA^2) was encountered. These numbers are globally maintained in the MD simulations performed for the dimer (average SASA of $20.1 \pm 6.8 \text{ \AA}^2$), showing that for properties

Table 1 SASA values calculated for the anandamide molecule in the monomer and dimer simulations

	Average SASA		Maximum SASA		Minimum SASA	
Anandamide	Å ²	%	Å ²	%	Å ²	%
Monomer	19.2 ± 5.7	2.8	44.2	6.2	3.5	0.5
Dimer	20.1 ± 6.8	2.9	46.3	6.5	3.3	0.5

involving simply active-site binding of substrate (and possibly inhibitor) molecules, a single monomer is enough to guarantee a good description of the dynamics effects involved. Results are summarized in Table 1.

Anandamide contact surface. Anandamide establishes relevant van der Waals interactions with a total of 30 active-site amino acids residues, most of them of hydrophobic nature, as expected. Results are summarized in Table 2. The amino acid residues that account for most of the anandamide contact surface are Leu192 (average 11.9 %, maximum 19.3 %), Thr488 (10.6 %, 15.8 %), Phe432 (10.4 %, 15.4 %), Leu404 (9.2 %, 14.8 %), Ile491 (7.9 %, 12.4 %), and Leu380 (6.1 %, 12.6 %), as illustrated in Fig. 5. While Leu192 and Phe432 are highly conserved amino acid residues (with conservation scores of 9 and 7 respectively), the remaining residues are poorly conserved among related protein sequences.

In addition, several polar amino acid residues are in contact with the anandamide contact surface. Examples include the poorly conserved Glu373 and Ser376, and the highly conserved Arg428 and the catalytic Ser241 amino acid residues.

Protein. The calculated SASA for the monomer protein was of $22,620 \pm 312 \text{ Å}^2$, while that of the dimer was of $40,379 \pm 364 \text{ Å}^2$. These results demonstrate that dimer formation buries about $2,050 \text{ Å}^2$ per subunit, a value that represents 9 % of the surface of each subunit, resulting in an accessible surface area per monomer of $20,574 \text{ Å}^2$ (Table 3).

Radial Distribution Function (RDF) analysis. To have a more quantitative picture of the distribution of water molecules around the anandamide molecule we have performed a radial distribution function analysis of water (from the water oxygen atom) around the two oxygen atoms and around the nitrogen atom of the anandamide molecule, i.e. all the non-carbon and non-hydrogen atoms present in this molecule. Results are presented in Fig. 6.

The results obtained are in agreement with the SASA pattern obtained for the anandamide molecule by showing that the water molecules are in general very far away from the anandamide molecule. In fact, no water molecule is present at a distance of less than 2.45 Å from any of these three key atoms in anandamide. For the O25 and N2 atoms this water free distance can be extended to 4 Å (Fig. 6). However, the RDF analysis reveals a well defined water sphere around the O11 atom, with a maximum probability distance at 2.65 Å, corresponding to the average presence of 1 water molecule. The distance for which in average 2 water molecules are present around O11 is 5.45 Å, but at a distance of 4 Å an average number of 1.6 water molecules can be inferred (Fig. 6). Visual inspection of the MD simulation,

Table 2 Analysis of the anandamide contact surface with 30 active-site amino acid residues, with indication of the average, maximum, and minimum percentages of anandamide contact surface for each amino acid residue during the MD simulation

Interacting residue	Average percentage anandamide contact surface (%)	Maximum percentage of anandamide contact surface (%)	Minimum percentage of anandamide contact surface (%)	Amino acid conservation score
MET191	0.0 ± 0.0	0.4	0.0	8
LEU192	11.9 ± 1.9	19.3	5.2	9
SER193	0.1 ± 0.2	2.0	0.0	7
PHE194	5.2 ± 1.2	9.4	1.4	7
GLY216	0.4 ± 0.3	1.6	0.0	9
SER217	0.0 ± 0.1	0.8	0.0	9
ILE238	2.3 ± 0.9	5.9	0.1	9
GLY239	0.3 ± 0.3	2.3	0.0	9
GLY240	0.1 ± 0.2	1.0	0.0	9
SER241	0.6 ± 0.3	1.9	0.0	9
PHE244	0.9 ± 0.6	4.2	0.0	6
VAL276	2.0 ± 1.0	7.1	0.0	6
TYR335	5.2 ± 1.1	9.0	1.3	1
LEU372	4.7 ± 0.8	8.2	2.5	5
GLU373	3.3 ± 1.0	7.4	0.6	1
SER376	1.0 ± 0.5	3.6	0.0	4
ALA377	4.0 ± 1.0	8.1	0.7	5
LEU380	6.1 ± 1.8	12.6	1.4	3
PHE381	3.2 ± 1.3	8.2	0.1	5
LEU404	9.2 ± 1.6	14.8	3.5	4
ARG428	0.8 ± 0.9	6.1	0.0	7
ALA431	1.4 ± 0.6	4.4	0.0	5
PHE432	10.4 ± 1.4	15.4	6.6	7
SER435	0.1 ± 0.1	1.4	0.0	6
THR488	10.6 ± 1.5	15.8	5.3	5
GLY489	1.7 ± 0.7	4.9	0.1	3
ILE491	7.9 ± 1.3	12.4	4.4	4
SER492	0.3 ± 0.3	2.0	0.0	6
VAL495	2.8 ± 1.1	6.8	0.0	3
TRP531	3.4 ± 1.2	7.8	0.0	4

particularly in the vicinity of the O11 atom and of the MD simulation, allows the presence of 2 water molecules within a 6 Å radius of the O11 atom. These two water molecules are retained around the O11 position during the full simulation, with one of them establishing a strong hydrogen bond with the O11 atom of Anandamide during most of the simulation.

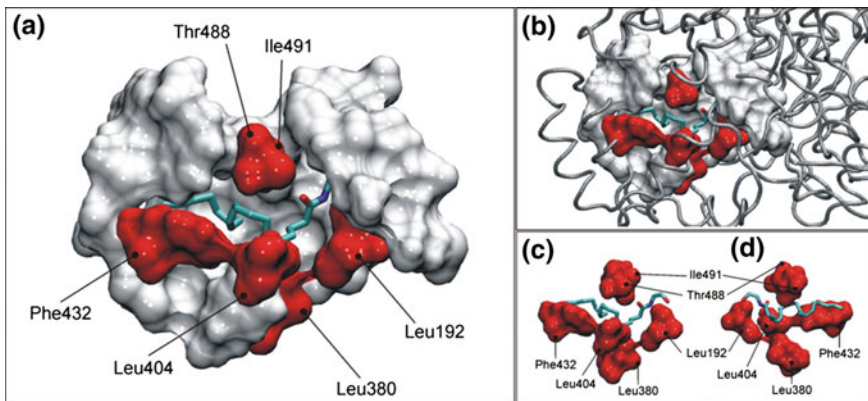


Fig. 5 Schematic representation of the anandamide contact surface prepared from the average structure in the monomer MD simulation, illustrating the binding pocket and the surface defined by the 30 interacting amino acid residues. The top 6 contact surface residues are the subject of particular attention. **a** The anandamide contact surface defined by the 30 amino acid residues; **b** Global view; **c** Top 6 residues—*front view*; **d** Top 6 residues—*rear view*

Table 3 SASA values calculated for FAAH in the monomer and dimer simulations

	Average SASA per monomer/Å ²	Maximum SASA per monomer/Å ²	Minimum SASA per monomer/Å ²
Monomer	22,620 ± 312	23,608	21,881
Dimer	20,574 ± 363	21,061	19,837

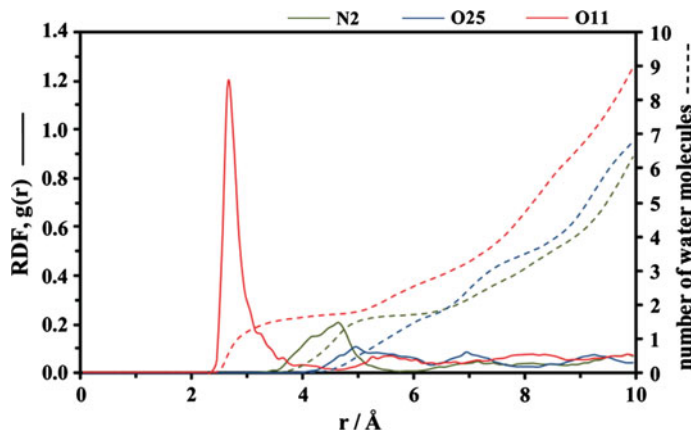


Fig. 6 Radial distribution functions (RDFs) and number of water molecules as a function of the distance to O25, O11, and N2 atoms in anandamide calculated from the FAAH monomer simulation

Table 4 Summary of the most relevant hydrogen bonds (i.e. those present during more than 5 % of the simulation) formed between the anandamide molecule (AEA) and the active-site amino acid residues of the FAAH enzyme and water molecules (only the hydrogen bonds that were present during more than 5 % of the total simulation time are included)

Donor			Acceptor		Occupation (%)	Distance ^b (Å)	Lifetime (ps)	Max occupation (ps)
Res	Atom1	Atom2	Res	Atom1				
AEA	N2	H	Ile238	O	87.1	2.82 ± 0.09	8.7 ± 12.0	91
AEA	O25	H	Leu192	O	65.9	2.79 ± 0.11	3.8 ± 5.0	53
Wat ^a	O	H1	AEA	O11	60.2	2.70 ± 0.11	19.4 ± 30.9	190
Wat ^a	O	H2	AEA	O11	34.7	2.71 ± 0.11	10.4 ± 17.1	99
AEA	O25	H	Ser193	O	9.9	2.80 ± 0.11	1.5 ± 1.1	8

^a The two hydrogen bonds are established with the same water molecule, but with different hydrogen atoms

^b The distance presented refers to the distance between the two heavy atoms involved

Hydrogen Bonding (H-Bond) analysis. To obtain a more atomic-level picture of the hydrogen bonds identified in the previous section from the RDF analysis and to identify additional relevant hydrogen bonds involving the anandamide substrate we decided to perform a full-hydrogen bonding analysis.

The results (Table 4) fail to show any significant hydrogen bond between anandamide and the amino acid side chains at the active-site. Interestingly however, three hydrogen bonds with backbone oxygen atoms of highly conserved amino acid residues have been identified. These are Leu192, Ser193 and Ile238. Particular attention should be focused on the interaction with Ile238, since it is part of the oxyanion hole of the active site [55]. The backbone oxygen atom of Ile238 establishes a very important hydrogen bond, present during more than 80 % of the simulation, with the hydrogen atom connected to N2 in anandamide. Leu192 interacts through its backbone oxygen atom with the hydrogen linked to O25 in anandamide, forming a hydrogen bond that is present during ca. 65 % of the simulation. The hydrogen at O25 partially interacts also with the oxygen atom of Ser193 (Fig. 7).

As seen in the RDF analysis one water molecule establishes a strong hydrogen bond with the anandamide O11 atom. Both hydrogen atoms of this water molecule participate alternatively in this interaction, with predominance of one of these atoms (62.0 % vs. 30.5 % of occupation). No other hydrogen bonds with duration higher than 5 % of the simulation were identified between any other water molecule and anandamide.

Interestingly no relevant hydrogen bonds were found with other oxyanion hole residues (Gly239, Gly240, and Ser241) as well as with Met191, thought to be relevant in the oleamide-FAAH complex. It is also relevant the fact that the reaction catalyzed by FAAH is mediated by a high-energy state [55, 56]. Hence, this analysis could be masking relevant reactive conformations, distinct from the predominant enzyme-substrate complex here described.

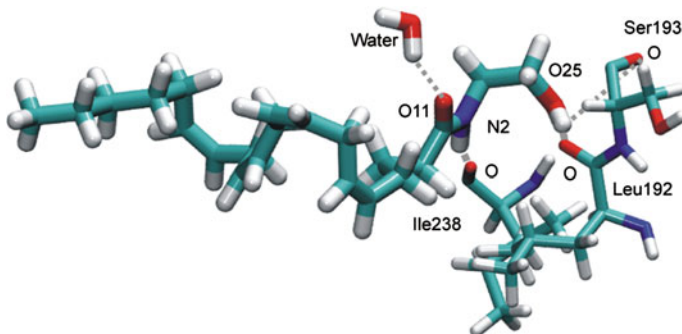


Fig. 7 Most relevant hydrogen bonds established with the anandamide substrate

4 Conclusions

Molecular modelling and molecular dynamics simulations are important tools in understanding the structure and function of biological ensembles. Molecular simulations can help to conceive and characterize conformational changes on proteins that play an essential role in their function, also providing a description at the atomic-level of the same changes. Hence, it allows the migration from a static and rigid protein structure conception to a more flexible and dynamic view. In enzymatic mechanistic studies, MD plays an important role, describing an enzyme-substrate conformational sampling, essential as a preliminary for mechanistic evaluations by methods such as QM/MM.

This study, in particular, provides a detailed analysis of key elements mediating the interaction between the FAAH enzyme and the anandamide substrate. In addition, it offers a characterization of the FAAH dimer model in contrast with the monomer, in terms of flexibility.

The results point towards pronounced differences between the flexibility profile for the monomer and dimer structures of the enzyme that could account for future considerations of the dimeric structure in future studies where the flexibility effects are relevant. Interestingly, with the monomer, the regions with higher flexibility are the regions of the enzyme with a more relevant interaction with the solvent. In the dimer case, the more flexible regions are those expected to interact with the membrane.

This study has also characterized 6 of the more relevant interacting residues in the active site with the substrate anandamide, in terms of the contact surface area. The more relevant residues ordered in terms of greater to lower extent are Leu192, Thr488, Phe432, Leu404, Ile491, and Leu380. Also, several polar amino acid residues are in contact with the anandamide surface. Examples include the poorly conserved Glu373 and Ser376, and the highly conserved Arg428 and catalytic Ser241 amino acid residues.

The analysis of RDF's and hydrogen bonding analysis accounted for 2 water molecules interacting with the anandamide substrate, as well as forming relevant hydrogen bonds through the simulation, with oxygen O11 of anandamide. Additionally, important hydrogen bonds were observed with anandamide and the residues Ile238, Ser193, Leu192 with both atoms O25 and N2 from the substrate.

The conformational and dynamics analysis of the anandamide-FAAH complex, point towards relevant active-site residue interactions with the anandamide substrate, which could be relevant in the stabilization of the substrate, and fruitful for future developments of FAAH inhibitors and enzymatic catalysis evaluations.

Acknowledgments We thank the financial support provided by FCT (PTDC/QUI-QUI/103118/2008 and grant no. Pest-C/EQB/LA0006/2011).

References

1. Schmid PC, Zuzarte-Augustin ML, Schmid HH (1985) Properties of rat liver N-acylethanolamine amidohydrolase. *J Biol Chem* 260(26):14145–14149
2. Cravatt BF, Giang DK, Mayfield SP, Boger DL, Lerner RA, Gilula NB (1996) Molecular characterization of an enzyme that degrades neuromodulatory fatty-acid amides. *Nature* 384 (6604):83–87
3. Bracey MH, Hanson MA, Masuda KR, Stevens RC, Cravatt BF (2002) Structural adaptations in a membrane enzyme that terminates endocannabinoid signaling. *Science* 298(5599):1793–1796
4. McKinney MK, Cravatt BF (2003) Evidence for distinct roles in catalysis for residues of the serine-serine-lysine catalytic triad of fatty acid amide hydrolase. *J Biol Chem* 278(39):37393–37399. doi:[10.1074/jbc.M303922200](https://doi.org/10.1074/jbc.M303922200)
5. McKinney MK, Cravatt BF (2005) Structure and function of fatty acid amide hydrolase. *Annu Rev Biochem* 74:411–432. doi:[10.1146/annurev.biochem.74.082803.133450](https://doi.org/10.1146/annurev.biochem.74.082803.133450)
6. Giang DK, Cravatt BF (1997) Molecular characterization of human and mouse fatty acid amide hydrolases. *Proc Natl Acad Sci USA* 94(6):2238–2242
7. Patricelli MP, Lovato MA, Cravatt BF (1999) Chemical and mutagenic investigations of fatty acid amide hydrolase: evidence for a family of serine hydrolases with distinct catalytic properties. *Biochemistry* 38(31):9804–9812. doi:[10.1021/bi990637z](https://doi.org/10.1021/bi990637z) bi990637z [pii]
8. Patricelli MP, Cravatt BF (1999) Fatty acid amide hydrolase competitively degrades bioactive amides and esters through a nonconventional catalytic mechanism. *Biochemistry* 38 (43):14125–14130. doi:[10.1021/bi991876p](https://doi.org/10.1021/bi991876p) bi991876p [pii]
9. Devane WA, Hanus L, Breuer A, Pertwee RG, Stevenson LA, Griffin G, Gibson D, Mandelbaum A, Etinger A, Mechoulam R (1992) Isolation and structure of a brain constituent that binds to the cannabinoid receptor. *Science* 258(5090):1946–1949
10. Pacher P, Batkai S, Kunos G (2006) The endocannabinoid system as an emerging target of pharmacotherapy. *Pharmacol Rev* 58(3):389–462. doi:[10.1124/pr.58.3.2](https://doi.org/10.1124/pr.58.3.2) 58/3/389 [pii]
11. Cravatt BF, Prospero-Garcia O, Siuzdak G, Gilula NB, Henriksen SJ, Boger DL, Lerner RA (1995) Chemical characterization of a family of brain lipids that induce sleep. *Science* 268 (5216):1506–1509
12. Lerner RA, Siuzdak G, Prospero-Garcia O, Henriksen SJ, Boger DL, Cravatt BF (1994) Cerebrodienol: a brain lipid isolated from sleep-deprived cats. *Proc Natl Acad Sci USA* 91 (20):9505–9508
13. Boger DL, Henriksen SJ, Cravatt BF (1998) Oleamide: an endogenous sleep-inducing lipid and prototypical member of a new class of biological signaling molecules. *Curr Pharm Des* 4 (4):303–314

14. Boger DL, Fecik RA, Patterson JE, Miyauchi H, Patricelli MP, Cravatt BF (2000) Fatty acid amide hydrolase substrate specificity. *Bioorg Med Chem Lett* 10(23):2613–2616
15. Lichtman AH, Shelton CC, Advani T, Cravatt BF (2004) Mice lacking fatty acid amide hydrolase exhibit a cannabinoid receptor-mediated phenotypic hypoalgesia. *Pain* 109(3):319–327. doi:[10.1016/j.pain.2004.01.022](https://doi.org/10.1016/j.pain.2004.01.022) S0304395904000545 [pii]
16. Clement AB, Hawkins EG, Lichtman AH, Cravatt BF (2003) Increased seizure susceptibility and proconvulsant activity of anandamide in mice lacking fatty acid amide hydrolase. *J Neurosci* 23(9):3916–3923. doi:[10.1523/JNEUROSCI.3916-03.2003](https://doi.org/10.1523/JNEUROSCI.3916-03.2003) [pii]
17. Cravatt BF, Lichtman AH (2003) Fatty acid amide hydrolase: an emerging therapeutic target in the endocannabinoid system. *Curr Opin Chem Biol* 7(4):469–475. doi:[S1367593103000796](https://doi.org/10.1016/j.cbpa.2003.09.006) [pii]
18. Cravatt BF, Demarest K, Patricelli MP, Bracey MH, Giang DK, Martin BR, Lichtman AH (2001) Supersensitivity to anandamide and enhanced endogenous cannabinoid signaling in mice lacking fatty acid amide hydrolase. *Proc Natl Acad Sci USA* 98(16):9371–9376. doi:[10.1073/pnas.161191698](https://doi.org/10.1073/pnas.161191698) 161191698 [pii]
19. Wise LE, Shelton CC, Cravatt BF, Martin BR, Lichtman AH (2007) Assessment of anandamide's pharmacological effects in mice deficient of both fatty acid amide hydrolase and cannabinoid CB1 receptors. *Eur J Pharmacol* 557(1):44–48. doi:[10.1016/j.ejphar.2006.11.002](https://doi.org/10.1016/j.ejphar.2006.11.002) S0014-2999(06)01262-3 [pii]
20. Osei-Hyiaman D, Depetrillo M, Harvey-White J, Bannon AW, Cravatt BF, Kuhar MJ, Mackie K, Palkovits M, Kunos G (2005) Cocaine- and amphetamine-related transcript is involved in the orexigenic effect of endogenous anandamide. *Neuroendocrinology* 81(4):273–282. doi:[10.1159/000087925](https://doi.org/10.1159/000087925) 87925 [pii]
21. Massa F, Marsicano G, Hermann H, Cannich A, Monory K, Cravatt BF, Ferri GL, Sibaev A, Storr M, Lutz B (2004) The endogenous cannabinoid system protects against colonic inflammation. *J Clin Invest* 113(8):1202–1209. doi:[10.1172/JCI19465](https://doi.org/10.1172/JCI19465)
22. Cravatt BF, Saghatelyan A, Hawkins EG, Clement AB, Bracey MH, Lichtman AH (2004) Functional disassociation of the central and peripheral fatty acid amide signaling systems. *Proc Natl Acad Sci USA* 101(29):10821–10826. doi:[10.1073/pnas.0401292101](https://doi.org/10.1073/pnas.0401292101) 0401292101 [pii]
23. Karsak M, Gaffal E, Date R, Wang-Eckhardt L, Rehne J, Petrosino S, Starowicz K, Steuder R, Schlicker E, Cravatt B, Mechoulam R, Buettner R, Werner S, Di Marzo V, Tuting T, Zimmer A (2007) Attenuation of allergic contact dermatitis through the endocannabinoid system. *Science* 316(5830):1494–1497. doi:[10.1126/science.1142265](https://doi.org/10.1126/science.1142265) 316/5830/1494 [pii]
24. Naidu PS, Varvel SA, Ahn K, Cravatt BF, Martin BR, Lichtman AH (2007) Evaluation of fatty acid amide hydrolase inhibition in murine models of emotionality. *Psychopharmacology* 192(1):61–70. doi:[10.1007/s00213-006-0689-4](https://doi.org/10.1007/s00213-006-0689-4)
25. Moreira FA, Kaiser N, Monory K, Lutz B (2008) Reduced anxiety-like behaviour induced by genetic and pharmacological inhibition of the endocannabinoid-degrading enzyme fatty acid amide hydrolase (FAAH) is mediated by CB1 receptors. *Neuropharmacology* 54(1):141–150. doi:[10.1016/j.neuropharm.2007.07.005](https://doi.org/10.1016/j.neuropharm.2007.07.005) S0028-3908(07)00214-6 [pii]
26. Huitron-Resendiz S, Sanchez-Alavez M, Wills DN, Cravatt BF, Henriksen SJ (2004) Characterization of the sleep-wake patterns in mice lacking fatty acid amide hydrolase. *Sleep* 27(5):857–865
27. Varvel SA, Wise LE, Niyuhire F, Cravatt BF, Lichtman AH (2007) Inhibition of fatty-acid amide hydrolase accelerates acquisition and extinction rates in a spatial memory task. *Neuropharmacology* 32(5):1032–1041. doi:[10.1038/sj.npp.1301224](https://doi.org/10.1038/sj.npp.1301224) 1301224 [pii]
28. Bambico FR, Cassano T, Dominguez-Lopez S, Katz N, Walker CD, Piomelli D, Gobbi G (2010) Genetic deletion of fatty acid amide hydrolase alters emotional behavior and serotonergic transmission in the dorsal raphe, prefrontal cortex, and hippocampus. *Neuropharmacology* 55(10):2083–2100. doi:[10.1038/npp.2010.80](https://doi.org/10.1038/npp.2010.80)
29. Gobbi G, Bambico FR, Mangieri R, Bortolato M, Campolongo P, Solinas M, Cassano T, Morgese MG, Debonnel G, Duranti A, Tontini A, Tarzia G, Mor M, Trezza V, Goldberg SR, Cuomo V, Piomelli D (2005) Antidepressant-like activity and modulation of brain monoaminergic transmission by blockade of anandamide hydrolysis. *Proc Natl Acad Sci USA* 102(51):18620–18625. doi:[10.1073/pnas.0509591102](https://doi.org/10.1073/pnas.0509591102) 0509591102 [pii]

30. Suplita RL, II, Farthing JN, Gutierrez T, Hohmann AG (2005) Inhibition of fatty-acid amide hydrolase enhances cannabinoid stress-induced analgesia: sites of action in the dorsolateral periaqueductal gray and rostral ventromedial medulla. *Neuropharmacology* 49(8):1201–1209. doi:[10.1016/j.neuropharm.2005.07.007](https://doi.org/10.1016/j.neuropharm.2005.07.007) S0028-3908(05)00263-7 [pii]
31. Lichtman AH, Leung D, Shelton CC, Saghatelian A, Hardouin C, Boger DL, Cravatt BF (2004) Reversible inhibitors of fatty acid amide hydrolase that promote analgesia: evidence for an unprecedented combination of potency and selectivity. *J Pharmacol Exp Ther* 311 (2):441–448. doi:[10.1124/jpet.104.069401](https://doi.org/10.1124/jpet.104.069401) jpet.104.069401 [pii]
32. Chang L, Luo L, Palmer JA, Sutton S, Wilson SJ, Barbier AJ, Breitenbucher JG, Chaplan SR, Webb M (2006) Inhibition of fatty acid amide hydrolase produces analgesia by multiple mechanisms. *Br J Pharmacol* 148(1):102–113. doi:[10.1038/sj.bjp.0706699](https://doi.org/10.1038/sj.bjp.0706699) 0706699 [pii]
33. Jayamanne A, Greenwood R, Mitchell VA, Aslan S, Piomelli D, Vaughan CW (2006) Actions of the FAAH inhibitor URB597 in neuropathic and inflammatory chronic pain models. *Br J Pharmacol* 147(3):281–288. doi:[10.1038/sj.bjp.0706510](https://doi.org/10.1038/sj.bjp.0706510) 0706510 [pii]
34. Ahn K, Johnson DS, Mileni M, Beidler D, Long JZ, McKinney MK, Weerapana E, Sadagopan N, Liimatta M, Smith SE, Lazerwith S, Stiff C, Kamtekar S, Bhattacharya K, Zhang Y, Swaney S, Van Becelaere K, Stevens RC, Cravatt BF (2009) Discovery and characterization of a highly selective FAAH inhibitor that reduces inflammatory pain. *Chem Biol* 16(4):411–420. doi:[10.1016/j.chembiol.2009.02.013](https://doi.org/10.1016/j.chembiol.2009.02.013) S1074-5521(09)00080-5 [pii]
35. Egertova M, Cravatt BF, Elphick MR (2003) Comparative analysis of fatty acid amide hydrolase and cb(1) cannabinoid receptor expression in the mouse brain: evidence of a widespread role for fatty acid amide hydrolase in regulation of endocannabinoid signaling. *Neuroscience* 119(2):481–496. doi:[S0306452203001453](https://doi.org/10.1016/j.neuroscience.2003.09.045) [pii]
36. Long JZ, LaCava M, Jin X, Cravatt BF (2011) An anatomical and temporal portrait of physiological substrates for fatty acid amide hydrolase. *J Lipid Res* 52(2):337–344. doi:[10.1194/jlr.M012153](https://doi.org/10.1194/jlr.M012153) jlr.M012153 [pii]
37. Schlosburg JE, Kinsey SG, Lichtman AH (2009) Targeting fatty acid amide hydrolase (FAAH) to treat pain and inflammation. *AAPS J* 11(1):39–44. doi:[10.1208/s12248-008-9075-y](https://doi.org/10.1208/s12248-008-9075-y)
38. Hwang J, Adamson C, Butler D, Janero DR, Makriyannis A, Bahr BA (2010) Enhancement of endocannabinoid signaling by fatty acid amide hydrolase inhibition: a neuroprotective therapeutic modality. *Life Sci* 86(15–16):615–623. doi:[10.1016/j.lfs.2009.06.003](https://doi.org/10.1016/j.lfs.2009.06.003) S0024-3205(09)00262-8 [pii]
39. Fowler CJ, Jonsson KO, Tiger G (2001) Fatty acid amide hydrolase: biochemistry, pharmacology, and therapeutic possibilities for an enzyme hydrolyzing anandamide, 2-arachidonoylglycerol, palmitoylethanolamide, and oleamide. *Biochem Pharmacol* 62(5):517–526. doi:[S0006-2952\(01\)00712-2](https://doi.org/10.1006/bph.2001.2153) [pii]
40. Lambert DM, Fowler CJ (2005) The endocannabinoid system: drug targets, lead compounds, and potential therapeutic applications. *J Med Chem* 48(16):5059–5087. doi:[10.1021/jm058183t](https://doi.org/10.1021/jm058183t)
41. Ahn K, McKinney MK, Cravatt BF (2008) Enzymatic pathways that regulate endocannabinoid signaling in the nervous system. *Chem Rev* 108(5):1687–1707. doi:[10.1021/cr0782067](https://doi.org/10.1021/cr0782067)
42. Ahn K, Johnson DS, Cravatt BF (2009) Fatty acid amide hydrolase as a potential therapeutic target for the treatment of pain and CNS disorders. *Expert Opin Drug Discov* 4(7):763–784. doi:[10.1517/17460440903018857](https://doi.org/10.1517/17460440903018857)
43. Sipe JC, Waalen J, Gerber A, Beutler E (2005) Overweight and obesity associated with a missense polymorphism in fatty acid amide hydrolase (FAAH). *Int J Obes (Lond)* 29(7):755–759. doi:[10.1038/sj.ijo.0802954](https://doi.org/10.1038/sj.ijo.0802954) 0802954 [pii]
44. Sipe JC, Chiang K, Gerber AL, Beutler E, Cravatt BF (2002) A missense mutation in human fatty acid amide hydrolase associated with problem drug use. *Proc Natl Acad Sci USA* 99 (12):8394–8399. doi:[10.1073/pnas.082235799](https://doi.org/10.1073/pnas.082235799) 99/12/8394 [pii]
45. Otrubova K, Ezzili C, Boger DL (2011) The discovery and development of inhibitors of fatty acid amide hydrolase (FAAH). *Bioorg Med Chem Lett* 21(16):4674–4685. doi:[10.1016/j.bmcl.2011.06.096](https://doi.org/10.1016/j.bmcl.2011.06.096) S0960-894X(11)00887-0 [pii]
46. Bachovchin DA, Cravatt BF (2012) The pharmacological landscape and therapeutic potential of serine hydrolases. *Nat Rev Drug Discov* 11(1):52–68. doi:[10.1038/nrd3620](https://doi.org/10.1038/nrd3620) nrd3620 [pii]

47. Romero FA, Du W, Hwang I, Rayl TJ, Kimball FS, Leung D, Hoover HS, Apodaca RL, Breitenbacher JG, Cravatt BF, Boger DL (2007) Potent and selective alpha-ketoheterocycle-based inhibitors of the anandamide and oleamide catabolizing enzyme, fatty acid amide hydrolase. *J Med Chem* 50(5):1058–1068. doi:[10.1021/jm0611509](https://doi.org/10.1021/jm0611509)
48. Ahn K, Johnson DS, Fitzgerald LR, Liimatta M, Arendse A, Stevenson T, Lund ET, Nugent RA, Nomanbhoy TK, Alexander JP, Cravatt BF (2007) Novel mechanistic class of fatty acid amide hydrolase inhibitors with remarkable selectivity. *Biochemistry* 46(45):13019–13030. doi:[10.1021/bi701378g](https://doi.org/10.1021/bi701378g)
49. Minkkila A, Saario S, Nevalainen T (2010) Discovery and development of endocannabinoid-hydrolyzing enzyme inhibitors. *Curr Top Med Chem* 10(8):828–858. doi: [BSP/ CTMC /E-Pub-0051-10-8](https://doi.org/10.2143/BSP/CTMC/E-Pub-0051-10-8) [pii]
50. Johnson DS, Stiff C, Lazerwith SE, Kesten SR, Fay LK, Morris M, Beidler D, Liimatta MB, Smith SE, Dudley DT, Sadagopan N, Bhattachar SN, Kesten SJ, Nomanbhoy TK, Cravatt BF, Ahn K (2011) Discovery of PF-04457845: a highly potent, orally bioavailable, and selective urea FAAH inhibitor. *Acs Med Chem Lett* 2(2):91–96. doi:[10.1021/ml100190t](https://doi.org/10.1021/ml100190t)
51. Patricelli MP, Cravatt BF (2000) Clarifying the catalytic roles of conserved residues in the amidase signature family. *J Biol Chem* 275(25):19177–19184. doi:[10.1074/jbc.M001607200](https://doi.org/10.1074/jbc.M001607200) M001607200 [pii]
52. Tubert-Brohman I, Acevedo O, Jorgensen WL (2006) Elucidation of hydrolysis mechanisms for fatty acid amide hydrolase and its Lys142Ala variant via QM/MM simulations. *J Am Chem Soc* 128(51):16904–16913. doi:[10.1021/ja065863s](https://doi.org/10.1021/ja065863s)
53. Lodola A, Mor M, Hermann JC, Tarzia G, Piomelli D, Mulholland AJ (2005) QM/MM modelling of oleamide hydrolysis in fatty acid amide hydrolase (FAAH) reveals a new mechanism of nucleophile activation. *Chem Commun (Camb)* 35:4399–4401. doi:[10.1039/b503887a](https://doi.org/10.1039/b503887a)
54. Capoferri L, Mor M, Sirirak J, Chudyk E, Mulholland AJ, Lodola A (2011) Application of a SCC-DFTB QM/MM approach to the investigation of the catalytic mechanism of fatty acid amide hydrolase. *J Mol Model* 17(9):2375–2383. doi:[10.1007/s00894-011-0981-z](https://doi.org/10.1007/s00894-011-0981-z)
55. Lodola A, Sirirak J, Fey N, Rivara S, Mor M, Mulholland AJ (2010) Structural fluctuations in enzyme-catalyzed reactions: determinants of reactivity in fatty acid amide hydrolase from multivariate statistical analysis of quantum mechanics/molecular mechanics paths. *J Chem Theory Comput* 6(9):2948–2960. doi:[10.1021/ct100264j](https://doi.org/10.1021/ct100264j)
56. Lodola A, Mor M, Zurek J, Tarzia G, Piomelli D, Harvey JN, Mulholland AJ (2007) Conformational effects in enzyme catalysis: Reaction via a high energy conformation in fatty acid amide hydrolase. *Biophys J* 92(2):L20–L22. doi:[10.1529/biophysj.106.098434](https://doi.org/10.1529/biophysj.106.098434)
57. Bowman AL, Makriyannis A (2011) Approximating protein flexibility through dynamic pharmacophore models: application to fatty acid amide hydrolase (FAAH). *J Chem Inf Model* 51(12):3247–3253. doi:[10.1021/ci200371z](https://doi.org/10.1021/ci200371z)
58. Palermo G, Branduardi D, Masetti M, Lodola A, Mor M, Piomelli D, Cavalli A, De Vivo M (2011) Covalent inhibitors of fatty acid amide hydrolase: a rationale for the activity of piperidine and piperazine aryl ureas. *J Med Chem* 54(19):6612–6623. doi:[10.1021/jm2004283](https://doi.org/10.1021/jm2004283)
59. Lodola A, Mor M, Rivara S, Christov C, Tarzia G, Piomelli D, Mulholland AJ (2008) Identification of productive inhibitor binding orientation in fatty acid amide hydrolase (FAAH) by QM/MM mechanistic modelling. *Chem Commun (Camb)* 2:214–216. doi:[10.1039/b714136j](https://doi.org/10.1039/b714136j)
60. Case DA, Darden TA, T. E. Cheatham I, Simmerling CL, Wang J, Duke RE, Luo R, Crowley M, Walker RC, Zhang W, Merz KM, Wang B, Hayik S, Roitberg A, Seabra G, Kolossváry I, Wong KF, Paesani F, Vanicek J, Wu X, Brozell SR, Steinbrecher T, Gohlke H, Yang L, Tan C, Mongan J, Hornak V, Cui G, Mathews DH, Seetin MG, Sagui C, Babin V, Kollman PA (2008) AMBER 10. San Francisco
61. Duan Y, Wu C, Chowdhury S, Lee MC, Xiong G, Zhang W, Yang R, Cieplak P, Luo R, Lee T, Caldwell J, Wang J, Kollman P (2003) A point-charge force field for molecular mechanics simulations of proteins based on condensed-phase quantum mechanical calculations. *J Comput Chem* 24(16):1999–2012. doi:[10.1002/jcc.10349](https://doi.org/10.1002/jcc.10349)

62. Wang J, Wang W, Kollman PA, Case DA (2006) Automatic atom type and bond type perception in molecular mechanical calculations. *J Mol Graph Model* 25(2):247–260. doi:[10.1016/j.jmgm.2005.12.005](https://doi.org/10.1016/j.jmgm.2005.12.005) S1093-3263(05)00173-7 [pii]
63. Wang J, Wolf RM, Caldwell JW, Kollman PA, Case DA (2004) Development and testing of a general amber force field. *J Comput Chem* 25(9):1157–1174. doi:[10.1002/jcc.20035](https://doi.org/10.1002/jcc.20035)
64. Ryckaert JP, Ciccotti G, Berendsen HJ (1977) Numerical integration of the Cartesian equations of motion of a system with constraints: molecular dynamics of n-alkanes. *J Comput Phys* 23:327–341
65. Essmann U, Perera L, Berkowitz ML, Darden T, Lee H, Pedersen LG (1995) A smooth particle mesh Ewald method. *J Chem Phys* 103(19):8577–8593
66. Glaser F, Rosenberg Y, Kessel A, Pupko T, Ben-Tal N (2005) The ConSurf-HSSP database: the mapping of evolutionary conservation among homologs onto PDB structures. *Proteins* 58 (3):610–617. doi:[10.1002/prot.20305](https://doi.org/10.1002/prot.20305)
67. Altschul SF, Madden TL, Schaffer AA, Zhang J, Zhang Z, Miller W, Lipman DJ (1997) Gapped BLAST and PSI-BLAST: a new generation of protein database search programs. *Nucleic Acids Res* 25(17):3389–3402. doi:[gka562](https://doi.org/gka562) [pii]
68. Bairoch A, Apweiler R (1999) The SWISS-PROT protein sequence data bank and its supplement TrEMBL in 1999. *Nucleic Acids Res* 27(1):49–54. doi:[gkc088](https://doi.org/gkc088) [pii]
69. Edgar RC (2004) MUSCLE: multiple sequence alignment with high accuracy and high throughput. *Nucleic Acids Res* 32(5):1792–1797. doi:[10.1093/nar/gkh340](https://doi.org/10.1093/nar/gkh340) 32/5/1792 [pii]
70. Mayrose I, Graur D, Ben-Tal N, Pupko T (2004) Comparison of site-specific rate-inference methods for protein sequences: empirical Bayesian methods are superior. *Mol Biol Evol* 21 (9):1781–1791. doi:[10.1093/molbev/msh194](https://doi.org/10.1093/molbev/msh194) msh194 [pii]

Part III

Molecular Dynamics

Intense Field Molecular Photodissociation: The Adiabatic Views

R. Lefebvre

Abstract The adiabatic theory requires the time scale of the changes in the Hamiltonian to be larger than the time scale of the changes in the system. The solution of the wave equation is expressed in terms of the instantaneous solutions. A formalism known as the adiabatic Floquet theory is being currently applied to describe photodissociation of molecules at high intensity in the optical range, where these conditions are not fulfilled. We show how to justify this approach, and we use the direct solution of the time-dependent Schrödinger equation to confirm its validity.

Keywords Molecular photodissociation · Adiabatic theory · Floquet formalism

1 Introduction

The adiabatic approach to treat a quantum system is considered as a useful tool which avoids the difficult task of looking for the exact solutions of the time-dependent Schrödinger equation [1–3]. The applicability of the method requires the time scale for the variation of the time-dependent contribution to the Hamiltonian to be larger than the time scale of the exposed system, given typically by the inverse of level separations. The method, first developed for Hermitian Hamiltonian, has also been applied to the dissipative case, that is to non-Hermitian Hamiltonians [4–6], with also some discussion for the conditions of applicability [5]. We wish, in this paper, to consider the case of a molecule exposed to a strong laser pulse. This problem has sometimes been treated by the method called the adiabatic Floquet

R. Lefebvre (✉)

Institut des Sciences Moléculaires d'Orsay (ISMO), CNRS and UMR8214, Bât. 350,
Université Paris-Sud, F91405 Orsay, France
e-mail: roland.lefebvre@u-psud.fr

R. Lefebvre

U.F.R. de Physique Fondamentale et Appliquée, Université Pierre et Marie Curie,
75321 Paris, France

© Springer International Publishing Switzerland 2015

M.A.C. Nascimento et al. (eds.), *Frontiers in Quantum Methods and Applications in Chemistry and Physics*, Progress in Theoretical Chemistry and Physics 29,
DOI 10.1007/978-3-319-14397-2_8

135

approach (see for instance [7–9]). We will show that this method is not in conformity with the standard adiabatic procedure. Adiabatic transport has also been recently discussed for the case of two neighbouring resonances which may coalesce at a so-called exceptional point in parameter space [8, 10–13]. We consider here only the case of an isolated resonance. The paper is organized as follows: Sect. 2 gives the elements of the description of a diatomic molecule exposed to a pulsed electromagnetic field. We then consider two options which are possible steps toward an adiabatic description of the dynamics. In Sect. 3 we follow the traditional adiabatic treatment based on the instantaneous solutions of the wave equation. In Sect. 4 we review a route leading to more acceptable results. In Sect. 5 a wave packet description, with a step by step solution of the time-dependent Schrödinger equation, confirms the results of Sect. 4. The system H_2^+ is considered in the applications.

2 The Time-Dependent Wave-Equation

We consider a one-dimensional model molecule involving only two electronic states $|1\rangle$ and $|2\rangle$. Potential energies $V_1(R)$ and $V_2(R)$ are associated to these two states, R being the interatomic distance. $V_1(R)$ accommodates a series of bound vibrational states while $V_2(R)$ is a repulsive potential. This is the situation met in the H_2^+ species, where $V_1(R)$ is in fact $V_g(R)$, the potential of the state described by a $1\sigma_g$ orbital, and $V_2(R)$ the potential $V_u(R)$ of the state described by a $1\sigma_u$ orbital. If the rotational period of the molecule is shorter than the laser pulse duration, R is enough to account for the nuclear motion. This is the case for H_2^+ where the rotational period can be estimated to be about 7 ps while we will be considering pulses of duration 30 fs. The wave function of the system is expanded on these two states

$$|\Psi(R, t)\rangle = \chi_1(R, t)|1\rangle + \chi_2(R, t)|2\rangle, \quad (1)$$

The two unknown functions $\chi_1(R, t)$ and $\chi_2(R, t)$ describe the field-assisted nuclear dynamics. After elimination of the electronic wave functions, the Hamiltonian for the molecule exposed to a laser pulse is

$$H(R, t) = T_N + \begin{bmatrix} V_g(R) & \mu(R)\mathcal{E}_0(t) \cos(\omega(t)t) \\ \mu(R)\mathcal{E}_0(t) \cos(\omega(t)t) & V_u(R) \end{bmatrix} \quad (2)$$

T_N is the nuclear kinetic energy operator. The wave function is now reduced to a column vector with two elements $\chi_1(R, t)$ and $\chi_2(R, t)$. This form of the Hamiltonian means that there is an envelope function $\mathcal{E}_0(t)$ for the electric field amplitude and a time dependent frequency $\omega(t)$. $\mu(R)$ is the transition dipole moment. This Hamiltonian is not periodic. There are two ways to proceed further. The common adiabatic approach [1–3] consists in defining first the instantaneous solutions, with t considered as a parameter. These wave functions $\Psi_{inst.}(R, t)$ can be obtained by solving

$$H(R, t)\Psi_{inst.}(R, t) = E_{inst.}(t)\Psi_{inst.}(R, t) \quad (3)$$

with

$$\Psi_{inst.}(R, t) = \tilde{\chi}_1(R, t)|1\rangle + \tilde{\chi}_2(R, t)|2\rangle, \quad (4)$$

The two functions $\tilde{\chi}_1(R, t)$ and $\tilde{\chi}_2(R, t)$ obey the two coupled equations

$$[T_N + V_g(R) - E_{inst.}(t)]\tilde{\chi}_1(R, t) + \mu(R)\mathcal{E}_0(t) \cos(\omega(t)t)\tilde{\chi}_2(R, t) = 0 \quad (5)$$

and

$$[T_N + V_u(R) - E_{inst.}(t)]\tilde{\chi}_2(R, t) + \mu(R)\mathcal{E}_0(t) \cos(\omega(t)t)\tilde{\chi}_1(R, t) = 0 \quad (6)$$

These equations are to be solved for fixed t . The consequences of this choice are developed in Sect. 3. We note that a diagonalization of the potential matrix leads to time-dependent potentials for the description of the nuclear motion. Time dependent potentials have already been considered in the context of an improvement of the Born-Oppenheimer scheme for a time-dependent Hamiltonian [14, 15].

We can also define quasi-adiabatic solutions by considering that the field amplitude and wavelength are functions of some parameter t' . The Hamiltonian takes the form

$$H(R, t, t') = T_N + \begin{bmatrix} V_g(R) & \mu(R)\mathcal{E}_0(t') \cos(\omega(t')t) \\ \mu(R)\mathcal{E}_0(t') \cos(\omega(t')t) & V_u(R) \end{bmatrix} \quad (7)$$

The Hamiltonian is made periodic, with period $T = 2\pi/\omega(t')$. The Floquet formalism is applicable [16]. We note the relation

$$H(R, t) = H(R, t, t')|_{t'=t} \quad (8)$$

Section 4 is devoted to the solutions issued from this approach.

3 The Instantaneous Solutions

Panel (a) of Fig. 1 shows the two lowest potentials of H_2^+ (taken from Bunkin and Tugov [17]). Panel (b) gives the potentials as modified by the matter-field coupling at the maximum intensity of the pulse ($I_{\max} = 0.2 \times 10^{13} \text{ W/cm}^2$). The potential matrix is diagonalized at every value of the internuclear distance R . The dipole transition moment is also taken from [17]. The potential adiabatic representation provides the best insight for the physical processes under way [18]. Because the coupling is asymptotically divergent, an important aspect emerges in these adiabatic potentials: The two potentials $V_+(R)$ and $V_-(R)$ tend to separate from each other, so

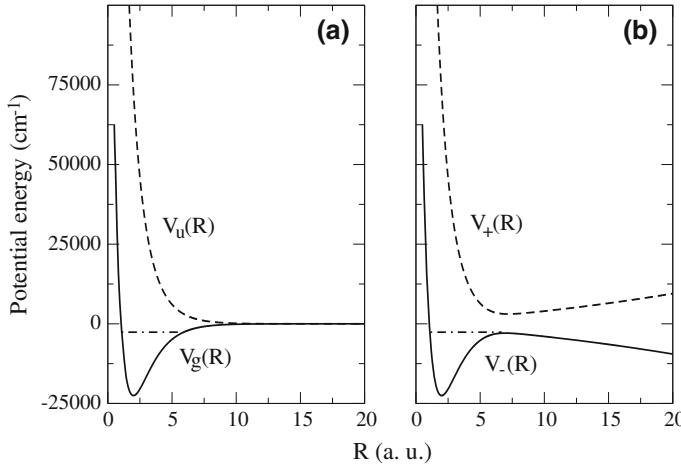


Fig. 1 Panel **a** $V_g(R)$ and $V_u(R)$ are the two lowest molecular potentials of H_2^+ . Panel **b** The adiabatic potentials $V_+(R)$ and $V_-(R)$ resulting from the diagonalization of the matter-field coupling. This is at the maximum intensity $I_{\max} = 0.2 \times 10^{13} \text{ W/cm}^2$ of the laser pulse introduced in this study. The *dashed-dotted horizontal line* in each panel shows the position of the unperturbed vibrational level of H_2^+ with quantum number $v = 12$. Its energy is $-2,673 \text{ cm}^{-1}$ below the dissociation limit taken as the zero of energy

that the lower potential acquires a barrier. Of course, if we have t as a parameter, this barrier will be parameter-dependent. When the field amplitude passes through zero, the two potentials have the same asymptotic limit, a feature which is present in the field-free molecule. The laser pulse to be considered has a duration of $T_f = 30 \text{ fs}$. The wavelength is $\lambda = 575 \times 10^{-7} \text{ cm}$. The intensity is given the form $I(t) = I_{\max} \sin(\pi t/T_f)$. There are 16 oscillations in the pulse, meaning that the intensity passes 32 times through maxima. The molecule is supposed to be in the $v = 12$ level before being submitted to the field. It is useful at this point to check that the resonances are well isolated. This is done in Fig. 2, showing the energy trajectories for the resonances issued from $v = 12$, but also for those issued from $v = 11$ and $v = 13$. However this isolation is not enough to justify an adiabatic treatment, since the field quantum ($17,391 \text{ cm}^{-1}$) is much larger than the level separations, of the order of $1,000 \text{ cm}^{-1}$. The Eqs. (5) and (6) are solved with the Fox-Goodwin algorithm [19], with matching of propagated inward and outward solutions [18]. Because we are looking for a resonance, we use complex scaling in the asymptotic region to change the normally divergent resonance wave functions into converging ones [20]. The resulting energy is complex, of the form $E_R(t) - i\Gamma_R(t)/2$, with an imaginary part giving the rate $\Gamma_R(t)/\hbar$. The main result is shown in Fig. 3. Panel (a) shows the quantity $\Gamma_R(t)$, which is practically zero except when the time is in the range 10–20 fs. Panel (b) shows how the top of the barrier is affected by the field. Its position is of course zero when the field vanishes (there

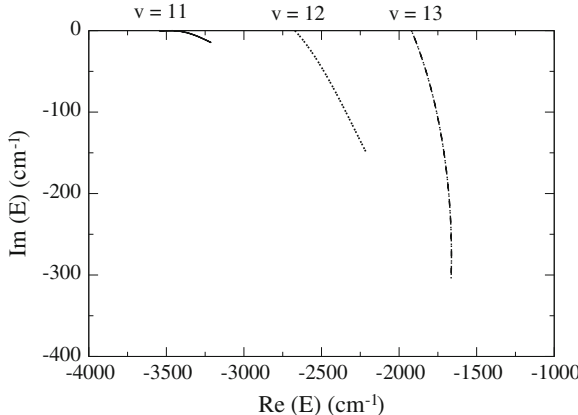


Fig. 2 The trajectories in the energy plane for the resonance energies issued from the level $v = 12$ (dotted curve) and for the two resonances immediately below ($v = 11$) (continuous curve) and immediately above ($v = 13$) (dashed-dotted curve). The representative points leave the real axis when the pulse is switched on and go back to this axis when the pulse is off. The rates are given by the imaginary parts multiplied by -2 . They are two orders of magnitude larger than those of the instantaneous approach. The resonance issued from the level $v = 12$ is well isolated

is in fact no barrier in this case). Also shown is the position of the energy of the field-free level ($E_{12} = -2,673 \text{ cm}^{-1}$). There is a strong correlation between the range of time when the barrier top is equal or below this energy and the appearance of a rate. Of course in this range it is still possible for the field to vanish. This explains the vanishing rates between two peaks in panel (a). The fact that the barrier has to be lowered by the field for the molecule to find its way toward dissociation is reminiscent of that described under the name of DDQ (Dynamic Dissociation Quenching) in [21], but with a major difference, since the field in this case in the infrared range. This is in fact the reason why the instantaneous solutions make sense in the DDQ case, whereas, as we will see in the next section, another approach, although not in conformity with the traditional adiabatic method, is to be preferred. A comparison to be made further down with the quasi-adiabatic approach and the wave-packet method will show how poor the instantaneous procedure is to evaluate the dissociation rate.

4 The Quasi-Adiabatic Solutions

According to the Floquet theorem the solutions of the wave equation with the Hamiltonian of Eq. (7) can be given the form [16]

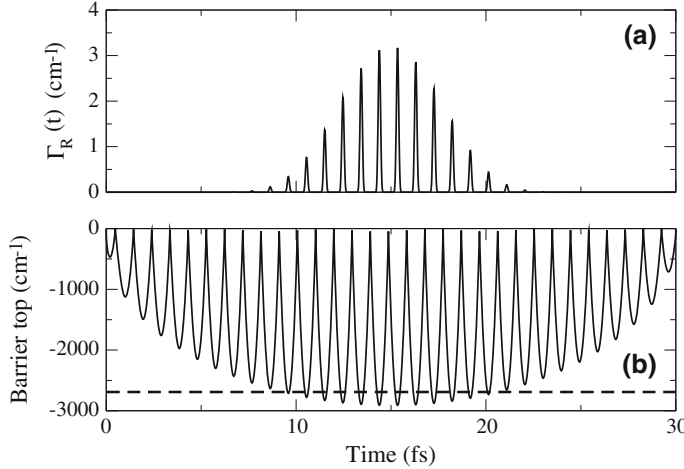


Fig. 3 Panel **a** The instantaneous rate as a function of time. Panel **b** The instantaneous position of the top of the barrier as a function of time. The *dashed horizontal line* shows the position of the unperturbed vibrational level with quantum number $v = 12$, at $-2,673 \text{ cm}^{-1}$. Only when the barrier top is below this position is there a non-zero rate. The rate maxima are strictly correlated with the barrier top minima

$$\begin{bmatrix} \chi_1(R, t, t') \\ \chi_2(R, t, t') \end{bmatrix} = e^{-iE_F(t')/\hbar} \begin{bmatrix} \phi_1(R, t, t') \\ \phi_2(R, t, t') \end{bmatrix} \quad (9)$$

E_F is the Floquet quasi-energy. The functions $\phi_k(R, t, t')$ ($k = 1, 2$) are periodic in time. They can be expanded in Fourier series

$$\phi_k(R, t, t') = \sum_{n=-\infty}^{+\infty} e^{in\omega(t')t} \phi_k^n(R, t'). \quad (10)$$

The functions $\phi_k^n(R, t')$ are the solutions of the coupled differential equations [16]

$$\begin{aligned} & [T_N + V_{1,2}(R) + n\hbar\omega(t') - E_F(t')] \phi_{1,2}^n(R, t') \\ & - 1/2\mathcal{E}_0(t')\mu(R) [\phi_{2,1}^{n-1}(R, t') + \phi_{2,1}^{n+1}(R, t')] \\ & = 0 \end{aligned} \quad (11)$$

If the field amplitude is small enough to avoid going beyond 2 channels (or one-photon absorption) there results the two coupled equations

$$[T_N + V_g(R) + \hbar\omega(t') - E_F(t')] \varphi_g(R, t') - 1/2\mathcal{E}_0(t')\mu(R)\varphi_u(R, t') = 0 \quad (12)$$

and

$$[T_N + V_u(R) - E_F(t')] \varphi_u(R, t') - 1/2\mathcal{E}_0(t')\mu(R)\varphi_g(R, t') = 0 \quad (13)$$

where g and u have been substituted to 1 and 2. Solution of these equations is made with the method described for the instantaneous case. The functions can be called diabatic as they are obtained from the coupled equations involving the so-called dressed potentials which cross each other [see Fig. 4, panel(a)]. It is of course possible, for each value of the coordinate R , to obtain, through a linear transformation, the adiabatic channel functions associated with the adiabatic potentials $\tilde{V}_+(R)$ and $\tilde{V}_-(R)$ [18]. The wave function can be written

$$\Psi(R, t, t') = e^{-iE_F(t')t/\hbar} \begin{bmatrix} \varphi_g(R, \mathcal{E}_0(t'), \omega(t')) e^{i\omega(t')t} \\ \varphi_u(R, \mathcal{E}_0(t'), \omega(t')) \end{bmatrix} \quad (14)$$

We let now the parametric dependence to be denoted simply by t' . The wave function can also be written

$$\Psi(R, t, t') = e^{-iE_F(t')t/\hbar} \begin{bmatrix} \varphi_g(R, t') e^{i\omega(t')t} \\ \varphi_u(R, t') \end{bmatrix} \quad (15)$$

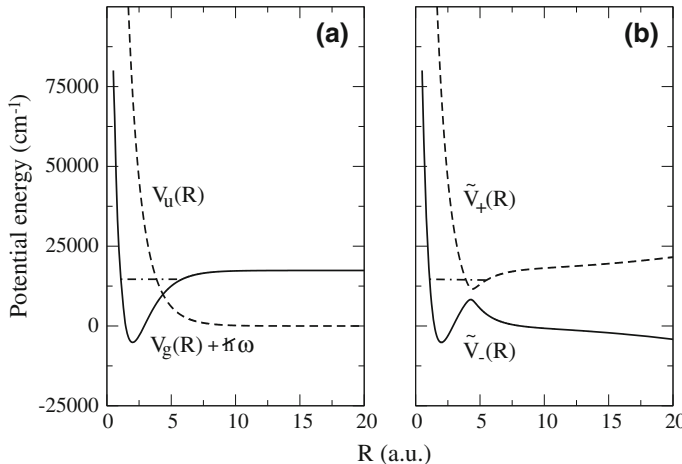


Fig. 4 Panel **a** The two lowest molecular potentials of H_2^+ in the dressed picture with a field of wavelength 575×10^{-7} cm. The photon energy, that is $17,391 \text{ cm}^{-1}$, has been added to the ground state potential. Panel **b** The dressed adiabatic potentials after diagonalization of the matter-field coupling. The intensity is $I = 0.2 \times 10^{13} \text{ W/cm}^2$. The *dashed-dotted horizontal line* in each panel shows the position of the unperturbed vibrational level of H_2^+ , with quantum number $v = 12$

This wave function fulfills

$$\left[H(R, t, t') - i\hbar \frac{\partial}{\partial t} \right] \begin{bmatrix} \varphi_g(R, t') e^{i\omega(t')t} \\ \varphi_u(R, t') \end{bmatrix} = E_F(t') \begin{bmatrix} \varphi_g(R, t') e^{i\omega(t')t} \\ \varphi_u(R, t') \end{bmatrix} \quad (16)$$

or also

$$\begin{aligned} H(R, t, t') \begin{bmatrix} \varphi_g(R, t') e^{i\omega(t')t} \\ \varphi_u(R, t') \end{bmatrix} &= i\hbar \begin{bmatrix} (i\omega(t') \varphi_g(R, t') e^{i\omega(t')t}) \\ 0 \end{bmatrix} \\ &\quad + E_F(t') \begin{bmatrix} \varphi_g(R, t') e^{i\omega(t')t} \\ \varphi_u(R, t') \end{bmatrix} \end{aligned} \quad (17)$$

Because in the Hamiltonian there is no derivative with respect to either t or t' we can let t' to be equal to t , so that

$$H(R, t) \begin{bmatrix} \varphi_g(R, t) e^{i\omega(t)t} \\ \varphi_u(R, t) \end{bmatrix} = i\hbar \begin{bmatrix} i\omega(t) \varphi_g(R, t) e^{i\omega(t)t} \\ 0 \end{bmatrix} + E_F(t) \begin{bmatrix} \varphi_g(R, t) e^{i\omega(t)t} \\ \varphi_u(R, t) \end{bmatrix} \quad (18)$$

We look now for a solution with the form

$$\Phi(R, t) = A(t) e^{-\frac{i}{\hbar} \int_0^t E_F(t') dt'} \begin{bmatrix} \varphi_g(R, t) e^{i\omega(t)t} \\ \varphi_u(R, t) \end{bmatrix} \quad (19)$$

In order to obtain an equation for the amplitude $A(t)$, we apply to $H(R, t)\Phi(R, t)$ the row vector

$$\begin{bmatrix} \varphi_g(R, t) e^{-i\omega(t)t}, \varphi_u(R, t) \end{bmatrix} \quad (20)$$

In the definition of this “bra” there is no complex conjugation of the coordinate dependent functions (cf the c-product of reference [22] valid for biorthogonal functions), but complex conjugation of the time dependent functions (cf the F-product of reference [23]). We adopt for the scalar product the notation $(\cdot | \cdot)$. There is obtained

$$\begin{aligned} &\left(\left[\varphi_g(R, t) e^{-i\omega(t)t}, \varphi_u(R, t) \right] | H(R, t) \Phi(R, t) \right) \\ &= A(t) e^{-\frac{i}{\hbar} \int_0^t E_F(t') dt'} \left[[i\hbar i\omega(t) (\varphi_g | \varphi_g) + E_F(t) [(\varphi_g | \varphi_g) + (\varphi_u | \varphi_u)]] \right] \end{aligned} \quad (21)$$

where, for instance, $(\varphi_g | \varphi_g)$ stands for

$$(\varphi_g|\varphi_g) = \int_0^\infty dR \varphi_g(R, t) \varphi_g(R, t) \quad (22)$$

On the other hand we have

$$\begin{aligned} i\hbar \frac{\partial \Phi(R, t)}{\partial t} = & e^{-\frac{i}{\hbar} \int_0^t E_F(t') dt'} \left[[i\hbar \dot{A}(t) + A(t) E_F(t)] \begin{bmatrix} \varphi_g(R, t) e^{i\omega(t)t} \\ \varphi_u(R, t) \end{bmatrix} \right. \\ & \left. + i\hbar A(t) \begin{bmatrix} [i\dot{\omega}(t)t + i\omega(t)] \varphi_g(R, t) + \dot{\varphi}_g(t) e^{i\omega(t)t} \\ \dot{\varphi}_u(R, t) \end{bmatrix} \right] \end{aligned} \quad (23)$$

so that

$$\begin{aligned} \left(\begin{bmatrix} \varphi_g(R, t) e^{-i\omega(t)t} \\ \varphi_u(R, t) \end{bmatrix} \middle| i\hbar \frac{\partial \Phi(R, t)}{\partial t} \right) = & e^{-\frac{i}{\hbar} \int_0^t E_F(t') dt'} [[i\hbar \dot{A}(t) + A(t) E_F(t)] [(\varphi_g|\varphi_g) \\ & + (\varphi_u|\varphi_u)] + i\hbar A(t) [(i\dot{\omega}(t)t + i\omega(t))(\varphi_g|\varphi_g) + (\varphi_g|\dot{\varphi}_g) + (\varphi_u|\dot{\varphi}_u)]] \end{aligned} \quad (24)$$

A quantity such as $(\varphi_g|\dot{\varphi}_g)$ is

$$(\varphi_g|\dot{\varphi}_g) = \int_0^\infty dR \varphi_g(R, t) \frac{\partial}{\partial t} \varphi_g(R, t) \quad (25)$$

Upon equaling Eq. (24) with Eq. (21) the ω dependent terms cancel as well as the energy dependent terms. We end with the equation

$$\dot{A}(t) [(\varphi_g|\varphi_g) + (\varphi_u|\varphi_u)] + iA(t) [\dot{\omega}(t)t(\varphi_g|\varphi_g) + (\varphi_g|\dot{\varphi}_g) + (\varphi_u|\dot{\varphi}_u)] = 0 \quad (26)$$

Now some simplifications are possible because the Floquet functions make up an orthonormal set. Normality implies that for the resonance wave function

$$(\varphi_g|\varphi_g) + (\varphi_u|\varphi_u) = 1 \quad (27)$$

From this relation there follows that

$$(\varphi_g|\dot{\varphi}_g) + (\varphi_u|\dot{\varphi}_u) = 0 \quad (28)$$

We note that for a closed system (with a Hermitian Hamiltonian) this term generates the geometrical phase [4]. For a non-Hermitian Hamiltonian generating symmetric complex matrices this is zero because of the properties of the c-product [12, 24]. Finally the amplitude $A(t)$ is solution of

$$\dot{A}(t) = -A(t)[i\dot{\omega}(t)t(\varphi_1|\varphi_1)] \quad (29)$$

Assuming that $A(0)$ is 1, the solution is

$$A(t) = e^{-i \int_0^t \dot{\omega}(t') t' (\varphi_g | \varphi_g) dt'} \quad (30)$$

This factor has been ignored in the application of the so-called adiabatic Floquet approach [7, 8]. It contributes to the damping because $(\varphi_1|\varphi_1)$ is a complex number. In our case, with a constant wavelength, this factor is unity. Finally the wave function has the familiar form

$$\Phi_{\text{adiab}}(R, t) = e^{-\frac{i}{\hbar} \int_0^t E_F(t') dt'} \begin{bmatrix} \varphi_g(R, t) e^{i\omega(t)t} \\ \varphi_u(R, t) \end{bmatrix} \quad (31)$$

This simple form is the result of reducing the dynamics to two channels. It has the appearance of an adiabatic wave function, with the major difference that it is not involving an instantaneous solution of the wave equation. Generalization to any number of channels is straightforward. The survival probability can be evaluated as the squared modulus of a scalar product

$$|(\begin{bmatrix} \varphi_g(R, t) e^{-i\omega(t)t} & \varphi_u(R, t) \end{bmatrix} | \Phi_{\text{adiab}}(R, t))|^2 = e^{-\hbar^{-1} \int_0^t \Gamma_R(t') dt'} \quad (32)$$

5 The Solution of the Time-Dependent Schrödinger Equation

Another procedure is of course to solve directly the time-dependent Schrödinger equation, with as initial condition the wave function of the field-free molecule, that is the wave packet

$$\Psi(R, t = 0) = \chi_{12}(R)|1\rangle \quad (33)$$

A third-order split-operator technique yields $\Psi(R, t)$ [9]. The survival probability at time t is given by

$$P_{\text{surv.}}(t) = |\langle \chi_{12}(R) | \Psi(R, t) \rangle|^2 \quad (34)$$

We are now able to compare the survival probabilities of the three methods: Panel (a) of Fig. 5 gives the survival probability of the instantaneous method: Because the rates are much too small there is almost no dissociation. In panel (b) we have the result of both the quasi-adiabatic formalism and of the direct solution. The agreement is quite satisfactory despite the rather high peak intensity of the pulse.

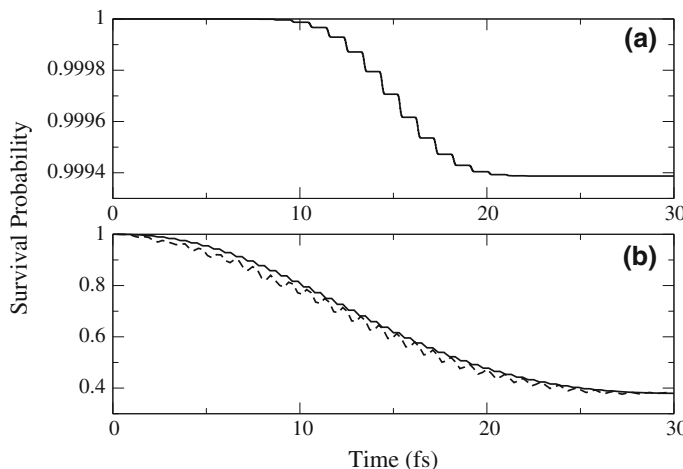


Fig. 5 Panel **a** The survival probability as a function of time calculated with the instantaneous solutions of the wave equation. Photodissociation occurs only when the intensity is large enough to bring the top of the barrier below the energy of the initial level. Panel **b** *Continuous curve* the survival probability derived from the quasi-adiabatic Floquet theory. *Dashed curve* the probability calculated with the time-dependent approach

6 Conclusion

The physical description of the quasi-adiabatic method is to let the system to be exposed to a field with a frequency and an intensity corresponding to some point along the curve describing the laser pulse and to let the field oscillate with these laser parameters. This is repeated for the next point, and so on. This is to be distinguished from the common adiabatic picture, with introduction of instantaneous eigenstates. The failure of the latter method is that the assumption of a slow variation of the parameters is not at all fulfilled for a field in the optical range. The quasi-adiabatic procedure can be validated by the full solution of the time-dependent Schrödinger equation in a case where there is no non-adiabatic contamination, because the resonance is well isolated from others for the range of parameters we have considered.

Acknowledgments I thank M. Desouter-Lecomte for providing the code for the wave packet calculations and O. Atabek for useful discussions.

References

1. Born M, Fock V (1928) Z Phys 51:165
2. Kato T (1950) J Phys Soc Jpn 5:435
3. Messiah A (1962) Quantum Mechanics. North Holland, Amsterdam
4. Sarandy MS, Lidar DA (2005) Phys Rev A 71:012331

5. Fleischer A, Moiseyev N (2005) *Phys Rev A* 72:032103
6. Leclerc A, Viennot D, Jolicard G (2012) *J Phys A: Math Theor* 45:415201
7. Atabek O, Lefebvre R, Lefebvre C, Nguyen-Dang TT (2008) *Phys Rev A* 77:043413
8. Gilary I, Moiseyev N (2012) *J Phys B: At Mol Opt Phys* 45:051002
9. Jaouadi A, Desouter-Lecomte M, Lefebvre R, Atabek O (2013) *J Phys B: At Mol Opt Phys* 46:470387
10. Nenciu G, Rasche G (1992) *J Phys* 25:5741
11. Dridi G, Guérin S, Jauslin HR, Viennot D, Jolicard G (2010) *Phys Rev A* 71:022109
12. Uzdin R, Mailybaev A, Moiseyev N (2011) *J Phys A: Math Theor* 44:435303
13. Berry MV, Uzdin R (2011) *J Phys A: Math Theor* 44:435302
14. Cederbaum LS (2008) *J Chem Phys* 128:124101
15. Abedi A, Maitra NJ, Gross EKU (2012) *J Chem Phys* 137:22A530
16. Atabek O, Lefebvre R, Nguyen-Dang TT (2003) In: Le Bris C (ed) *Handbook of Numerical Analysis*, Vol X. Elsevier, New York
17. Bunkin FV, Tugov II (1973) *Phys Rev A* 8:601
18. Chrysos M, Atabek O, Lefebvre R (1993) *Phys Rev A* 48:3845
19. Fox L, Goodwin ET (1953) *Trans R Soc* 245:501
20. Moiseyev N (1998) *Phys Rep* 302:212
21. Châteauneuf F, Nguyen-Dang TT, Oueillet N, Atabek O (1998) *J Phys Chem* 108:3974
22. Moiseyev N (2011) *Non-Hermitian Quantum Mechanics*. Cambridge University Press, Cambridge
23. Moiseyev N, Lein M (2003) *J Phys Chem A* 107:7181
24. Keck E, Korsch HJ, Mossmann S (2003) *J Phys A: Math Theor* 36:2125 (2003)

Photoionization Spectra and Ionization Potentials of Energetic Molecules

Itamar Borges Jr. and Elmar Uhl

Abstract We examine theoretically photoionization processes of molecules component of explosives having at least one explosophore group NO_2 . We review previous results obtained for the nitramide, N,N -dimethylnitramine and 1,1-diamino-2,2-dinitroethylene (FOX-7 or DADNE) molecules and present new results for the two conformers of nitromethane. A systematization of the results is given. The calculations employed the Symmetry-Adapted-Cluster Configuration Interaction (SAC-CI) ab initio wave function and the monopole approximation to compute photoionization cross sections. Assignments of the ionization bands are provided. The overall agreement between computed spectra, ionization potentials and experiment is very good. We show that the SAC-CI ionization potentials are far superior when compared with Koopmans theorem values and much closer to experimental values.

Keywords Photoionization · Ionization Potential · Energetic materials · Koopman's theorem · Excited states · ab initio wave function · SAC-CI

1 Introduction

Propellants and explosives composed of nitro compounds are an important class of energetic materials. They have numerous applications and their decomposition processes are especially important because occur at relatively low temperatures and are involved in the detonation of explosives [14, 19]. The considerable experimental difficulties related to examining the complex chemical processes associated with the decomposition of nitro molecules give especial relevance to theoretical investigations in this field.

I. Borges Jr. (✉) · E. Uhl

Departamento de Química e Programa de Pós-Graduação em Engenharia de Defesa,
Instituto Militar de Engenharia, Rio de Janeiro 22290-270, Brazil
e-mail: itamar@ime.eb.br

Knowledge of the electronic spectra of energetic molecules supplies an understanding of associated processes and can improve practical applications [1]. It is experimentally known that detonation initiation of energetic materials is related to electronic excitation phenomena [1, 4, 18, 27, 36, 44, 45]. Moreover, the component molecules have diffuse electronic spectra and propensity to dissociate and rearrange [22].

In the detonation initiation of these materials, different photochemical processes play important roles [5–7, 20, 21, 34, 41]. Furthermore, because nitro compounds strongly absorb in the UV region, detailed knowledge of the molecular electronic excited states can also assist the design of detectors of explosives, an important issue in these days [37].

Despite the importance of excited states in energetic materials research, only few studies are available [4].

The especial properties of explosive materials result from a combination of electron—donating and electron—acceptor groups. Nitro explosives are characterized by having NO_2 as the electron acceptor group; different combinations of electron-donating groups determine the properties of the explosive material [2].

Energetic materials are usually thermally unstable and composed of easily broken covalent bonds such as N–N, O–C and C–N. These molecules have $\text{X}-\text{NO}_2$ bonds ($\text{X} = \text{N, C}$), typical of widely used energetic materials. The explosophore NO_2 group of these molecules, so named for giving the explosive properties of the material, is easily released.

The study of ionization processes is an important tool to investigate the electronic structure of atoms, molecules and solids [24]. Recent advances in synchrotron radiation have led to a myriad of useful spectroscopies and new measurements await interpretation. From the standpoint of theory, over the decades different theoretical methods have been developed to address the complicated problem of photoionization. However, most of these methods are limited to atoms or small molecules and in most cases electron correlation is included very approximately [29].

In spite of the challenges involved in computing absolute photoelectron cross sections, relative intensities can be simulated in the monopole approximation [28, 39]. When this approximation is combined with an ab initio wave function to accurately describe electron correlation, accurate and enlightening comparisons with experimental photoelectron spectra can be achieved. In this work, we explore the combination of the monopole approximation with the Symmetry-Adapted-Cluster (SAC) [33]—Configuration Interaction (CI) wave function [23, 30–32] of Nakatsuji to compute relative photoionization cross sections. This method can provide accurate ionization energies and relative intensities for molecules as large as the typical molecules of biological interest [15, 16].

The SAC-CI wave function belongs to the family of coupled-cluster (CC) approaches [20], being equivalent to the Equation-of-Motion-CC (EOM-CC) [38] and the CC-Linear Response Theory (CC-LRT) methods [26], but it was developed much earlier. The SAC-CI wave function provides an accurate and balanced description of excited states and good comparison with available experimental data, as we verified in previous studies [7, 9–11, 13, 38].

We previously investigated using high-level ab initio wave functions the electronic excitation spectra of nitro molecules component or precursor of representative energetic materials [7, 9–11, 38]. We also studied the photoionization spectra using the monopole approximation and the SAC-CI wave function *N,N*-dimethylnitramine, $(\text{CH}_3)_2\text{NNO}_2$ [7], nitramide, H_2NNO_2 [8] and 1,1-diamino-2,2-dinitroethylene, known as FOX-7 or DADNE [11]. In this work, in addition to discussing these works, we present new photoionization results of nitromethane.

2 Methods

We converged the geometries of the *N,N*-dimethylnitramine, nitramide, H_2NNO_2 and 1,1-diamino-2,2-dinitroethylene molecules with density functional theory (DFT) using the B3LYP exchange-correlation functional and respectively the following Gaussian basis sets: the 6-31+G(d,p) and the aug-cc-pVTZ for the latter two molecules. The two conformers of nitromethane were converged with the MP2/6-311 G(3df,3pd) method. Frequency calculations confirmed the minimum character in each case.

The SAC [33] and the SAC-CI [30–32] wave functions were used respectively for the ground and excited state calculations of the four molecules. The SAC-CI wave function is based on a cluster expansion of a CI calculation carried out over selected configurations. For this wave function, all singly excited configurations are included without selection, the most important doubly excited configurations are treated through linked operators while triply and quadruple excited configurations are generated by products of previous single and double excitations—the so called unlinked operators. The doubly excited configuration operators for the ground and excited states are selected according to perturbation threshold coefficients. This method is called SAC-CI SD (single double) R.

For the calculation of the SAC (ground state) and the SAC-CI (excited states) wave functions all orbitals were correlated in the four systems. Therefore, the active space comprised sets of occupied and virtual orbitals for each molecule. All singly and selected doubly excited orbitals configurations were included in the wave function. The perturbation selection scheme used to select the important doubly excited configurations, known as level three scheme, involves two energy thresholds: 1.0×10^{-6} a.u. for the ground state and 1.0×10^{-7} a.u. for the excited state. The SAC wave function was used to obtain the ground state of the neutral molecule. We used the Gaussian 03 program for the geometry optimizations and the SAC/SAC-CI calculations [17].

For the SAC-CI calculations we used the following basis sets (between parentheses): *N,N*-dimethylnitramine (6-31+G(d,p)), nitramide (D95V+(d,p)), 1,1-diamino-2,2-dinitroethylene (6-31+G*) and nitromethane (aug-cc-pVTZ).

The ionization cross sections were computed according to the monopole approximation [28, 39] which employs the dipole approximation, a plane wave function for describing the removed electron, the SAC wave function for the ground

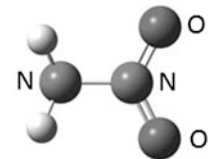
(initial)—neutral—state and the SAC-CI wave function for the final—ionized—state. This approach allows the calculation of the relative intensity of the peaks and includes both initial- and final-state correlation effects.

In this work, we compared the calculated ionization potentials with the values obtained from the Koopmans theorem. This theorem states that for an N -electron Hartree-Fock (HF) single-determinant wave function the ionization potential (I.P.) to ionize an electron from a certain orbital equals minus the HF energy of this orbital [12]. The reported Koopman's values correspond to these values.

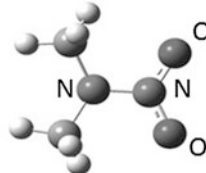
In Fig. 1 we present the optimized structures of three molecules previously studied. In Fig. 2 we display the geometries of the two converged conformers of nitromethane obtained in this work.

The reported nitromethane spectrum is a convolution of the computed discrete SAC-CI/Monopole Approximation results for both conformers. We employed the same weights for both spectra because the electronic barrier between them is very small (see below). For this purpose, we used two Gaussian distribution functions with two different full width at half maximum (FWHM) values for different regions of the spectrum. We did not shift the energies of the calculated spectra.

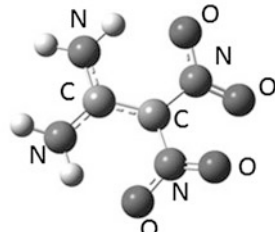
Fig. 1 Converged geometries of previously studied molecules



Nitramide, NH_2NO

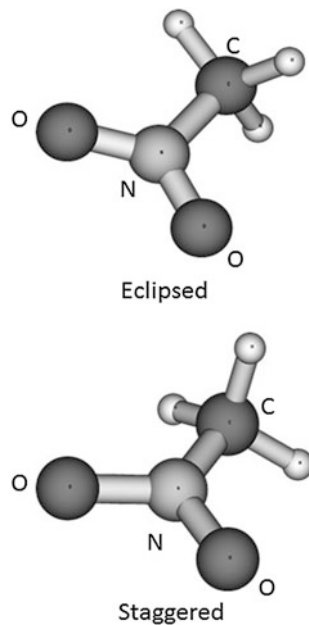


$\text{N,N dimethylnitramide, } (\text{CH}_3)_2\text{NNO}_2$



1,1-diamino-2,2-dinitroethylene, FOX-7

Fig. 2 The two conformers of nitromethane converged in this work



3 Results and Discussion

3.1 Nitromethane

The converged geometries of the two conformers of nitromethane are shown at Fig. 2. The lowest energy structure is the eclipsed conformer. The computed electronic energy difference between them equals only 0.019 kcal/mol. Therefore, the two conformers are almost degenerate and for this reason were given equal weights in the construction of the convoluted spectra.

Both conformers have C_s symmetry and the occupied orbitals are in order of increasing energy:

$$(1a')^2 (2a')^2 (3a')^2 (4a')^2 (5a')^2 (6a')^2 (7a')^2 (8a')^2 (9a')^2 (1a'')^2 (10a')^2 (11a')^2 (2a'')^2 (12a')^2 (13a')^2 (3a'')^2$$

In Fig. 3 we show the measured photoelectron spectrum of nitromethane [35] and our SAC-Cl/Monopole Approximation results obtained according to the procedure described in the last section. The experimental spectrum displays a vibrational structure not included in our calculations. We also make comparisons with other measurements of I.P's below [25, 42].

The computed spectra of the two conformers (Fig. 3) are very similar because: (1) essentially the only geometric difference between them are the distinct orientations of the methyl group and; (2) the ionized spectra is dominated by transitions involving the atoms in the NO_2 group. The position of the computed peaks without

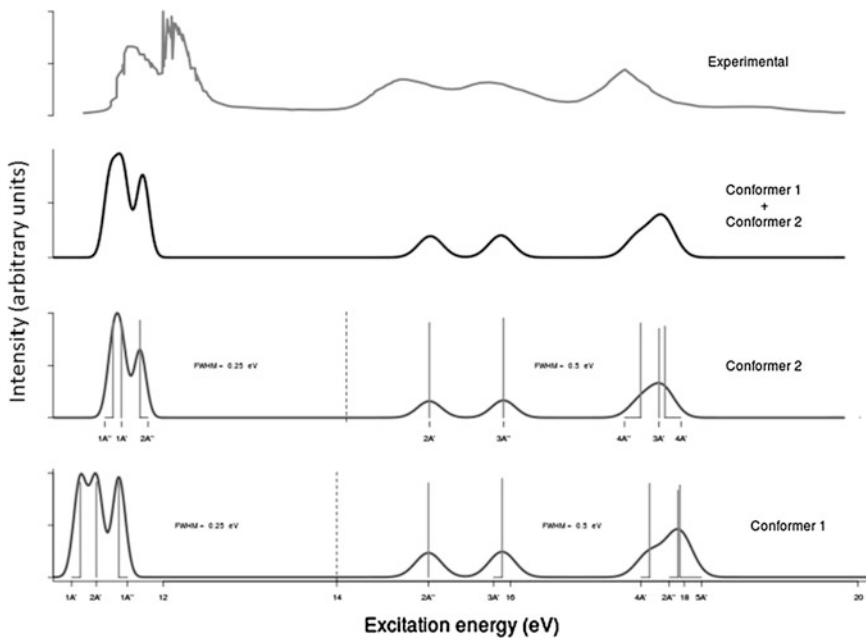


Fig. 3 The photoionization of nitromethane computed employing the SAC-CI/monopole approximation and experimental results of Rabalais [35]. The state of each computed peak is shown. The two different full width at half maximum (FWHM) values used for different regions of the computed spectra are indicated

any energy shift has a very good agreement with the measurements. Although the relative intensity of the two peaks in the measured first band inverts compared with our convoluted spectrum, the overall agreement of the computed relative intensity of the bands and the experiment spectrum is quite good.

For the eclipsed conformer, which has the smallest energy, Table 1 collects the character of the ionized states, the relative ionization intensities and three sets of I.P. values: SAC-CI/Monopole Approximation, experimental and Koopmans. The character of the ionized states of the staggered conformer is very similar to the eclipsed conformer, as can be seen from the spectra in Fig. 3, and it is not reported. Rabalais [35] reports two types of I.P.: adiabatic and vertical, and interpreted the results with the help of INDO calculations. We consider his adiabatic I.P. value to be more accurate.

The first I.P. of nitromethane is not due to ionization from the highest occupied ionization orbital (HOMO) as would be expected from Koopmans' theorem. The same happens with the two following I.P.'s and with inner ionizations. The agreement of the 1st I.P. with the experimental values is very good, the largest difference being 0.28 eV while the corresponding Koopmans' value overestimates by more than 1 eV. The agreement with the 2nd and the 4th I.P.'s is also good, but there are relevant discrepancies with experiment for the 3rd, 5th and the 6th I.P.'s.

Table 1 Ellipsed conformer of nitromethane: SAC-Cl/Monopole photoionization results including different sets of ionization potentials (I.P.) in electron-volts

State	Character of Ionized state	Intensity	I.P.	I.P. (exp)	I.P. Koopmans
1 ² A'	(n _o , 14) ⁻¹	0.91128	11.045	11.07 ^a /11.32 ^b	11.34 ± 0.09 ^d
2 ² A'	(σ _{O+CN} , 15) ⁻¹	0.91528	11.270	11.73 ^a /11.73 ^b	12.49
1 ² A''	(n _o , HOMO, 16) ⁻¹	0.93227	11.510	13.85 ^a /14.73 ^b	13.54
2 ² A''	(π _{NNO} , 13) ⁻¹	0.90531	15.070	15.75 ^b	13.59
3 ² A'	(n, 12) ⁻¹	0.94911	15.939	~16.7 ^a /17.45 ^b	16.41
4 ² A'	(π _{NNO} , 11) ⁻¹	0.90255	17.661	19.1 ^b	17.11
5 ² A'	(σ, 9) ⁻¹	0.88468	17.969		20.10
3 ² A''	(n _{NNO₂} , 10) ⁻¹	0.83490	18.039		20.11
6 ² A'	(15 → 21) (n _o , HOMO, 16) ⁻¹	0.00385	20.414		20.61
7 ² A'	(14 → 21) (n _o , HOMO, 16) ⁻¹	0.05856	20.745		23.75
8 ² A'	(σ _{NNO} , 8) ⁻¹	0.84184	20.992		
9 ² A'	(12 → 21) (n _o , HOMO, 16) ⁻¹	0.00113	23.819		
10 ² A'	(13 → 21) (n _o) ⁻¹	0.00951	24.119		
11 ² A'	(14 → 21) (π _{NNO}) ⁻¹	0.00582	24.574		
12 ² A'	(13 → 21) (σ _{O+CN}) ⁻¹	0.01442	24.799		
13 ² A'	(15 → 21) (π _{NNO}) ⁻¹	0.01090	25.605		

^a Experimental adiabatic I.P. Rabalais [35]^b Experimental vertical I.P. Rabalais [35]^c Experimental results Watanabe et al. [42]^d Experimental results Kandel [25]

This discrepancy could be due to limitations either from our calculations or from the experiment, but we cannot establish its origin.

When examining the SAC-CI character of each ionized state, there are inversions in comparison with the order of the HF molecular orbitals according to the increasing energies in the spirit of the Koopmans' theorem. These inversions were seen before in previous studies of molecules having nitro groups using the SAC-CI/Monopole Approximation [7–9, 11].

3.2 The Photoionization Spectra of the Four Molecules

In this section, we discuss the common features of calculations of photoionization spectra of the four energetic molecules (Figs. 1 and 2).

The first ionized states of the four closed-shell molecules are characterized by single configurations (i.e., one-electron processes) involving single ionization from orbitals mostly localized in the NO_2 moiety of the molecules. The role of the NO_2 group is also prominent in the electronic excitation processes of energetic molecules having this moiety, as we showed before [7–11]. In the four molecules of the present work, the character of the deeper inner-shell ionized states can be a combination of a single excitation and a single ionization—these are satellite or correlation peaks; see an illustration of that in the results of nitromethane (Table 1).

For each molecule, the computed ionization peaks typically appear in sets dominated by ionizations from orbitals having close energies. For the nitramide, *N,N*-dimethylnitramine [8] and nitromethane molecules [7], which have experimental photoionization spectra, there are sets of computed ionization peaks describing wide bands that may span some electron-volts—see Figs. 3 and 4, the latter displaying the computed and measured spectra of dimethylnitramine and nitromethane. For the four molecules we provided the assignments of the measured ionization bands. Because FOX-7 has two NO_2 moieties thus more available orbitals for ionizations, it has more sets of computed peaks [11].

We can evaluate the accuracy of our results by comparing them with the available measured spectra. Overall, when the SAC-CI/Monopole Approximation ionization energies are compared to available measured values, the agreement is very good. For the *N,N*-dimethylnitramine molecule [7], the largest difference is 0.01 eV and for nitramide [8] the worst agreement has a difference of 0.43 eV for the 7th-ionization potential, while the remaining differences are lower than 0.1 eV. For nitromethane, as discussed above, the agreement is also good. Although the 1,1-diamino-2,2-dinitroethylene molecule (FOX-7) still does not have photoelectron measurements, we expect the SAC-CI/Monopole Approximation results to be accurate because of the favorable results for the other three molecules also having an NO_2 moiety.

The comparison between the SAC-CI/Monopole Aproximation computed photoionization spectra and measured spectra can be seen at Figs. 3 (nitromethane) and 4 (nitramide and *N,N*-dimethylnitramine). The experimental peak maximum was

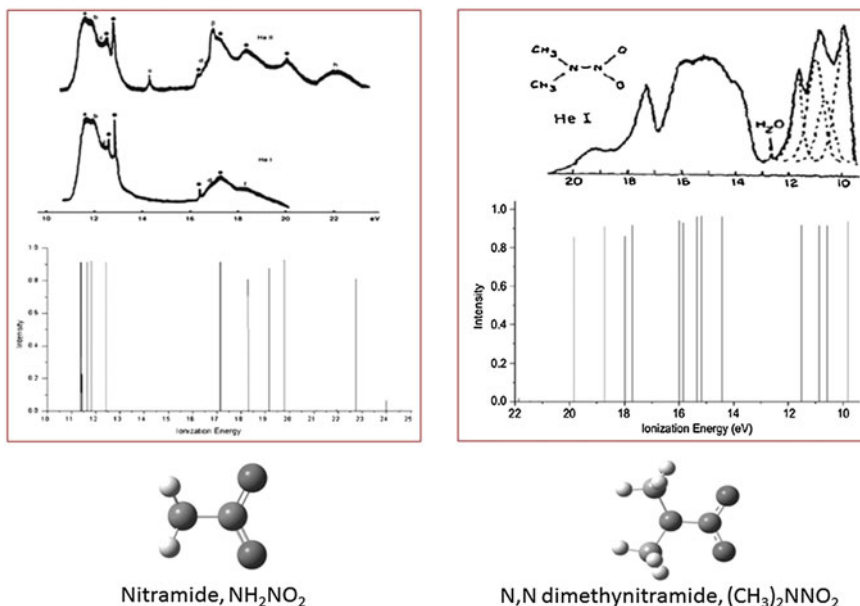


Fig. 4 The SAC-Cl/monopole photoionization spectra of nitramide and *N,N*-dimethylnitramide. Also shown are the measurements of nitramide [3] and *N,N*-dimethylnitramide [43]

taken to be equal to the computed peak maximum in all cases. The agreement between the computed relative intensities and the measured spectra is not smooth on the experimental data ranges.

Comparison of both relative intensities and ionization energies with experimental values was very favorable for the energetic molecules nitramide [8], *N,N*-dimethylnitramine [7] and nitromethane.

An additional relevant comparison is between our results and the widely used Koopmans' theorem for closed-shell molecules. The eventual success of Koopmans' theorem for computed values of the ionization potentials, especially the first I.P., compared with measured values, is due to a fortuitous cancellation of the unconsidered relaxation of the spin-orbitals and the lack of electron correlation in the single-determinant wave function [40].

The first ionization potential, as would be expected from Koopmans' theorem, is not always due to an electron removal from the highest occupied molecular orbital (HOMO). These inversions as related to Koopmans' theorem happens for *N,N*-dimethylnitramine and FOX-7 but not for nitramide and nitromethane. This feature can be understood by examining the HF energy of the highest orbitals: when they have close HF energies, inclusion of correlation through the SAC-CI wave function can change the molecular orbital expected to be ionized.

4 Conclusion

In this work, we presented SAC-CI/Monopole Approximation calculations of the photoionization spectra of four energetic molecules having at least one NO_2 group. For one of them, nitromethane, the results are new.

Nitromethane has two almost degenerate conformers. The convoluted spectra of the two conformers showed very good agreement with the measured spectrum. The 1st I.P. also agreed very well with the experiment, but the character of the state was not the result of ionizing the electron from the HOMO as would be expected from Koopmans' theorem. For other nitromethane I.P.'s, there is good agreement but also some discrepancy with experimental values.

For the four energetic molecules, we discussed the common features of the computed photoionization spectra. For the nitramide, N,N -dimethylnitramine and nitromethane molecules, the agreement with the experimental spectra is very good. Concerning the I.P.'s values of these three molecules, in general the agreement is very good with measured I.P.'s, especially with the 1st I.P., although there are some discrepancies for the higher I.P.'s of nitromethane. The comparison of our I.P.'s values and character of the ionized states shows important differences when compared with the corresponding properties according to the Koopmans' theorem. Moreover, even for the 1st I.P., the inclusion of correlation via the SAC-CI wave function can lead to a different character of this state compared with the single HOMO ionization according to Koopmans'.

To sum up, we have shown that the SAC-CI wave function combined with the Monopole Approximation can provide assignments, I.P.'s and spectral information in good agreement with experimental data. Furthermore, we could highlight in this work that the indiscriminate use of the Koopmans' both to interpret and obtain I.P.'s values can lead to severe misinterpretations.

Acknowledgments We thank Faperj, CNPq and Capes, Brazilian Agencies, for support of this work.

References

1. Ali AN, Son SF, Asay BW, Sander RK (2005) Importance of the gas phase role to the prediction of energetic material behavior: an experimental study. *J Appl Phys* 97:7
2. Anders G, Borges I (2011) Topological analysis of the molecular charge density and impact sensitivity models of energetic molecules. *J Phys Chem A* 115:9055–9068
3. Attina M, Cacace F, Ciliberto E, Depetris G, Grandinetti F, Pepi F et al (1993) Gas-phase ion chemistry of nitramide—a mass-spectrometric and ab-initio study of $\text{H}_2\text{N-NO}_2$ and the $\text{H}_2\text{N-NO}_2\text{radical+}$, $[\text{H}_2\text{N-NO}_2]\text{H}^+$, and $[\text{HN-NO}_2]^-$ ions. *J Am Chem Soc* 115:12398–12404
4. Bernstein ER (2005) Role of excited electronic states in the decomposition of energetic materials. In: Shaw RW, Brill TB, Thompson DL (eds) *Overviews of recent research on energetic materials*, vol 16. World Scientific, Singapore, p 161

5. Bhattacharya A, Bernstein ER (2011) Nonadiabatic decomposition of gas-phase RDX through conical intersections: an ONIOM-CASSCF study. *J Phys Chem A* 115:4135–4147
6. Bhattacharya A, Guo YQ, Bernstein ER (2010) Nonadiabatic reaction of energetic molecules. *Acc Chem Res* 43:1476–1485
7. Borges I (2008) Excited electronic and ionized states of *N,N*-dimethylnitramine. *Chem Phys* 349:256–262
8. Borges I (2008) Excited electronic and ionized states of the nitramide molecule, H₂NNO₂, studied by the symmetry adapted-cluster configuration method. *Theoret Chem Acc* 121:239–246
9. Borges I, Aquino AJ, Barbatti M, Lischka H (2009) The electronically excited states of RDX (hexahydro-1,3,5-trinitro-1,3,5-triazine): vertical excitations. *Int J Quantum Chem* 109:2348–2355
10. Borges I, Barbatti M, Aquino AJA, Lischka H (2012) Electronic spectra of nitroethylene. *Int J Quantum Chem* 112:1225–1232
11. Borges I Jr (2014) Electronic and ionization spectra of 1,1-diamino-2,2-dinitroethylene, FOX-7. *J Mol Model* 20:1–7
12. Cramer CJ (2004) Essentials of computational chemistry: theories and models. Wiley, Chichester
13. de Souza GGB, Rocco MLM, Boechat-Roberty HM, Lucas CA, Borges I, Hollauer E (2001) Valence electronic excitation of the SiF₄ molecule: generalized oscillator strength for the 5t (2) → 6a(1) transition and ab initio calculation. *J Phys B-Atomic Mol Opt Phys* 34:1005–1017
14. Dewar MJS, Ritchie JP, Alster J (1985) Ground-state of molecules. 65. Thermolysis of molecules containing NO₂ groups. *J Org Chem* 50:1031–1036
15. Farrokhpour H, Fathi F (2011) Theoretical study of valance photoelectron spectra of hypoxanthine, xanthine, and caffeine using direct symmetry-adapted cluster/configuration interaction methodology. *J Comput Chem* 32:2479–2491
16. Farrokhpour H, Ghandehari M (2013) Photoelectron spectra of some important biological molecules: symmetry-adapted-cluster configuration interaction study. *J Phys Chem B* 117:6027–6041
17. Frisch MJ, Trucks GW, Schlegel HB, Scuseria GE, Robb MA, Cheeseman JR et al (2003) Gaussian 03, Revision C 02, Gaussian Inc., Pittsburgh
18. Gilman JJ (1995) Chemical-reactions at detonation fronts in solids. *Philos Mag B-Phys Condens Matter Stat Mech Electron Opt Magn Prop* 71:1057–1068
19. Gindulyte A, Massa L, Huang LL, Karle J (1999) Ab initio study of unimolecular decomposition of nitroethylene. *J Phys Chem A* 103:11040–11044
20. Gonzalez L, Escudero D, Serrano-Andres L (2012) Progress and challenges in the calculation of electronic excited states. *ChemPhysChem* 13:28–51
21. Guo YQ, Greenfield M, Bhattacharya A, Bernstein ER (2007) On the excited electronic state dissociation of nitramine energetic materials and model systems. *J Chem Phys* 127:10
22. Harris LE (1973) Lower electronic states of nitrite and nitrate ion, nitromethane, nitramide, nitric-acid, and nitrate esters. *J Chem Phys* 58:5615–5626
23. Hasegawa J, Miyahara T, Nakashima H, Nakatsuji H (2012) SAC-CI methodology applied to molecular spectroscopy and photo-biology. In: Clementi E, Andre JM, McCammon JA (eds) Theory and applications in computational chemistry: the first decade of the second millennium, vol 1456. American Institute of Physics, Melville, pp 101–108
24. Hollas JM (1995) Modern spectroscopy, 2nd edn. Wiley, Chichester
25. Kandel RJ (1955) Appearance potential studies. 2. nitromethane. *J Chem Phys* 23:84–87
26. Koch H, Jorgensen P (1990) Coupled cluster response functions. *J Chem Phys* 93:3333–3344
27. Kuklja MM, Aduve BP, Aluker ED, Krasheninin VI, Krechetov AG, Mitrofanov AY (2001) Role of electronic excitations in explosive decomposition of solids. *J Appl Phys* 89:4156–4166
28. Martin RL, Shirley DA (1976) Theory of core-level photoemission correlation state spectra. *J Chem Phys* 64:3685–3689
29. Morita M, Yabushita S (2008) Calculations of photoionization cross-sections with variationally optimized complex gaussian-type basis functions. *Chem Phys* 349:126–132

30. Nakatsuji H (1979) Cluster expansion of the wavefunction—calculation of electron correlations in ground and excited-states by SAC and SAC CI theories. *Chem Phys Lett* 67:334–342
31. Nakatsuji H (1979) Cluster expansion of the wavefunction—electron correlations in ground and excited-states by SAC (symmetry-adapted-cluster) and SAC CI theories. *Chem Phys Lett* 67:329–333
32. Nakatsuji H (1978) Cluster expansion of wavefunction—excited-states. *Chem Phys Lett* 59:362–364
33. Nakatsuji H, Hirao K (1978) Cluster expansion of wavefunction—symmetry-adapted-cluster expansion, its variational determination, and extension of open-shell orbital theory. *J Chem Phys* 68:2053–2065
34. Plasser F, Barbatti M, Aquino AJA, Lischka H (2012) Electronically excited states and photodynamics: a continuing challenge. *Theor Chem Acc* 131
35. Rabalais JW (1972) Photoelectron spectroscopic investigation of electronic-structure of nitromethane and nitrobenzene. *J Chem Phys* 57:960–967
36. Sharma J, Beard BC, Chaykovsky M (1991) Correlation of impact sensitivity with electronic levels and structure of molecules. *J Phys Chem* 95:1209–1213
37. Singh S (2007) Sensors—an effective approach for the detection of explosives. *J Hazard Mater* 144:15–28
38. Stanton JF, Bartlett RJ (1993) The equation of motion coupled-cluster method—a systematic biorthogonal approach to molecular-excitation energies, transition-probabilities, and excited-state properties. *J Chem Phys* 98:7029–7039
39. Suzer S, Lee ST, Shirley DA (1976) Correlation satellites in atomic photoelectron-spectra of group-iiia and group-iiib elements. *Phys Rev A* 13:1842–1849
40. Szabo A, Ostlund NS (1996) Modern quantum chemistry: introduction to advanced electronic structure theory. Dover Publications, Mineola
41. Szalay PG, Muller T, Gidofalvi G, Lischka H, Shepard R (2012) Multiconfiguration self-consistent field and multireference configuration interaction methods and applications. *Chem Rev* 112:108–181
42. Watanabe K, Nakayama T, Mottl J (1962) Ionization potentials of some molecules. *J Quant Spectrosc Radiat Transfer* 2:369–382
43. White MG, Colton RJ, Lee TH, Rabalais JW (1975) Electronic-structure of *N,N*-dimethylnitramine and *N,N*-dimethylnitrosamine from X-ray and UV electron-spectroscopy. *Chem Phys* 8:391–398
44. Williams F (1971) Electronic states of solid explosives and their probable role in detonations. *Advances in chemical physics*. Wiley, pp 289–302
45. Windawi HM, Varma SP, Cooper CB, Williams F (1976) Analysis of lead azide thin-films by Rutherford backscattering. *J Appl Phys* 47:3418–3420

Theoretical Study of Coherent π -Electron Rotations in a Nonplanar Chiral Aromatic Molecule Induced by Ultrafast Linearly Polarized UV Pulses

H. Mineo and Y. Fujimura

Abstract We present the results of a theoretical study of π -electron dynamics in a nonplanar chiral aromatic molecule (*P*)-2,2'-biphenol. Coherent ring currents, which are one of the main observables of coherent π -electron dynamics, are generated by applying the linearly polarized UV pulse laser, where a pair of coherent quasi-degenerated excited states is created. In this paper we review the formulations of the time-dependent coherent ring currents and angular momentum which were obtained using the density matrix theory based on the LCAO MO approximation. The results of the numerical simulation of coherent π -electron ring currents and angular momentum in (*P*)-2,2'-biphenol are shown. We also propose an ultrafast quantum switching method of π -electron rotations and perform the sequential switching among four rotational patterns which are performed by the overlapped pump-dump laser pulses with properly selected laser polarizations, time delay and relative phases. Finally we refer to an outline for the extension of our method to N aromatic rings chain ($N \geq 3$).

Keywords Coherent π -electron ring current • Nonplanar chiral aromatic molecule • Two-dimensional ultrafast switching

H. Mineo (✉)

Institute of Atomic and Molecular Sciences, Academia Sinica, Taipei 10617, Taiwan
e-mail: mineo@gate.sinica.edu.tw

Y. Fujimura

Department of Applied Chemistry, Institute of Molecular Science and Center for Interdisciplinary Molecular Science, National Chiao-Tung University, Hsin-Chu 300, Taiwan

Y. Fujimura

Department of Chemistry, Graduate School of Science, Tohoku University, Sendai 980-8578, Japan

1 Introduction

Electron dynamics induced by ultrafast short laser pulses in molecular systems have been actively studied in recent years [1–8], because of its potential usefulness for realization of organic electronic devices [9, 10]. In particular, rotational dynamics of π -electron with mobile and polarizable characters in aromatic ring molecules is interesting since large magnitudes of π -electron ring currents are in principle generated by intense laser pulses. There are two types of electron ring currents depending on whether its molecule is of highly symmetric like benzene or lower symmetry like chiral aromatic molecules. The quantum simulations of π -electron ring current were performed in highly symmetric planar molecules, Mg-porphyrin [11–13], and benzene [14]. Here degenerated electronic states are excited by using circularly polarized UV laser pulses. The rotational direction of the resultant π -electron ring current depends on whether the right or left circularly polarized laser pulse is applied, and the current is unidirectional. On the other hand, linearly polarized UV laser pulses can create a “coherent” π -electron ring current in a chiral aromatic molecule. Kanno et al. carried out the π -electron rotation simulations for 2,5-dichloro[n](3,6) pyrazinophane [15–19], which is a planar chiral aromatic molecule. The rotational direction of π -electron ring current is determined by whether the superposition of quasi-degenerate states excited by linearly polarized UV laser pulse is in-phase or out-phase. The simulation results indicate that the chiral aromatic molecule is a candidate of ultrafast switching device.

Recently we have investigated coherent π -electron dynamics of a nonplanar chiral aromatic molecule (*P*)-2,2'-biphenol [20–23]. This is a nonplanar chiral aromatic molecule with axial chirality, which has two aromatic rings (called *L* and *R* hereafter) linked through a single chemical bridge bond. We have classified four possible rotational patterns of π -electron rotations [20, 21] as CC, AC, CA, and AA where C(A) represents clockwise (anticlockwise) rotational direction. Because of the nonplanar geometrical structure of (*P*)-2,2'-biphenol, the resultant π -electron ring current and angular momenta are two dimensional. This indicates that nonplanar chiral aromatic molecules like (*P*)-2,2'-biphenol may serve as a two-dimensional ultrafast switching device. For an effective quantum control of the ultrafast sequential switching among the above four rotational patters, overlapped pump and dump pulses with a properly selected relative phase and a laser polarization direction are necessary in addition to the time delay between two pulses.

In this review our attention is focused on the theoretical foundations of coherent π -electron rotations in a nonplanar chiral aromatic molecule. In Sect. 2 we derive an expression of π -electron ring current and angular momentum by solving the density matrix method under Markov approximation. In Sect. 3 we show our numerical results of π -electron ring current and angular momentum of (*P*)-2,2'-biphenol as an example. Here, we provide an efficient method for a creation of coherent two electronic excited states by using a properly selected linearly polarized UV pulse,

which is the initial step for coherent π -electron rotations. The four directional patterns of the ring currents and angular momentum on each ring L and R are presented. We also demonstrate an ultrafast two-dimensional quantum switching of π -electron ring currents and angular momentum. Finally we describe an outline of an extension of the theoretical treatment to aromatic molecules in nano-scale with covalently linked N aromatic rings ($N \geq 3$). The summary and conclusion are given in Sect. 4.

2 Coherent π -Electron Angular Momentum and Current

2.1 Equations of Motion for π -Electrons in a Pulsed Laser Field

Electric angular momentum and current operators are single electron operator. Expectation values of these operators of an aromatic molecule excited by a pump laser field are generally defined as

$$\langle \hat{O}(\vec{r}, t) \rangle = n \int d^3 r_1 \dots d^3 r_n \delta(\vec{r} - \vec{r}_1) \Psi^*(t) \hat{O}(\vec{r}_1) \Psi(t). \quad (1)$$

Here, $\hat{O}(\vec{r}_1)$ is a single-electron operator for the angular momentum or current, $\Psi(t)$ is an electronic wave function at time t , n is the number of electrons, and \vec{r}_i denotes the electron coordinates of the i -th electron. Since we are interested in optically allowed electronic excited states of conjugated aromatic molecules, we expand the electronic wave function in terms of electronic configurations within CIS calculations, the ground electronic Φ_0 and singly excited electronic ones Φ_α as

$$\Psi(t) = C_0(t) \Phi_0 + \sum_\alpha C_\alpha \Phi_\alpha, \quad (2)$$

where Φ_0 is given as a single Slater determinant $\Phi_0(\vec{r}_1, \dots, \vec{r}_n) = \|\phi_1 \dots \phi_a \dots \phi_n\|$ with $\phi_n \equiv \phi_n(\vec{r}_n)$, and Φ_α is the electronic wave function for a singly excited electronic configuration $\alpha : a \rightarrow a'$, i.e., single electron transition from occupied MO a to unoccupied MO a' , $\Phi_\alpha(\vec{r}_1, \dots, \vec{r}_n) = \|\phi_1 \dots \phi_{a'} \dots \phi_n\|$.

The electronic dynamics induced by a pulsed laser field, $\vec{F}(t)$, can be directly obtained by solving the coupled equations of motion of the electronic-state density matrix element, $\rho_{\alpha\beta}(t)$,

$$\frac{d\rho_{\alpha\beta}(t)}{dt} = -\frac{i}{\hbar} \sum_\gamma (V_{\alpha\gamma}(t) \rho_{\gamma\beta}(t) - \rho_{\alpha\gamma}(t) V_{\gamma\beta}(t)) - (i\omega_{\alpha\beta} + \gamma_{\alpha\beta}) \rho_{\alpha\beta}(t), \quad (3)$$

with the initial conditions

$$\rho_{00}(0) = 1, \quad (4a)$$

and

$$\rho_{\alpha\alpha}(0) = 0 \text{ for } \alpha \neq 0; \quad \rho_{\alpha\beta}(0) = 0 \text{ for } \alpha \neq \beta. \quad (4b)$$

Here, the density matrix element, $\rho_{\alpha\beta}(t)$, is defined as $\rho_{\alpha\beta}(t) \equiv C_\alpha(t)C_\beta^*(t)$, and $\hat{V}(t)_{\alpha\gamma}$ denotes the coupling between states α and γ through the molecule-field interaction, $\hat{V}(t) = -\vec{\mu} \cdot \vec{F}(t)$, where $\vec{\mu}$ is the transition dipole moment operator, $\omega_{\beta\alpha}$ is the angular frequency difference between two electronic states α and β . Here $\gamma_{\alpha\beta}$ is given in Markov approximation as

$$\gamma_{\alpha\beta} = \frac{1}{2}(\gamma_\alpha + \gamma_\beta) + \gamma_{\alpha\beta}^{(d)}. \quad (5)$$

$\gamma_\alpha(\gamma_\beta)$ is the nonradiative transition rate constant of state $\alpha(\beta)$, and $\gamma_{\alpha\beta}^{(d)}$ is the pure dephasing constant which is induced by the interactions between the molecular system and heat baths.

In this work, the nuclear-frozen approximation was adopted and the magnitudes of dephasing constants adopted are specified in the figure captions.

2.2 Coherent Electric Angular Momentum and Current for a Chiral Aromatic Molecule with Two Aromatic Rings

Since we are interested in coherent behaviours of nearly-degenerated π -electronic excited states in the visible or UV region of a chiral aromatic ring molecule, we evaluate Eq. (1) in terms of singly excited configurations as

$$\langle O(\vec{r}, t) \rangle = n \int d^3 r_1 \dots d^3 r_n \delta(\vec{r} - \vec{r}_1) \left(\text{Tr} \rho(t) O(\vec{r}_1) \right), \quad (6)$$

where $O_{\alpha\beta}(\vec{r}) = \langle \Phi_\alpha | \hat{O}(\vec{r}) | \Phi_\beta \rangle$. In Eq. (6), the coherence between the ground state and a singly excited state configuration is omitted because the coherence time is too short compared with that between singly excited configurations, and only the coherence between singly excited state configurations is taken into account. Here we treat coherent electric angular momentum and current within a linear combination of atomic orbitals-molecular orbitals LCAO-MO approximation.

Molecular orbital ϕ_k associated with optical transition is expanded in terms of a linear combination of atomic orbitals χ_i as

$$\phi_k = \sum_i c_{k,i} \chi_i, \quad (k = a, a', b, b'), \quad (7)$$

where i specifies the atomic orbital and $c_{k,i}$ is the molecular orbital coefficient.

Equation (6) can be rewritten in terms of Eq. (7) as

$$\langle \hat{O}(\vec{r}, t) \rangle = 2n \sum_{\alpha < \beta} \text{Im} \rho_{\beta\alpha}(t) \sum_{ij} (\delta_{ab} c_{a'i}^* c_{b'j} + \delta_{a'b'} c_{ai}^* c_{bj}) \chi_i^* i \hat{O}(\vec{r}) \chi_j. \quad (8)$$

Here, it should be noted that the time evolution of the expectation value is expressed in terms of the off-diagonal density matrix elements. Suffixes (a, a') and (b, b') depend on electronic configurations α and β , respectively.

Let us consider a space-fixed chiral aromatic molecule with two aromatic rings connected through a single bond. The total electron angular momentum operator can be expressed as the sum of the angular momentum operator of each aromatic ring, which is defined as

$$\hat{O}(\vec{r}) = \vec{l}_{zL} + \vec{l}_{zR}, \quad (9)$$

where

$$\vec{l}_{zK} = -i\hbar(x_K \partial/\partial y_K - y_K \partial/\partial x_K) \vec{n}_K, \quad (10)$$

the electric angular momentum operator of the Z-component of ring K ($=L$ or R). Here, L and R denote the ring on the left-hand side and that on the right-hand side, respectively. Coordinates x_K and y_K are defined on ring K , and \vec{n}_K is the unit vector perpendicular to the ring. The expectation value of the angular momentum operator is given, for example, in terms of a $2p_z$ carbon AOs as

$$\langle \vec{l}(t) \rangle = \int d^3 r_L \langle \vec{l}_{zL} \rangle + \int d^3 r_R \langle \vec{l}_{zR} \rangle \equiv \vec{l}_L(t) + \vec{l}_R(t). \quad (11)$$

Here

$$\begin{aligned} \vec{l}_K(t) \equiv \int d^3 r_K \langle \vec{l}_{zK} \rangle &= -2n\hbar \vec{n}_K \sum_{\alpha < \beta} \text{Im} \rho_{\beta\alpha}(t) \sum_{ij \in K} (\delta_{ab} c_{a'i}^* c_{b'j} + \delta_{a'b'} c_{ai}^* c_{bj}) \\ &\times \frac{x_{K,i} y_{K,j} - x_{K,j} y_{K,i}}{15a_2^2} \left(3 + 3 \left(\frac{r_{ij}}{a_2} \right) + \left(\frac{r_{ij}}{a_2} \right)^2 \right) \exp(-r_{ij}/a_2). \end{aligned} \quad (12)$$

In Eq. (12), a_2 is a constant related to the orbital exponent of the $2p_z$ atomic orbital and r_{ij} is the distance between i and j carbon atom sites. It should be noted in

Eq. (12) that the laser intensity dependence in the electron angular momentum is involved in the imaginary part of the off-diagonal density matrices, $\text{Im}\rho_{\beta\alpha}(t)$.

An electric current passing through a surface S at time t is generally defined as

$$\langle J(t) \rangle \equiv \int_S d^2 r_{\perp} \vec{n}_{\perp} \cdot \langle \Psi(t) | \hat{J}(\vec{r}) | \Psi(t) \rangle, \quad (13)$$

where \vec{n}_{\perp} is a unit vector perpendicular to a surface S ,

$$\hat{J}(\vec{r}) = \frac{e\hbar}{2m_e i} \left(\vec{\nabla} - \bar{\nabla} \right), \quad (14)$$

is the current density operator. Here, $\vec{\nabla}(\bar{\nabla})$ denotes the nabla operating the atomic orbital on the right-hand (left-hand) side.

This can be expressed as

$$\begin{aligned} \langle J(t) \rangle &= \frac{2ne\hbar}{m_e} \sum_{\alpha < \beta} \text{Im}\rho_{\beta\alpha}(t) \sum_{ij} (\delta_{ab} c_{a'i}^* c_{b'j} + \delta_{a'b'} c_{ai}^* c_{bj}) \int_S d^2 r_{\perp} \chi_i^* \vec{n}_{\perp} \cdot \vec{\nabla} \chi_j \\ &\equiv \sum_{ij} \langle J(t) \rangle_{ij} \end{aligned} \quad (15)$$

Here, surface integration in Eq. (13) is carried out over a half-plane S .

Since the L and R rings are not round but consist of nonequivalent C–C bonds, we introduce the bond current $\langle J(t) \rangle_{ij}$ from the nearest neighbor atoms at sites j to i , which is given in terms of inter-atomic bond current (IABC) J_{ij}^{IABC} as

$$\langle J(t) \rangle_{ij} = \frac{2ne\hbar}{m_e} \sum_{\alpha < \beta} \text{Im}\rho_{\beta\alpha}(t) (\delta_{ab} (c_{a'i}^* c_{b'j} - c_{b'i}^* c_{a'j}) + \delta_{a'b'} (c_{ai}^* c_{bj} - c_{bi}^* c_{aj})) J_{ij}^{\text{IABC}}, \quad (16)$$

where

$$J_{ij}^{\text{IABC}} = \int_S d^2 r_{\perp} \chi_i^* \vec{n}_{\perp} \cdot \vec{\nabla} \chi_j \left(\equiv J_{ij}^{\text{IABC}(S \text{ at center})} \right). \quad (17)$$

Here, surface S is set to be perpendicular to the C_i and C_j bond at the center, and $\vec{n}_{\perp} = \frac{\vec{r}_i - \vec{r}_j}{|\vec{r}_i - \vec{r}_j|}$.

Equation (17) is given in the $2p$ carbon AO basis set, $\{\chi_i\}$, as

$$J_{ij}^{IABC(S \text{ at center})} = \frac{\cos \theta r_{ij}}{2a_2^6} \int_0^\infty dr \frac{r^3 \exp\left(-2\sqrt{r_{ij}^2/4 + r^2}/a_2\right)}{\sqrt{r_{ij}^2/4 + r^2}}. \quad (18)$$

Here, $\theta = \pi$ for the bond current of the chemical bond belonging to one of the two aromatic rings, L or R , while $\theta = \theta_d$ for the bridge bond current of bond C_i-C_j with a dihedral angle between the two rings θ_d . $C_i(C_j)$ refers to the bridge carbon belonging to the $R(L)$ ring.

An effective ring current $\langle J(t) \rangle_K$ is now defined along ring $K = L$ or R , by taking the average over all of the bond currents on ring K as

$$\langle J(t) \rangle_K \approx \frac{1}{N_K} \sum_{(ij) \subset K}^{N_K} \langle J(t) \rangle_{ij}, \quad (19)$$

where $N_K = 6$ for benzene ring, is the number of bonds of ring K .

3 Results and Discussion

3.1 Geometry and Excited States of (*P*)-2,2'-Biphenol

Consider a (*P*)-2,2'-biphenol, which is a simple, and a real nonplanar chiral aromatic molecule with two covalently bonded aromatic rings. The ground state geometry of (*P*)-2,2'-biphenol was optimized by using the DFT B3LYP level of theory in the GAUSSIAN09 program. The energy levels of the electronic excited states were calculated at the optimized ground state geometry by the TDDFT B3LYP level of theory. The 6-31G+(d,p) basis sets were used in our calculations. The dihedral angle between the two phenyl groups is found to be 108.8° from our DFT calculations. For generation of coherent angular momentum and ring current of (*P*)-2,2'-biphenol, we focus on the three optically allowed excited states (a , b_1 and b_2) as shown in Fig. 1. The electronic excited energies at the a , b_1 and b_2 states, which were calculated at the optimized ground state geometry using the TD-DFT B3LYP level of theory are 6.67, 6.78, and 6.84 eV, respectively. The transition dipole moment from the ground state to excited state a (A), $\vec{\mu}_{ga} (= (0, 0, -0.77))$ [a.u.], is parallel to the Z-axis, and the others, $\vec{\mu}_{gb1} (= (0.08, 1.93, 0))$ and $\vec{\mu}_{gb2} (= (1.24, -0.34, 0))$ [a.u.], are nearly orthogonal to each other in the XY -plane as shown in Fig. 1.

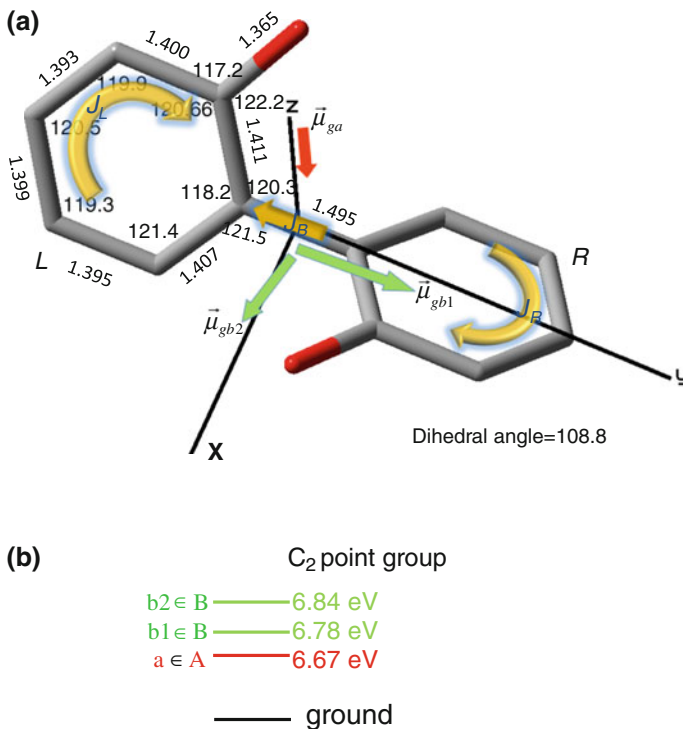


Fig. 1 **a** Geometrical structure of (P)-2,2'-biphenol with transition dipole moments between the ground state and three electronic excited states a , b_1 and b_2 , and **b** energy levels of excited state. The unit of bond lengths is in angstrom ($=10^{-10}$ m). Directions of ring currents (J_L , J_R) on L and R rings, and a bridge bond current J_B are defined for numerical simulations shown in Fig. 3

3.2 Creation of Coherent Two Electronic Excited States by the Linearly Polarized UV Laser Pulses

Coherent two electronic excited states $(a \pm b_1)$, $(a \pm b_2)$ and $(b_1 \pm b_2)$ are generated by applying a UV laser pulse with a properly selected polarization direction. Here $(\alpha + \beta)$, $(\alpha - \beta)$ represents a phase between two electronic excited states is in-phase (out-phase). For example, for $(a \pm b_2)$ electronic coherence, the condition for a linearly polarized UV laser pulse with polarization vector $\vec{e}_{ab2}^{(\pm)}$ is given as

$$\vec{\mu}_{ga} \cdot \vec{e}_{ab2}^{(\pm)} = \pm \vec{\mu}_{gb2} \cdot \vec{e}_{ab2}^{(\pm)} \text{ and } \vec{\mu}_{gb1} \cdot \vec{e}_{ab2}^{(\pm)} = 0, \quad (20a)$$

or equivalently,

$$\vec{e}_{ab2}^{(\pm)} = \vec{\mu}_{gb1} \times (\vec{\mu}_{gb2} \mp \vec{\mu}_{ga}) / |\vec{\mu}_{gb1} \times (\vec{\mu}_{gb2} \mp \vec{\mu}_{ga})|. \quad (20b)$$

Thus, even laser pulse overlaps with an a, b_1 and $b_2, (a + b_2)$ or $(a - b_2)$ electronic coherent state can be selectively generated.

3.3 Four Initial Directional Patterns of Ring Currents and Angular Momentum

The initial directional patterns of ring currents on each ring L and R are schematically depicted in Fig. 2a. Here the selective electronic excited states with in- or out-phase are initially prepared by the UV laser pulse with the polarization direction $\vec{e}_{ab1}^{(\pm)}$, $\vec{e}_{ab2}^{(\pm)}$ and $\vec{e}_{b1b2}^{(\pm)}$. From Fig. 2a it is observed that in the cases (i) and (ii) in which a superposition of same irreducible representations: $(b_1 \pm b_2)$, ring currents on each ring L and R oscillate in the same direction, whereas the bridge bond current is permanently zero. Whereas in other cases ring currents on each ring L and R oscillate in the opposite direction, as a characteristic feature a bond current between two rings L and R is generated.

Figure 2b shows the resultant angular momentum $\vec{l} = \vec{l}_L + \vec{l}_R$ corresponding to each initial directional pattern of ring currents respectively. The π -electron angular momentum \vec{l}_L (\vec{l}_R) is perpendicular to the L (R) phenol ring, and in the cases (i) and (ii), i.e., in which a superposition of $(b_1 \pm b_2)$, the resultant total angular momentum (denoted as l_Z) is parallel to the Z axis, whereas in other cases in which a superposition of different irreducible representations: $(a \pm b_1)$ or $(a \pm b_2)$, the resultant total angular momentum (denoted as l_X) is parallel to the X axis, in the XZ plane.

3.4 Time Evolution of Coherent Ring Currents

Figure 3 shows the time evolution of the ring currents J_L, J_R , which are averaged over the bond currents at the L and R rings, and the bridge bond current J_B for three types of electronic coherence with in-phase, $(a + b_1)$, $(a + b_2)$ and $(b_1 + b_2)$. We remark that positive amplitudes of currents mean rotation or oscillation toward the directions as indicated in Fig. 1. The pulse amplitude $F = 2.5$ GV/m and $F = 4.5$ GV/m are used for $(a + b_1)$ and $(a + b_2)$ respectively. That of $F = 1.2$ GV/m is used for $(b_1 + b_2)$. Here the dephasing constant $\gamma_{\alpha\beta} = 0$ is used, the results of ring currents with non-zero dephasing constants are shown in our previous papers [21]. For coherent excitations $(a + b_1)$ and $(a + b_2)$ as shown in Fig. 3a, b, J_L and J_R oscillate with opposite phase. The characteristic feature is that non-zero bridge bond currents J_B appear and oscillate with same phases with J_L . For $(b_1 + b_2)$ electronic coherence as is shown in Fig. 3c, J_L

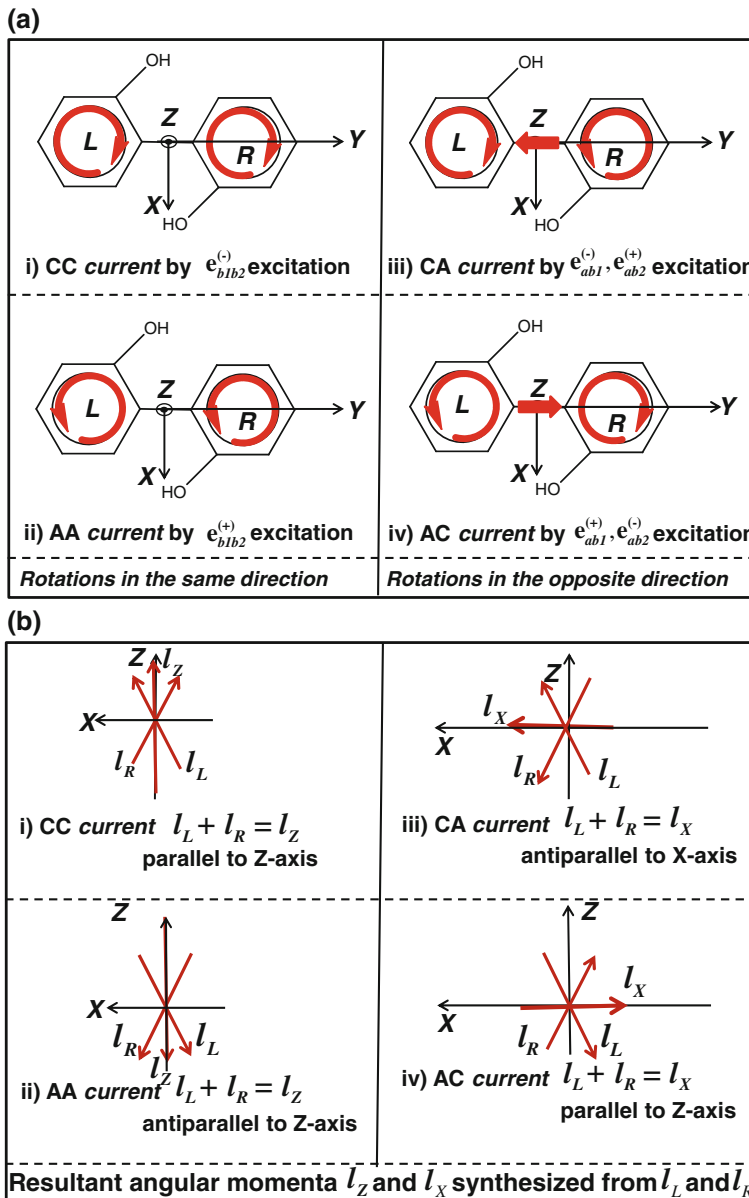
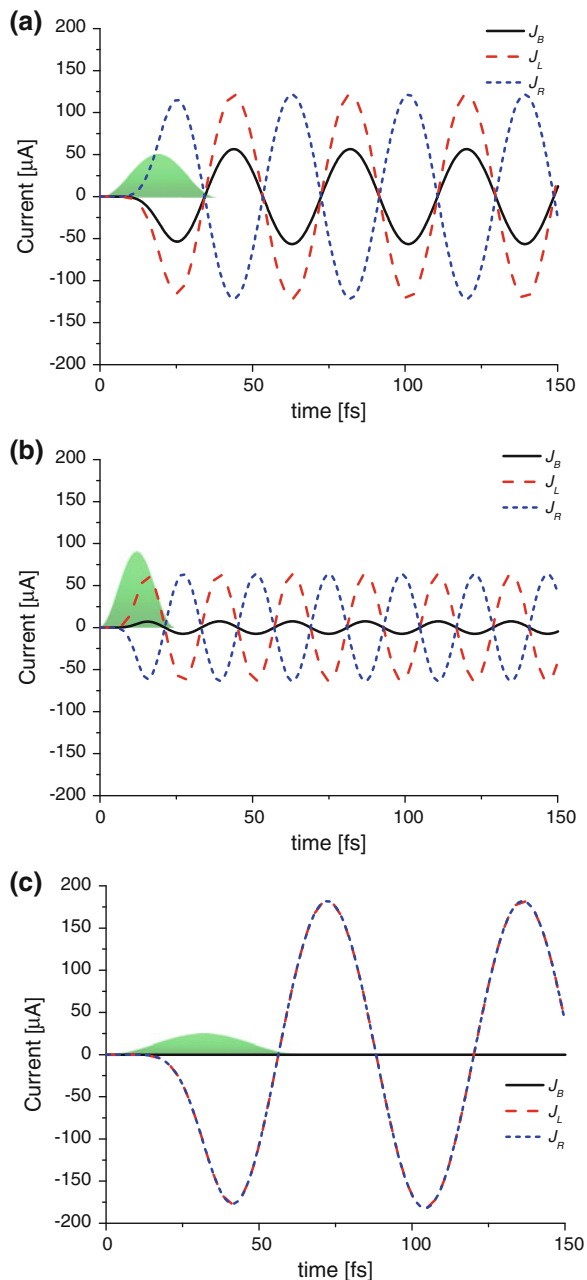


Fig. 2 **a** The initial directional patterns of ring currents on each ring L and R induced by selective coherent electronic excited states $(a \pm b_1)$, $(a \pm b_2)$ and $(b_1 \pm b_2)$. For example, CA current means directions of ring currents on L and R are clockwise and anticlockwise respectively. **b** Resultant angular momentum l_x and l_z corresponding to each pattern of ring currents are plotted respectively. l_L (l_R) denotes the angular momentum created on the L (R) ring

Fig. 3 Time dependence of ring currents and bridge bond currents created by π pulse laser excitation with a laser pulse shape (shaded area): **a** for coherent excited states $(a + b_1)$ created by a laser pulse with a magnitude $F = 2.5$ GV/m, **b** for coherent excited states $(a + b_2)$ created by a laser pulse with a magnitude $F = 4.5$ GV/m, **c** for coherent excited states $(b_1 + b_2)$ created by a laser pulse with a magnitude $F = 1.2$ GV/m. Laser pulse envelopes are also drawn in plots of ring currents by green shaded areas in arbitrary units



and J_R oscillate with same phase whereas J_B vanishes. The time-dependence of ring current quantum beat originates from the creation of two electronic states, the oscillation period corresponds to a frequency difference of two electronic states. Similarly

for out-of phase electronic coherence ($a - b_1$), ($a - b_2$) and ($b_1 - b_2$) each current can be expressed by that corresponding in-phase coherent currents with π -phase shift.

3.5 Time Dependent Angular Momentum for Three Types of Electron Coherence

Figure 4 shows the results of a numerical calculation of time-dependent angular momentum for three types of electronic coherence with in-phase, ($a + b_1$), ($a + b_2$) and ($b_1 + b_2$). The same laser pulses in Fig. 3 are adopted for Fig. 4. For ($a + b_1$) and ($a + b_2$) electronic coherences, the generated angular momenta are along X-axis with π -phase shift, while for ($b_1 + b_2$) electronic coherence the angular momentum is generated along Z-axis. Directions of total angular momentum can be understood from Fig. 2b.

3.6 Design of Ultrafast Multi-dimensional Quantum Switching

As a more developed application of our method to a design of ultrafast multi-dimensional quantum switching, we proposed a quantum sequential switching of angular momentum along X and Z-axis [20]. Figure 5 (which is cited from Fig. 3 of Ref. [20]) shows a three-dimensional plot of the resultant angular momentum switching based on the sequential four-step scheme. It can be seen from Fig. 5a that the angular momenta were successfully controlled by the pulses depicted in Fig. 5b, i.e., both the rotational axis (parallel to the Z or X axis) and the rotational direction around the axis (clockwise or anticlockwise) were satisfactorily controlled by the sequential four-step process. In Fig. 5b, the quantum control at each switching step was carried out by using overlapped pump and dump pulses with specific polarization directions. A pulsed laser with amplitude of $F = 1.2$ GV/m was used in the second and fourth steps, while $F = 0.3$ GV/m was used in the first and third steps. The pulses shown in Fig. 5b have two features: first, the pump (dump) pulse for each step has $\vec{e}_{\alpha\beta}^{(+)}(\vec{e}_{\alpha\beta}^{(-)})$ or $\vec{e}_{\alpha\beta}^{(-)}(\vec{e}_{\alpha\beta}^{(+)})$ polarization. Second, the pump and dump pulses partially overlap. For the first step (i.e., creation of CC rotation), for example, the electric field of the pump pulse was $\vec{E}_{b1b2}^{(+)}(t) = \vec{e}_{b1b2}^{(+)}E_{b1b2}^0 \sin^2(\pi t/T_{b1b2}) \sin(\omega_{c,b1b2}t)$, while that of the dump pulse was $\vec{E}_{b1b2}^{(-)}(t) = \vec{e}_{b1b2}^{(-)}E_{b1b2}^0 \sin^2(\pi(t - t_{b1b2}^{pd})/T_{b1b2}) \sin(\omega_{c,b1b2}t + \pi/2)$, where E_{b1b2}^0 is the amplitude of the pulse, T_{b1b2} (here equal to 60.9 fs) is the oscillation period between the two excited states b_1 and b_2 , $\omega_{c,b1b2}$ is the central frequency between the two excited states, and t_{b1b2}^{pd} is the time interval between the pump and dump pulses, which was set to $T_{b1b2}/2$.

Fig. 4 Time dependence of coherent angular momentum created by π pulse laser excitation, **a** for coherent excited states $(a + b_1)$, **b** for coherent excited states $(a + b_2)$ and **c** for coherent excited states $(b_1 + b_2)$. The same laser pulses as those in Fig. 3 are used respectively

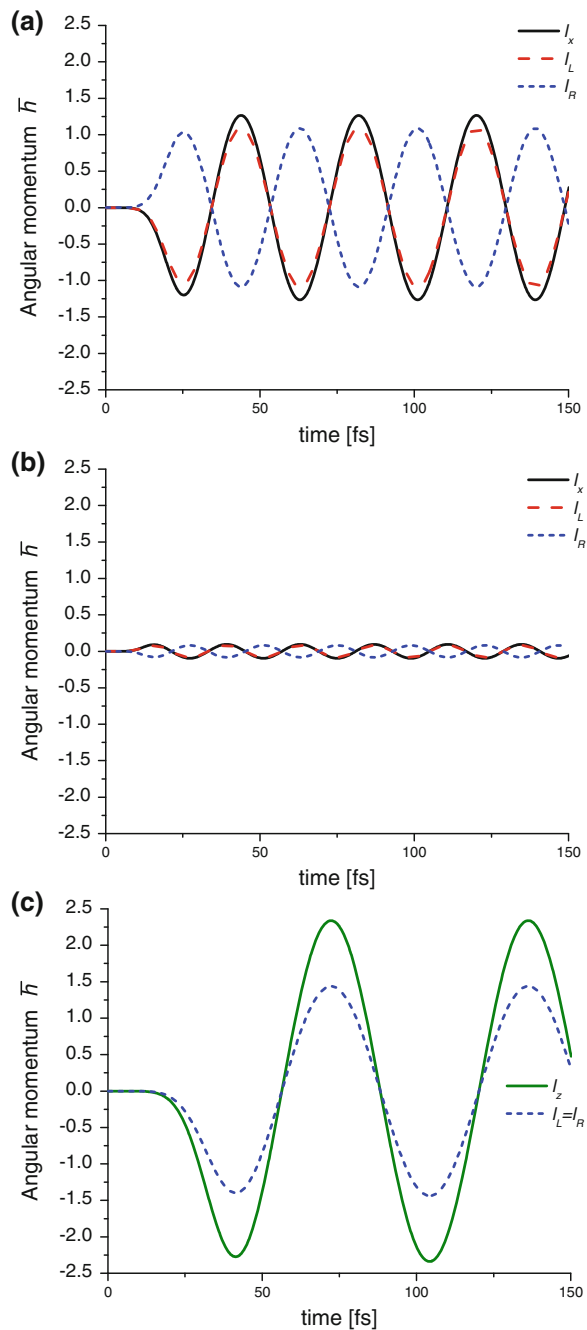
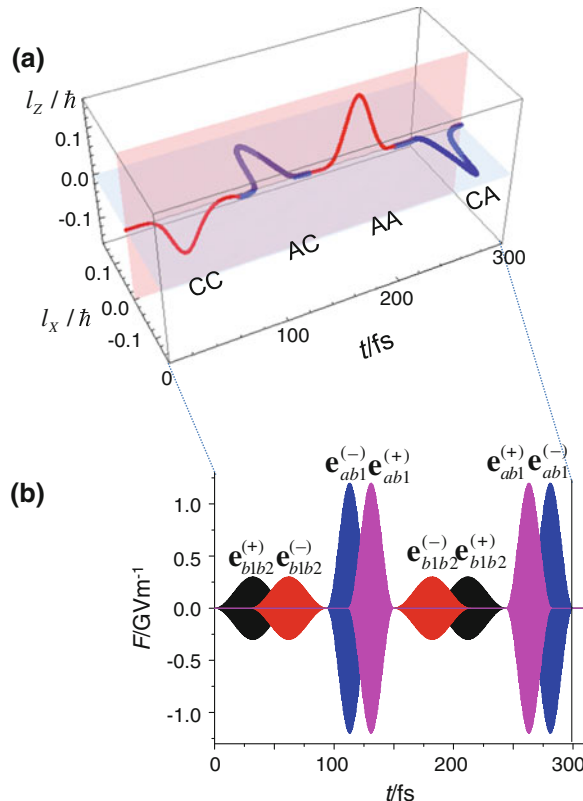


Fig. 5 **a** Sequential four-step switching of π -electron rotations in (*P*)-2,2'-biphenol. **b** Electric fields of the sequence of overlapped pump and dump pulses



For the present effective ultrafast quantum switching, overlap between the pump and dump pulses is essential: the resultant electric field is rotated as an elliptically polarized one in the overlapped region, and the electric field forces the rotating π electrons to induce the reverse rotation that occurs in this overlapped region. As a result, the electronic angular momentum or coherence between two electronic quasi-degenerate states is erased.

3.7 Coherent π -Electron Rotations in Aromatic Chain Molecules

For a more general application of our method, we are interested in a covalently linked large molecular chain consisting of n -aromatic rings. Here we briefly introduce our approach to a covalently linked aromatic ring molecule with point group C_2 . Here for simplicity, phenol and benzene are taken as aromatic ring molecules. We also note that this approach is *not* necessarily restricted to a planar chiral aromatic molecule, but can be directly applied to nonplanar one. In Fig. 6 we

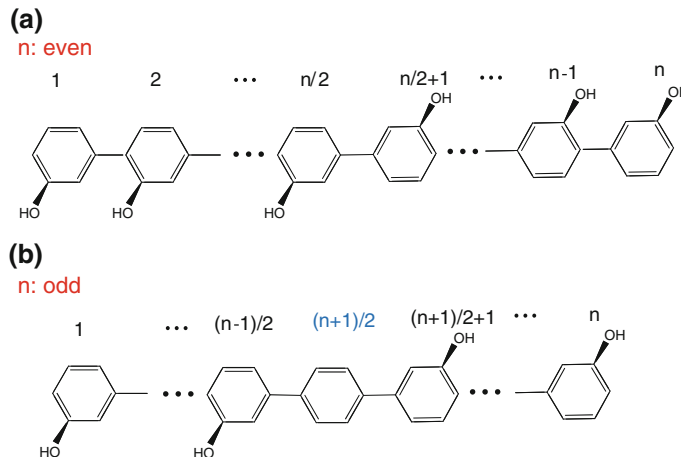


Fig. 6 n -aromatic ring molecules with point group C_2 are depicted in two cases: **a** $n =$ even, n -phenyl, and **b** $n =$ odd, $(n - 1)$ -phenyl benzene. In both cases the numbering of aromatic ring starts from the end of left

schematically depict two cases of n -aromatic ring molecules with point group C_2 , i.e., depending on $n =$ even or odd numbers. For $n =$ even, each aromatic ring consists of phenyl group, whereas $n =$ odd case, $(n - 1)$ aromatic rings are all phenyl groups, and one benzene is at the center of the n -aromatic molecule. Here, for convenience, we number the aromatic ring from the end of the left in a covalently linked molecular system. Here we choose the excited states of this molecular system $\alpha_1, \dots, \alpha_{n_A} (\beta_1, \dots, \beta_{n_B})$ which belong to the symmetric irreducible representation A(B). The angular momentum created on the m -th aromatic ring $\vec{l}_m(t)$ can be given by

$$\vec{l}_m(t) = 2\vec{n}_m f(m) \sum_{i,p} l_{\alpha_i \beta_p}^m \text{Imp} \rho_{\alpha_i \beta_p} + 2\vec{n}_m \left(\sum_{i < j} l_{\alpha_i \alpha_j}^m \text{Imp} \rho_{\alpha_i \alpha_j} + \sum_{p < q} l_{\beta_p \beta_q}^m \text{Imp} \rho_{\beta_p \beta_q} \right), \quad (21a)$$

with

$$f(m) = \begin{cases} +1 & \text{for } m \leq n/2 \text{ (even } n\text{),} \\ -1 & \text{for } m \geq n/2 + 1 \text{ (even } n\text{),} \\ 0 & \text{for } m = (n + 1)/2 \text{ (odd } n\text{)} \end{cases} \quad m \leq (n - 1)/2 \text{ (odd } n\text{)} \quad (21b)$$

where \vec{n}_m is perpendicular to the m -th aromatic ring, $l_{\alpha \beta}^m$ is an expectation value of angular momentum generated on the m -aromatic ring by a pair of two excited states α and β . Equation (21a) corresponds to a generalization of Eq. (12) which represents the angular momentum in two-aromatic rings molecule. We note that the

second term in Eq. (21a) representing the magnitude and direction of the angular momentum created on each ring is symmetric with respect to a rotation of 180° around the Z-axis, whereas the first term in Eq. (21a) gives asymmetric contribution of angular momentum by a rotation of 180° around the Z-axis.

By combining with the laser optimal control theory [24–26] we can selectively localize the angular momentum or ring current on a particular aromatic ring in a covalently linked molecular system, i.e., $\vec{l}_m \neq \vec{0}$, $\vec{l}_1 = \dots = \vec{l}_{m-1} = \vec{l}_{m+1} = \dots = \vec{l}_n = \vec{0}$.

Finally we remark that Eq. (21a) can also be applied to a ring current by replacing $l_{\alpha\beta}^m$ to an expectation value of ring current $J_{\alpha\beta}^m$.

4 Summary and Conclusion

In conclusion we have developed a density matrix theory for a coherent π electron angular momentum and current induced by the ultrafast linearly polarized UV pulses, and applied the theory to (*P*)-2,2'-biphenol. The expressions of coherent ring current and angular momentum are derived analytically within LCAO MO approximation. We showed time-dependent coherent ring currents and angular momentum for three types of in-phase electronic coherent excited states ($a + b_1$), ($a + b_2$) with B symmetry and ($b_1 + b_2$) with A symmetry in the point group C_2 . As a characteristic feature for electronic coherent states ($a + b_1$) and ($a + b_2$), a non-zero bridge bond current appears and oscillates between two phenol rings, while for electronic coherence ($b_1 + b_2$) the bridge bond current disappears permanently. The direction of resultant angular momentum for electronic coherences ($a + b_1$) and ($a + b_2$) is parallel to Z-axis, while for electronic coherence ($b_1 + b_2$) is parallel to X-axis. The initial directions of ring currents and angular momenta are determined from the initial phases of electronic coherences.

As an application of our study we demonstrated an ultrafast two-dimensional switching of π -electron angular momentum in (*P*)-2,2'-biphenol using a sequence of overlapped pump-dump pulses with different phase and polarization direction. The key to multi-dimensional switching is to coherently excite π -electronic states of a nonplanar aromatic ring molecules with covalently bonded aromatic rings. Finally it would be fascinating to explore a method for directly measuring the coherent electronic dynamics of a nonplanar chiral aromatic molecule.

Acknowledgments This work was supported by the National Science Council of Taiwan (Grant No. 102-2112-M-001-003-MY3). H.M. would like to thank Professor J.-L. Kuo for his critical comments and support.

References

1. Remacle F, Levine RD (2011) *Phys Rev A* 83:013411
2. Ulusoy IS, Nest M (2011) *J Am Chem Soc* 133:20230
3. Fujimura Y, Sakai H (2011) *Electronic and nuclear dynamics in molecular systems*. World Scientific, Singapore, p 117
4. Krausz F, Ivanov M (2009) *Rev Mod Phys* 81:163
5. Nest M, Remacle F, Levine RD (2008) *New J Phys* 10:025019
6. Remacle F, Nest M, Levine RD (2007) *Phys Rev Lett* 99:183902
7. Krause P, Klamroth T, Saalfrank P (2005) *J Chem Phys* 123:074105
8. Kral P, Seideman T (2005) *J Chem Phys* 123:184702
9. Anthony JE (2006) *Chem Rev* 106:5028
10. Bonifas AD, McCreery RL (2010) *Nat Nanotechnol* 5:612
11. Barth I, Manz J (2006) *Angew Chem Int Ed* 45:2962
12. Barth I, Manz J, Shigeta Y, Yagi K (2006) *J Am Chem Soc* 128:7043
13. Barth I, Manz J (2010) *Progress in ultrafast intense laser science*, vol VI. Springer, Berlin, p 21
14. Nobusada K, Yabana K (2007) *Phys Rev A* 75:032518
15. Kanno M, Kono H, Fujimura Y (2006) *Angew Chem Int Ed* 45:7995
16. Kanno M, Hoki K, Kono H, Fujimura Y (2007) *J Chem Phys* 127:204314
17. Kanno M, Kono H, Fujimura Y, Lin SH (2010) *Phys Rev Lett* 104:108302
18. Kanno M, Kono H, Fujimura Y (2011) *Progress in ultrafast intense laser science*, vol VI. Springer, Berlin, p 53
19. Kanno M, Ono Y, Hirohiko K, Fujimura Y (2012) *J Phys Chem A* 116:11260
20. Mineo H, Teranishi Y, Yamaki M, Hayashi M, Lin SH, Fujimura Y (2012) *J Am Chem Soc* 134:14279
21. Mineo H, Lin SH, Fujimura Y (2013) *J Chem Phys* 138:074304
22. Mineo H, Lin SH, Fujimura Y, Xu J, Xu RX, Yan YJ (2013) *J Chem Phys* 139:214306
23. Mineo H, Lin SH, Fujimura Y (2014) *Chem Phys* 442:103
24. Zhu W, Botina J, Rabitz H (2003) *J Chem Phys* 108:1953
25. Brumer PM, Shapiro M (2003) *Principles of the quantum control of molecular processes*. Wiley, New York
26. Serban I, Werschnik J, Gross EKU (2005) *Phys Rev A* 71:053810

Full Quantum Calculations of the Diffusion Rate of Adsorbates

Thiago Firmino, Roberto Marquardt, Fabien Gatti, David Zanuttini and Wei Dong

Abstract The dynamical structure factor $S(\mathbf{q}, E)$ related to the scattering of particles on mobile adsorbates is evaluated quantum mechanically from the formula proposed by van Hove (Phys. Rev. 95: 249–262, 1954) using eigenfunctions and eigenvalues obtained with the Multiconfiguration Time Dependent Hartree method. Three different one dimensional models for the CO/Cu(100) system and a three dimensional model for H/Pd(111) are investigated. Results are discussed in connection with recent ${}^3\text{He}$ spin echo experiments reported in the literature.

Keywords Quantum diffusion · High dimensional quantum dynamics · Heterogeneous catalysis

1 Introduction

The motion of hydrogen atoms adsorbed on metal surfaces has been explored with picosecond time resolution in ${}^3\text{He}$ spin-echo experiments for H/Pt(111) [1] and H/Ru(0001) [2]. The primary quantity determined in these experiments is the intermediate scattering function (ISF) $I(\mathbf{q}, t)$, where \mathbf{q} is the wave vector related to the momentum transferred from the scattered ${}^3\text{He}$ atoms to the hydrogen atoms moving on the surface, and t is the time.

T. Firmino · R. Marquardt (✉)

Laboratoire de Chimie Quantique, Institut de Chimie UMR 7177 CNRS/UdS,
Université de Strasbourg, 1 rue Blaise Pascal, BP 296/R8, 67008 Strasbourg Cedex, France
e-mail: roberto.marquardt@unistra.fr

F. Gatti · D. Zanuttini

CTMM, Institut Charles Gerhardt UMR 5253, CNRS/Université de Montpellier,
34095 Montpellier Cedex 05, France

W. Dong

Laboratoire de Chimie UMR 5182 CNRS/Ecole Normale Supérieure de Lyon,
46 Allée d'Italie, 69364 Lyon Cedex 07, France

In a previous work, Alexandrowicz et al. [3] reported on quasi-elastic broadening measurements from ^3He -spin-echo experiments on CO/Cu(100). They observe a quasi-elastic broadening that varies from 0 to about 1 μeV as a function of the momentum transferred to CO molecules along either the $\langle 100 \rangle$ or the $\langle 100 \rangle$ direction.

The observed quasi-elastic energy broadening can in principle be related to the width Γ of the dynamical structure factor (DSF) $S(\mathbf{q}, E)$, which is the temporal Fourier transform of the ISF. The ISF is the spatial Fourier transform of the pair correlation function proposed by van Hove [4], who also derived a general expression for the DSF in terms of the eigenvalues and eigenfunctions pertaining to the stationary vibrational states of the adsorbates. This expression was never evaluated, to our knowledge, from within a fully quantum mechanical treatment of the adsorbate's dynamics. In the present work, we perform such an evaluation using eigenvalues and eigenfunctions derived from global potential energy surfaces (PES) for the H/Pd(111) [5] and CO/Cu(100) [6] systems. The problem is treated in full dimensionality for the hydrogen/palladium system with static metal atoms. The carbon monoxide quantum dynamics will be treated in one dimension, only, in the present work. More extended, full dimensional quantum wave packet studies of the dynamics are in preparation for both systems and will be published elsewhere.

A key parameter in the present work is the intrinsic energy broadening Γ_i related to the lifetime $\tau_i \propto 1/\Gamma_i$ of vibrational eigenstates. This finite lifetime can be related to the coupling of the vibrational motion of the adsorbates with either the motion of the substrate atoms (phonons), or to the motion of electrons beyond the Born-Oppenheimer approximation (electron-hole pair formation), or to both. Depopulation of vibrational eigenstates of adsorbates on metal substrates via formation of electron-hole pairs is expected to proceed on the picosecond time scale [7, 8], or even faster [9], which would be much faster than the relaxation due to the coupling to phonons [10]. Note that the picosecond time scale is about the time scale that can be reached with the ^3He spin-echo technique. However, a lifetime $\tau = 1 \text{ ps}$ corresponds to an energy broadening of 1.3 meV, which is about two to three orders of magnitude larger than the broadening typically observed in the aforementioned ^3He spin-echo experiments. We shall see that it is possible to accommodate the different time domains by setting

$$\Gamma = \Gamma_i + \Gamma_d \quad (1)$$

where Γ is the overall width (full width at half maximum, FWHM) of the DSF; Γ_i is the aforementioned intrinsic broadening and Γ_d can be interpreted as the portion of the broadening that is caused by diffusion.

2 Theory and Methods

2.1 Dynamical Structure Factor

The quasi-elastic broadening can be calculated as the width of the dynamical structure factor (DSF) $S(\mathbf{q}, E)$ at $E = 0$ —see, for instance Fig. 9 and the corresponding text in [11]. An expression for this quantity was proposed by van Hove in 1954, i.e. Equation (4) in [4]:

$$S(\mathbf{q}, E) = \sum_n P_n \sum_m |\langle m | e^{i\mathbf{q}\mathbf{x}} | n \rangle|^2 \delta(E - (E_m - E_n)) \quad (2)$$

In this equation, $|n\rangle$ and $|m\rangle$ are eigenstates of the scattering center at energies E_n and E_m ; P_n is the Boltzmann population distribution; \mathbf{x} is the position vector of the adsorbed particle. If x is its projection on the direction of the momentum transfer, i.e. parallel to the substrate, $\mathbf{q}\mathbf{x} = qx$. In the original equation, matrix elements of a sum over many particles of individual exponential operators (with particle position vectors \mathbf{x}_j) are used. In the present work, we shall restrict the study to a single adsorbed particle.

We shall consider that the vibrational eigenstates are not truly stationary but have individual lifetimes $\tau_n = h/(\pi\gamma_n)$ due to the coupling with a continuous or semi-continuous set of closely lying states pertaining to the motion of other particles (electrons or phonons); h is the Planck constant and γ_n is the width (FWHM) of the energy distribution of this state in the set of the true eigenstates of the full system. Spectral lines such as those occurring in Eq. (2) involve a pair of eigenstates, and will hence have an intrinsic width (FWHM) $\Gamma_{nm} = 1/2(\gamma_n + \gamma_m)$. Consequently, we replace the δ -function in Eq. (2) by the Lorentzian distribution

$$L(E; (E_m - E_n), \Gamma_{nm}) = \frac{1}{2\pi} \frac{\Gamma_{nm}}{(E - (E_m - E_n))^2 + \Gamma_{nm}^2/4} \quad (3)$$

In the following, we assume for simplicity that all eigenstates will have the same intrinsic width $\Gamma_{nm} \equiv \Gamma_i$. This very simple model will indeed allow us to extract some interesting conclusions, while more elaborate and more realistic models, which we have considered and which will be presented elsewhere, do not alter the qualitative picture of the present results.

Instead of Eq. (2), we shall use hence the following formula to evaluate the DSF:

$$S(\mathbf{q}, E) = \sum_n P_n \sum_m |\langle m | e^{i\mathbf{q}\mathbf{x}} | n \rangle|^2 L(E; E_m - E_n, \Gamma_i) \quad (4)$$

2.2 Models

For the CO/Cu(100) system, to mimic the 0.1 monolayer coverage situation of the experiment from Ref. [3], a periodic grid of 3 Wigner-Seitz (WS) cells was used. This grid would correspond in a 2D situation to having 1 molecule in a (3×3) surface cell, i.e. a coverage of $1/9 \approx 0.1$. In each cell, it was sufficient to retain 24 eigenvalues for the temperature of 190 K, as this choice yields converged calculations.

To evaluate Eq. (4), we test the following 1D models for the diffusion motion along the $\langle 100 \rangle$ direction, i.e. the x coordinate of the carbon atom position parallel to the substrate, which links two top sites via a bridge site.

Model 1 The potential $V(x)$ is given by the formula

$$V(x) = V_2 \sin(\pi x/L)^2 \quad (5)$$

where $V_2 = 100 \text{ hc cm}^{-1} \approx 12.4 \text{ meV}$ is the diffusion barrier of this model and $L = 255.6 \text{ pm}$ was defined above as the bulk Cu-Cu nearest neighbor distance.

Model 2 The potential $V(x)$ is given by the formula

$$V(x) = \sum_{k=4,6,8} V_k \sin(\pi x/L)^k \quad (6)$$

where $V_4 \approx 656$, $V_6 \approx -1,203$, and $V_8 \approx 1,003 \text{ hc cm}^{-1}$. This form fits excellently the relaxed potential over the bridge site from [6, Fig. 8b therein]. The barrier height from [6] is 465 hc cm^{-1} , whereas Eq. (6) yields $456 \text{ hc cm}^{-1} \approx 56.5 \text{ meV}$.

Model 3 The potential $V(x)$ is given by the same formula as in Eq. (6), but with parameter values $V_4 \approx 381$, $V_6 \approx -698$, and $V_8 \approx 582 \text{ hc cm}^{-1}$. This form describes the first “adiabatic channel” for the diffusion, in which the variation of the zero point energy was included approximately from the variation of the harmonic zero point energies between the top and bridge sites as calculated in [6]. The barrier for this potential is $270 \text{ hc cm}^{-1} \approx 33.5 \text{ meV}$.

Figure 1 shows plots of the model potentials.

For the H/Pd(111) system, the analytical potential energy surface derived originally in [5] for the H₂/Pd(111) system was first modified such as to describe a single hydrogen atom adsorbed on the palladium substrate. To achieve this, all hydrogen-hydrogen two-body terms, as well as the hydrogen-palladium-hydrogen three-body terms in the PES defined in [5] were zeroed, and the function definition

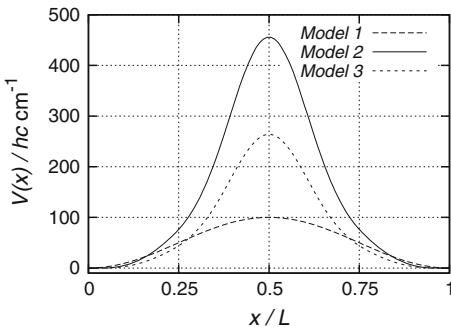


Fig. 1 Comparison of the three model potentials used to investigate the diffusion dynamics of the CO molecule adsorbed on Cu(100). $L = 255.6$ pm is the bulk Cu-Cu distance [16]

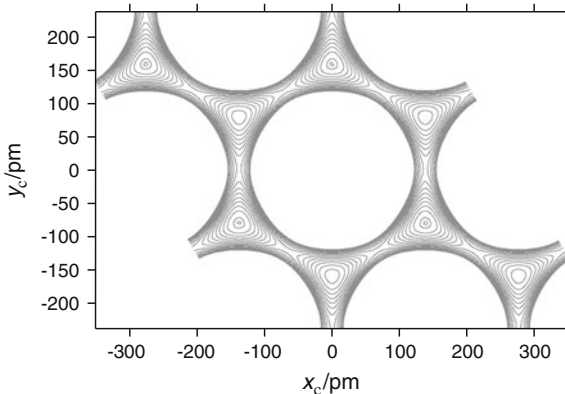


Fig. 2 Section of the PES at a distance $z = 90$ pm of the hydrogen atom from the substrate. x_c and y_c are the Cartesian coordinates. Contour lines of the PES are separated by 200 hc cm^{-1} , the smallest value indicated at the fcc sites is 50 hc cm^{-1}

was changed such as to depend on the coordinates of a single hydrogen atom. The PES is then represented in a (2×2) surface cell. Figure 2 shows a two dimensional section of the resulting PES.

2.3 Quantum Dynamics

We use the Multiconfiguration Time Dependent Hartree (MCTDH) program suite [12] to calculate vibrational eigenstates of the adsorbed particles. For the calculations on the one dimensional models for the CO/Cu(100) system, the MCTDH version 85.2 with “exact” diagonalization using the short iterative Lanczos (SIL)

integrator and eigenfunctions are calculated individually with the mode eigenfunction selector (*meignf*) in the initial wave function section.

For the H/Pd(111) system, the analytical model potential was used to generate a natural potential representation [13, 14] with the aid of the “potfit” program contained in the MCTDH program package. Eigenfunctions were then calculated within the MCTDH program with the aid of the “block relaxation method” [15] (here, the version 84.8 of the MCTDH code was used).

The matrix elements of the e^{iqx} operator are calculated for several values of q with the *crosscorr* utility program contained in the MCTDH program package. Matrix elements obtained in this way were tested analytically for the particle in the box problem (i.e. when $V_2 \approx 0$ with the *Model 1* potential used to describe the CO/Cu(100) system, see above). Because the potential energy surface commutes with the parity operator, $|\langle m | e^{iqx} | n \rangle| = |\langle n | e^{iqx} | m \rangle|$, hence only the upper half of this matrix needs to be computed.

Calculations for the CO/Cu(100) system were carried out on a grid ranging from -383.4 to 383.4 pm for the coordinate of the carbon atom that links two nearest Cu atoms (the Cu-Cu distance is fixed to its bulk value 255.6 pm [16]). This corresponds to including 3 Wigner-Seitz surface cells in the grid. A FFT discrete variable representation (DVR) was used with a basis set of 72 functions. The equations of motion were solved with the “short iterative Lanczos” (SIL/ALL) integrator, a maximal order of 20, an accuracy parameter of 10^{-8} and parameters $\text{eps_inv} = \text{eps_no} = 10^{-8}$ (see also [12] and [17] for the definition of the acronyms and the related parameters). For this system, the CO mass of 27.9949 Da was used.

The H/Pd(111) system is represented in a periodic (2×2) grid in skewed x and y coordinates to describe the position of the hydrogen atom on the hexagonal structured surface (see Fig. 3); a third coordinate (z) describes its distance from the surface. These coordinates are given in terms of Cartesian coordinates x_c and y_c by the linear transformation $x = x_c + y_c/\sqrt{3}$, $y = 2y_c/\sqrt{3}$. Note that, because of the

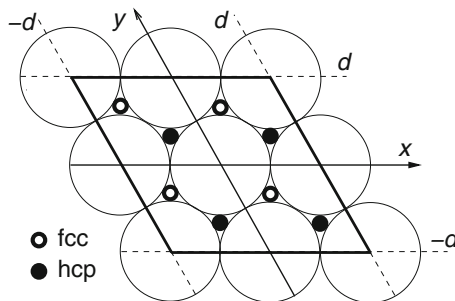


Fig. 3 Scheme of the surface (2×2) grid used to characterize the H/Pd(111) system. x and y are the skewed coordinates used in the dynamics. Palladium atoms are indicated by the *large spheres* of diameter d ($d = 275.114$ pm is the Pd-Pd bulk distance on the PES from [5]). Stable adsorption sites are indicated by the *small open* and *closed spheres* (fcc and hcp sites)

non-orthogonality of the coordinates, expressions for scalar products are more involved. In particular the kinetic energy operator becomes

$$\hat{T} = -\frac{2h^2}{12\pi^2m} \left(\frac{\partial^2}{\partial x^2} + \frac{\partial^2}{\partial y^2} + \frac{\partial^2}{\partial x\partial y} \right) - \frac{h^2}{8\pi^2m} \left(\frac{\partial^2}{\partial z^2} \right) \quad (7)$$

where h is the Planck constant and $m = 1.007825$ Da is the mass of the hydrogen atom used in this work. We shall evaluate Eq. (4) for a momentum transfer along the surface vector linking two nearest Pd neighbors (which corresponds to the $\langle 11\bar{2}0 \rangle$ crystallographic direction in hexagonal closed packed cells). In this direction the scalar product is $qx = qx_c = q(x - y/2)$. Details related to the calculations for the H/Pd(111) system will be reported elsewhere.

3 Results

3.1 CO/Cu(100) System

3.1.1 Eigenvalues

Table 1 reproduces the eigenvalues obtained with the different models. All eigenvalues can be collected in *bands*, which are levels of nearly degenerate states. The following is to be noted:

1. The lowest eigenvalues are (almost) 3-fold degenerate, which means that there are 3 (almost) uncoupled states per energy which can hence be localized in each of the 3 potential wells of the grid considered here. The bandwidth related to these states is (almost) zero.
2. Degeneracy starts to be lifted quite readily for *Model 1*, due to the coupling between the wells, at the level with about 27 hc cm^{-1} . The width of the corresponding band becomes $8 \times 10^{-5} \text{ hc cm}^{-1} \approx 0.01 \mu\text{eV}$. The next largest degeneracy lift is for the level at 44.5 hc cm^{-1} : $4 \times 10^{-4} \text{ hc cm}^{-1} \approx 0.05 \mu\text{eV}$. The next degeneracy lift occurs at the level at 60.4 hc cm^{-1} : $8 \times 10^{-3} \text{ hc cm}^{-1} \approx 1 \mu\text{eV}$.
3. For model *Model 2*, a similar first degeneracy lift occurs at the level at $196.98 \text{ hc cm}^{-1}$, and for *Model 3* at the level at 74.13 hc cm^{-1} . For all models, this degeneracy lift, which is potentially the first to be related to a broadening of the dynamical structure factor $S(\mathbf{q}, E)$ beyond any intrinsic broadening Γ_i , occurs at levels located well below the diffusion barrier.
4. For *Model 1*, levels at or above the barrier (100 hc cm^{-1}) turn rapidly into the level structure of a periodic potential, with two degenerate states per level. For *Model 2* and *Model 3*, this feature is somewhat quenched.

Table 1 Eigenvalues in units of $hc\text{ cm}^{-1}$ for the three models of the CO/Cu(100) system studied in this work

	Model 1	Model 2	Model 3
1	9.3044927	7.4514339	6.0324626
2	9.3044927	7.4514339	6.0324626
3	9.3044927	7.4514339	6.0324626
4	27.420351	25.614879	20.573429
5	27.420351	25.614879	20.573429
6	27.420431	25.614879	20.573429
7	44.499464	47.398140	37.739086
8	44.499867	47.398140	37.739086
9	44.499867	47.398140	37.739086
10	60.417300	69.890443	55.460539
11	60.417300	69.890443	55.460539
12	60.424881	69.890443	55.460539
13	74.926166	93.159297	74.132113
14	75.020613	93.159297	74.132193
15	75.020613	93.159297	74.132193
16	87.586489	117.41747	93.926894
17	87.586489	117.41747	93.926894
18	88.361427	117.41747	93.927056
19	96.662485	142.82966	114.80141
20	99.297740	142.82966	114.80246
21	99.297740	142.82966	114.80246
22	106.48987	169.38522	136.56717
23	106.48987	169.38522	136.56717
24	113.72861	169.38522	136.57257
25	114.53251	196.98068	158.98108
26	123.22184	196.98076	159.00624
27	123.22184	196.98076	159.00624
28	133.38709	225.46084	181.78842
29	133.38709	225.46084	181.78842
30	144.53068	225.46141	181.89650
31	144.54085	254.66626	204.44147
32	156.61231	254.66803	204.85862
33	156.61231	254.66803	204.85862
34	169.58364	284.45941	226.70818
35	169.58364	284.45941	226.70818
36	183.42814	284.46764	228.19893
37	183.42822	314.29362	246.01999
38	198.13123	314.32725	249.85903
39	198.13123	314.32725	249.85903
40	213.68224	345.02875	266.05981
41	213.68224	345.02875	266.05981

(continued)

Table 1 (continued)

	Model 1	Model 2	Model 3
42	230.07328	345.16844	275.49714
43	230.07328	373.79604	281.47492
44	247.29846	374.28796	293.65333
45	247.29846	374.28796	293.65333
46	265.35319	403.40401	310.08147
47	265.35319	403.40401	310.08147
48	284.23382	405.13367	327.40344
49	284.23414	428.73482	327.78373
50	303.93802	433.30339	346.24293
51	303.93802	433.30339	346.24293
52	324.46290	453.03469	365.92940
53	324.46290	453.03469	365.92940
54	345.79723	463.54273	386.39144
55	345.81659	475.71283	386.71188
56	367.96554	486.30708	408.10268
57	367.96554	486.30708	408.10268
58	390.93936	507.84265	430.55441
59	390.93936	507.84265	430.55441
60	414.35573	520.92375	453.53298
61	415.10534	547.97656	454.22428
62	439.06178	551.62404	475.43053
63	439.06178	551.62404	475.43053
64	464.45155	611.16308	502.61997
65	464.45155	611.16308	502.61997
66	485.48649	617.38323	519.97896
67	498.09826	690.80436	554.78839
68	512.91717	691.55147	558.18552
69	512.91717	691.55147	558.18552
70	565.97796	845.59458	678.50078
71	565.97796	845.59458	678.50078
72	587.36513	853.39888	689.65857

3.1.2 Dynamical Structure Factors

To evaluate the dynamical structure factor from Eq. (4), we shall consider two values for the intrinsic broadening Γ_i . First, we take a value for this quantity that is smaller than the experimental widths reported in Fig. 1 in [3], which gives an upper limit $\Gamma_i \approx 0.125 \text{ } \mu\text{eV}$. The second value used is on the order of $100 \text{ } \mu\text{eV}$, hence about 10^3 times larger than the first value. The second value is closer to values obtained from realistic estimations of non-adiabatic couplings, i.e. $0.1\text{--}1 \text{ meV}$ [7–9].

Fig. 4 $S(q, E)/S(q, 0)$ as a function of E (the energy transfer at scattering), for several values of q (the transferred momentum modulo \hbar), *Model 1* (the inset is a magnified version). $\Gamma_i = 0.125 \mu\text{eV}$ is assumed

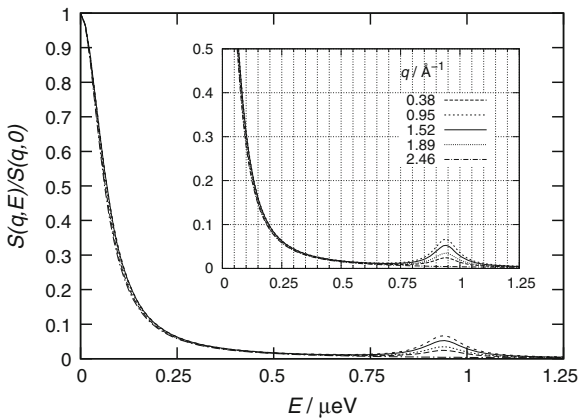
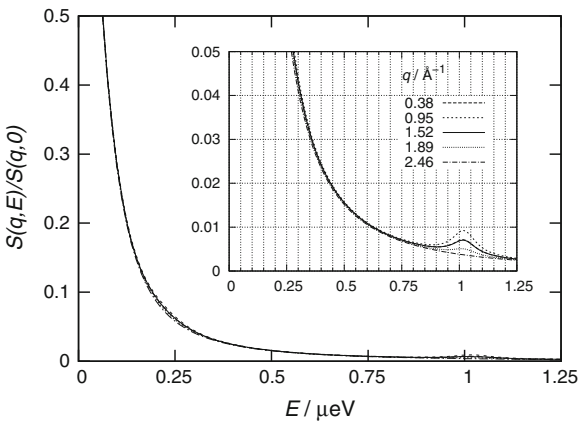


Fig. 5 As Fig. 4 but for *Model 2*

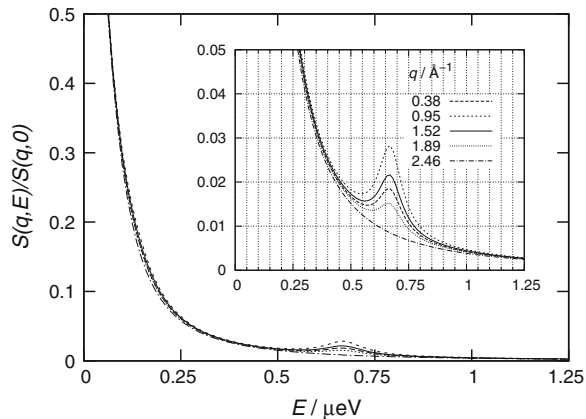


Calculations with $\Gamma_i = 0.125 \mu\text{eV}$. The evaluation of the DSF using the eigenfunctions discussed above and an intrinsic width $\Gamma_i = 0.125 \mu\text{eV}$ yields the functions depicted in Figs. 4, 5 and 6.

We note:

1. The graphs for all values of q shown here decrease nearly as Lorentzians in the region between 0 and about $0.5 \mu\text{eV}$. They all cross the 0.5 line at about $0.06 \mu\text{eV}$. The quasi-elastic broadening corresponds hence to the intrinsic width Γ_i , nearly for all values of q . For *Model 1*, there seems to be a slightly enhanced variation of the broadening as a function of q , but this variation is insignificant, when compared to the experimental result shown in Fig. 1 of [3].
2. The first peak at non-zero energy transfer occurs at about $1 \mu\text{eV}$ for all three models. This peak is related, in all three models, to the occurrence of the first significant degeneracy lift of eigenvalues reported in the previous section; the term “significant” means a degeneracy lift larger than the intrinsic width Γ_i used for the calculations. The intensity of the peak is the lowest for *Model 2*, which

Fig. 6 As Fig. 4 but for *Model 3*



can be related to the higher barrier of this model and the higher energies of the states involved in the peak (see Table 1). These states consequently have a lower Boltzmann weight than the corresponding states of *Model 3*, which in their turn have a lower Boltzmann weight than the corresponding states of *Model 1*. This explains the intensity variation of the peaks as a function of the model.

3. For all three models, the values of the first non-zero energy transfer peak vary strongly as a function of q . This variation is coherent with the observed variation of the quasi-elastic broadening in Fig. 1 of [3] (with $\Delta K = q$) and minima at $q = 0$ and $q \approx 2.5 \text{ \AA}^{-1}$ and a maximum at about $q \approx 1 \text{ \AA}^{-1}$.

Calculations with $\Gamma_i = 100 \mu\text{eV}$. Here, we report results for *Model 3*, only. Figure 7 shows the form of $S(q, E)$. The half width (HWHM) is determined by the solution of $S(q, E) = 0.5 S(q, 0)$. The full width (FWHM) is twice this value. Apparently, this variation is very feeble. When magnified one sees, however, a neat progression of values (inset in Fig. 7a). Linking these values by a smooth cubic spline interpolation results in what is shown in Fig. 7b—here, the differential width $\Delta\Gamma = \Gamma - \Gamma_i$ is plotted, for convenience. The function shown in this graph is in quite a remarkable qualitative agreement with the experimentally determined function depicted in Fig. 1 in [3].

3.1.3 Discussion

When we assume that the intrinsic broadening is smaller than the observed quasi-elastic broadening related to the diffusion of the adsorbates ($\Gamma_i \sim 0.1 \mu\text{eV}$), the overall quasi-elastic broadening Γ does apparently not depend on q . A nearly constant value of the quasi-elastic broadening cannot be related to the diffusion motion, as it would occur also for very high potential barriers. This model cannot be used to simulate the experimentally observed behavior, and one could argue that this weakness might be due to the reduced dimensionality and that one has to

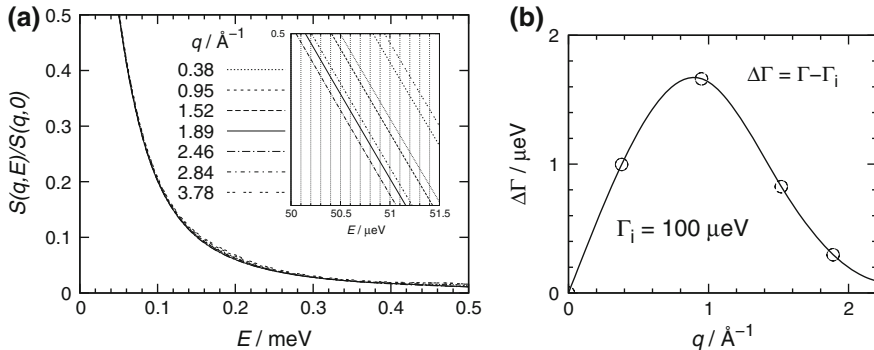


Fig. 7 $S(q, E)/S(q, 0)$ as a function of E and q (a), for *Model 3*, but with an intrinsic broadening $\Gamma_i = 100 \mu\text{eV}$. The *inset* is a magnification of the function in the region of $S(q, E) = 0.5 S(q, 0)$, which can be used to determine graphically the widths, for each individual value of q . b shows the full width at half maximum, relative to Γ_i , obtained as twice the values of the solutions of $S(q, E) = 0.5 S(q, 0)$. Results are for $T = 190 \text{ K}$

extend the study to the full 6D treatment of the adsorbate's dynamics. Such studies are currently being carried out and will be presented elsewhere.

When we assume that the intrinsic broadening is 0.1 meV, i.e. about 100 times larger than the observed diffusion broadening, we obtain the result that the broadening difference $\Delta\Gamma = \Gamma - \Gamma_i$ reproduces the experimental results qualitatively well. Furthermore, the value adopted for Γ_i is in the expected range of values.

The following hypothesis can then be obviously deduced: the overall broadening of the DSF must be composed of an intrinsic part, Γ_i , which is independent of the motion of the adsorbates, and a diffusion part, which we call Γ_d and which is q -dependent. The constant broadening is due to the “friction” of the adsorbates.

From the results obtained at low Γ_i , we saw the occurrence of a non-elastic peak at 1 μeV. Normally, this feature is interpreted as arising from the vibration of the adsorbates, at a very low wave number (0.008 cm^{-1}), in this case. Here, we understand this peak as arising from the first significant bandwidth in Table 1, which is a consequence of tunneling, rather than a vibrational motion. Other features do occur at even smaller wave numbers, if an even smaller value for Γ_i is chosen in the calculation—we refrain here from showing the plot. These features are related to the smallest calculated bandwidths larger than zero; to within the numerical accuracy of the present results, these bandwidths are 0.00008 and 0.00016 cm^{-1} , for *Model 3* in Table 1, and belong to the bands at 74.13 and 93.93 cm^{-1} , respectively.

The variation of the intensity of these peaks as a function of the momentum transfer correlates with the variation of the diffusion broadening in Fig. 7b. It is then obvious to deduce that all the “fine grained” features, that would be observed at very small intrinsic widths, are buried under the quasi-elastic peak, the width of which is dominated by the large intrinsic width. Their presence is nevertheless manifested by the variation of the broadening difference, $\Delta\Gamma$, with the momentum transfer.

Within the hypothesis that $\Delta\Gamma = \Gamma_d$ is the diffusion related broadening, its variation on top of the much larger, and constant “friction” related broadening must be explained by the occurrence of the very first degeneracy lifts of eigenstates far below the barrier for diffusion. These splittings are due to the tunneling motion of the adsorbates, and hence, the variation of the diffusion broadening with q cannot really be simulated by classical mechanics.

Note that the full 6D treatment should be closest to *Model 3* from the present study. We could henceforth conclude that the expected effective barrier for the diffusion of CO on Cu(100) should be about 30 meV, which is indeed the value estimated by Toennies and Graham [18].

The hypothesis presented in this section can be rationalized both within a kinetic model and from a statistical theory of the quantum dynamics, the details of which is the object of separate works.

3.2 H/Pd(111) System

While the extension of the aforementioned study on the CO/Cu(100) system to 6 dimensions is in progress, we can report here on the full 3 dimensional study of the H/Pd(111) system and check, whether the aforementioned hypothesis is correct. The section of the potential energy surface for this system is represented in Fig. 2. One clearly sees the stable adsorption sites, “fcc” and “hcp”, which are also indicated in the scheme of Fig. 3. On this PES, the hcp site is about 190 hc cm^{-1} less stable than the fcc site and the barrier between the two sites is at about $1,150 \text{ hc cm}^{-1}$ above the fcc site.

There are 4 fcc and 4 hcp sites per unit cell. The hcp/fcc occupation ratio is about 0.37 at room temperature, and we can therefore assume that the occupation of sites is approximately homogeneous, which makes the present study mimic a coverage degree of 12.5 %.

Figure 8 shows the form of $S(q, E)$ for this system, when $\Gamma_i = 1 \text{ meV}$ is assumed. As for the CO/Cu(100) system, the variation of the width is very feeble on the scale of the intrinsic broadening, but nicely structured when magnified. Figure 9 shows this variation in terms of the corresponding diffusion rate, defined here as $\alpha = \pi\Delta\Gamma/h \approx 0.7596 \text{ ps}^{-1} \times \Delta\Gamma/\text{meV}$, where $\Delta\Gamma = \Gamma - \Gamma_i$. There is currently no experimental result for this function. We may compare the present theoretical result, however, with experimental results for systems that should be rather similar, i.e. H/Ru(0001) [2, Fig. 1 therein], and H/Pt(111) [1]: the general behavior of the rate function shown in Fig. 9 reproduces qualitatively very well the form of the experimental functions; however, the variation range for the rate is a factor 10 smaller than that observed for H/Ru(0001), and a factor 100 smaller than what is observed for H/Pt(111). Also, the dip occurring at $q \approx 1.6 \text{ \AA}^{-1}$ cannot possibly be related to the “de Gennes” narrowing of the quasi-elastic broadening [19], which would be expected to be around 1.14 \AA^{-1} for palladium.

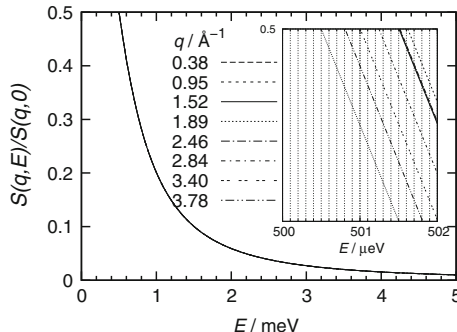


Fig. 8 $S(q, E)/S(q, 0)$ for the H/Pd(111) system, assuming an intrinsic broadening $\Gamma_i = 1$ meV. The *inset* is a magnification of the function in the region of $S(q, E) \approx 0.5 S(q, 0)$. Results are for the $\langle 11\bar{2}0 \rangle$ crystallographic direction, at $T = 250$ K

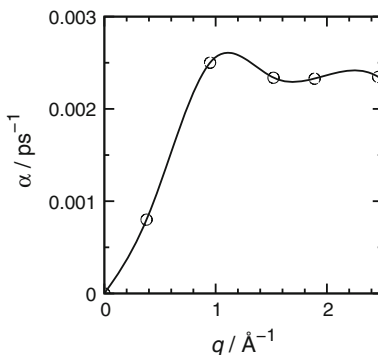


Fig. 9 Calculated diffusion rate $\alpha(q)$ for atomic hydrogen on Pd(111) along the $\langle 11\bar{2}0 \rangle$ crystallographic direction, at $T = 250$ K. $\alpha = \pi \Delta \Gamma / h$ and $\Delta \Gamma$ is the differential broadening with respect to Γ_i , obtained as twice the values of the solutions of $S(q, E) = 0.5 S(q, 0)$ in Fig. 8

More detailed investigations are necessary, however, in order to make a true prediction for the diffusion rate of H/Pd(111). These studies, which include a more realistic modeling of vibrational lifetimes, are currently being carried out. It can be shown that the variation range of the diffusion rate increases, if a much larger value of the intrinsic broadening is assumed, meaning a much shorter relaxation time due to “friction”. Relaxation times shorter than those assumed here for hydrogen on ruthenium or palladium can indeed be expected from theory [20].

A second investigation route includes the study of di-hydrogen structures. It is known that hydrogen atoms, even if adsorbed at low coverage degrees, form clusters of di-hydrogen on the substrate [21]. H_2 dissociates upon adsorption on

palladium or ruthenium, the adsorbed atoms may interact with each other, however, even at distances larger than the distance between two neighboring metal atoms. Six dimensional calculations on the $H_2/Pd(111)$ system are currently being carried out and will be published elsewhere, together with a scrutinized discussion of the vibrational structure of the adsorbates.

4 Conclusions

The present studies of the diffusion motion of CO on Cu(100) have revealed two facts:

1. Realistic 1D models of the diffusion motion in combination with the theory developed by van Hove [4] allow us to rationalize the quasi-elastic broadening of the 3He spin echo experiments observed in [3]. To this end, we have to assume that the total quasi-elastic broadening is given as the sum of the diffusion broadening and the broadening due to non-adiabatic couplings, or couplings to the phonon bath—the latter being related to the “friction” rate. Furthermore, assuming reasonable values for the “friction” rate, we show that the broadening observed in the experiments is an actual broadening difference.
2. When setting the “friction” rate to much smaller values, these models allow us to correlate the observed variation of the quasi-elastic broadening as a function of the momentum transfer with the tunneling splitting of low lying vibrational levels. These splittings occur at low coverage degrees and are a genuine manifestation of a quantum effect.

Similar findings are found for the $H/Pd(111)$ system, for which the present results are so far predictions based on vague assumptions and simple models regarding the intrinsic lifetimes of vibrational states. Full 6D treatments of the diffusion dynamics of CO/Cu(100) as well as of $H_2/Pd(111)$, in which we shall also consider in a more realistic way lifetimes of vibrational states of the adsorbates will shed more light into the problem. In particular, such studies would enable us to truly simulate the experimentally determined intermediate scattering function and herewith give accurate values for the diffusion rate of adsorbates from first principle calculations.

Acknowledgments This work was carried out within a research program from the *Agence Nationale de la Recherche* (project ANR 2010 BLAN 720 1). We thank ANR for the generous financial support, as well as CNRS and Université de Strasbourg.

Note: Since the submission of this manuscript, the diffusion rate for the $H/Pd(111)$ system has been calculated from the DSF with in a realistic model and no adjustable parameters. These results have been published recently [22].

References

1. Jardine AP, Lee EYM, Ward DJ, Alexandrowicz G, Hedgeland H, Allison W, Ellis J, Pollak E (2010) Determination of the quantum contribution to the activated motion of hydrogen on a metal surface: H/Pt(111). *Phys Rev Lett* 105:136101. doi:[10.1103/PhysRevLett.105.136101](https://doi.org/10.1103/PhysRevLett.105.136101). URL: <http://link.aps.org/doi/10.1103/PhysRevLett.105.136101>
2. McIntosh EM, Wikfeldt KT, Ellis J, Michaelides A, Allison W (2013) Quantum effects in the diffusion of hydrogen on Ru(0001). *J Phys Chem Lett* 4:1565–1569. doi:[10.1021/jz400622v](https://doi.org/10.1021/jz400622v). URL: <http://pubs.acs.org/doi/abs/10.1021/jz400622v>
3. Alexandrowicz G, Jardine AP, Fouquet P, Dworski S, Allison W, Ellis J (2004) Observation of microscopic CO dynamics on Cu(001) using ^3He spin-echo spectroscopy. *Phys Rev Lett* 93:156103
4. van Hove L (1954) Correlations in space and time and born approximation scattering in systems of interacting particles. *Phys Rev* 95:249–262
5. Xiao Y, Dong W, Busnengo HF (2010) Reactive force-field for surface chemical reactions: a case study with hydrogen dissociation on Pd surfaces. *J Chem Phys* 132, 014704
6. Marquardt R, Cuvelier F, Olsen RA, Baerends EJ, Tremblay JC, Saalfrank P (2010) A new analytical potential energy surface for the adsorption system CO/Cu(100). *J Chem Phys* 132:074108
7. Frischkorn C, Wolf M (2006) Femtochemistry at metal surfaces: nonadiabatic reaction dynamics. *Chem Rev* 106:4206–4233
8. Morin M, Levino NJ, Harris AL (1992) Vibrational energy transfer of CO/Cu(100): nonadiabatic vibration/electron coupling. *J Chem Phys* 96:3950
9. Vazhappilly T, Beyvers S, Klamroth T, Luppi M, Saalfrank P (2007) vibrationally enhanced associative photodesorption of molecular hydrogen from Ru(0001). *Chem Phys* 338:299
10. Head-Gordon M, Tully JC (1992) Vibrational relaxation on metal surfaces: molecular-orbital theory and application to CO/Cu(100). *J Chem Phys* 96(5):3939–3949
11. Jardine AP, Hedgeland H, Alexandrowicz G, Allison W, Ellis J (2009) ^3He spin echo: principles and application to dynamics at surfaces. *Prog Surf Sci* 84:323–379
12. Worth GA, Beck MH, Jäckle A, Meyer HD (2007) The MCTDH package, Version 8.2, (2000). H-D Meyer, Version 8.3 (2002), Version 8.4 (2007), Revision 8 (2012). <http://mctdh.uni-hd.de/>
13. Jäckle A, Meyer HD (1996) Product representation of potential energy surfaces. *J Chem Phys* 104:7974–7984
14. Jäckle A, Meyer HD (1998) Product representation of potential energy surfaces. II. *J Chem Phys* 109:3772–3779
15. Meyer HD, Le Quéré F, Léonard C, Gatti F (2006) Calculation and selective population of vibrational levels with the multiconfiguration time-dependent Hartree (MCTDH) algorithm. *Chem Phys* 329:179–192
16. Massalski TB (ed) (1986) Binary alloy phase diagrams. ASM Internations, Ohio
17. Beck MH, Jäckle A, Worth GA, Meyer HD (2000) The multiconfiguration time-dependent Hartree (MCTDH) method: a highly efficient algorithm for propagating wavepackets. *Phys Rep* 324:1
18. Graham AP Toennies JP (1999) Determination of the lateral potential energy surface of single adsorbed atoms and molecules on single crystal surfaces using helium atom scattering. *Surf Sci* 427/428:1
19. Gennes PD (1959) Liquid dynamics and inelastic scattering of neutrons. *Physica* 25(7–12):825–839 doi:[http://dx.doi.org/10.1016/0031-8914\(59\)90006-0](https://doi.org/10.1016/0031-8914(59)90006-0). URL: <http://www.sciencedirect.com/science/article/pii/0031891459900060>
20. Tremblay JC (2013) A unifying model for non-adiabatic coupling at metallic surfaces beyond the local harmonic approximation: from vibrational relaxation to scanning tunneling microscopy. *J Chem Phys* 138(24):244106. doi:[http://dx.doi.org/10.1063/1.4811150](https://doi.org/10.1063/1.4811150). URL: <http://scitation.aip.org/content/aip/journal/jcp/138/24/10.1063/1.4811150>

21. Jewell AD, Peng G, Mattera MFG, Lewis EA, Murphy CJ, Kyriakou G, Mavrikakis M, Sykes ECH (2012) Quantum tunneling enabled self-assembly of hydrogen atoms on Cu(111). *ACS Nano* 6(11):10115–10121. doi:[10.1021/nn3038463](https://doi.org/10.1021/nn3038463). URL: <http://pubs.acs.org/doi/abs/10.1021/nn3038463>
22. Firmino T, Marquardt R, Gatti F, Dong W (2014) Diffusion Rates for Hydrogen on Pd(111) from Molecular Quantum Dynamics Calculations. *J Phys Chem Lett* 5(24):4270–4274 doi:[10.1021/jz502251w](https://doi.org/10.1021/jz502251w)

Part IV

Fundamental Theory

Relativistic Quantum Chemistry: An Advanced Approach to the Construction of the Green Function of the Dirac Equation with Complex Energy and Mean-Field Nuclear Potential

**A.V. Glushkov, A.A. Svinarenko, O.Yu. Khetselius,
V.V. Buyadzhi, T.A. Florko and A.N. Shakhman**

Abstract We present an advanced approach to construction of the electron Green's function of the Dirac equation with a non-singular central nuclear potential and complex energy. The Fermi-model and relativistic mean-field (RMF) nuclear potentials are used. The radial Green's function is represented as a combination of two fundamental solutions of the Dirac equation. The approach proposed includes a procedure of generating the relativistic electron functions with performance of the gauge invariance principle. In order to reach the gauge invariance principle performance we use earlier developed QED perturbation theory approach. In the fourth order of the QED perturbation theory (PT) there are diagrams, whose contribution into imaginary part of radiation width $\text{Im } \delta E$ for the multi-electron system accounts for multi-body correlation effects. A minimization of the functional $\text{Im } \delta E$ leads to integral-differential Dirac-Kohn-Sham-like density functional equations. Further check for the gauge principle performance is realized by means of the Ward identities. In the numerical procedure we use the effective Ivanova-Ivanov's algorithm, within which a determination of the Dirac equation fundamental solutions is reduced to solving the single system of the differential equations. This system includes the differential equations for the nuclear potential and equations for calculating the integrals of $\int dr_1 dr_2$ type in the Mohr's formula for definition of the self-energy shift to atomic levels energies. Such a approach allows to compensate a main source of the errors, connected with numerical integration $\int d\xi$ and summation on χ in the Mohr's expressions during calculating the self-energy radiative correction to the atomic levels energies. As illustration, data on the nuclear finite size effect and self-energy Lamb shift contributions to the energy of $2s-2p_{1/2}$ transition for the Li-like ions of argon, iron, krypton and uranium are presented and compared with available theoretical and experimental results.

A.V. Glushkov (✉) · A.A. Svinarenko · O.Yu. Khetselius · V.V. Buyadzhi · T.A. Florko ·

A.N. Shakhman

Odessa State Environmental University (OSENU), L'vovskaya Str, 15,
Odessa 65016, Ukraine

e-mail: glushkovav@gmail.com; dirac13@mail.ru

Keywords Relativistic quantum chemistry · Green's function method · Dirac equation with complex energy · Relativistic mean-field nuclear potential · Fermi model potential

1 Introduction

As it is well known, in quantum mechanics and quantum field theory, the probability amplitude for a quantum particle to travel from one place to another in a given time, or to travel with a certain energy and momentum is given by the propagator [1–8]. Since the propagator or Green's function of the wave equation was introduced to calculate the scattering matrix by Stückelberg and Feynman [1, 2], it has become an important tool of quantum field theory [5–7]. As usually, in the Feynman diagrams, which describe the rate of collisions in quantum field theory, virtual particles contribute their propagator to the rate of the scattering event described by the diagram. They also can be viewed as the inverse of the wave operator appropriate to the particle, and are called as Green's functions. The Green's function plays a central, very important role as in atomic and molecular physics as in the statistical physics, physics of plasma and solids physics. A development of the effective analytical and numerical algorithms for computing the electron Green's function of the Dirac equation with arbitrary central potential and complex energy is of great importance in a modern relativistic many-body theory [1–52]. One could guess that the different fundamental characteristics of the atomic and molecular systems can be expressed through the electron and photon Green's functions. Usually the energy corrections to levels and oscillation strengths in quantum theory of atoms and molecules are defined by the electron Green's function with a complex energy parameter E and integration on E is spread on the indefinite interval. In spectral representation of the electron Green's function can be represented as follows:

$$G(r_1 r_2 | E) = \sum_{n\chi m} \Psi_{n\chi m}(r_2) \Psi_{n\chi m}(r_1) / (E_{n\chi} - E) \quad (1)$$

One can separate the partial contributions with fixed value of χ (angular quantum number) (c.f. [8, 27–31]). Each partial contribution is presented by multiplying the radial $G(r_1, r_2 | E, \chi)$ the Green's function of the radial Dirac equation and angle parts. According to Refs. [50–54], as a rule, the contributions with $|\text{Im}E| \leq |10E_0|$ and $|\chi| \leq 15$ (here E_0 is the bond energy of the studied state) are important in the modern calculations of the multi-electron systems. The similar expansion for the photon Green's function (expansion over the spherical harmonics) separates the radial part—the Green's function of the Bessel equation. Usually under calculating the corresponding matrix elements an integration over all angle variables is performed analytically, and integration over the radial variables—numerically.

Very useful review has been presented [9] for the Green's function expressions of field equations. Namely, the explicit form of the Green's functions of the Klein-Gordon-Fock and Dirac equations is derived, and then the decay rate of the solution to the linear equations is estimated.

An overview of the two-time Green's function method is presented in [10]. This [10] method allows one to calculate level shifts in two-electron highly-charged ions by including in principle all QED effects, for any set of states (degenerate, quasi-degenerate or isolated) and as example, an evaluation of the contribution of the screened self-energy to a finite-sized effective Hamiltonian, that yields the energy levels through diagonalization, is presented.

It is obvious that a development of the effective numerical algorithms for calculating the electron Green's function for the Dirac equation with arbitrary potential and complex energy is of great importance for modern relativistic quantum chemistry [1–31]. Our interest to this problem is connected with running computing the self-energy corrections to atomic levels in the heavy atomic systems and multicharged ions (c.f. [23, 48–68]). Besides, we believe that the similar problem will be arisen in the quantum chemistry of the heavy and super heavy (ZX , $Z > 100$) molecules in some time [23]. In this task all master formulas are conserved, except of the symmetry of the task. It is obvious that the latter in the molecular case differ from the atomic symmetry.

From the viewpoint of the modern quantum calculations of the heavy atoms and multicharged ions it should be mentioned that calculation of the self-energy corrections to the atomic levels energies (radiation widths) have been carried out for low states of the hydrogen-like ions and nuclear charge $Z < 110$ (c.f. [32]). The nuclear finite size correction is usually implemented to the calculation scheme (for example, the relativistic Hartree-Fock or Dirac-Fock methods) by means of using several nuclear models (model of the homogeneous charged sphere, the Gauss model and the Fermi-model) [24–54]. The screening of a nucleus by atomic (molecular) electrons is usually taken into account for within the Dirac-Fock (Dirac-Kohn-Sham) approximations. By the way, studying the excited heavy and super heavy ($Z \gtrsim 173$) quantum systems with an accurate modelling the nuclear potential (in a whole, nuclear effects in quantum calculations) and accounting for the screening of a nucleus (nuclei) by electrons and radiative effects of the electron shell polarization and probably the Dirac equation non-linear terms remain by very actual problem of the modern theory of multi-electron systems. One could mention here the known difficulties of the modern calculation procedures of quantum chemistry, in particular, in calculating the radiation (self-energy) correction to levels energies of the heavy atomic and molecular systems.

In order to treat correctly a problem of calculating the self-energy correction to atomic (molecular) levels energies in the relativistic quantum chemistry it is important to have an effective algorithm of calculating the electron Green's function for the Dirac equation. As it is well known, the radial electron Green's function is presented as a combination of the fundamental solutions of the Dirac equation. One can mention the Whittaker functions as the fundamental solutions of the Dirac

equation in a case of the Coulomb potential. As it was noted in Refs. [23, 50–54], the known expansions to the Taylor expansion with numerical calculating in the separated blocks are usually used, but there are two significant disadvantages. First of all, calculating the Whittaker function in the separated block increases the dimension of the calculation procedure. Secondly, the corresponding Taylor expansion has a bad convergence for large values of ξ [that is very important for problem (1)] and contains the significant compensations of the separated terms (look more detailed explanation in Refs. [23, 50–54]).

Here we present an advanced approach to construction of the electron Green's function for the Dirac equation with a non-singular central nuclear potential and complex energy, which generalizes the known scheme [23, 50–54] by Ivanov et al. Here firstly the Fermi-model and relativistic mean-field nuclear potentials are used. Naturally we will also represent the radial Green's function as a combination of two fundamental solutions of the Dirac equation. The approach proposed has two new blocks: (i) a procedure of generating the relativistic electron functions Ψ with performance of the gauge invariance principle; (ii) the Fermi model for nuclear finite size potential.

In order to reach the gauge invariance principle performance we use the QED approach, which has been earlier developed in Refs. [53, 54]. The detailed consideration of the exchange-correlation (the screening and polarization effects, self-energy correction to mass operator etc.) diagrams is performed within the QED PT formalism and. In the fourth order of the QED PT [53, 54] there are diagrams, whose contribution into an imaginary part of the radiation width ImE for the multi-electron system accounts for multi-body correlation effects. A minimization of the functional ImE leads to integral-differential density functional Kohn-Sham-like equations. Further check for the gauge principle performance is realized by means of the Ward identities. In the numerical procedure we use the effective algorithm, which has been earlier approbated by us in many calculations of different characteristics of the atomic and molecular systems [45–68]. Within this procedure a definition of the Dirac equation fundamental solutions is reduced to solving the single system of the differential equations. This method is usually called as the method of differential equations by Ivanov-Ivanova (c.f. [45–47]). The general system in our version includes also the differential equations for the Fermi-model and relativistic mean-field nuclear potentials and equations for calculating the integrals of the $\int dr_1 dr_2$ type in formula for definition of the self-energy shift to atomic levels energies (look below).

Let us remember that following to the Mohr papers [34–36], within the covariant regularization of the Feynman S-matrix results the self-energy shift to the level energy can be written as follows (c.f. [50–56] too):

$$E = E_L + E_H(\Lambda) - \frac{1}{\tilde{\alpha} \pi Z} \left(\frac{3}{2} \ln \Lambda \tilde{\alpha}^2 + \frac{3}{8} \right) \langle \beta \rangle, \quad \Lambda \rightarrow \infty. \quad (2)$$

And the high-energy part is as follows:

$$E_H(\Lambda) = \operatorname{Re} \frac{1}{\pi Z} \int_0^\infty d\xi [E(\xi, 0) - E(\xi, \Lambda)], \quad (3)$$

$$E(\xi, \Lambda) = \iint dr_1 dr_2 \frac{1}{r_{12}} \exp \left[(E_0 - i\xi)^2 - \Lambda^2 \right]^{1/2} \psi^+(r_2) \alpha^\mu G(r_1 r_2) \alpha^\mu \psi(r_1) \quad (4)$$

where $\tilde{\alpha} = \alpha Z$ and $\Psi(r)$ is the wave function—solution of the Dirac equation. Let us note that above presented formula are written in the Coulomb units (in the Coulomb units: 1 C.u. of length = 1 a.u.Z; 1 C.u. of energy = 1 a.u. Z^2).

It is important to note that the energy parameter $E = i\xi$ in (3) is purely imaginary one and the Green's function is complex. This is a direct motivation of the task we are solving here.

As it has been earlier mentioned [16, 17, 34–47], two last terms in (4) is logarithmically diverged at $\Lambda \rightarrow \infty$. In the Mohr's paper [34–36] it has been received the important result, connected with understanding the mechanism of their compensations, and the finite expressions without divergences are received. From the other side, this procedure is not obligatorily, especially from the point of view of the numerical calculation. In fact, the numerical compensation of the diverged expressions could result in loss of an accuracy. But, as it is indicated in Refs. [45–56] this is not main source of the mistake with taking into account for the weak logarithmic divergence (it is meant that the acceptable accuracy in calculating E_H no worse than 1 %). The main source of mistakes is connected with the numerical integration $\int d\xi$ and summation on χ . Naturally, one can present the exact quantitative estimates on the basis of the concrete calculation allowing the variations of different parameters. Following to Refs. [45–59], we calculate the self-energy shift strictly on the basis of the formula (2)–(4). The Λ -dependent part of the contribution will be presented in the following form: $\Lambda E_H / (\Lambda + a)$, where the parameters E_H , a are empirically defined using two reference points: $\Lambda = 40 \cdot |E_0|$ and $\Lambda = 80 \cdot |E_0|$.

2 Dirac Equation with Complex Energy: Fundamental Solutions

The radial Dirac equations can be written as follows (in the Coulomb units):

$$\begin{aligned} f' &= -(\chi + 1)f/r - V^- g\tilde{\alpha}; \\ g' &= (\chi - 1)g/r + V^+ f\tilde{\alpha}; \end{aligned} \quad (5)$$

$$V^\mp = V(r) - i\xi \mp \tilde{\alpha}^{-2}; \quad (6)$$

where $V(r)$ is the potential of a nucleus. We are interested by a case when the potential is regular for $r \rightarrow 0$. It is easy to show (c.f. [45–47]) that for such a potential the solutions of two types (regular and non-regular at $r \rightarrow 0$) exist for each value of ξ and χ :

for $\chi < 0$

$$f \sim r^{|\chi|-1}, g \sim r, \tilde{f} \sim r^{-|\chi|}, \tilde{g} \sim r^{-|\chi|-1}, \quad (7)$$

for $\chi > 0$

$$f \sim r^{|\chi|}, g \sim r^{|\chi|-1}, \tilde{f} \sim r^{-|\chi|-1}, \tilde{g} \sim r^{-|\chi|}.$$

The regular solution (f, g) at $r \rightarrow 0$ is simply defined by the condition (6) with the accuracy to a normalization. At the same time the singular solutions are not defined by these conditions.

For large values of $|\chi|$ the functions (7) have a strong degree dependence at $r \rightarrow 0$ that is a reason of the known computational difficulties during the numerical integration of the Dirac equations. At large χ the radial functions F and G vary rapidly at the origin of co-ordinates (c.f. [45–47, 59]):

$$\begin{aligned} F(r), G(r) &\approx r^{\gamma-1} \\ \gamma &= \sqrt{\chi^2 - \alpha^2 z^2} \end{aligned} \quad (8)$$

As usually, in order to prevent the integration step becoming too small, as usually (c.f. [45–47, 59, 60]), it is convenient to introduce the new functions isolating the main power dependence:

$$\begin{aligned} (F, G) &= (f, g) \cdot r^{1-|\chi|}; \\ (\tilde{F}, \tilde{G}) &= (\tilde{f}, \tilde{g}) \cdot r^{|\chi|+1}. \end{aligned} \quad (9)$$

The Green's function is a combination of the Dirac equation modified (the power dependence is separated) fundamental solutions:

$$F' = (\chi + |\chi|)F/r + V^- \tilde{\alpha}G; \quad G' = (\chi - |\chi|)G/r + V^+ \tilde{\alpha}F; \quad (10a)$$

$$\tilde{F}' = -(\chi + |\chi|)\tilde{F}/r + V^- \tilde{\alpha}\tilde{G}; \quad \tilde{G}' = (|\chi| + \chi)\tilde{G}/r + V^+ \tilde{\alpha}\tilde{F}. \quad (10b)$$

The functions (F, G) represent the first fundamental solution, which is regular for $r \rightarrow 0$ and singular for $r \rightarrow \infty$. Any combination

$$(\tilde{F}, \tilde{G}) + Cr^{2|\chi|}(F, G)$$

satisfies to above written equations for (\tilde{F}, \tilde{G}) and represents singular solution at zero [50–56].

The right chosen combination (\hat{F}, \hat{G}) for the single value of the mixing coefficient C (regular for $r \rightarrow \infty$) is second fundamental solution (\hat{f}, \hat{g}) . Finally, the Green's function electron function is a four-component matrices with the functions (F, G) and (\hat{F}, \hat{G}) , which are the Dirac equations solutions with account of the corresponding asymptotic conditions. Further one can get from Eqs. (10a) and (10b) that for $r \rightarrow \infty$:

$$(F, G) \sim \exp Ar; \quad (\hat{F}, \hat{G}) \sim \exp(-Ar); \quad A = (\tilde{\alpha}^{-2} + \xi^2 \tilde{\alpha}^2)^{1/2}. \quad (11)$$

The exponential power is obviously real (i.e., no oscillations). Let us note that this is specifically for purely imaginary energy parameter E . The condition (11) defines the functions (\hat{F}, \hat{G}) . As the bi-linear combinations of the function components (7) are presented in the Green's function, it is obvious that only their relative normalization is important. It is defined by the Wronscian condition as follows:

$$W = (F\hat{G} - \hat{F}G \equiv 1). \quad (12)$$

The electron radial Green's function is the four component matrices as follows:

$$G(r_1 r_2 | E, \chi) = \begin{pmatrix} \hat{F}(r_>)F(r_<) & \hat{F}(r_>)G(r_<) \\ \hat{G}(r_>)F(r_<) & \hat{G}(r_>)G(r_<) \end{pmatrix}, \quad (13)$$

where $r_>$ ($r_<$) is more (or less) value of r_1, r_2 the functions (F, G) and (\hat{F}, \hat{G}) satisfy the Dirac equations (5, their asymptotical conditions (10a), (10b) and (12) and the Wronscian normalization condition. It can be easily shown (c.f. [50–54]) that exchanging the solution (\hat{F}, \hat{G}) by any combinations $(\hat{F}, \hat{G}) + Br^{2|\chi|}(F, G)$ does not break the Wronscian condition (c.f. [29, 30, 50–56]).

3 Non-Singular Nuclear Potential of the Dirac Equation: Relativistic Mean-Field and Fermi Models

In many papers (c.f. [13–20, 34–69] and Refs. therein) the energy and spectral characteristics of hydrogen-like and other multi-electron ions were computed with using the nuclear charge distribution in the form of a uniformly charged sphere and Gaussian form. The advantage of the Gaussian form nuclear charge distribution is provided by using the smooth function instead of the discontinuous one as in the model of a uniformly charged sphere. It is obvious that it simplifies the calculation procedure and permits to perform a flexible simulation of the real distribution of the charge in a nucleus.

The authors of Refs. [23, 55, 56, 63, 64, 70–72] used the RMF model to define the nuclear charge distribution in atomic calculations. In these papers it has been noted that it is possibly a strict bridging between nuclear structure theory and quantum

chemistry (atomic and molecular physics). The formulation and application of the RMF theory has been the most striking development in the field of nuclear structure. The RMF (c.f. [73, 74]) is now established to be one of the most successful and satisfactory theory for the description of the nuclear structure properties. The RMF models are effective field theories for nuclei below an energy scale of 1 GeV, separating the long- and intermediate-range nuclear physics from short-distance physics, involving, i.e., short-range correlations, nucleon form factors, vacuum polarization etc., which is absorbed into the various terms and coupling constants. Let us firstly describe the RMF model, which is used here. Usually one starts with a Lagrangian density describing Dirac spinor nucleons interacting via meson and photon fields. This leads then to the Dirac equation with the potential terms describing the nucleon dynamics and the Klein-Gordon-type equations involving nucleonic currents and densities as source terms for mesons and the photon. This set of coupled, nonlinear differential equations (the RMF equations) is required to be solved self-consistently. In our approach we have adapted so called NL3-NLC (see details in Refs. [70–76]), which is among the most successful parameterizations available. The resulted charge density is defined as follows:

$$\rho_c(R) = A \int dx \exp[-\mu(R - x)] \rho_p(x), \quad (14a)$$

with the proton density ρ_p constructed from the RMF (A , μ are the numerical coefficients) and normalized to the charge number Z :

$$\int dR \rho_p(r) = Z. \quad (14b)$$

All corresponding model parameters are explained and given in Refs. [73–76].

Another effective model approach to determine nuclear potential (the nuclear density distribution) is given by the known Fermi model. This model gives the following definition of the charge distribution in the nucleus $\rho(r)$:

$$\rho(r) = \rho_0 / \{1 + \exp[(r - c)/a]\}, \quad (15a)$$

where the parameter $a = 0.523$ fm, the parameter c is chosen by such a way that it is true the following condition for average-squared radius:

$$\langle r^2 \rangle^{1/2} = (0.836 \times A^{1/3} + 0.5700) \text{ fm}. \quad (15b)$$

Further let us present the formulas for the finite size nuclear potential and its derivatives on the nuclear radius. If the point-like nucleus has the central potential $W(R)$, then a transition to the finite size nuclear potential is realized by exchanging $W(r)$ by the potential:

$$W(r|R) = W(r) \int_0^r dr r^2 \rho(r|R) + \int_r^\infty dr r^2 W(r) \rho(r|R) \quad (16)$$

We assume it as some zeroth approximation. Further the derivatives of various characteristics on R can be calculated. They describe the interaction of the nucleus with outer electron; this permits recalculation of results, when R varies within reasonable limits. The Coulomb potential for the spherically symmetric density $\rho(r|R)$ is:

$$V_{nucl}(r|R) = -(1/r) \int_0^r dr' r'^2 \rho(r'|R) + \int_r^\infty dr' r' \rho(r'|R) \quad (17)$$

It is determined by the following system of differential equations [29, 30, 45–47]:

$$\begin{aligned} V'_{nucl}(r, R) &= (1/r^2) \int_0^r dr' r'^2 \rho(r', R) \equiv (1/r^2) y(r, R), \\ y'(r, R) &= r^2 \rho(r, R), \\ \rho'(r) &= (\rho_0/a) \exp[(r - c)/a] \{1 + \exp[(r - c)/a]\}^2 \end{aligned} \quad (18)$$

with the boundary conditions:

$$\begin{aligned} V_{nucl}(0, R) &= -4/(\pi r), y(0, R) = 0 \\ \rho(0) &= \rho_0 / \{1 + \exp[-c/a]\}. \end{aligned} \quad (19)$$

The corresponding system of equations includes the equations for the density distribution function too. The corresponding derivative of potential on the nuclear radius is as follows:

$$\partial W(r|R)/\partial r = W(r) \int_0^r dr r^2 \partial \rho(r|R)/\partial R + \int_0^\infty dr r^2 W(r) \partial \rho(r|R)/\partial r. \quad (20)$$

The derivative of the physical characteristics, corresponding to potential $W(r|R)$, on the nuclear radius is represented by the matrix element:

$$\partial W(R)/\partial R = \int_0^\infty dr r^2 [F_{nlj}^2(r) + G_{nlj}^2(r)] \partial W(r|R)/\partial R \quad (21)$$

It should be remembered that the nuclear finite size correction is not correctly taken into account within the perturbation theory as a matrix element of two potentials

difference. It is well known that the functions of a state for two nuclear potentials differ significantly in the important region. Calculation of the potentials, their derivatives, matrix elements is reduced to solving the single system (in fact 1D procedure) of the differential equations (c.f. [45–54, 60, 70–72]).

For example, in order to calculate the potentials $W(r|R)$ and $\partial W(r|R)/\partial R$ the following system of differential equations should be solved:

$$\begin{aligned} dW(r|R)/dr &= P(r|R)dW(r)/dr, \\ dP(r|R) &= r^2\rho(r|R), \\ d[\partial W(r|R)/\partial R]/dr &= S(r|R)dW(r)/dr, \\ dS(r|R)/dr &= r^2[\partial r(r|R)/\partial R] \end{aligned} \quad (22)$$

with known analytical functions $W(r)$, $\rho(r|R)$. The boundary values at $r \rightarrow 0$ are found by expansion to a set on r .

In Refs. [50–56] the Dirac equations system is presented and the boundary values of functions (for $r = 0$) for calculating the potential $W(r)$ ($V(r)$) are given. The potential (16), (17) can be expanded to a set on the even degrees:

$$V(r) = V_1 + \sum_{K=2}^{\infty} V_K r^{2K}, \quad (23)$$

$$V_1 = -\frac{4\pi}{R}; \quad V_{K>1} = -\frac{4\gamma^{3/2}}{\pi^{1/2}} \cdot \frac{(-\gamma)^{K-2}}{(2K-2)(2k-1)(k-2)!}. \quad (24)$$

Below we also use the complex combinations:

$$V_1^{\pm} = -R\gamma - i\xi \pm \tilde{\alpha}^{-2}. \quad (25)$$

The expansion of the potential to the Taylor set generates the corresponding expansions for the Dirac equations solutions. These conditions are used for the small values r as the boundary values. The first fundamental condition is stable in relation to the little perturbations of the boundary values. So here one could be limited by the first expansion terms:

for $\chi < 0$

$$\begin{aligned} F &= 1 + V_1^- \cdot V_1^+ r^2 / 2(2\chi - 1), \\ G &= V_1 r / (2\chi - 1); \end{aligned} \quad (26)$$

for $\chi > 0$

$$G = -1 + V_1^- \cdot V_1^+ r^2 / 2(2\chi + 1), \quad F = -V_1 r / (2\chi + 1). \quad (27)$$

The functions (\hat{F}, \hat{G}) have the following form:

$$\tilde{F} = (f_1 + f_2 r^2 + \dots) r; \quad \tilde{G} = g_1 + g_2 r^2 + \dots, \quad (28)$$

where for $\chi < 0$

$$\begin{aligned} g_1 &= 1, & (2\chi + 1)f_1 &= V_1^- g_1, \\ -2g_2 &= V_1^+ f_1, & (2\chi + 3)f_2 &= V_1^- g_2 + V_2 g_1, \\ -4g_3 &= V_1^+ f_2 + V_2 f_1, & (2\chi + 5)f_3 &= V_1^- g_3 + V_2 g_2 + V_3 g_1, \end{aligned} \quad (29)$$

and for $\chi > 0$

$$\tilde{F} = f_1 + f_2 r^2 + \dots; \quad \tilde{G} = (g_1 + g_2 r^2 + \dots) r, \quad (30)$$

$$\begin{aligned} f_1 &= 1, & (2\chi - 1)g_1 &= V_1^+ f_1, \\ -2f_2 &= V_1^- g_1, & (2\chi - 3)g_2 &= V_1^+ f_2 + V_2 f_1, \\ -4f_3 &= V_1^- g_2 + V_2 g_1, & (2\chi - 5)g_3 &= V_1^+ f_3 + V_2 f_2 + V_3 f_1. \end{aligned} \quad (31)$$

The recurrent procedure allows to calculate any number of terms in the expansions (28)–(31). It is naturally important to define the first χ terms, which are general for all functions (\hat{F}, \hat{G}) . It should be noted that the high power terms in the “right” solution (\hat{F}, \hat{G}) are defined by the mixture $Cr^{2|\chi|} (F, G)$. In order to calculate the mixing coefficient one could use the algorithm [50–52]. In further calculations the RMF and Fermi models will be used for determination of the nuclear charge distribution and respectively nuclear potentials. Other possibilities are considered in Refs. [70–72, 77–81].

4 Construction of the Optimal One-Quasi-Electron Representation

In many calculations of characteristics of the atomic elementary processes it has been shown that an adequate description of these characteristics requires using the optimized basis's of the wave functions. Some time ago Davidson had pointed the principal disadvantages of the traditional representation based on the self-consistent field approach and suggested the optimal “natural orbitals” representation [82, 83]. Nevertheless, there remain insurmountable calculational difficulties in the realization of the Davidson program. One of the simplified recipes represents, for example, the Kohn-Sham density functional method [84, 85]. Unfortunately, this method doesn't provide a regular refinement procedure in a case of the complicated atomic systems with several quasiparticles (electrons or vacancies above a core of the closed electron shells). Our version of the density functional method, based on the formally exact QED PT, uses some effective bare potential for this purpose [45–54].

In Refs. [29, 30, 53, 54] it has been proposed “ab initio” optimization principle for construction of the relativistic orbital basis’s. The minimization condition of the gauge dependent multielectron contribution of the lowest QED PT corrections to the radiation widths of the atomic levels is used. The details of procedure can be found in Refs. [53, 54].

Here we briefly describe the key moments. In the fourth order of QED PT there appear diagrams, whose contribution into the $\text{Im } \delta_E$ accounts for the exchange-polarization effects. This contribution describes the collective effects and it is dependent upon the electromagnetic potentials gauge (the gauge non-invariant contribution).

Let us examine the multi-electron atom with 1QP in the first excited state, connected with the ground state by the electric dipole radiation transition. In the zeroth order of QED PT we use the 1-electron bare potential $V_N(r) + V_C(r)$. The mean field potential $V_C(r)$ is related to the electron density $\rho_C(r)$ in a standard way [45–47]. Moreover, all the results of the approximate calculations are the functionals of the density $\rho_C(r)$.

Further one may treat the lowest order multi-electron effects, in particular, the gauge dependent radiative contribution for a certain class of the photon propagator calibration. This value is considered to be the typical electron correlation effect, whose minimization is a reasonable criterion in searching the optimal one-electron basis of PT. All the gauge non-invariant terms are multi-electron by their nature (the particular case of the gauge non-invariance manifestation is the non-coincidence of the oscillator strengths values, obtained in the approximate calculations with the “length” and “velocity” transition operator forms). Quite complicated calculation of contribution of the QED PT fourth order polarization diagrams into $\text{Im } E$ gives the following result [53, 54]:

$$\begin{aligned} \text{Im } \delta E_{\text{inv}}(\alpha - s; b) = & -C \text{d}r_1 \text{d}r_2 \text{d}r_3 \text{d}r_4 \sum_{\substack{n > f \\ m \leq f}} \left(\frac{1}{\omega_{mn} + \omega_{zs}} + \frac{1}{\omega_{mn} - \omega_{zs}} \right) \\ & \psi_\alpha^+(r_1) \psi_m^+(r_2) \psi_s^+(r_4) \psi_n^+(r_3) \frac{1 - \alpha_1 \alpha_2}{r_{12}} \{ [(\alpha_3 \alpha_4 - \alpha_3 n_{34} \alpha_4 n_{34}) / r_{14}] \\ & \sin[w_{zn}(r_{12} + r_{34})] + w_{zn} \cos[w_{zn}(r_{12} + r_{34})] (1 + \alpha_3 n_{34} \alpha_4 n_{34}) \} \\ & \psi_m(r_3) \psi_\alpha(r_4) \psi_n(r_2) \psi_s(r_1). \end{aligned} \quad (32)$$

Here, C is a gauge constant, f is the boundary of the closed shells; $n \geq f$ indicating the unoccupied bound and the upper continuum electron states; $m \leq f$ indicates the finite number of states in the core and the states of the negative continuum (accounting for the electron vacuum polarization).

The minimization of the density functional $\text{Im } \Delta E_{\text{inv}}$ leads to the integral differential equation for the ρ_c , that can be numerically solved. In Refs. [53, 54] it is developed more simplified calculational procedure. In result one can get the optimal relativistic one-quasiparticle representation. Below we first use such a representation in calculation of the radiative corrections to atomic levels energies.

5 Procedure for Determination of the Second Fundamental Solution of the Dirac Equation and Anti-Wronscian

In Refs. [50–52] it has been introduced the bi-linear combination, which was called as the anti-Wronscian:

$$W^- = F \cdot \hat{G} + \hat{F} \cdot G. \quad (33)$$

Below we follow to Refs. [50–56]. It can be received from the Dirac equation and the Wronscian condition that

$$\begin{aligned} F \cdot \hat{G} &= 1/2 + O(r), & \text{for } r \rightarrow \infty, \\ \hat{F} \cdot G &= -1/2 + O(r) \end{aligned} \quad (34)$$

where \hat{F}, \hat{G} is the regular solution at $r \rightarrow \infty$.

It means that \tilde{W}^- is the finite function elsewhere and it is right for any energy E (even $E > 0$, when the Dirac equation solutions are oscillating for $r \rightarrow \infty$):

$$W^- \sim 1/r \quad \text{for } r \rightarrow \infty. \quad (35)$$

The main advantage for the W^- introduction is connected with a simpleness of asymptotes, that is make more simple its integration, analysis of the numerical errors and modelling in the region of the asymptotically large values r . Taking into account the Wronscian condition, one may write as follows:

$$\hat{F} = (W^- - 1)/2G, \quad G = (\tilde{W}^- + 1)/2F, \quad (36)$$

So, the second fundamental solution can be easily found if the first solution (F, G) and the anti-Wronscian are known. Further, following to Refs. [50–52], one may write the differential equation for function W^- :

$$W^{-\prime} = \tilde{\alpha}V^-(\tilde{W}^- + 1)G/F - \tilde{\alpha}V^+(W^- - 1)F/G \quad (37)$$

with asymptotic conditions:

$$W^{-\prime} \rightarrow -W/r \quad \text{for } r \rightarrow \infty. \quad (38)$$

It can be shown that if some function \tilde{W}^- satisfies to Eq. (37) then any function of the following type

$$\tilde{W}^- + C r^{2|\zeta|} F \cdot G. \quad (39)$$

satisfies to this equation too.

The performance of the condition (38) can be reached by means of the corresponding choice of the complex coefficient C for given (F, G) and \tilde{W}^- . At the same time as the regular solution of Eq. (30) as the regular solution of (10a) and (10b) for $r \rightarrow \infty$ can be unstable in relation to the boundary values (for small r) and can exponentially diverge at $r \rightarrow \infty$ because of the little mixture of the second fundamental solution. It is quite possible that a contribution of the diverged mixture can become sufficiently significant in a process of the numerical integration.

Another very important aspect of the problem is a correct output of the integrated functions (\hat{F}, \hat{G}) and W^- to the asymptotes. An effective procedure for realization rational output has been proposed in Refs. [50–52] and based on using the asymptotical equations for W^- . Really, one may represent W^- in the form:

$$W^-(r) = e^{\varphi(r)}. \quad (40)$$

where $\varphi(r)$ is the complex function. The differential equation for anti-Wronscian is as follows:

$$dW^-/dr = W^- d\varphi/dr. \quad (41)$$

$$\varphi' = \tilde{\alpha} [V^-(W^- + 1)G^2 - V^+(W^- - 1)F^2]/GFW^-. \quad (42)$$

Further in a region of the asymptotically large values r one may transit from the exact Eq. (30) to the asymptotic equations as follows [50–52]:

$$W^{-\prime} = W^{-\prime} \operatorname{Re} \varphi' + W^- \tilde{\alpha} \operatorname{Im} \{ [V^-(W^- + 1)G^2 - V^+(W^- - 1)F^2]/GFW^- \} \quad (43)$$

with the model function:

$$\operatorname{Re} \varphi' = -1/r + \sigma_2/r^2 + \sigma_3/r^3. \quad (44)$$

It is important that all solutions of the asymptotic differential equations are stable in relation to the numerical errors of integration and, besides, they satisfy to the condition (37). This is opposite to a behaviour of the exact Eq. (37) solutions.

The constants σ_2, σ_3 are simply connected with $1/r$ expansion for W^- [50–52]. A control of quality for the integration is fulfilled on the function $X(r) = W^- W^{-*}$. In a region of the asymptotically large values r it is correct the following chain of inequalities:

$$X'(r) < 0, X''(r) > 0, X'''(r) < 0, X''''(r) > 0, X^V < 0 \dots \quad (45)$$

for absolutely exact function $X(r)$. The non-fulfilling these condition can be used for earlier diagnostics of the integration numerical errors and transition to the asymptotical differential equations. More details about above described procedure can be found in Refs. [50–56].

6 General Scheme of Calculation for a Three-Electron System

Taking into account for the further application of the algorithm in calculation of the radiative corrections to the levels energies of the heavy Li-like multicharged ions let us describe briefly the calculation procedure for three-electron systems. More detailed description of all method is given in Refs. [59, 60].

One may consider the Dirac-Fock type equations for a three-electron system $1s^2nlj$. Formally they fall into one-electron Dirac equations for the orbitals $1s$ and nlj with the potential:

$$V(r) = 2V(r|1s) + V(r|nlj) + V_{ex}(r) + V(r|R), \quad (46)$$

where $V(r|R)$ includes the electrical and the polarization potentials of a nucleus; the components of the Hartree potential:

$$V(r|i) = \frac{1}{Z} \int d\vec{r}' \rho(r|i)/|\vec{r} - \vec{r}'| \quad (47)$$

Here $\rho(r|i)$ is a distribution of the electron density in the state $|i\rangle$, V_{ex} is the exchange inter-electron interaction.

The main exchange effect will be taken into account if in the equation for the $1s$ orbital we assume

$$V(r) = V(r|1s) + V(r|nlj) \quad (48)$$

and in the equation for the nlj orbital

$$V(r) = 2V(r|1s) \quad (49)$$

The rest of the exchange and correlation effects are taken into account for in the first two orders of the PT by the total inter-electron interaction [45–50, 59, 60]. The used expression for $\rho(r|1s)$ coincides with the precise one for a one-electron relativistic atom with a point nucleus. The finiteness of a nucleus and a presence of the second $1s$ electron are included effectively into the energy E_{1s} .

Actually, for determination of the properties of the outer nlj electron one iteration is sufficient. Refinement resulting from second iteration (by evaluations) does not exceed correlation corrections of the higher orders omitted in the present calculation. The relativistic potential of core (the “screening” potential)

$$2V^{(1)}(r|1s) = V_{scr} \quad (50)$$

has correct asymptotic at zero and in the infinity; at $\alpha \rightarrow 0$ it changes to an appropriate potential constructed on the basis of the hydrogen-like functions. The other details can be found in the papers [59, 60].

7 Calculation Results for Self-Energy Shifts to Atomic Level Energies: Li-like Ions

In Refs. [55, 59, 60] the calculation of spectra for a number of the Li-like heavy ions with nuclear charge $Z = 18\text{--}100$, in particular, Li-like argon and uranium, has been carried out. First of all, let us note that in a concrete calculation transition from exact Eq. (37) to asymptotical ones (41) and (42) is under simultaneous fulfilling four conditions

$$X' < 0, X'' > 0, X''' < 0, X^{IV} > 0. \quad (51)$$

Using the exact equations for large r leads to non-fulfilling the third condition and then first one that is meant the divergence of the function. The attempt to make more long the chain (51) resulted to sharp increasing of the calculation time and does not provide increasing accuracy of the result. In Fig. 1 the calculated curves for $X = W^-W^{-*}$ in dependence upon r (for $\chi = -1$ (a) and $\chi = 7$ (b)) are presented. The points where the derivatives $X' < 0, X'' > 0, X''' < 0, X^{IV} > 0$. change a sign, are shown on the curves $X(r)$. The scale of r on the x-axe is given for two values ξ .

Below the results of calculation [55, 56, 59] for the Li-like ions with the nuclear charge $Z_{nucl} = 18, 26, 36$ and 92 are presented. It is interesting to note that the results obtained are practically identical for the RMF (present paper), Fermi [55, 56] and Gauss [45–52] models of the nuclear charge distribution.

For $\chi = -1$ the behaviour of function after extremum $X(r)$ is not qualitatively dependent upon ξ . For more large values of χ function X'' oscillates. The function X'' reaches the asymptotical value righter than the functions X''', X^{IV} . This is entirely corresponding to the sequence principle (38).

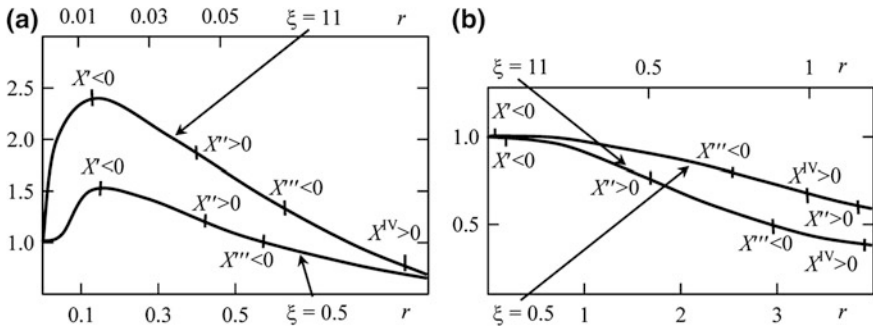


Fig. 1 The curves of the $X = W^-W^{-*}$ (results for the Fermi-model of a nuclear charge distribution) in dependence upon r : **a** $\chi = -1$; **b** $\chi = 7$. The points where the derivatives X', X', X''', X^{IV} . change a sign, are shown on the curves $X(r)$. The scale of r on the x-axe is given for two values ξ

In Table 1 we present the experimental (Exp.) and theoretical data for the energies of $2s_{1/2}$ - $2p_{1/2}$ transition in spectrum of the Li-like U^{89+} ion, obtained by different methods: E2—our data (this work) within the QED PT; A—QED PT with the Dirac-Fock zeroth approximation by Shabaev et al.; B—multi-configuration Dirac-Fock method by Cheng-Kim-Desclaux; C—relativistic PT on the inter-electron interaction; D—the relativistic many-body PT with zeroth Dirac-Fock potential by Ivanov et al. (D); E1—QED PT [37, 38] (look Refs. [34–42, 45–47, 55, 56, 86–92]).

Let us also mention the values of the $2s$ - $2p_{1/2}$ transition energy, which are obtained by Persson-Lindgren-Salomonson ($22,634 \times 10^2 \text{ cm}^{-1}$) [41, 42] and Blundell ($22,650 \times 10^2 \text{ cm}^{-1}$) [37, 38].

In Table 2 data for the nuclear finite size effect (NFSE) and self-energy (Lamb shift = LS) contributions to the energy of $2s$ - $2p_{1/2}$ transition for the Li-like ions of argon, iron, krypton and uranium are presented [55, 56].

In Table 3 we present available experimental data (Exp.) and different calculation results for the energy of the $2s_{1/2}$ - $2p_{1/2}$ transition in spectra of the Li-like ions of iron and krypton. The theoretical values are obtained on the basis of different calculation methods: relativistic PT on inter-electron interaction [86]; PT on parameters $1/Z$ and αZ [87], B-multi-configuration Dirac-Fock method [39, 40], the relativistic many-body PT with zeroth Dirac-Fock potential [45–47] and local Dirac-Fock (and others) potential [86, 87] and relativistic PT [55, 56], this paper (see also Refs. [59, 60]). The corresponding theoretical value of the transition energy for Li-like argon is $25,720$ (in 10 cm^{-1}); in Refs. [93, 94] it is listed the value $25,815 \text{ cm}^{-1}$ (this is the electron structure value without accounting for the QED corrections).

Agreement between the theoretical data and experimental results is more or less satisfactory, but the most exact results are presented in Refs. [34–36, 41, 42, 55, 56, 86, 87]. The calculation has shown that presented generalization of the Ivanov et al. approach [50–56] to construction of the electron Green's function for the Dirac equation with a non-singular nuclear potential and its implementation to the general

Table 1 Energy (in 10^2 cm^{-1}) of $2s_{1/2}$ - $2p_{1/2}$ transition in the spectra of Li-like ions of uranium (see text)

Transition	Exp.	A	B	C	D	E1	E2
$2s_{1/2}$ - $2p_{1/2}$	22,635 22,631	22,644	22,795	22,795	22,636	22,635	22,632
$2s_{1/2}$ - $2p_{1/2}$	—	—	336,923	336,923	336,218	336,229	336,226

Table 2 The NFSE and LS contributions (in cm^{-1}) to energy of $2s$ - $2p_{1/2}$ transition for the Li-like ions with $Z = 18, 26, 36, 92$

Contribution	$Z = 18$	$Z = 26$	$Z = 36$	$Z = 92$
R	3.15	3.56	3.97	5.42
NFSE	−10	−88	−463	−267,328
−LS	950	3,975	12,472	333,215

R is an effective nuclear radius; in 10^{-13} cm

Table 3 Energy (in 10 cm^{-1}) of $2s_{1/2}-2p_{1/2}$ transition in the spectra of Li-like ions of iron and krypton (see text)

Li-like ion	$Z = 26$	$Z = 36$
RPT [86]	39,158	57,628
PT [87]	39,335	57,628
DF [39, 40]	39,335	57,628
PT DF [45–47]	39,296	57,455
QED PT [55, 56]	39,205	57,461
QED DF _L [57, 58]	39,199 39,604*	57,463 58,718*
Exp.	39,199; 39,201	57,460; 57,463

Note *The electron structure values without accounting for the QED corrections

QED PT formalism [29, 30, 53, 54, 59, 60] allows to reach a physically reasonable description of the radiative and other contributions to the transition energies, especially, for high-Z ions of the Li-like isoelectronic sequence.

It is known that the standard relativistic PT usually fails to provide (or the total accuracy is significantly decreased) the accurate results for low-Z and intermediate-Z ions and neutral atoms of astrophysical (laser physics, physics of plasma etc.) interest. In order to check the possibilities of a new approach (within the QED PT [45–47, 59, 60]), we have studied the Li-like ions of argon, iron and krypton. These ions are of the great practical interest for X-ray laser physics etc. (look, for example, [88–92, 95–101] and Refs. therein). Analyzing the obtained data, in particular, for the Li-like ions of iron and krypton, one could conclude that the approach presented (with using the consistent relativistic PT [29, 30, 53–60]) can provide sufficiently high accuracy and physically reasonable description of the corresponding energy and spectral parameters of the multicharged ions.

Acknowledgments One of authors (A.V.G.) would like to thank Professor Marco Nascimento for the invitation to present the invited lecture at the International workshop on Quantum Systems in Chemistry, Physics and Biology (QSCP-XVIII; Paraty, Rio de Janeiro, Brazil). The help in editing the manuscript by Ms. Radhika Sree V. is very much appreciated.

References

1. Feynman RP (1949) Phys Rev 76:749
2. Stueckelberg ECG, Rivier D (1949) Helv Phys Acta 13:215
3. Sakurai JJ (1967) Advanced quantum mechanics. Addison-Wesley, New York
4. Sakurai JJ (2011) Physics 221B quantum mechanics. Notes 34 green's functions in quantum mechanics. University of California, Berkeley
5. Itzykson C, Zuber J-B (1980) Em quantum field theory. McGraw-Hill Inc., New York
6. Landau LD, Lifshits EM, Pitaevsky LP (1985) Quantum electrodynamics. Nauka, Mposcow
7. Schweber SS (1961) An introduction to relativistic quantum field theory. Evanston, Illinois
8. Bjorken JD, Drell SD (1965) Relativistic quantum field theory. McGraw-Hill, New York
9. Braun MA, Gurchumeliya AD, Safronova UI (1984) Relativistic theory of atom. Nauka, Moscow, pp 1–268

10. Aglitsky EV, Safranova UI (1985) Spectroscopy of autoionization states of atomic systems. Energoatomizdat, Moscow, pp 1–160
11. Meucci A, Giusti C, Pacati FD (2005) Nucl Phys A 756:359
12. Gu Y-Q (2006) High energy physics—theory (hep-th). [arXiv:hep-th/0612214](https://arxiv.org/abs/hep-th/0612214)
13. Driker MN, Ivanova EP, Ivanov LN (1981) Opt Spectr 50:551
14. Driker MN, Ivanova EP, Ivanov LN (1983) Opt Spectr 55:224
15. Ivanova EP, Ivanov LN, Kalinkin AN (1985) Nucl Phys 42:355
16. Shabaev VM (2002) Phys Rep 356:119
17. Shabaev VM, Tupitsyn II, Pachucki K, Plunien G, Yerokhin VA (2005) Phys Rev A 72:062105
18. Éric-Olivier LB, Indelicato P, Shabaev VM (2001) The hydrogen atom, vol 570. In: Lecture notes in physics, p 746
19. Dzuba VA, Flambaum VV, Silvestrov PG, Sushkov DE (1991) Phys Rev A 44:2828
20. Flambaum VV, Ginges JSM (2005) Phys Rev A 72:052115
21. Neto AA, Ferreira LG (1976) Phys Rev B 14:4390
22. Köppel H, Domcke W, Cederbaum LS (1984) Adv Chem Phys 57:59
23. Glushkov AV (2010) Green's function method in relativistic quantum chemistry. Odessa, Astroprint, pp 1–450
24. Grant IP (2007) Relativistic quantum theory of atoms and molecules. Theory and computation, Springer series on atomic, optical, and plasma physics, vol 40, pp 587–626
25. Grant IP, Quiney HM (2000) Int J Quant Chem 80:283
26. Grant IP, Quiney HM (1993) Phys Scripta 46:132
27. Wilson S (2007) Recent advances in theoretical physics and chemistry systems, vol 16. In: Maruani J, Lahmar S, Wilson S, Delgado-Barrio G (eds) Series: progress in theoretical chemistry and physics, p 11
28. Wilson S (2001) J MolStr Theochem 547:279
29. Glushkov AV, Ivanov LN, Ivanova EP (1986) Autoionization phenomena in atoms. Moscow University Press, Moscow, p 152
30. Glushkov AV (2006) Relativistic and correlation effects in spectra of atomic systems. Nauka, Moscow-Odessa, pp 1–700
31. Bell KL, Berrington KA, Crothers DSF, Hibbert A, Taylor KT (2002) Bertha: 4-component relativistic molecular quantum mechanics, in supercomputing, collision processes, and application. IN: Series: physics of atoms and molecules. Springer, Berlin, pp 213–224
32. Reiher M, Hess B (2000) Modern methods and algorithms of quantum chemistry, vol 3. In: Grotendorst J (ed) John von Neumann Institute for Computing, Julich, NIC Series, pp 479–505
33. Quiney HM (2002) Relativistic quantum mechanics of atoms and molecules. new trends in quantum systems in chemistry and physics. In: Series: progress in theoretical chemistry and physics, vol 6, pp 135–173
34. Mohr PJ (1993) Phys Scripta 46:44–52
35. Mohr PJ (1983) Atom Data Nucl Data Tabl 24:453–470
36. Mohr PJ (1982) Phys Rev A 26:2338–2354
37. Gould H (1993) Phys Scripta 46:61–64
38. Blundell SA (1993) Phys Scripta 46:144–150
39. Indelicato P, Desclaux J (1990) Phys Rev A 42:5139–5148
40. Cheng K, Kim Y, Desclaux J (1979) Atom Data Nucl Data Tabl 24:11–88
41. Persson H, Lindgren L, Salomonson S (1993) Phys Scripta 46:125–131
42. Sapirstein J, Cheng KT (2005) Phys Rev A 71:022503
43. Johnson WR, Idrees M, Sapirstein J (1987) Phys Rep 35:3218–3222
44. Ionescu DC, Reinhardt R, Muller B et al (1988) Phys Rep 38:618–625
45. Ivanov LN, Ivanova EP (1974) Theor Math Phys 20:282
46. Ivanov LN, Ivanova EP, Aglitsky EV (1988) Phys Rep 188:315
47. Ivanov LN, Ivanova EP, Aglitsky EV (1986) Izv AS USSR 50:1349
48. Ivanova EP, Ivanov LN, Glushkov AV, Kramida AE (1985) Phys Scripta 32:512
49. Ivanova EP, Glushkov AV (1985) Opt Spectr 58:931

50. Ivanov LN, Ivanova EP, Zaridze G (1988) Soviet Phys 41:87
51. Ivanov LN, Ivanova EP, Zaridze G (1991) Preprint of Institute of Spectroscopy of Russian Academy of Sciences, N2, Troitsk
52. Ivanov LN, Ivanova EP, Glushkov AV (1992) Preprint of Institute of Spectroscopy of Russian Academy of Sciences, N AS-4, Troitsk
53. Glushkov AV, Ivanov LN (1992) Phys Lett A 170:33
54. Glushkov AV, Ivanov LN (1992) Preprint of Institute of Spectroscopy of Russian Academy of Sciences, N AS-1, Troitsk
55. Glushkov AV, Malinovskaya SV, Khetselius OY, Loboda AV, Sukharev DE, Lovett L (2009) Int J Quant Chem 109:1717
56. Khetselius OY (2012) Quantum systems in chemistry and physics: progress in methods and applications. In: Nishikawa K, Maruani J, Brändas E, Delgado-Barrio G, Piecuch P (eds) Series: progress in theoretical chemistry and physics, vol 26. Springer, Berlin, pp 217–230
57. Glushkov AV, Ambrosov SV, Loboda AV et al (2004) Nucl Phys A Nucl Hadr Phys 734S:21
58. Glushkov AV (2012) J Phys C 397:012011
59. Glushkov AV, Ambrosov SV, Loboda AV, Gurnitskaya EP, Khetselius OY (2006) Recent advances in the theory of chemical and physical systems. In: Julien P, Maruani J, Mayou D, Wilson S, Delgado-Barrio G (eds) Series: progress in theoretical chemistry and physics, vol 15. Springer, Berlin, pp 285
60. Glushkov AV, Khetselius OY, Loboda AV, Gurnitskaya EP, Florko TA, Sukharev DE, Lovett L (2008) Frontiers in quantum systems in chemistry and physics. In: Wilson S, Grout PJ, Maruani J, Delgado-Barrio G, Piecuch P (eds) Series: progress in theoretical chemistry and physics, vol 18. Springer, Berlin, p 505 (2008)
61. Glushkov AV (2012) Quantum systems in chemistry and physics: progress in methods and applications. In: Nishikawa K, Maruani J, Brändas E, Delgado-Barrio G, Piecuch P (eds) Series: progress in theoretical chemistry and physics, vol 26. Springer, Berlin, pp 231–254
62. Glushkov AV, Malinovskaya SV (2003) In: Fazio G, Hanappe F (eds) New projects and new lines of research in nuclear physics. World Scientific, Singapore, pp 242–280
63. Glushkov AV (2005) In: Grzonka D, Czyzykiewicz R, Oelert W, Rozek T, Winter P (eds) Low energy antiproton physics, vol 796. AIP, New York, pp 206–210
64. Glushkov AV, Lovett L, Khetselius OYu, Gurnitskaya EP, Dubrovskaya YuN, Loboda AV (2009) Int J Mod Phys A Part Fields Gravitation Cosmol Nucl Phys 24:611
65. Glushkov AV, Malinovskaya SV, Svinarenko AA, Chernyakova YuG (2004) Int J Quant Chem 99:879
66. Glushkov AV, Ambrosov SV, Loboda AV, Gurnitskaya EP, Prepelitsa GP (2005) Int J Quant Chem 104:562
67. Glushkov AV, Khetselius OYu, Malinovskaya SV (2008) Eur Phys J ST 160:195
68. Glushkov AV, Khetselius OYu, Malinovskaya SV (2008) Mol Phys (UK) 106:1257
69. Glushkov AV, Khetselius OY, Malinovskaya SV (2008) Frontiers in quantum systems in chemistry and physics. In: Wilson S, Grout PJ, Maruani J, Delgado-Barrio G, Piecuch P (eds) Series: progress in theoretical chemistry and physics, Springer, Berlin, pp 523–540
70. Khetselius OYu (2009) Int J Quant Chem 109:3330
71. Khetselius OYu (2009) Phys Scripta T135:014023
72. Khetselius OYu (2012) J Phys C 397:012012
73. Serot BD, Walecka JD (1986) Advances in nuclear physics, vol 16. In: The relativistic nuclear many body problem. Plenum Press, New York, p 1
74. Sahoo BK, Gopakumar G, Chaudhuri RK, Das BP, Merlitz H, Mahapatra US, Makherjee D (2003) Phys Rev A 68:040501
75. Bürvenich T, Madland DG, Maruhn JA, Reinhard P-G (2002) J Nucl Radiochem Sci 3:191
76. Nagasawa T, Haga A, Nakano M (2004) Phys Rev C 69:034322
77. Tomaselli M, Schneider SM, Kankeleit E, Kuhl T (1995) Phys Rev C 51:2989
78. Labzowsky LN, Johnson WR, Soff G, Schneider SM (1995) Phys Rev A 51:4597

79. Glushkov AV, Khetselius OY, Lovett L (2010) Advances in the theory of atomic and molecular systems dynamics, spectroscopy, clusters, and nanostructures. In: Piecuch P, Maruani J, Delgado-Barrio G, Wilson S (eds) Series: progress in theoretical chemistry and physics, vol 20. Springer, Berlin, pp 125–172
80. Glushkov AV, Malinovskaya SV, Vitavetskaya LA, Dubrovskaya YuV, Khetselius OY (2006) Recent advances in theoretical physics and chemistry systems. In: Julien J-P, Maruani J, Mayou D, Wilson S, Delgado-Barrio G (eds) Series: progress in theoretical chemistry and physics, vol 15. Springer, Berlin, pp 301–318
81. Glushkov AV, Khetselius OY, Svinarenko AA (2012) in: Advances in the theory of quantum systems in chemistry and physics. In: Hoggan PE, Brandas E, Delgado-Barrio G, P.Piecuch (eds) Series: progress in theoretical chemistry and physics, vol 22. Springer, Berlin, pp 51–70
82. Davidson ER (1972) *Rev Mod Phys* 44:451
83. Davidson ER, Feller DJ (1981) *Chem Phys* 74:3977
84. Hohenberg P, Kohn W (1964) *Phys Rev B* 136:864
85. Kohn W, Sham LJ (1965) *Phys Rev A* 140:1131
86. Shestakov AF (1979) *Opt Spectr* 46:51–55
87. Vainstein LA, Safronova UI (1975) *Phys Scripta* 31:519
88. Ivanova EP, Glushkov AV (1986) *J Quant Spectr Rad Transfer (USA)* 36:127
89. Glushkov AV, Ivanov LN (1992) Shift and deformation of radiation atomic lines in the laser emission field. Multiphoton processes. Preprint of Institute for Spectroscopy of the USSR Academy of Sciences, ISAN, Moscow-Troitsk, AS N3, pp 1–12
90. Glushkov AV, Ivanov LN (1992) A broadening of the thulium atom autoionization resonances in a weak electric field. Preprint of Institute for Spectroscopy of the USSR Academy of Sciences, ISAN, Moscow-Troitsk, AS N3, pp 1–10
91. Ivanova EP, Grant IP (1998) *J Phys B* 31:2871
92. E.P. Ivanova, and I.P. Grant, S.J. Rose, X-ray Lasers (1998) *Proc. (1999)*, pp. 383–386
93. Yerokhin VA, Artemyev AN, Shabaev VM (2007) *Phys Rev A* 75:062501
94. Yerokhin VA, Indelicato P, Shabaev VM (2006) *Phys Rev Lett* 97:253004
95. Ivanova EP, Zinoviev NA (1999) *Quant Electron* 29:484
96. Ivanova EP, Zinoviev NA (2000) *Phys Lett A* 274:239
97. Ivanova EP (2009) *Atom Data Nucl Data Tabl* 95(6):786
98. Ivanova EP (2010) *Phys Rev A* 82(4):043824
99. Ivanova EP (2011) *Atom Data Nucl Data Tabl* 97(1):1
100. Indelicato P, Boucard S, Covita DS et al (2007) *Nucl Instr Methods Phys Res A* 580:8
101. Glushkov AV (2012) *J Phys C Ser* 397:012011

Spacetime-Based Foundation of Quantum Mechanics and General Relativity

John A. Macken

Abstract This work makes the case that everything in the universe (all particles, fields and forces) is derived from the single building block of 4 dimensional spacetime. The tremendously large impedance of spacetime (c^3/G) permits small amplitude waves in spacetime to be the universal building block. The spacetime wave-based fermion model is shown to plausibly possess the correct spin, energy and the ability to appear to be point particles in experiments. This model also generates the weak gravity curvature of spacetime and the gravitational force between particles. The electrostatic force between fundamental particles is also derived and shown to be related to the gravitational force through a simple difference in exponents. A new constant of nature is proposed which converts electrical charge into a strain of space. The distortion of spacetime produced by photons is also analyzed.

Keywords Spacetime field · Impedance of spacetime · Zero point energy · Gravitation · Unification of forces · Theory of everything · Aether

1 Introduction

Quantum systems present many characteristics which can be described mathematically but cannot be understood conceptually. For example, a carbon monoxide molecule isolated in a vacuum can only rotate at integer multiples of 115 GHz. What enforces this quantized angular momentum? Why do fundamental particles exhibit wave-particle duality and probabilistic characteristics? What is the mechanism by which particles produce curved spacetime?

Generations of physicists have been unable to bring conceptual understanding to the foundational questions of both quantum mechanics (QM) and general relativity

J.A. Macken (✉)

Macken Instruments Inc., 3186 Coffey Ln, Santa Rosa, CA, USA
e-mail: jmacken@stmarys-ca.edu

(GR). In physics, we start with assumptions and extract hidden implications using advanced mathematical analysis. However, if a problem is missing an essential assumption, no amount of mathematical analysis of the other required assumptions can successfully solve the problem. It is proposed that our current view of the universe is missing an essential starting assumption. The currently accepted starting assumptions are sufficient to achieve mathematical equations which agree with experiments, but they are not sufficient to give conceptually understandable explanations of many QM and GR effects including the mechanism by which matter curves spacetime. This paper will attempt to show that the missing fundamental assumption is: The universe is only spacetime.

This assumption is intended to convey the idea that all particles, all fields and all forces are just different aspects of 4 dimensional spacetime. If this assumption can be proven correct, it has a great deal of appeal. It would unify not only the forces of nature, but also the 17 particles of the standard model would all be related because they would be different excitations of the single spacetime field. Even the modeling of molecules in physical chemistry would achieve a new level of conceptual understanding. What is being proposed is that the fabled “theory of everything” might actually be possible if it can be shown that physics has an underlying simplicity expressed in the proposed missing assumption: The universe is only spacetime.

To understand how this assumption is plausible, it is first necessary to describe the model of spacetime that allows spacetime to be the single building block of everything in the universe. The usual descriptions of spacetime come from GR. However, it is proposed that GR describes only the macroscopic properties of 4 dimensional spacetime. For spacetime to be the single constituent of everything, it is necessary to expand the model of spacetime to include the small scale properties of the vacuum obtained from QM. As John Archibald Wheeler said [1] “Empty space is not empty... The density of field fluctuation energy in the vacuum argues that elementary particles represent percentage-wise almost completely negligible change in the locally violent conditions that characterize the vacuum.” It is this energetic form of the vacuum that must be combined with the macroscopic properties of spacetime to obtain the proposed single building block of all particles, fields and forces in the universe.

2 Zero Point Energy and the Spacetime Field

Taking John Wheeler’s advice, we will start by modeling the energetic vacuum rather than initially attempting to model particles or forces. The quantum mechanical properties of the vacuum goes by many names including zero point energy (ZPE), vacuum energy, vacuum fluctuations, quantum foam, etc. Even the uncertainty principle and the virtual particle pair formation/annihilation will be attributed to these vacuum fluctuations. Field theory states that the vacuum can be

viewed as if it is filled with harmonic oscillators [2] with energy $E = \frac{1}{2}\hbar\omega = \frac{1}{2}\hbar c/\bar{\lambda}$ where lambda bar is $\bar{\lambda} = c/\omega = \lambda/2\pi$. The volume V of each harmonic oscillator is a function of the wavelength which will be expressed as volume $V = k\bar{\lambda}^3$ where k is a numerical factor near 1. This implies that the quantum vacuum has a tremendous energy density [2]. For example, the implied energy density U is $U = k\hbar\omega^4/c^3$ where the angular frequency ranges from zero to a maximum of ω . In quantum field theory it is commonly assumed that the maximum frequency is equal to Planck angular frequency $\omega_p = \sqrt{c^5/\hbar G} \approx 1.9 \times 10^{43} \text{ s}^{-1}$. The implied energy density of the quantum vacuum is therefore approximately equal to Planck energy density $U_p = c^7/\hbar G^2 \approx 4.6 \times 10^{113} \text{ J/m}^3$. For comparison, the “critical” energy density of the universe obtained from GR is about 10^{-9} J/m^3 . This is the famous 10^{120} discrepancy between the GR and QM. It is usually assumed that the energy density of the universe obtained from GR and cosmological observation must be correct and that some unknown large effect must cancel out what appears to be a ridiculously large energy density from QM. However, there are two problems with this. First, the cancellation must be carefully calibrated to cancel 10^{113} J/m^3 but leaving the 10^{-9} J/m^3 energy density that we observe. Second, a cancellation must also leave all the physical and theoretical effects required by QM, quantum electrodynamics and quantum chromodynamics.

If we are assuming that the universe is only spacetime, then we are not anxious to get rid of the tremendous energy density of the vacuum. In fact, the vacuum energy is essential to the spacetime model that allows spacetime to build everything in the universe. Rather than declaring that this large vacuum energy must be eliminated, we will accept and quantify the fluctuations of spacetime that result in this vacuum energy density. Once this is done, we can see if the models of the vacuum energy and the observable energy in the universe are somehow different in a way that allows both to peacefully coexist.

The obvious way that the vacuum might possess energy is if there are oscillating distortions (waves) in the vacuum. However, the wave amplitude would have to be small because large amplitude waves would be detectable and violate conservation laws. The uncertainty principle does allow waves to exist in spacetime provided that the amplitude of these waves are so small that the waves are not detectable as discrete waves. If these random waves existed, they would introduce noise into our distance and time measurements. The question of the theoretical limit (device independent) to the accuracy of a distance measurement between two points has been examined and found [3–7] to be on the order of Planck length $L_p = \sqrt{\hbar G/c^3} \approx 1.6 \times 10^{-35} \text{ m}$. In other words, waves which modulate the distance between two points by \pm Planck length would be undetectable and therefore allowed. Similarly, an analysis of the fundamental minimum detectable unit of time (difference between clocks) has been made [4, 5] and found to be on the order of Planck time $T_p = \sqrt{\hbar G/c^5} \approx 5.4 \times 10^{-44} \text{ s}$. Therefore, waves in spacetime can slightly modulate the rate of time. Clocks in flat spacetime can speed up and slow down in a way that produces a maximum difference between clocks of $\pm T_p$. Waves

in spacetime which have displacement amplitudes of $\pm L_p$ and $\pm T_p$ will be called “Planck amplitude waves”. Unlike virtual particle pairs, Planck amplitude waves in spacetime can exist indefinitely because these waves are undetectable even with a long observation time. This is a fundamental property of spacetime that is not only allowed by the uncertainty principle, but in this model this turbulence causes the uncertainty principle.

It should be mentioned that the Planck amplitude waves in spacetime are a completely different concept than the granularity or pixelation proposed by loop quantum gravity. This granularity (pixelation) of loop quantum gravity is not sinusoidal wave oscillations. The pixelation model of spacetime is stagnant. It does not possess the tremendous energy density required to explain the 10^{113} J/m³ of ZPE. In the remainder of this paper, the term “spacetime field” will be used to indicate the model of spacetime proposed here which is filled with Planck amplitude waves ($\pm L_p$ and $\pm T_p$) at all frequencies up to Planck angular frequency $\omega_p = \sqrt{c^5/\hbar G} \approx 1.9 \times 10^{43}$ s⁻¹.

There is another insight that can be extracted from our starting assumption. Since an objective is to construct fundamental particles out of waves in spacetime, those waves must be able to affect proper volume and the rate of time. This is said because a particle (mass) affects the rate of time and proper volume in the surrounding spacetime (matter curves spacetime). If this model is going to explain this effect, it is most reasonable to first explore the possibility that particles are made of waves in spacetime that modulate both the rate of time and proper volume. Gravitational waves are waves in the medium of spacetime, but they do not modulate the rate of time or proper volume. For example, a gravitational wave would convert a spherical volume into an oscillating ellipsoid which has the same volume and rate of time as the spherical volume. The only type of wave that would affect time and volume is a dipole wave in spacetime. This is a theoretical concept that would be the simplest type of wave in spacetime. However, it barely gets mentioned in standard texts on GR because dipole waves in spacetime are impossible on the macroscopic scale covered by GR. For example, in the 1,300 page tome titled **Gravitation** [1], dipole waves in spacetime receive only a three line mention which can be paraphrased as *there can be no mass dipole radiation because the second time derivative of mass dipole is zero $\ddot{d} = \dot{p} = 0$* . If dipole waves existed in spacetime on the macroscopic scale, they would violate the conservation of momentum and the conservation of energy. However, QM permits dipole waves to exist in spacetime provided that the displacement amplitude is limited to $\pm L_p$ and $\pm T_p$. This is no problem because we have already accepted this limitation for any energetic waves to exist in spacetime. Therefore, the spacetime field model being developed will assume dipole waves in spacetime with the Planck amplitude limitation.

To test the contention that ZPE is Planck amplitude dipole waves in spacetime, we will start with an equation that gives the intensity I of a wave with amplitude A at angular frequency ω propagating in a medium with impedance Z .

$$I = kA^2\omega^2Z \quad (1)$$

This is a universal equation applicable to waves of any kind provided that the terms in this equation have compatible units. For example, electromagnetic (EM) radiation usually has intensity expressed as electric field strength and the impedance is expressed as the impedance of free space Z_0 which has units of Ohms $Z_0 \approx 377 \Omega$. These units are not compatible with the units of intensity (watts/m² = kg/s³) and frequency (s⁻¹) in Eq. (1). However, Eq. (1) can be used to express the intensity of sound waves, gravitational waves and the proposed Planck amplitude dipole waves in spacetime. For waves in spacetime, we would need to designate the impedance associated with the properties of spacetime. Fortunately Ref. [8] has identified the impedance of spacetime Z_s from gravitational wave equations.

$$Z_s \equiv c^3/G \approx 4.04 \times 10^{35} \text{ kg/s} \quad (2)$$

In order to use $Z_s = c^3/G$ in Eq. (1) it is necessary to express the amplitude A in compatible units. When impedance is expressed in units of kg/s, the amplitude must be expressed as dimensionless strain amplitude. For example, if the spatial displacement of spacetime is $\pm L_p$, then the strain amplitude (maximum slope) of a wave with wavelength λ would be $A = L_p/\bar{\lambda}$ where $\bar{\lambda} \equiv \lambda/2\pi = c/\omega$. Similarly, if the temporal displacement of flat spacetime is $\pm T_p$, then the strain amplitude is $A = T_p\omega$. These are equivalent, therefore Planck length and Planck time displacements of spacetime translate into strain amplitudes of: $A = L_p/\bar{\lambda} = T_p\omega$.

It is possible to expand Eq. (1) into several useful equations if we presume that the fluctuations of spacetime represent strongly interacting energy propagating at the speed of light (explained later). Such a wave would exert radiation pressure if it interacted with an object in a way that caused the wave to be transformed in some way. For example, absorption or emission of a wave propagating at c with power P exerts a force $F = P/c$. Combining this with Eq. (1) we obtain Eq. (3) which is the force exerted by a wave with amplitude A and angular frequency ω propagating at the speed of light in a medium with impedance Z exerted over area a . Equation (4) is the energy density U of energy propagating at c and Eq. (5) is the energy E in a wave propagating at the speed of light filling volume V .

$$F = kA^2\omega^2Za/c \quad (3)$$

$$U = kA^2\omega^2Z/c \quad (4)$$

$$E = kA^2\omega^2ZV/c \quad (5)$$

We will test the concept that ZPE is caused by Planck amplitude fluctuations of spacetime. We will use Eq. (5) and assume a wave with strain amplitude $A = L_p/\bar{\lambda}$ at angular frequency $\omega = \bar{\lambda}/c$ in volume $V = k\bar{\lambda}^3$.

$$E = \frac{kA^2\omega^2\mathcal{Z}V}{c} = k\left(\frac{L_p}{\lambda}\right)^2\omega^2\left(\frac{c^3}{G}\right)\left(\frac{\lambda^3}{c}\right) = k\hbar\omega \quad (6)$$

This calculation yields $E = k\hbar\omega$ which is the general form of the energy in the harmonic oscillators of ZPE ($E = \frac{1}{2}\hbar\omega$). We cannot establish that $k = 1/2$ for this equation, but this is merely a plausibility calculation intended to show a connection between ZPE and the spacetime field filled with Planck amplitude waves in spacetime. Also if these same substitutions are made into the energy density Eq. (4) we obtain $U = k\hbar\omega^4/c^3$. Reference [2] shows that this is the equation for the energy density of ZPE for all frequencies between zero and a cutoff frequency of ω . If we presume that this cutoff frequency is equal to Planck angular frequency $\omega_p = \sqrt{c^5/\hbar G}$ then the total energy density of ZPE would be a numerical factor k times Planck energy density $U_p = c^7/\hbar G^2 \approx 10^{113} \text{ J/m}^3$. This corresponds to the energy density of ZPE [2]. Also this tremendous energy density implies that the spacetime field generates a tremendous pressure. This will be discussed later.

Therefore, this is a successful test of the contention that ZPE can be explained using the starting assumption that the universe is only spacetime. This is also the first step in converting the starting assumption (the universe is only spacetime) into equations. Even though the fluctuations only displace spacetime by Planck length and Planck time, this small displacement is in a medium which has a tremendously large impedance $Z_s \equiv c^3/G \approx 4.04 \times 10^{35} \text{ kg/s}$. The fact that the spacetime field has impedance means that it has elasticity. In order for a sound wave to propagate through an acoustic medium, the acoustic medium must be capable of absorbing energy and returning energy to the sound wave. Similarly, a wave propagating in a sea of Planck amplitude waves in the spacetime field would slightly compress and expand these waves thereby slightly changing the energy of the waves that create ZPE. This gives spacetime the ability to absorb and return energy to waves. The spacetime field does not merely **have** waves, the spacetime field fundamentally **is** a sea of Planck amplitude waves. This model of the proposed energetic spacetime field explains why spacetime is such a stiff medium for gravitational wave propagation and how spacetime achieves the tremendously large impedance of c^3/G .

We know that virtual particle pairs are continuously being formed in the energetic vacuum and annihilated back into the vacuum. It is not too great a stretch to assume that these virtual particle pairs are actually another form of spacetime. Real particles possess quantized angular momentum (spin) while virtual particle pairs have no total angular momentum. We will test the hypothesis that real particles are also a form of spacetime which incorporates angular momentum. Next a spacetime based model of a fundamental particle will be presented. The initial presentation will not include the underlying reasoning. However, once the characteristics are established, the proposed spacetime particle model will be subjected to 8 plausibility tests which include a test of energy, angular momentum and the ability to appear to be a point particle. Therefore, the viability of the particle model will be determined in the testing phase.

3 Spacetime Model of a Fundamental Particle

To help explain the proposed model of a spacetime particle, we will first make an analogy to a superfluid which contains a small amount of angular momentum. For example, a Bose-Einstein condensate is a superfluid. When angular momentum is introduced into this condensate, the bulk of the superfluid does not rotate. Instead, the angular momentum is broken into small rapidly rotating vortices which each contain \hbar of quantized angular momentum. These are surrounded by the vast majority of the superfluid which is not rotating. References [9–11] show pictures of these rapidly rotating vortices and give a more detailed explanation.

The analogy to a vortex in a superfluid is that a fundamental fermion such as an electron is proposed to be a rapidly rotating Planck amplitude wave in spacetime with $\hbar/2$ of quantized angular momentum. It is confined and isolated by the surrounding sea of superfluid-like Planck amplitude waves which lack angular momentum. More specifically, a fundamental fermion with internal energy E_i is proposed to be a Planck amplitude wave propagating at the speed of light but circulating within a spherical volume one Compton wavelength λ_c in circumference. The rotating wave does not have a sharp boundary, but for mathematical analysis, it can be considered to have a radius equal to the reduced Compton wavelength $\tilde{\lambda}_c$. Its rotational rate is equal to the Compton angular frequency ω_c and its strain amplitude will be designated as A_s . Equations (7–9) quantify these terms.

$$\omega_c = E_i/\hbar = c/\tilde{\lambda}_c \quad (7)$$

$$\tilde{\lambda}_c = \hbar c/E_i = c/\omega_c = \hbar/mc \quad (8)$$

$$A_s = L_p/\tilde{\lambda}_c = T_p\omega_c \quad (9)$$

The sea of Planck amplitude waves in spacetime are proposed to be the most perfect superfluid possible. Angular momentum that originated at the Big Bang is isolated into $1/2\hbar$ and \hbar quantized units. While angular momentum cannot be destroyed, only specific combinations of wave amplitude and rotational frequency achieve stability through the interaction with the surrounding spacetime field. These few amplitudes and frequencies that are stable or semi-stable are the fermions and bosons of the standard model. They can propagate through the superfluid spacetime field without energy loss. The previously mentioned 10^{120} discrepancy in the energy density of the universe between GR and QM is proposed to be the difference between the average energy density of fermions and bosons which possess quantized angular momentum and the energy density of the Planck amplitude waves which lack angular momentum and form the spacetime field.

There is no conflict between these two energy densities. The homogeneous waves in spacetime which lack angular momentum are responsible for giving flat spacetime its properties (its physical constants) such as Z_s , c , G , \hbar , ε_o , etc.

The fermions with quantized angular momentum represent distortions in the otherwise homogeneous spacetime field. If we average these distortions over all space, they represent only about 1 part in 10^{120} of the average energy density possessed by the spacetime field. However, a high density of fermions, for example in a neutron star, can produce a substantial localized excess energy density. The conditions that create a black hole can be related to producing 100 % modulation of the properties of the spacetime field at a particular wavelength, amplitude and frequency. This point will be analyzed later.

The energy density of the homogeneous spacetime field does not create its own gravity. Instead, gravity is the distortion of this homogeneous field caused by inhomogeneities in the form of rotating Planck amplitude waves possessing quantized angular momentum. These distortions of the spacetime field extend far beyond the particle's spherical volumes previously described. This external effect will be discussed later.

In this model, a counter rotating virtual particle pair is two Planck amplitude waves of the spacetime field which momentarily achieve the amplitude and frequency of a fundamental particle pair. However, there is no quantized angular momentum. Therefore, the deception lasts for only for a time equal to $1/\omega_c$ at which point the virtual particle pair appears to be annihilated. ($1/\omega_c \approx \Delta t$ in the uncertainty principle) The universal spacetime field can appear to be the multiple fields of the standard model because there are multiple resonances which produce different types of virtual particle pairs. Currently, field theory considers that each of the 17 fundamental particles of the standard model has its own field [12]. This implies that the universe has at least 17 overlapping fields. This unappealing concept is replaced by the more appealing concept of a single spacetime field with multiple resonances which achieve all the particles, fields and forces.

4 Testing of the Particle Model

4.1 Energy and Angular Momentum Test

The first of the plausibility tests will examine whether this model plausibly achieves the required energy for a fundamental particle. We will not be attempting to predict the energy of specific fundamental particles. Instead we will take Eq. (5) and substitute $A = A_s$, $\omega = \omega_c$, $Z = Z_s$, and $V = k\tilde{\lambda}_c^3$. The answer obtained with these substitutions is: $E = kE_i$. In words, the proposed amplitude A_s , frequency ω_c , radius $\tilde{\lambda}_c$ and impedance Z_s generates the correct internal energy E_i of a fundamental particle if $k = 1$. For example, an electron has strain amplitude of $A_s \approx 4.18 \times 10^{-23}$, a Compton angular frequency of $\omega_c \approx 7.76 \times 10^{20} \text{ s}^{-1}$, and a reduced Compton wavelength of $\tilde{\lambda}_c \approx 3.86 \times 10^{-13} \text{ m}$. This is an extremely weak rotating distortion of spacetime. However, because of the large value of Z_s , substituting the electron's

values into Eq. (5) achieves the electron's energy of $E_i \approx 8.19 \times 10^{-14}$ J. For comparison, if a point particle model is used, then there is no internal structure that connects to the electron's Compton frequency, Compton wavelength or internal energy. The implied infinite energy density speaks to the inadequacy of the point particle concept.

Next, we will check if the spacetime particle model can plausibly possess angular momentum of $\mathcal{L} = \hbar/2$. If the particle model had all the wave energy circulating at the speed of light around the circumference like a rotating hoop, then the particle model would have angular momentum of $\mathcal{L} = \hbar$. This follows from $\mathcal{L} = pr$ where the rotating hoop model would have $p = E_i/c$ and $r = \tilde{\lambda}_c = \hbar c/E_i$. However, the spacetime model has the energy more uniformly distributed throughout the internal volume. This lowers the momentum term to $p < E_i/c$. This is equivalent to having a moment of inertia more like a rotating disk than a rotating hoop. The rotation is also somewhat chaotic which also reduces the angular momentum. The exact energy distribution has not been determined, but there is a wide range of possibilities that can achieve $\mathcal{L} = \hbar/2$. In fact, achieving this angular momentum would become a design criteria in choosing the "correct" energy distribution. For comparison, a point particle or even a Planck length vibrating string is physically incompatible with achieving the angular momentum requirement.

At the start of this paper the question was asked: What mechanism enforces quantized angular momentum on a rotating CO molecule? It is common for physics professors to explain to their students that a fundamental particle such as an electron possess "intrinsic angular momentum" or "spin" which is QM phenomena with no interpretation from classical mechanics. While it is impossible to see any physical rotation of an electron, molecules possess a quantized physical rotation (quantized angular momentum) which can be physically proven. In this model, the quantized angular momentum of a molecule is "enforced" by the fact that the molecule is itself made of rotating quantum of spacetime energy existing in the sea of the superfluid spacetime field. Is it not reasonable that fundamental particles also have a physical rotation? Saying that an electron has "spin" without physical angular momentum is an admission that the currently accepted models of fermions are inadequate.

For comparison, the spacetime particle model does not just have angular momentum as an added feature. Instead angular momentum is the central feature that imparts quantization. Quantized angular momentum is the feature that distinguishes fermions and bosons from ZPE which has about 10^{120} times more energy in the universe. This proposed model offers a conceptually understandable explanation of "spin".

4.2 Curved Spacetime Test

The next test is to see if the spacetime particle model plausibly produces the correct curvature of spacetime in the surrounding spacetime. According to GR, matter

causes the surrounding spacetime to have a decrease in the rate of time and an increase in proper volume relative to Euclidian geometry.

$$\frac{dt}{d\tau} = \frac{dr}{dR} = \left(1 - \left(\frac{2Gm}{c^2R}\right)\right)^{-1/2} \approx 1 + \frac{Gm}{c^2r} \quad (10)$$

- t coordinate time measured on a stationary clock infinitely far from the mass—effectively zero gravity
- τ proper time measured on a local clock in gravity moving along the same world line as a test particle
- r proper radial distance
- R circumferential radius—radial coordinate—circumference around a mass divided by 2π .

Equation (10) is standard for general relativity and will not be explained further. This is the temporal and spatial curvature of spacetime caused by mass m . The weak gravity approximation is $dt/d\tau \approx 1 + Gm/c^2r$. In flat spacetime $dt/d\tau = 1$, therefore the term that expresses the curvature of spacetime is Gm/c^2r . For a single fundamental particle at a distance equal to or greater than λ_c , this weak gravity approximation is accurate to better than about 1 part in 10^{40} .

The next plausibility test will be to see if the spacetime particle model can generate this spacetime curvature. If a fundamental particle is imagined as a point particle, and if spacetime is visualized as an empty void, then there is no obvious way that the particle can cause spacetime curvature. However, if the energetic spacetime field surrounds a rotating spacetime dipole wave which modulates the rate of time and proper volume, this is a promising combination to achieve spacetime curvature.

The spacetime field has finite characteristics such as a maximum frequency, a maximum strain and a maximum energy density. Therefore it follows from these boundary conditions that **spacetime should be a nonlinear medium for wave propagation**. The fundamental particle model (rotating dipole wave) produces a long range disturbance (standing waves) in the surrounding spacetime field. If the spacetime field is a nonlinear medium, then waves in spacetime should have both a linear component and a nonlinear component. The spacetime particle model has a strain amplitude of A_s at distance $r = \lambda_c$. The dynamic strain produced by the rotating dipole wave in the nonlinear spacetime field typically would be: $Strain = A_s \sin \omega t + (A_s \sin \omega t)^2 \dots$ There would also be higher order terms where A_s is raised to higher powers. However, since A_s is typically in the range of 10^{-20} for known fundamental particles, we will calculate an approximation which ignores powers higher than the square term. Therefore the dominant linear component is $A_s \sin \omega t$ and the much weaker nonlinear component is $(A_s \sin \omega t)^2$. The physical interpretation of this is that the distortion of the spacetime field produced by the presence of a spacetime particle (fermion) has a linear component associated with

the particle's electric field and a nonlinear component associated with the particle's gravitational field. We will first examine the nonlinear (gravitational) component.

$$(A_s \sin \omega t)^2 = \frac{1}{2} A_s^2 - \frac{1}{2} A_s^2 \sin 2\omega t \quad (11)$$

Equation (11) expands, this nonlinear component to reveal a non-oscillating term A_s^2 and a term that is oscillating at twice the Compton angular frequency $A_s^2 \sin 2\omega t$. This oscillating component of gravity is essential for the generation of curved spacetime and is a prediction of this spacetime model of gravity. However, this oscillating component is not measurable and will not be discussed further.

At this point we are going to pause for a moment and explain that the following analysis is initially going to be somewhat simplified. It will result in the correct magnitude of forces, but the implied vector direction of the gravitational force will initially be wrong. However, this analysis is valuable because it introduces important correct concepts in a simplified way. Later a revised analysis will be offered which is based on pressure differences. This will give the same magnitude of forces but with the correct vector.

We know the linear amplitude (A_s) and nonlinear amplitude (A_s^2) at distance $r = \bar{\lambda}_c$ measured from the center of the particle. However, how does this nonlinear amplitude change with distance? Since we are dealing with amplitude, we will assume the amplitude decreases inversely with distance and it must match the known amplitude (A_s^2) at distance $r = \bar{\lambda}_c$. To achieve this match, the non-oscillating distortion of spacetime must scale inversely with the number N of reduced Compton wavelengths $\bar{\lambda}_c$ units measured from the center of the particle model. This is said because $N = 1$ at $r = \bar{\lambda}_c$ if we define $N \equiv r/\bar{\lambda}_c$.

Combining these factors, the non-oscillating gravitational amplitude should decrease with $1/N$. We can then define a new amplitude associated with the non-oscillating distortion of spacetime: $A_G \equiv A_s^2/N$. Next we find the magnitude of A_G .

$$A_G = \frac{A_s^2}{N} = \left(\frac{L_p^2}{\bar{\lambda}_c^2} \right) \left(\frac{\bar{\lambda}_c}{r} \right) = \frac{Gm}{c^2 r} \quad (12)$$

This is an important success for the spacetime model of particles. When we evaluate the non-oscillating distortion of spacetime produced by spacetime being a nonlinear medium, we obtain the weak gravity curvature of spacetime induced by a single fundamental particle. Since the gravitational effect is extremely weak for any of the known fundamental particles even at distance $\bar{\lambda}_c$, this is virtually exact to an accuracy better than 1 part in 10^{40} . Finally, it is usually assumed that matter causes curved spacetime. However, the proposed model implies that waves in spacetime cause both matter and a non-oscillating strain in spacetime we know as curved spacetime.

4.3 Gravitational and Electrostatic Force Test

Next we will calculate the magnitude of the gravitational force between two of the same spacetime particles, each with energy E_i . For this calculation, we will use Eq. (3) and make the following substitutions: $A = A_G = Gm/c^2r$, $\omega = \omega_c = c/\lambda_c$, $Z = Z_s = c^3/G$, $\lambda_c = \hbar c/E_i = \hbar/mc$ $a = k\lambda_c^2$

$$F_G = \frac{kA_G^2 \omega_c^2 Z_s a}{c} = k \left(\frac{Gm}{c^2 r} \right)^2 \frac{c^2}{\lambda_c^2} \frac{c^3}{G} \frac{\lambda_c^2}{c} = k \frac{Gm^2}{r^2} \quad (13)$$

Therefore we have successfully obtained the magnitude of the gravitational force between two of the same particles $m_1 = m_2$ if we assume $k = 1$.

Next we will calculate the magnitude of the force for the linear term (the first order effect). We know that at distance $r = \lambda_c$ the strain amplitude is $A_s = L_p/\lambda_c$. Again we assume that it decreases inversely with distance which implies $1/N$ scaling. Combining these we obtain an amplitude that will be designated $A_E = kA_s/N = kL_p/\lambda_c N$. Another substitution that will be used is Planck charge: $q_p = \sqrt{4\pi\epsilon_0\hbar c}$.

$$F_E = \frac{kA_E^2 \omega_c^2 Z_s a}{c} = k \left(\frac{L_p}{\lambda_c N} \right)^2 \frac{c^2}{\lambda_c^2} \frac{c^3}{G} \frac{\lambda_c^2}{c} = k \frac{\hbar c}{r^2} = k \frac{q_p^2}{4\pi\epsilon_0 r^2} \quad (14)$$

Therefore when we assume $A = A_E = kL_p/\lambda_c N$ and $k = 1$, then we obtain the Coulomb force equation that corresponds to the magnitude of the electrostatic force between two electrically charged particles which each have Planck charge ($q = q_p = \sqrt{4\pi\epsilon_0\hbar c}$). Planck charge is about 11.7 times larger ($\alpha^{-1/2}$ times larger) than elementary charge e . It is not surprising that this calculation would result in the force generated by Planck charge and not the force generated by elementary charge e . We are actually calculating the theoretical maximum electrostatic force which assumes a coupling constant equal to 1. For electrostatic force, Planck charge corresponds to a coupling constant of 1 whereas elementary charge e is known to have a coupling constant equal to α , the fine structure constant. The source of α is unknown. We will accept Planck charge as the more fundamental value of charge for a comparison of gravitational and electrostatic forces. The symbol F_E will indicate the force between two Planck charge spacetime particles. Later some equations will be converted to elementary charge e . The symbol F_e will be used to indicate the force between two elementary charge e spacetime particles.

Previously we assumed the simplified case of two of the same energy particles. We will next assume two spacetime particles with different energies (energy E_1 and E_2). Then there would be two different reduced Compton wavelengths λ_{c1} and λ_{c2} which results in a single separation distance r having two different values of N which will be designated as $N_1 = r/\lambda_{c1}$ and $N_2 = r/\lambda_{c2}$. Also there would be two

different strain amplitudes $A_{s1} = L_p/\lambda_{c1}$ and $A_{s2} = L_p/\lambda_{c2}$ as well as a composite area $a = k\lambda_{c1}\lambda_{c2}$.

$$F_G = k \left(\frac{A_{s1}^2 A_{s2}^2}{N_1 N_2} \right) \left(\frac{c^2}{\lambda_{c1} \lambda_{c2}} \right) \left(\frac{c^3}{G} \right) \left(\frac{\lambda_{c1} \lambda_{c2}}{c} \right) = k \frac{G m_1 m_2}{r^2} \quad (15)$$

$$F_E = k \left(\frac{A_{s1} A_{s2}}{N_1 N_2} \right) \left(\frac{c^2}{\lambda_{c1} \lambda_{c2}} \right) \left(\frac{c^3}{G} \right) \left(\frac{\lambda_{c1} \lambda_{c2}}{c} \right) = k \frac{q_p^2}{4\pi\epsilon_0 r^2} \quad (16)$$

Note that the only difference between the intermediate portion of (15) and (16) is that the gravitational force Eq. (15) has the strain amplitude terms squared ($A_{s1}^2 A_{s2}^2$) and the electrostatic force Eq. (16) has the strain amplitude terms not squared ($A_{s1} A_{s2}$). The tremendous difference between the gravitational force and the electrostatic force is predominantly due to a difference in exponents. For example, an electron has strain amplitude of $A_s \approx 4.18 \times 10^{-23}$. Therefore the vast difference between the gravitational force and the electrostatic force comes from the difference in exponents: $(A_s^2)^2 \approx 10^{-90}$ versus $A_s^2 \approx 10^{-45}$. Other factors such as α are relatively unimportant.

4.4 Unification of Forces

The spacetime model of the universe predicted that gravity was a nonlinear effect that scaled with wave amplitude squared (higher powers ignored) while the electrostatic force scales with wave amplitude to the first power. This is a tangible step towards the unification of forces. While Eqs. (13–16) show this square exponent relationship, a search was initiated for equations that would better demonstrate the predicted difference in exponents between these two forces. This difference in exponents is most apparent when the force equations are expressed in dimensionless Planck units and the separation distance is given using N , the number of reduced Compton wavelengths λ_c which corresponds to the number of particle radius units. When force magnitude is expressed in dimensionless Planck units, this will be designated with an underline such as: $\underline{F} = F/F_p$. This represents a ratio between the specified force F and Planck force $F_p = c^4/G$ which is the largest force that spacetime can exert [13]. For example Planck force is the force between two of the same size black holes as they are about to merge (ignoring a numerical factor near 1). Similarly, energy in dimensionless Planck units will be $\underline{E} = E/E_p$ where Planck energy is $E_p = \sqrt{\hbar c^5/G}$. When a particle's energy is expressed in dimensionless Planck units, it is a ratio between the particle's energy and the largest energy that a quantized particle can possess. In addition to previously mentioned substitutions, the following substitutions will be used: $m_1 = m_2$, $k = 1$ and $A_s = L_p/\lambda_c = E/E_p = \underline{E}$.

$$\underline{F}_G = \frac{F_G}{F_p} = \frac{kA_G^2 \omega_c^2 \mathcal{Z}_s a}{cF_p} = \left(\frac{A_s^2}{N}\right)^2 \frac{c^2}{\tilde{\lambda}_c^2} \frac{c^3}{G} \frac{\tilde{\lambda}_c^2}{c} \frac{G}{c^4} = \frac{\underline{E}^4}{N^2} \quad (17)$$

$$\underline{F}_E = \frac{F_E}{F_p} = \frac{kA_E^2 \omega_c^2 \mathcal{Z}_s a}{cF_p} = \left(\frac{A_s}{N}\right)^2 \frac{c^2}{\tilde{\lambda}_c^2} \frac{c^3}{G} \frac{\tilde{\lambda}_c^2}{c} \frac{G}{c^4} = \frac{\underline{E}^2}{N^2} \quad (18)$$

Equations (17, 18) can be written as $\underline{F}_G N^2 = \underline{E}^4$ and $\underline{F}_E N^2 = \underline{E}^2$ which are plotted in Fig. 1. This is a log-log graph that uses dimensionless Planck units of force and energy. To give a sense of the energy scale in dimensionless Planck units, three familiar energies are designated. These are: Planck energy $\underline{E} = 1$, an electron's energy $\underline{E} = 4.18 \times 10^{-23}$ and a muon's energy $\underline{E} = 8.65 \times 10^{-21}$. Planck energy is the largest energy that a particle with quantized spin can have. If a photon or fermion had Planck energy, it would form a black hole.

The Y axis is values of the product $\underline{F} N^2$ which is force in dimensionless Planck units (either \underline{F}_E or \underline{F}_G) times N^2 . The equation $\underline{F}_E N^2 = \underline{E}^2$ assumes both particles have Planck charge therefore a coupling constant of 1. The close dashed line shows the force that would be exerted if both particles have charge e rather than charge q_p . This dashed line is a factor of α less than the Planck charge line but on this log-log graph a factor of 137 is small when the entire Y axis scale covers a factor of 10^{100} .

Figure 1 is best understood with some examples. Since both particles have the same radius ($\tilde{\lambda}_c$), we will initially make the assumption that the two particles are separated by this distance ($r = \tilde{\lambda}_c$ and $N = 1$ therefore $F_G = \underline{E}^4$ and $F_E = \underline{E}^2$). This is actually an unrealistic assumption because at this distance quantum mechanics becomes dominant and the uncertainty in position prevents a precise designation of position. Also the work done bringing two charged particles this close together would substantially increase the energy of the two particles and distort the forces. However, it is possible to assume $r = \tilde{\lambda}_c$ if we think of this as merely an extrapolation from a longer distance to a distance equal to the radius of the spacetime particle model. At this important separation distance we obtain the following relationships:

$$F_G = \underline{F}_E^2 \quad (19)$$

$$F_G/F_E = F_E/F_p \quad (20)$$

Equation (19) is so important that it needs to be restated in words. Assuming two of the same energy particles with charge $q = q_p$ and separated by $r = \tilde{\lambda}_c$, the gravitational force equals the square of the electrostatic force when both forces are in dimensionless Planck units. Also, Eq. (20) states that at this important separation distance, the ratio of the gravitational force to the electrostatic force equals the ratio of the electrostatic force to Planck force. This implies that at $r = \tilde{\lambda}_c$ a symmetry exists between the gravitational force, the electrostatic force and Planck force.

If these forces are assumed to be transferred by the exchange of virtual photons, gravitons or the geometry of spacetime, then the distance $\tilde{\lambda}_c$ should not be particularly important and there should be no exponent relationship between the

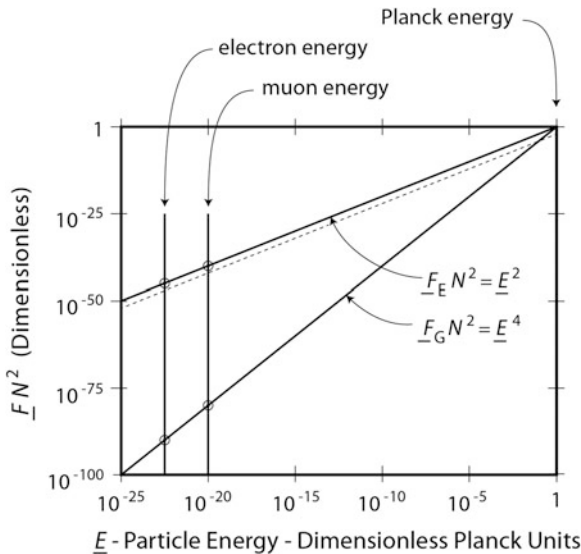


Fig. 1 Comparison of forces between two hypothetical fundamental particles, each with Planck charge and the same mass/energy. Underlined symbols \underline{F}_E , \underline{F}_G , and \underline{E} are in dimensionless Planck units. The plotted equations relate dimensionless electrostatic force \underline{F}_E and gravitational force \underline{F}_G to particle energy \underline{E} and the number N of reduced Compton wavelengths separating particles

gravitational and electrostatic forces. The spacetime particle is stabilized by an interaction with the surrounding spacetime field. This produces distortions in the spacetime field which extend into the surrounding spacetime and scale as a function of $\bar{\lambda}_c$. Details of these external distortions have not been discussed before, but they give rise to curved spacetime, electric/magnetic fields and de Broglie waves all of which scale with $\bar{\lambda}_c$. These are large subjects beyond the scope of this paper. However, these and all the concepts presented in this paper are explained in greater detail in the online book titled **The Universe Is Only Spacetime** [14].

The equation $\underline{F}_G = \underline{F}_E^2$ clearly shows the square relationship between forces at the specific separation distance of $r = \bar{\lambda}_c$ for $m_1 = m_2$ and $q = q_p$. Equation (21) below shows that when separation distance is expressed as N multiples of $\bar{\lambda}_c$, the square force relationship exists at arbitrary distance. To bring out this square relationship, Eq. (21) is written in a way that does not cancel some terms. Equation (22) is the same as (21) except it is rewritten to express the ratio between forces F_G/F_E and duplicate terms are canceled.

$$\left(\frac{F_G}{F_p} N^2\right) = \left(\frac{F_E}{F_p} N^2\right)^2 \quad (21)$$

$$\frac{F_G}{F_E} = \frac{F_E}{F_p} N^2 \quad (22)$$

So far the electrostatic force equations have assumed Planck charge as implied by the symbol F_E . Since $q_p^2 = e^2/\alpha$, the conversion to the force exerted between two elementary charges e is: $F_E = F_e/\alpha$. For example, Eq. (22) becomes Eq. (23) below.

$$\frac{F_G}{F_e} = \frac{F_e N^2}{F_p \alpha^2} \quad (23)$$

Equation (23) applies not only to charged leptons such as electrons or muons, but it can also be used to express the ratio of forces between two of the same hadrons, each with charge $\pm e$. For hadrons, the reduced Compton wavelength of the entire hadron is used. For example, the force ratio between two protons at any distance is $F_G/F_e \approx 8.1 \times 10^{-37}$. The right side of the Eq. (23) is also independent of separation because of offsetting effects of F_e and N^2 .

Until now the forces have only been between two fundamental particles. However these forces are additive. Every particle in body A interacts with every particle in body B . The total of all these individual forces add up to the total gravitational and electrostatic forces between bodies A and B (still assuming weak gravity). A goal for the future will be to see if incorporating additional nonlinear effects achieves the exact equations of GR.

It is often said that gravity was united with the other forces at the start of the Big Bang when all the particles had Planck energy. Figure 1 shows that indeed the electrostatic and gravitational force graphs intersect (the same magnitude of force) when particle energy equals Planck energy $\underline{E} = E_p/E_p = 1$. However, the point of this graph and analysis is that even today when $E \neq E_p$ there is still a unification between the gravitational and electrostatic forces. For example, the electrostatic force graph line in Fig. 1 is the square root of the gravitational force graph line. The vast difference in the magnitudes of these forces comes from a simple difference in exponents. This relationship was previously unnoticed until the missing assumption (the universe is only spacetime) was adopted. The existence of these simple relationships provides support for this assumption and the proposed spacetime particle model.

The previous explanation was simplified. It contained correct components, but the model implied the continuous emission of waves and a repulsive force. The more complete explanation takes two chapters in the online companion book [14] and therefore is beyond the scope of this paper. However, a brief explanation of the key conceptual points will be given here. The proposed particle model has energy density which can be calculated using Eq. (4). Energy density U and pressure \mathbb{P} both have units of $\text{kg}/\text{m}^2 \text{ s}$. Since the spacetime particle model has energy propagating at the speed of light in a confined volume, the energy density is directly equated to pressure. For example, an electron has a pressure of about $10^{24} \text{ N}/\text{m}^2$ which produces a force of about 0.2 N over the area of $\tilde{\lambda}_c^2$ for an electron. An electron is stable because its amplitude, frequency etc. interact with the surrounding spacetime field and achieve an offsetting pressure which stabilizes the structure.

In a gravitational field there is a gradient in the rate of time and proper volume (curved spacetime). The curved spacetime gradient affects the pressure exerted on opposite sides of an electron or other spacetime particle. This unequal pressure on opposite sides of the particle produces a net force. This net force is the gravitational force with the correct direction and magnitude. Even though gravity appears to be a force of attraction, it actually results from an imbalance in pressure which is a repulsive force exerted by the spacetime field.

This explanation involving pressure can be restated in a way that emphasizes the rotating dipole wave that forms a spacetime particle. The rotation occurs in curved spacetime which results in a type of modulation which incorporates many of the elements of the “simplified” explanation previously given.

4.5 Point Particle Test

Perhaps the biggest objection to the spacetime particle model is the fact that the model implies that fundamental particles have volume and internal structure. High energy collision experiments [15] seem to imply that an electron cannot be larger than roughly 10^{-18} m. Highly relativistic electrons can also probe the internal structure of a proton which has a radius of about 10^{-15} m. How can a particle with a radius larger than 10^{-13} m probe the internal structure of a proton with a radius of 10^{-15} m? Is the relatively large size of an electron not conclusive proof that the spacetime model of fundamental particles must be wrong? To analyze this question it is necessary to analyze the experiments more carefully. However, first it is necessary to add one characteristic to the spacetime particle model.

An analogy is going to be made between the communication that takes place between two entangled photons and the communication that takes place within a single spacetime particle. The single spacetime particle possesses quantized angular momentum of $\hbar/2$. It is not possible to momentarily interact with less than the entire quantized angular momentum. The interaction is all or nothing. If the probability of an interaction results in “nothing”, then the two rotating distortions of spacetime merely pass through each other and there is no collision. There would be some electrostatic deflection but there would be no classical collision that would be expected if both particles were elastic spheres with a radius of 3.86×10^{-13} m. If there is a strong interaction (collision) the quantization implies that the internal communication within the spacetime particle must be instantaneous—just like the communication between entangled particles. The “news” of the collision is transferred instantaneously throughout the volume of the quantized wave and gives it particle-like properties. This is purely an internal property that allows the distributed spacetime wave with quantized angular momentum to respond to a perturbation as a single unit. No external information can be communicated faster than the speed of light because of this property.

The spacetime particle model is merely a rotating distortion of spacetime existing in a sea of spacetime waves that lack angular momentum. This is not a physical object like a vibrating string or a hard sphere with definable dimensions. The spacetime particle model has zero physical radius if the expectation is an object other than spacetime. Instead, an electron is essentially a quantum of angular momentum which produces a rotating distortion of the spacetime field. The amplitude, frequency, distribution and size of this rotating distortion of spacetime can change depending on the experiment or boundary conditions. For example, when an electron is bound to a proton to form a hydrogen atom, the electron loses energy and experiences different boundary conditions that change its volume and distribution compared to an isolated electron.

Similarly, colliding electrons also change their characteristics. Suppose that we imagine two electrons with internal energy of $E_i \approx 0.5 \text{ MeV}$ colliding with kinetic energy of $E_k \approx 50 \text{ GeV}$. If they do interact (collide) the kinetic energy E_k is momentarily added to the spacetime particle's internal energy producing a new total energy of $E_i + E_k$. This would momentarily increase the rotational frequency to $\omega_{ck} = \hbar(E_i + E_k)$ and decrease the radius to $\tilde{\lambda}_{ck} = \hbar c / (E_i + E_k)$ where $\tilde{\lambda}_{ck}$ is the designation used to indicate the momentary reduced Compton wavelength when the colliding spacetime particle has absorbed additional energy E_k . For a 50 GeV collision, this momentarily decreases the radius by a factor of about 100,000 to $\tilde{\lambda}_{ck} \approx 10^{-18} \text{ m}$. This increase in energy and decrease in radius maintains the angular momentum at $\hbar/2$. An uncertainty principle calculation for an ultra-relativistic collision with special relativity $\gamma \approx E_k/mc^2$ has a momentum uncertainty of $\Delta p \approx \gamma mc$ and the uncertainty in position of $\Delta x \approx \frac{1}{2} \hbar c / E_k \approx \frac{1}{2} \tilde{\lambda}_{ck}$. Considering that there can also be partial overlap of these spacetime particles, it can be seen that the momentary radius $\tilde{\lambda}_{ck}$ is comparable to the uncertainty of the experiment. The electron's radius can never be measured because $\Delta x \approx \tilde{\lambda}_{ck}$. It is a classic case of the experiment distorting the property being measured and invalidating the measurement.

The maximum size of an electron has also been estimated by Dehmelt [16, 17] from a comparison of the theoretical and experimental value of the electron's anomalous magnetic dipole moment (electron's g -factor). The QED theoretical g -factor calculation assumes the electron has zero radius and this theoretical value agrees with the experimental value to about 10 significant figures. This virtually exact agreement between experiment and theory is interpreted as implying that the electron must have a physical radius smaller than 10^{-22} m .

However, this reasoning does not apply to the proposed spacetime model of an electron. This model merely organizes a small part of the chaotic Planck amplitude waves in spacetime into a rotating quantized unit. The spacetime model of an electron has spatial and temporal strain with amplitude of $A_s \approx 4.18 \times 10^{-23}$. To put this incredibly small strain of spacetime in perspective, the rate of time difference (distortion) within an electron is so small that two clocks which differed by this factor would take 50,000 times the age of the universe before they differed by one second. Similarly, the spatial distortion within an electron is so small that

expanding space by this factor would enlarge the radius of Jupiter's orbit by about the radius of a hydrogen atom. These considerations imply that an electron would produce a virtually undetectable difference between the experimental and theoretical values of the g-factor.

One final point concerning particle size. The highly successful Dirac equation [18] also supports this model. The Dirac equation assumes that an electron is always propagating at the speed of light. The average speed is less than c because the motion is mathematically characterized as $\pm c$. Erwin Schrodinger interpreted the Dirac equation. References [19, 20] as implying that a point charge is undergoing "zitterbewegung" (a trembling motion) at the speed of light. The frequency is equal to ω_c and the distributed volume of the motion can be interpreted as having dimensions comparable to λ_c . Other physicists [21–25] have since proposed variations of the Schrodinger model, also with dimensions on the order of λ_c .

The proposed spacetime particle model satisfies the Dirac equation and has both similarities and differences compared to the Schrodinger model. The similarity is that the spacetime wave model has speed of light propagation within a volume with radius λ_c at a frequency of ω_c . The difference is that there is no point particle. Instead a dipole wave in spacetime with quantized angular momentum **fills** a volume with radius λ_c and undergoes a somewhat chaotic propagation at the speed of light.

4.6 Inertia Test

Previously, we saw that the spacetime particle model passes the test of having the correct energy. When we substituted ω_c , λ_c , and A_s into Eq. (5) we obtained $E = kE_i$. However, is it fair to assume that merely because we obtained the correct energy this automatically translates into obtaining the correct inertia (rest mass)? To examine the origin of inertia, we will start with a thought experiment. Suppose that there was a hypothetical box with 100 % reflecting internal walls. Any light trapped in such a box is "confined light". A freely propagating photon is a massless particle but what about a confined photon in the 100 % reflecting box? Suppose that the box initially contains an electron and a positron. Then after some time these two particles interact and their energy is converted to two confined gamma ray photons. Would there be any difference in the box's total inertia when the energy is in the form of confined particles compared to the same energy in the form of confined photons? If there is any difference, then this would be a violation of the conservation of momentum. This implies that a "confined photon" acquires inertia that is indistinguishable from a particle's inertia even under relativistic conditions.

The mathematical proof that confined light exhibits inertia is available [14] but the concept is easy to explain. Suppose that two 100 % reflecting mirrors are aligned to form an optical resonant cavity similar to a laser. It would be possible to have a specific amount of energy in the form of electromagnetic (EM) radiation confined between the two reflectors. Now suppose that the two aligned mirrors are

accelerated in a direction parallel to the cavity's optical axis. Then we can designate one mirror as the "front" mirror and one mirror as the "rear" mirror. During the time that it takes for the light to propagate from the front to rear mirror, the optical cavity has some change in velocity. The light striking the rear mirror exerts a slightly larger force on the rear mirror than was exerted on the front mirror. This difference is due to the different Doppler shifted frequencies at the two mirrors. When this force difference is calculated, it exactly equals the inertial force that would be expected for a mass of equal energy. This equivalence extends even to relativistic conditions. In other words, photons are only massless when they are freely propagating. Confined photons have mass.

The model of a spacetime particle has a Planck amplitude wave propagating at the speed of light but circulating within a spherical volume one Compton wavelength in circumference. Even though there are no physical reflectors (other than the surrounding spacetime field), this fermion model meets the criteria of energy propagating at the speed of light but confined to a specific frame of reference. Therefore accelerating the spacetime model of a fermion with internal energy E_i exhibits the same inertial force F as accelerating an equal energy of confined photons. The conservation of momentum requires that there is an exact match between the inertia of a particle and an equal amount of energy in the form of confined photons.

5 Charge, Electric Fields and Black Holes

So far, it has been shown that adopting the assumption that the universe is only spacetime gives new insights into particles and forces. However, if the single building block of everything in the universe is the energetic spacetime field, then the implication is that all of the effects associated with electrical charge, electric fields, etc. should also be able to be explained using only the properties of spacetime. This is a severe test of the starting assumption.

To obtain an insight into the electrical properties of nature, we will express the electrical potential \mathbb{V} (the voltage relative to neutrality) and the electric field \mathbb{E} in dimensionless Planck units because Planck units are fundamentally based on the properties of spacetime. In both cases we will assume Planck charge q_p . Therefore: $\mathbb{V}_E \equiv q_p / 4\pi\epsilon_0 r$ and $\mathbb{E}_E \equiv q_p / 4\pi\epsilon_0 r^2$. Converting these to dimensionless Planck units (underlined) we divide by Planck voltage $\mathbb{V}_p = \sqrt{c^4/4\pi\epsilon_0 G} \approx 10^{27}$ V and Planck electric field $\mathbb{E}_p = \sqrt{c^7/4\pi\epsilon_0 \hbar G^2}$.

$$\underline{\mathbb{V}}_E = \frac{\mathbb{V}_E}{\mathbb{V}_p} = \frac{\sqrt{4\pi\epsilon_0 \hbar c}}{4\pi\epsilon_0 r} \sqrt{\frac{4\pi\epsilon_0 G}{c^4}} = \sqrt{\frac{\hbar G}{c^3}} \frac{1}{r} = \frac{L_p}{r} \quad (24)$$

$$\underline{\mathbb{E}}_E = \frac{\mathbb{E}_E}{\mathbb{E}_p} = \frac{\sqrt{4\pi\epsilon_0 \hbar c}}{4\pi\epsilon_0 r^2} \sqrt{\frac{4\pi\epsilon_0 \hbar G^2}{c^7}} = \frac{\hbar G}{c^3 r^2} = \frac{L_p^2}{r^2} \quad (25)$$

What is the physical interpretation of $\mathbb{V}_E = L_p/r$ and $\mathbb{E}_E = L_p^2/r^2$? First, an electrical charge only affects the spatial properties of spacetime because there is no time term in Eqs. (24, 25). Second, only the radial spatial dimension is affected. Third, the dimensionless ratio L_p/r is proposed to represent the slope of a spatial strain in spacetime. We also know that an electric field is non-reciprocal. A polarized distortion of spacetime is required since there is a difference when we proceed from + to - compared to the opposite direction. Spacetime must exhibit different properties proceeding in opposite directions.

The proposed spacetime based model of an electric field is a polarized (non-reciprocal) distortion of space such that the one-way distance (time of flight) between a positive and negative charge would be slightly different proceeding from + to - compared to the reverse direction. It is not known which direction is shorter. However, the round trip distance should be unchanged. Even though there are some unknowns, we can calculate the magnitude of the effect. To quantify the effect on spacetime produced by a charge, we will define a proposed new constant, designated eta (η). This constant converts units of electrical charge (coulomb) into a polarized strain of space with dimensions of length. This relationship can be extracted from Eq. (24). The validity of this conversion factor will be determined by testing. From Eq. (24) we have:

$$\begin{aligned}\mathbb{V}_E &= \frac{q_p}{4\pi\epsilon_0 r} = \frac{L_p \mathbb{V}_p}{r} \\ q_p &= \frac{L_p \mathbb{V}_p 4\pi\epsilon_0 r}{r} = L_p \sqrt{\frac{4\pi\epsilon_0 c^4}{G}} \\ \eta &\equiv \sqrt{\frac{G}{4\pi\epsilon_0 c^4}} = \frac{L_p}{q_p} \approx 8.61 \times 10^{-18} \text{ m/C}\end{aligned}\quad (26)$$

We will first test the conversion of several constants incorporating electrical charge. These are: elementary charge e , the Coulomb force constant $1/4\pi\epsilon_0$ ($\text{m}^3 \text{kg/s}^2 \text{C}^2$), the magnetic permeability constant $\mu_0/4\pi$ (kg m/C^2), and the impedance of free space Z_0 (kg m/s C^2). To eliminate $1/\text{C}^2$ requires multiplying these constants by $1/\eta^2$. We will also use: $\alpha = e^2/4\pi\epsilon_0\hbar c$

$$e(\eta) = \sqrt{\alpha 4\pi\epsilon_0 \hbar c} \sqrt{\frac{G}{4\pi\epsilon_0 c^4}} = \sqrt{\alpha \hbar G} = \sqrt{\alpha} L_p \quad (\text{units: m}) \quad (27)$$

$$\frac{1}{4\pi\epsilon_0} \left(\frac{1}{\eta^2} \right) = \left(\frac{1}{4\pi\epsilon_0} \right) \left(\frac{4\pi\epsilon_0 c^4}{G} \right) = \frac{c^4}{G} = F_p \quad (\text{units: N}) \quad (28)$$

$$\frac{\mu_0}{4\pi} \left(\frac{1}{\eta^2} \right) = \left(\frac{1}{4\pi\epsilon_0 c^2} \right) \left(\frac{4\pi\epsilon_0 c^4}{G} \right) = \frac{c^2}{G} \quad (\text{units: kg/m}) \quad (29)$$

$$Z_o \left(\frac{1}{\eta^2} \right) = \left(\frac{1}{\varepsilon_o c} \right) \left(\frac{4\pi \varepsilon_o c^4}{G} \right) = 4\pi \frac{c^3}{G} = 4\pi Z_s \quad (\text{units: kg/s}) \quad (30)$$

We will perform several tests before commenting. From the above $\mu_o = 4\pi c^2/G$, $\varepsilon_o = G/4\pi c^4$ and $Z_o = 4\pi c^3/G$. When we convert: $c = \sqrt{1/\varepsilon_o \mu_o}$ and $Z_o = \sqrt{\mu_o/\varepsilon_o}$ to the equivalent equations substituting the spacetime conversions, the equations are still correct. Also, we will test the conversion by calculating the force between two electrons (charge e) two different ways. Equation (31) below uses the standard Coulomb law and Eq. (32) uses the spacetime conversions for $1/4\pi\varepsilon_o$ and e . They give the same answer.

$$F_e = \frac{e^2}{4\pi\varepsilon_o r^2} = \frac{\alpha\hbar c}{r^2} \quad (31)$$

$$F_e = \frac{F_p \alpha L_p^2}{r^2} = \frac{c^4 \alpha \hbar G}{G r^2 c^3} = \frac{\alpha\hbar c}{r^2} \quad (32)$$

In Eq. (28), it is reasonable that the Coulomb force constant $1/4\pi\varepsilon_o$ should convert to Planck force c^4/G . Planck force is the largest force that spacetime can exert. However, the most important revelation is Eq. (30). The impedance of free space ($Z_o = \mathbb{E}/\mathbb{H}$) converts to c^3/G , the impedance of spacetime obtained from GR (ignore 4π). Since Z_o converts to Z_s , this implies that EM radiation experiences the same impedance as gravitational waves which propagate in the medium of spacetime. The implication is that photons also are waves propagating in the medium of the spacetime field. Photons are not packets of energy propagating THROUGH the empty void of spacetime. Photons are waves with quantized angular momentum propagating IN the medium of the spacetime field.

If EM radiation propagates in the medium of spacetime, does this mean that spacetime is the new aether? Spacetime does have energy density and c^3/G impedance that permits waves to propagate at the speed of light but there are also important differences compared to the properties attributed to the aether. First, a photon possesses angular momentum which is quarantined by the superfluid spacetime field. This produces quantization of angular momentum. Photons acquire a particle-like property because quantized angular momentum also affects energy. Absorption results in a collapse of waves so that the entire angular momentum and energy are deposited in a single absorbing unit (atom, molecule, etc.). The superfluid spacetime field causes “wave-particle duality”.

A second difference between the aether and the spacetime field is that the aether was presumed to have a frame of reference which should have been detected by the Michelson-Morley experiment. The spacetime field is strongly interacting dipole waves propagating at the speed of light. It is not possible to detect motion relative to this medium. For example, ε_o , μ_o and G are properties of the spacetime field and are unchanged in all frames of reference. Also, suppose that it was possible to do a

Michelson-Morley experiment using gravitational waves rather than light. Gravitational waves are undeniably propagating in the medium of spacetime and experience impedance of c^3/G . However, gravitational waves are always propagating at the speed of light, from all frames of reference. A Michelson-Morley experiment using gravitational waves would be unable to detect motion relative to the spacetime field. Similarly, if photons are a quantized wave propagating in the spacetime field, they also would be observed to always propagate at the speed of light. The explanation of this paradox is that particles, fields and forces are also spacetime and compensate (Lorentz transformations) to keep the locally measured speed of light constant.

Next we will attempt to quantify the magnitude of the distortion of spacetime produced by photons to see if it is experimentally measurable. To simplify the calculation and maximize the effect, we will imagine confining photons in the smallest possible volume for a given wavelength. Circularly polarized photons can exist in a cylindrical waveguide that is slightly larger than $1/2$ wavelength in diameter and further confined by two flat mirrors perpendicular to the cylindrical axis and separated by $1/2$ wavelength. This forms the smallest possible vacuum resonant cavity which we will call “maximum confinement”. The maximum oscillating electric field strength is at the center of the cavity and the electric field is zero at all the surfaces. Even though the cavity is $1/2 \lambda$ long and $1/2 \lambda$ in diameter with nonuniform electric and magnetic fields, a dimensional analysis plausibility calculation can make the simplifying assumption that the excitation (stressed spacetime) is uniform over a volume of λ^3 , and zero everywhere else. The energy of n photons is $E = n\hbar\omega$ and the energy density in λ^3 is $U = n\hbar\omega/\lambda^3 = n\hbar\omega^4/c^3$. Combine this with Eq. (4):

$$\begin{aligned} U &= \frac{A^2\omega^2Z_s}{c} = \frac{n\hbar\omega^4}{c^3} \\ A &= \sqrt{\left(\frac{n\hbar G}{c^3}\right)\left(\frac{\omega^2}{c^2}\right)} = \frac{\sqrt{n}L_p}{\lambda} = \frac{\Delta L}{\lambda} \\ \Delta L &= \sqrt{n}L_p \end{aligned} \tag{33}$$

The indication is that n coherent circularly polarized photons produce an oscillating length change of $\sqrt{n}L_p$ over a distance of λ if we assume a maximum confinement cavity. This is another prediction. To analyze this, suppose that we have a microwave cavity designed to achieve maximum confinement of a reduced wavelength of $\lambda = 0.1$ m. The cavity would be slightly larger than 0.314 m in diameter and the flat reflectors would be separated by 0.314 m. An interferometer with oppositely propagating beams would attempt to detect a polarized path length changed caused by the rotating electric field.

Without attempting to describe the experiment in more detail, it is possible to calculate whether the effect would be large enough to measure. Theoretically it is physically possible to detect length changes larger than Planck length ($\sim 10^{-35}$ m) [3–7]. However, current interferometer technology such as the LIGO experiment

can currently detect modulated length changes in the range of 10^{-18} m. Since $L_p \approx 10^{-35}$ m we would have to have $n \approx 10^{34}$ photons in the maximum confinement cavity to achieve a 10^{-18} m effect ($\sqrt{10^{34} \times 10^{-35}} \text{ m} \approx 10^{-18} \text{ m}$). If we assume a microwave cavity tuned for $\lambda = 0.1 \text{ m}$ ($\omega = 3 \times 10^9 \text{ s}^{-1}$) the energy of confined microwave photons would have to be about $3 \times 10^9 \text{ J}$. This experiment is beyond current technology.

However, all is not lost. Suppose that we imagine a thought experiment where it is possible to increase the number of the confined photons to any desired level. The spacetime based model of photons predicts that EM radiation should have a maximum intensity limit for a maximum confinement experiment where spacetime is simply not able to transmit a higher intensity. This would occur if the intensity reached the condition which demanded that the spatial displacement of spacetime (ΔL) equaled the reduced wavelength λ of the EM radiation causing the effect. In the case of microwave radiation with a reduced wavelength of 0.1 m, this would occur when $\Delta L = \lambda = 0.1 \text{ m}$. This is demanding 100 % modulation of the spacetime volume in the maximum confinement resonant cavity (ignoring numerical factors near 1).

This theoretical maximum intensity limit will be calculated. The critical number of photons n_c that achieves $\Delta L = \lambda$ is $n_c = E_c \lambda / \hbar c$ where the critical energy is designated E_c .

$$\begin{aligned} \Delta L &= \sqrt{n_c} L_p = \sqrt{\frac{E_c \lambda}{\hbar c}} \sqrt{\frac{\hbar G}{c^3}} \quad \text{set } \lambda = \Delta L \\ \Delta L &= \frac{GE_c}{c^4} = \frac{Gm_c}{c^2} = R_s \end{aligned} \quad (34)$$

Equation (34) gives the classical Schwarzschild radius $R_s = Gm_c/c^2$ of a black hole with energy of E_c . It is not necessary to do an experiment! The prediction that there should be a maximum intensity limit is confirmed by GR because the intensity which achieves 100 % modulation of spacetime (achieves $\Delta L = \lambda$) also forms a black hole which blocks further transmission of EM radiation. For example, assuming a reduced wavelength of 0.1 m, it would take about 10^{68} confined photons ($\sim 10^{43} \text{ J}$) to achieve $\Delta L = \lambda \approx 0.1 \text{ m}$. This energy in this radius achieves a black hole with a classical Schwarzschild radius of 0.1 m. For more information about the spacetime based model of a photon, see a related article titled: *Spacetime-Based Model of EM Radiation* [26].

Another hypothetical experiment would use a cubic vacuum capacitor consisting of two flat and parallel plates, each with dimensions $D \times D$ and separated by distance D . If the voltage on this capacitor is \mathbb{V} , then this voltage in dimensionless Planck units (underlined) would be $\underline{\mathbb{V}} = \mathbb{V}/\mathbb{V}_p$. A time of flight distance measurement across the capacitor would experience a path length difference of ΔL between opposite propagation directions. Using previously stated principles, the polarized strain equation is: $\Delta L = D\underline{\mathbb{V}}$. Since Planck voltage is about 10^{27} volts, even 10^6 V would be $\Delta L \approx 10^{-21} D$ and unmeasurable.

However, $\Delta L = D\mathbb{V}$ also predicts that the properties of spacetime specify a maximum possible voltage. At Planck voltage $\mathbb{V} = 1$, therefore the distortion is $\Delta L = D$. This is 100 % distortion of the volume within the cubic vacuum capacitor. The spacetime model of charge predicts that it should be impossible to exceed this voltage. A calculation similar to Eq. (34) shows that any size cubic vacuum capacitor would form a black hole with radius of $R_s = D$ when the voltage equals Planck voltage. Therefore this is another prediction of the spacetime-based model which is verifiable.

6 Summary and Conclusion

This paper attempts to show that it is plausible for the entire universe to be made of just 4 dimensional spacetime. The key step in this endeavor is that the large energy density of the vacuum implied by quantum electrodynamics and quantum chromodynamics is characterized as a sea of dipole waves in spacetime with spatial displacement amplitude of $\pm L_p$ (Planck length) and temporal displacement amplitude of $\pm T_p$ (Planck time). These undetectable small amplitude waves exist in spacetime which is a medium with impedance of $Z_s = c^3/G \approx 4 \times 10^{35} \text{ kg/s}$.

Therefore, the spacetime field is pictured as being a sea of these Planck amplitude waves at all frequencies up to Planck frequency. This achieves a vacuum energy density of about 10^{113} J/m^3 required to explain zero point energy. These waves have no angular momentum and would exhibit superfluid properties. Quantized angular momentum present in spacetime since the Big Bang is proposed to be isolated by the spacetime field into quantized units of $\hbar/2$ which are the fermions.

A model of a fundamental particle (fermion) has been suggested as a rotating dipole wave distortion of the spacetime field. This dipole wave in spacetime is propagating at the speed of light but is confined to a spherical volume one Compton wavelength in circumference. The rotation frequency is equal to the particle's Compton frequency ω_c and the radius is equal to the reduced Compton wavelength $\tilde{\lambda}_c$. An interaction with the surrounding spacetime field stabilizes this rotating wave.

This fermion model has quantifiable structure such as amplitude, frequency, radius, etc. Therefore it is possible to confirm that this particle model plausibly exhibits a particle's energy, angular momentum, inertia and ability to appear to be a point particle. This proposed model would also create a disturbance in the surrounding spacetime field. The nonlinear portion of the disturbance was shown to have amplitude corresponding to the weak gravity curvature of spacetime. The linear portion is proposed to be associated with the particle's electric field. Also the magnitude of the gravitational force was derived without making an analogy to acceleration. The model makes predictions about the electrostatic and gravitational forces. One prediction is that both forces scale as a fundamental function of $\tilde{\lambda}_c$. Equations (17–23) show that dramatic simplifications occur when separation is expressed as N multiples of $\tilde{\lambda}_c$. A second prediction is that these forces should be

related by a simple difference in exponents. Equations (15–21) support this prediction.

Electric and magnetic fields were also proposed to be a distortion of spacetime. A charge conversion constant $\eta \equiv L_p/q_p$ was derived with units of meter/coulomb. When this proposed constant is used to convert the Coulomb force constant $1/4\pi\epsilon_0$, it becomes Planck force c^4/G . Also, the impedance of free space Z_0 becomes the impedance of spacetime $Z_s = c^3/G$. The conclusion is that photons experience the same impedance as gravitational waves and therefore photons are proposed to be quantized waves propagating in the medium of the spacetime field. Another prediction of this model is that EM radiation produces a physical distortion of spacetime that would be measurable if the intensity could be made large enough. The prediction implies that there should be a set of conditions which achieve a maximum intensity limit. This transmission limit is confirmed because this limit corresponds to the condition which makes a black hole. Similarly, the spacetime model predicts that a vacuum capacitor has a maximum possible voltage. This limit corresponds to the energy density that forms a black hole. All these factors give a broad base of support for the proposed starting assumption—the universe is only spacetime.

References

1. Misner CW, Thorne KS, Wheeler JA (1973) *Gravitation*. W. H. Freeman and Company, New York, p 975
2. Milonni PW (1994) *The quantum vacuum: an introduction to quantum electrodynamics*. Academic Press, San Diego, pp 9–16, 49
3. Padmanabhan T (1987) Limitations on the operational definition of spacetime events and quantum gravity. *Class Quantum Gravity* 4:L107
4. Garay LJ (1995) Quantum gravity and minimum length. *Int J Mod Phys A* 10:145–166. [arXiv: gr-qc/9403008](https://arxiv.org/abs/gr-qc/9403008)
5. Baez JC, Olson SJ (2002) Uncertainty in measurements of distance. *Class Quantum Gravity* 19:L121–L125. [http://arxiv.org/abs/gr-qc/0201030](https://arxiv.org/abs/gr-qc/0201030)
6. Calmet X, Graesser M, Hsu SD (2004) Minimum length from quantum mechanics and general relativity. *Phys Rev Lett* 93:211101. [http://arxiv.org/abs/hep-th/0405033](https://arxiv.org/abs/hep-th/0405033)
7. Calmet X (2008) On the precision of length measurement. *Eur Phys J C* 54:501–505. [http://arxiv.org/abs/hep-th/0701073](https://arxiv.org/abs/hep-th/0701073)
8. Blair DG, McClelland DE, Bachor HA, Sandeman RJ (1991). In: Blair DG (ed) *The detection of gravitational waves*. Cambridge University Press, Cambridge, p. 45
9. Danaila I (2005) Three-dimensional vortex structure of a fast rotating Bose-Einstein condensate with harmonic-plus-quartic confinement. [http://arxiv.org/pdf/cond-mat/0503122.pdf](https://arxiv.org/pdf/cond-mat/0503122.pdf)
10. Madison KW, Chevy F, Wohleben W, Dalibard J (2000) Vortex lattices in a stirred Bose-Einstein condensate. [http://arxiv.org/abs/cond-mat/0004037](https://arxiv.org/abs/cond-mat/0004037)
11. Yarmchuk EJ, Gordon MJ, Packard RE (1979) Observation of stationary vortex arrays in rotating superfluid helium. *Phys Rev Lett* 43:214–217
12. Hobson A (2013) There are no particles, there are only fields. *Am J Phys* 81:211–223
13. Gibbons GW (2002) The maximum tension principle in general relativity. *Found Phys* 32:1891. [http://arxiv.org/pdf/hep-th/0210109v1.pdf](https://arxiv.org/pdf/hep-th/0210109v1.pdf)

14. Macken JA (2013) The universe is only spacetime. <http://onlyspacetime.com/>
15. Bender D et al (1984) Tests of QED at 29 GeV center-of-mass energy. *Phys Rev D*30:515–527
16. Dehmelt H (1988) A single atomic particle forever floating at rest in free space: new value for electron radius. *Physica Scripta* T22:102
17. Dehmelt H (1990) *Science* 4942:539–545
18. Dirac PAM (1958) The principles of quantum mechanics, Chaps. 11–12, 1st edn 1930, 4th edn 1958. Clarendon Press, Oxford
19. Schrödinger E (1930) Über die kräftefreie Bewegung in der relativistischen Quantenmechanik. *Sitzungsber. Preuss Akad Wiss Berlin, Phys Math Kl* 24:418–428
20. Schrödinger E (1931) Zur Quantendynamik des Elektrons. *Sitzungsber Preuss Akad Wiss Berlin, Phys Math Kl* 25:63–72
21. Huang K (1952) On zitterbewegung of the Dirac electron. *Am J Phys* 20:479–484
22. Barut AO, Bracken AJ (1981) Zitterbewegung and the internal geometry of the electron. *Phys Rev D*23:2454–2463; D24:3333–3342
23. Barut AO, Pavšic M (1987) Quantization of the zitterbewegung in the Schrödinger picture. *Class Quantum Gravity* 4:L131–L136
24. Maruani J (2012) The Dirac electron: spin, zitterbewegung, the Compton wavelength, and the kinetic foundation of rest mass. In: Nishikawa K et al (eds) vol 26. Springer, Berlin, pp 23–46 (Prog Theor Chem Phys B)
25. Maruani J (2013) The Dirac electron as a massless charge spinning at light speed: implications on some basic physical concepts. In: Hotokka M et al (eds) vol 27. Springer, Berlin, pp 53–74 (Prog Theor Chem Phys B)
26. Macken JA (2013) Spacetime-based model of EM radiation. In: Proceedings of SPIE 8832, the nature of light: what are photons? p 88320Q

A Zero Energy Universe Scenario: From Unstable Chemical States to Biological Evolution and Cosmological Order

Erkki J. Brändas

Abstract A Zero-Energy Universe Scenario (ZEUS) is portrayed and its implications are examined and clarified. The formulation is based on the algebra of observables, e.g. the momentum-energy and their canonical conjugate partner space-time. Operators represent them in quantum theory and classical canonical variables in nonquantum applications. Conjugate operator/variable arrays impart a united edifice for a zero-energy universe scenario, which corresponds to using a non-positive definite metric for the manifestation of unstable states as recently employed in the field of chemical physics. Analogous formulations within a general complex symmetric setting provide a compelling analogy between Einstein's theory of general gravity and Gödel's first incompleteness theorem. This scenario brings together up-to-date theories in chemical physics with modern research in biology, physics, and astronomy. This unification establishes an edifice for the various arrows of time as well as authenticates Darwin's Paradigm of Evolution from the microscopic realm to the cosmological domain.

Keywords Conjugate operators · Quantum-classical dichotomy · Time concepts · Gravitational interactions · Black holes · Zero energy scenario · Darwinian evolution · Gödel's first incompleteness theorem

1 Introduction

Is our universe finite or infinite? Are there multiple copies of our universe? How did the universe begin and how will it end? Does the world, as we know it, contain both a physical- and a mental part, and if so, how are they related in the process of evolution? Interweaved in this conundrum of fundamental problems waits

E.J. Brändas (✉)

Department of Chemistry—Ångström Laboratory, Institute for Quantum Chemistry,
Uppsala University, Box 518, 751 20 Uppsala, Sweden
e-mail: Erkki.Brandas@kemi.uu.se

corollaries and implications regarding the origin and emergence of life, the evolution of semiotic properties like language, mathematics, music, art, science etc., and in general extending the recognition to society, ecology and culture.

In addition to the ontological question about nature as an organisation subordinate to evolution, lie fundamental questions of a microscopic understanding of Darwinian evolution. For instance, when referring to natural phenomena we include the physical laws of nature, implying interactions between the constituents of matter. These interactions become gradually more complex for biological systems constituting nature's self-organisation with intrinsic modes of communication between life forms. The extended notion of communication, containing features like function, reception, submission, transmission, regulation and adaptation, starts already on the molecular intra-cell level and develops between cells, cellular aggregates, amongst protein segments, in 3D arrangements of folding and multi-subunit complexes, mapping concepts, perceptions and possibly thoughts on the neurological level in e.g. the teleodynamic development of the human brain.

There are several ways to provide a taxonomy for universes, e.g. observable universes and beyond, ending up with the Ultimate Ensemble or the mathematical universe hypothesis of the highest level according to Tegmark [1], or in the so-called parallel universe classification from branes and strings via Everett's Many Worlds interpretation to holographic multiverses, complex computer simulated multiverses culminating with the ultimate multiverse containing any mathematically possible universe that is commensurate with the appropriate physical laws, Greene [2]. While many models predict infinite universes, repeating themselves into parallel worlds, others connect with one of the many interpretations of quantum mechanics. Abstract mathematics defining any conceivable Theory of Everything (never mind that self-referential authentications seem to rule out the possibility of ToE's), will bring together hierarchies of multiverses to the highest category.

It goes beyond the focus of this article to examine the various pros and cons in support of the various arguments. Suffice it to say that a non-contradictory universe scenario should account for consistent size boundaries, commensurate with known quantum-classical physical laws, comprising a realistic evolution package from beginning to end, where the mental- and the physical parts are ontologically entangled. This portrayal should have built-in accounts of some of the currently most inexplicable paradoxes, such as the dark energy enigma responsible for the puzzling expansion of the universe, the abundance of particles over antiparticles and the commensuration between evolution, self-organization and the second law.

In advancing ZEUS, the Zero-Energy Universe Scenario,¹ we will build on earlier work on operator arrays of momentum-energy and their space-time conjugates to recover Einstein's law of general relativity. We will focus on the following questions: the Schwarzschild metric for a non-rotating black hole and extensions to rotational degrees of freedom (Kerr metric), the arrow of time, the gravitational matrix formulation and Gödel's incompleteness theorem. In particular the Paradigm

¹ The notion of “zero-energy universe” has been coined before, see note added in proof.

of Evolution comprises teleomatic- and teleonomic physical laws, merging communication and information—from molecules to life forms. This incorporates the genetic code and higher order semiotics (mathematics, language) affecting the theory of consciousness and artificial intelligence (AI). In conclusion we integrate the beginning and end of our Universe with the Paradigm of Evolution.

In passing we will touch upon open problems like fundamental symmetry violations connected with biomolecular homochirality and the problem of the absolute nature of the second law.

The article will be arranged as follows. In Sect. 1, the conjugate variables (operators) are introduced as the most natural and essential forms of Kantian perception. By ordering the units in a two separate, but interrelated matrix arrays, it is possible to derive Einstein's laws of special and general relativity, the latter extended in Sect. 3 to portray a combination of classical and quantum aspects of gravity including the line element for the Schwarzschild metric and a general quantum conception of a black hole. In paragraph 4 a novel formulation of the Gödel paradox related to his celebrated inconsistency theorem, is presented, in some detail, by using unconventional linear algebra and generalized eigenvalue theorems for complex symmetric matrices. It is an unexpected surprise that the mathematical formulation here becomes identical to the complex symmetric result of Sect. 3.

Employing an essentially identical formulation extended to arbitrary dimensions, the formalism is applied to condensed matter systems and to complex enough systems like biological organisations. It is advocated that the paradigm of evolution adds a teleonomic physical law, which by the definition of the word teleonomic, imparts processes, which owes it goal-directedness to the influence of an evolved program, contrasting present end-directed laws of physics, which in this nomenclature are automatically endowed and designated as teleomatic, see more below. Section 5 gives a brief overview of recent extensions to non-Hermitian quantum mechanics and so-called unstable states of the continuous spectra, of rising use in contemporary theoretical chemical physics.

Subsequent Sects. 6–10, concern the projection of these states in non-equilibrium statistical mechanics, to free energy configurations, the correlated dissipative ensemble and the spatio-temporal mnemonic entity as actors of basic communication practices from the molecular level to the social and cosmological echelon. In Sect. 11 communications on channel SELF is advanced as an ultra-wide broadband distributed via Poisson distributed protocols. In the concluding Sect. 12, the physical description incorporates a quantum theoretical examination of black hole conformations in terms of its mass and angular momentum quantum numbers.

Although some of the ideas listed above, may not be given in full detail or more or less abridged to near disappearance, there should be a sufficient nexus of references where supplementary details can be found. We conclude the account by referring to the title and the objectives and goals behind the conception of the Zero-Energy Universe Scenario, ZEUS, and all its ingredients from the micro-, meso-, macro- and to the highest ranks.

2 Conjugate Variables and Einstein's Law of Special Relativity

Since our efforts concern both material and immaterial organisations, examined at the very limit of physical theory, our formulation starts at the microscopic level of atomic and molecular constituents in the grey zone between quantum and classical readings. It is important to understand that we do not refer to popular developments in terms of exotic dimensions at unconventional scales, as we do believe that a solution of the problems indicated above does not originate in any of the popular superstring theories, Green et al. [3].

Many physicists today are undeniably epistemologists. However, brane and string scientist seem to have a different ontology in that they consider the vibrating string to be the particle itself rather than merely dictating the properties of its host particle. This view may not be commensurate with a quantum theoretic hierarchy of concepts, i.e. representing nature via accumulation of knowledge through unbiased and systematic research. Indeed the absolute being of material bodies, obtains self-referential consequences, provoking further discussions in relation to Gödel's incompleteness theorem(s) [4]. In short Gödel's self-referential account will be the guide for teleonomic processes, already emerging on the molecular level, introducing viable communication protocols via Poisson distributed channels, for details see more below. In contrast modern p -branes, while being spatially extended strings, originate in mathematical concepts that appear to conflate matter with its mathematical description, i.e. do not exhibit the proper fabric for a self-referential examination. We will here advance an ontology that entangles the physical- and the mental world, while embedding evolution as a template for self-organization and associated teleodynamical processes.

It is then most natural to begin the formulation by quoting Kant: *Space and Time are the two essential forms of human sensibility*. Once space and time are mathematically well defined their conjugate variables follow naturally, i.e. as originally expressed by Einstein, via the energy, represented as E_{op} below, and momentum, \vec{p}_{op} , combined in the four-momentum or the energy- momentum tensor. The conjugate variables of energy-momentum, time and space are further characterized as $\tau = T_{\text{op}}$ and \vec{x}_{op} below, with \hbar being Planck's constant divided by 2π , and $\vec{\nabla}$ being the nabla operator. Thus we have the following four key operators for our general exposition

$$E_{\text{op}} = i\hbar \frac{\partial}{\partial t}; \quad \vec{p}_{\text{op}} = -i\hbar \vec{\nabla}_{\vec{x}} \quad (2.1)$$

$$\tau = T_{\text{op}} = -i\hbar \frac{\partial}{\partial E}; \quad \vec{x}_{\text{op}} = i\hbar \vec{\nabla}_{\vec{p}} \quad (2.2)$$

The operators above do not out of context define any proper physical realizations as their relevance is acquired from the insertion of appropriate boundary conditions

commensurate with the physical situations at hand. In general, there is no problem to define the operators above on an interval $(-\infty, +\infty)$. Nevertheless we will have the option to delay our choice of the actual boundary conditions, or representations in terms of classical canonical variables, until the physical situation is fully determined.

The modus operandi is achieved as follows. Consider the operator matrix (c is the velocity of light)

$$\begin{pmatrix} i\hbar \frac{\partial}{\partial t} & -i\vec{p}_{\text{op}}c \\ -i\vec{p}_{\text{op}}c & -i\hbar \frac{\partial}{\partial t} \end{pmatrix} \quad (2.3)$$

which conforms to a complex symmetric construction, whose determinant, $\hbar^2 \frac{\partial^2}{\partial t^2} - \hbar^2 c^2 \nabla^2$, set equal to zero yields a direct link with Maxwell's equations in vacuum. Furthermore the eigenvalues, $\lambda^2 = m_0^2$ of Eq. (2.3), with the rest mass of the particle $m_0 \neq 0$, gives a Klein-Gordon-like equation, i.e.

$$-\frac{E_0^2}{c^2} = \vec{p}^2 - \frac{E^2}{c^2} \quad (2.4)$$

where the energy mass relations, $E = mc^2$ and $E_0 = m_0 c^2$, results in the well-known mass-formula of Einstein's law of special relativity

$$m = \frac{m_0}{\sqrt{1 - \beta^2}} \quad (2.5)$$

with $\beta = v/c = p/mc$. Note the generality invoked by the choice to interpret the entities above as abstract operators. In this way one needs to define the velocity v properly as the group velocity of the particle/wave, a description that is valid also in the theory of special relativity.

Repeating the procedure, Eqs. (2.3–2.5) for the conjugate variables/operators one gets

$$\begin{pmatrix} c\tau & -i\vec{x} \\ -i\vec{x} & -c\tau \end{pmatrix} \quad (2.6)$$

with the familiar eigentime expression given by

$$-c^2 \tau_0^2 = \vec{x}^2 - c^2 \tau^2 \quad (2.7)$$

and ($x = |\vec{x}|$)

$$\tau = \frac{\tau_0}{\sqrt{1 - \beta^2}}; \quad x = \frac{x_0}{\sqrt{1 - \beta^2}} \quad (2.8)$$

Consequently Einstein's law of special relativity is valid irrespective of whether we represent classical wave propagation, quantum matter waves or classical particles. Note also that any matrix construction refers to a particular basis and a realization of a relevant scalar product. Thus one considers the kets

$$|\vec{x}, ict\rangle; \quad |\vec{p}, iE/c\rangle \quad (2.9)$$

with the scalar product for a free particle given by

$$\langle \vec{x}, -ict | \vec{p}, \frac{iE}{c} \rangle = (2\pi\hbar)^{-2} e^{i(\vec{p} \cdot \vec{x} - Et)} \quad (2.10)$$

Note that $(ict)^* = -ict$ occurs in the bra-position in concert with complex symmetry. As already stressed there is no loss of generality as representations include classical canonical forms with Segre characteristics larger than one. As an example we will consider the case of a zero rest-mass particle like the photon. Here $E = pc$, $p = |\vec{p}|$ and thus Eq. (2.3) takes the form

$$\begin{pmatrix} p/c & -ip/c \\ -ip/c & -p/c \end{pmatrix} = p/c \begin{pmatrix} 1 & -i \\ -i & -1 \end{pmatrix} \quad (2.11)$$

whose classical canonical form is

$$2p/c \begin{pmatrix} 0 & 1 \\ 0 & 0 \end{pmatrix} \quad (2.12)$$

This imparts a symmetric form corresponding to a photon that cannot be diagonalized at any space-time point. The photon is in transition between its complex symmetric partners. This indicates a crucial difference between zero- and non-zero rest-mass particles. The latter becomes a fundamental property when extending the formulation to the theory of general relativity. Moreover the results, Eqs. (2.5) and (2.8), imply that the respective eigenvectors portray small combinations of components from associated antiparticles as recognized by the superposition from the dual space. Hence the origin of the Einstein laws, e.g. time dilation and length contraction, goes beyond the postulates of special relativity providing a direct link between matter and antimatter. For more on the technicalities involved in the actual interpretations see Refs. [5, 6].

3 Einstein's Laws of General Relativity and the Schwarzschild Gauge

It has been demonstrated that conjugate operator arrays combining classical- and quantum configurations carry a unified structure of relativity. Direct extension leads to the modifications below, where μ is the gravitational radius, G the gravitational

constant, $v = p/c$, M a spherically symmetric (non-rotating) mass, which does not change sign when $m \rightarrow -m$, i.e.

$$\begin{pmatrix} m(1 - \kappa(r)) & -iv \\ -iv & -m(1 - \kappa(r)) \end{pmatrix} \quad (3.1)$$

with

$$m\kappa(r) = \frac{m\mu}{r}; \quad \mu = G \cdot \frac{M}{c^2} \quad (3.2)$$

In principle one can continue to make a formulation in analogy with the special theory by solving the corresponding secular equation

$$\lambda^2 = m^2(1 - \kappa(r))^2 - p^2/c^2 \quad (3.3)$$

with the notation

$$\lambda_{\pm} = \pm m_0(1 - \kappa(r)) \quad (3.4)$$

However, as already stated, we must accommodate the operator algebra consistently by synchronously adapting the space-time background in concert with the conjugate correspondence. This problem is not entirely trivial since an appropriate inclusion must tweak the epitome of both zero- and non-zero rest-mass particles. An apt derivation, in consideration of this difference, yields directly the Schwarzschild line element, see Refs. [6, 7]

$$-c^2 ds^2 = -c^2 d\tau^2(1 - 2\kappa(r)) + dr^2(1 - 2\kappa(r))^{-1} \quad (3.5)$$

from which follows Einstein's laws of general relativity—the gravitational light deflection, the time delay, and the red shift—and the perihelion precession of planet Mercury [7].

Note that Eq. (3.1) cannot be diagonalised if $\kappa(r) = 1/2$. The reason is that the angular momentum is a constant of motion with the ensuing relation $p/c = m\kappa(r)$. Hence for $\kappa(r) \neq 1/2$ one obtains

$$m \begin{pmatrix} (1 - \kappa(r)) & -i\kappa(r) \\ -i\kappa(r) & -(1 - \kappa(r)) \end{pmatrix} \rightarrow m \begin{pmatrix} \sqrt{1 - 2\kappa(r)} & 0 \\ 0 & -\sqrt{1 - 2\kappa(r)} \end{pmatrix} \quad (3.6)$$

while at $\kappa(r) = 1/2$, i.e. at the Schwarzschild radius $r = 2\mu$ one obtains a degeneracy corresponding to a Jordan block of order two, i.e.

$$\frac{1}{2}m \begin{pmatrix} 1 & -i \\ -i & -1 \end{pmatrix} \rightarrow \begin{pmatrix} 0 & m \\ 0 & 0 \end{pmatrix} \quad (3.7)$$

The singularity at the Schwarzschild radius befalls a boundary inside which space and time do no longer exist in the standard sense. Our complex symmetric framework reveals a black-hole-like structure, displaying precise quantum features. One recognizes that the present configuration is uncharged due to the particle-antiparticle superposition instigated by the transformation in Eq. (3.7) above, see also Refs. [6, 7] for more details. Extensions to rotating black hole-like objects will be discussed separately in Sect. 12, necessitating the incorporation of the Kerr metric [8].

Although not explicitly indicated, the present operator array is equipped with an abstract linear space, spanned by suitably defined vectors and their dual reciprocals, see e.g. Löwdin [9] for details.

In passing we recognize a significant result regarding the likelihood of any size limitations to our physical universe. The black-hole object derived above, imparts that space-time have a finite lower bound given by the Schwarzschild radius. The authentic space-time property is not defined inside this boundary, which means that their conjugate partners, energy and momentum, must both be limited at infinity. This conclusion follows naively from the commutation relationships between conjugate variables (operators). In the same way the energy and the momentum will never evolve arbitrary close to zero and hence, *mutatis mutandis*, the spatio-temporal “size” will also be correspondingly limited. This veracity prompts the conception of a zero-energy universe in that the energy-momentum will be limited with most of its energy positioned in a black-hole structure around “zero”. We will say more about it below in connection with self-referential interactions and a reformulation of Gödel’s theorem(s).

4 Gödel’s Theorem and the Law of Self-Reference

To begin with, it is imperative to know that we do not intend to advise a new reading of the logical derivation of Gödel’s arguments in connection with the proof of his first incompleteness theorem. In fact the interpretation of the mathematical theorem(s) has been manifold as was recently stated by Feferman [10] in his critique of the utilization of the results of Gödel [4] and Turing [11] in connection with the positions of Artificial Intelligence, AI: *it is hubris to think that by mathematics alone we can determine what the human mind can or cannot do*. While we will here argue that communication in biological systems starts already on the basic level of molecular interactions within and between cellular aggregates, transfer of information instigates on a built-in structure of mathematics, see e.g. Brändas [12], we will recognize that Gödel’s paradox exhibits a consistent mathematical formulation within the logical framework of quantum mechanics. Consequently we will belabour Penrose’s contention [13] that “physical action evoking awareness cannot be properly simulated computationally” by simply formulating the Gödel inconsistency theorem as a higher order singularity in linear algebra, i.e. as a Jordan

block with a Segre characteristic equal to two (the dimension of the largest block). The purpose is (i) the insight that a living system cannot decohere or halt the computation corresponding to the Gödel sentence and (ii) to utilize this validation to make conclusions about the physical world we live in, extending the description to complex enough system of biological relevance.

In the molecular dynamics of many energy surfaces, there is the famous non-crossing rule, when energy curves or surfaces veer very close to each other the reason being the underlying complex crossings on the second Riemann sheet of the energy plane. Current interest in these structures as well as the possibility to obtain crossings on the first sheet, has rapidly developed into a hot topic today, as the concept of conical intersections has become a major paradigm in non-adiabatic chemistry, Domcke and Yarkony [14]. The philosophy may physically be a bit different when imbedding the theory in a non-adiabatic environment, but we are nevertheless talking about similar mathematical structures.

To belabour the analogy outlined above and setting the stage for a quantum logical interpretation we will consider a formal system, in which the formulae represent propositions, studying some simple ideas on propositional logics. We will not go into technical questions like ω -consistency etc., since our purpose is only to reproduce the formal system satisfying the necessary hypothesis embodying propositions consisting of so-called well-formed formulas (wffs). We will hence deliberate on Gödel's first incompleteness theorem [4], viz. there will always be statements (wffs) in a consistent system of axioms, listed e.g. as an algorithm, which are not provable within the system, e.g. truths about natural numbers, or simply about arithmetic. If the theory, generated by wffs, includes statements of its own completeness, then it becomes inconsistent; for some recent discussions on the proof of the second theorem, see Feferman [10].

In order to translate the interpretation of a truth-functional propositional calculus, i.e. assigning to each proposition one or the other of the truth values-symbol by their usual truth-functional meanings truth or falsity (provable or non-provable in the formulation of Gödel), we will consider the proposition \mathfrak{P} and $\mathfrak{Q} = \neg\mathfrak{P}$ (\mathfrak{P} and not \mathfrak{P}). This leads to the following extension of the logical negation, i.e. a truth table for the pair \mathfrak{P} and $\neg\mathfrak{P}$. It reads as follows: if \mathfrak{P} is true and \mathfrak{Q} is false then the first row, see the table below, asks whether \mathfrak{P} is true (yes!) and \mathfrak{Q} is true (no!), while the second row asks whether \mathfrak{P} is false (no!) and \mathfrak{Q} is false (yes!). Hence the matrix Eq. (4.1) below becomes “diagonal”, i.e. reads a diagonal “yes” and an off-diagonal “no”, i.e.

$$\text{Extended logical negation: } \begin{array}{cc|cc} & & \text{true} & \text{false} \\ & \text{true} & \left(\begin{array}{cc} \mathfrak{P} & \mathfrak{Q} \\ \mathfrak{P} & \mathfrak{Q} \end{array} \right) & = \left(\begin{array}{cc} \text{yes} & \text{no} \\ \text{no} & \text{yes} \end{array} \right) \end{array} \quad (4.1)$$

Converting to a linear algebra vernacular \mathcal{L}_n with the probability functions p and $(1 - p)$

$$\mathcal{L}_n = \begin{pmatrix} \langle \text{true} | & | \text{true} \rangle & | \text{false} \rangle \\ \langle \text{false} | & (p) & (1-p) \\ & (1-p) & p \end{pmatrix} \quad (4.2)$$

one obtains, in the abstract (orthonormal) basis $|\text{true}\rangle$ and $|\text{false}\rangle$,² the real symmetric secular problem corresponding to \mathcal{L}_n giving the following “classical” solutions

$$\lambda_{\pm} = p \pm (1-p); \quad \begin{cases} \lambda_1 = 1 \\ \lambda_2 = 2p - 1 \end{cases} \quad (4.3)$$

with the eigenfunctions given by

$$\lambda_1; \quad |\overline{\text{true}}\rangle = \frac{1}{\sqrt{2}}(|\text{true}\rangle + |\text{false}\rangle) \quad (4.4)$$

$$\lambda_2; \quad |\overline{\text{false}}\rangle = \frac{1}{\sqrt{2}}(|\text{true}\rangle - |\text{false}\rangle) \quad (4.5)$$

In this picture the eigenvalue $\lambda_1 = 1$ corresponds to the sum of probabilities, while $\lambda_2 = 2p - 1$ portrays the difference or the bias as indicated below.

$$\lambda_2 = \begin{cases} 1; & p = 1 \\ 0; & p = \frac{1}{2} \\ -1; & p = 0 \end{cases} \quad (4.6)$$

We can also define it as a positive quantity, i.e. $|2p - 1|$. For instance by assuming $p \geq 1/2$, then λ_2 will always remain positive (if not let $p \rightarrow 1 - p$).

To express the propositional analogy onto a deeper level, one may carry out the “Dirac trick”, which essentially corresponds to “taking the square root of the Klein-Gordon equation”, cf. the ansatz equation (2.3). Rewriting the truth table as

$$\text{Bias Table:} \quad \begin{array}{c} \text{true} & \text{false} \\ \text{true} & \left(\begin{array}{cc} \mathfrak{P} & \mathfrak{Q} \\ \neg \mathfrak{Q} & \neg \mathfrak{P} \end{array} \right) \\ \text{false} & \end{array} \quad (4.7)$$

assigning a positive signature (+), for \mathfrak{P} and \mathfrak{Q} and a negative one (-), for $\neg \mathfrak{Q}$ and $\neg \mathfrak{P}$. Hence the “Bias” matrix \mathcal{B} becomes, note that the space corresponding to Eq. (4.2) is of course different to that of Eqs. (4.8) and (4.8'),

² In quantum theory the Dirac bra-ket is an abstract set of vectors and dual vectors in a general mathematical theory, subject to the axioms of linear algebra, i.e. the scalar product bra-ket depends linearly (antilinearly) on the ket (bra). In the case above the abstract vector space symbolizes a lower level description that consistently portrays the singularity associated with Gödel's proposition.

$$\mathcal{B} = \begin{pmatrix} \langle \text{true} | & | \text{true} \rangle & | \text{false} \rangle \\ \langle \text{false} | & p & (1-p) \\ & -(1-p) & -p \end{pmatrix} \quad (4.8)$$

Note that \mathcal{B} may be obtained from a real symmetric matrix by the multiplication with a non-positive definite metric Δ with $\Delta_{11} = -\Delta_{22} = 1$ and $\Delta_{12} = \Delta_{21} = 0$. The secular equation corresponding to \mathcal{B} leads to the following solutions

$$\lambda_{\pm} = \pm \sqrt{2p - 1} \quad (4.9)$$

and

$$\lambda_+ = \lambda; | \overline{\text{true}} \rangle = c_1 | \text{true} \rangle + c_2 | \text{false} \rangle \quad (4.10)$$

$$\lambda_- = -\lambda; | \overline{\text{false}} \rangle = -c_2 | \text{true} \rangle + c_1 | \text{false} \rangle \quad (4.11)$$

with

$$c_1 = \sqrt{\frac{p + \lambda}{2p}}; \quad c_2 = \frac{-(1-p)}{\sqrt{2p(p + \lambda)}}; \quad c_1^2 + c_2^2 = 1 \quad (4.12)$$

If $p \geq 1/2$ then $2p - 1$ is positive and the eigenvalues are real. However if $p < 1/2$ then the eigenvalues are purely imaginary and complex conjugate to each other. As a result the c_i 's are complex-valued and the normalization condition in Eq. (4.12) are not related to probabilities as when the coefficients are real. The construction Eq. (4.8) is indeed of the same generality as our previous complex symmetric ansatz, see e.g. Eqs. (2.3) and (3.1). This will indeed be explicit when one studies the “problematic situation” $p = 1/2$, cf. Eq. (4.7) above. Before examining the singular case $p = 1/2$, one notes that rewriting the Bias Chart as

$$\text{Bias Chart : } \begin{array}{c} \text{true} & \text{false} \\ \text{true} & \left(\begin{array}{cc} \mathfrak{P} & \neg \mathfrak{P} \\ \neg \mathfrak{Q} & \mathfrak{Q} \end{array} \right) \\ \text{false} \end{array} \quad (4.7')$$

and assigning the \neg symbol with multiplication with $-i$, one obtains instead, cf. Eq. (2.3)

$$\mathcal{B}' = \begin{pmatrix} \langle \text{true} | & | \text{true} \rangle & | \text{false} \rangle \\ \langle \text{false} | & p & -i(1-p) \\ & -i(1-p) & -p \end{pmatrix} \quad (4.8')$$

which, however, due to its complex symmetric property entails the a similar irreducible state as above at $p = 1/2$. In the two cases one obtains for Eq. (4.8)

$$\mathcal{B} = (|\text{true}\rangle, |\text{false}\rangle) \begin{pmatrix} \frac{1}{2} & \frac{1}{2} \\ -\frac{1}{2} & -\frac{1}{2} \end{pmatrix} \begin{pmatrix} \langle \text{true}| \\ \langle \text{false}| \end{pmatrix} \quad (4.13)$$

$$|\overline{\text{true}}\rangle = \frac{1}{\sqrt{2}}(|\text{true}\rangle - |\text{false}\rangle) \quad (4.14)$$

$$|\overline{\text{false}}\rangle = \frac{1}{\sqrt{2}}(|\text{true}\rangle + |\text{false}\rangle) \quad (4.15)$$

and for Eq. (4.8')

$$\mathcal{B}' = (|\text{true}\rangle, |\text{false}\rangle) \begin{pmatrix} \frac{1}{2} & -i\frac{1}{2} \\ -i\frac{1}{2} & -\frac{1}{2} \end{pmatrix} \begin{pmatrix} \langle \text{true}| \\ \langle \text{false}| \end{pmatrix} \quad (4.13')$$

$$|\overline{\text{true}}\rangle = \frac{1}{\sqrt{2}}(|\text{true}\rangle - i|\text{false}\rangle) \quad (4.14')$$

$$|\overline{\text{false}}\rangle = \frac{1}{\sqrt{2}}(|\text{true}\rangle + i|\text{false}\rangle) \quad (4.15')$$

In both cases the Jordan block with Segre characteristic 2 writes

$$\mathcal{B} = (|\overline{\text{true}}\rangle, |\overline{\text{false}}\rangle) \begin{pmatrix} 0 & 1 \\ 0 & 0 \end{pmatrix} \begin{pmatrix} \langle \overline{\text{true}}| \\ \langle \overline{\text{false}}| \end{pmatrix} = |\overline{\text{true}}\rangle \langle \overline{\text{false}}| \quad (4.16)$$

Thus $p = \frac{1}{2}$ is a singularity, i.e. at this point the matrix \mathcal{B} (or \mathcal{B}') cannot be diagonalised and the bias does not decohere to a classical state $|\overline{\text{true}}\rangle$ or $|\overline{\text{false}}\rangle$. Instead one gets a “higher order” situation where the bias “super operator” portrays a transition as shown in Eq. (4.16). To connect with a traditional representation we define the classical probability information from the system operators $\Gamma^\pm = \frac{1}{2}(\mathcal{I} \pm \mathcal{B}^2)$, with \mathcal{I} the identity as before,

$$\begin{aligned} \frac{1}{2}(\mathcal{I} + \mathcal{B}^2) &= p\mathcal{I} \\ \frac{1}{2}(\mathcal{I} - \mathcal{B}^2) &= (1-p)\mathcal{I} \end{aligned} \quad (4.17)$$

Although our operator \mathcal{B} (or \mathcal{B}') would be related to the square root of $\lambda_2 = 2p - 1$ portraying the difference (or the bias) as indicated above, we will, in what follows denote \mathcal{B} (or \mathcal{B}') as the proper bias operator of the present quantum representation. Thus the conventional classical—quantum enigma plaguing contemporary world-views transcend to the extended “truth tables” or equivalently the operator matrices, Eq. (2.3) or (2.6). Hence the general problem of interpreting the

extended logical negation should incorporate classical and quantum features equivalently.

Summarizing, one finds that the classical contradiction or paradox related to the Gödel proposition, choosing $\mathfrak{P} = \mathfrak{G}$, where \mathfrak{G} is Gödel's famous arithmetical proposition so constructed that neither \mathfrak{G} nor $\neg\mathfrak{G}$ are provable within the given set of axioms, is formulated as a well-defined singularity in the extended logical description presented above. Hence (4.16) tells that simultaneously \mathfrak{G} is not true and $\neg\mathfrak{G}$ is not false neither \mathfrak{G} nor $\neg\mathfrak{G}$ are false. Nevertheless classical truth-values, being undecidable, will not reveal any singular behaviour since $\mathcal{B}^2 = 0$, while the canonical vectors in (4.14) or (4.14') replicates inclusive uncertainty with respect to the input information.

The classical inconsistency or paradox has been represented by a matrix degeneracy, reproducing the truth functional proposition calculus by “quantum-like” states, and allowing the case $p = 1/2$ to be expressed as a quantum transition between truth and falsity. Of course Gödel used the terminology “provable” and “not provable”, which is vital in the logical proofs, but nonetheless will not essentially influence our present argument.

Finally one can directly compare (4.8) and (4.13) or (4.8') and (4.13') translating the bias matrix \mathcal{B} (or \mathcal{B}') into Eqs. (3.6) and (3.7) displaying a precise relation with the theory of general gravity, identifying $p(r) = (1 - \kappa(r))$.³ The self-referential aspects of the present argument translates into a fundamental law, which will advance important generalizations to biotic organizations in complex enough systems giving way to biological order and communication. In particular one notes that decoherence into a quantum or classical state is impossible due to Gödel's inconsistency theorem, here portraying the paradox as a crossing phenomenon, e.g. as a genuine bifurcation, authentically prohibiting or code forbidding any state collapse.

5 Non-Hermitian Quantum Mechanics

The scope of this presentation will not permit portrayals of all the microscopically relevant formulations that can be deduced from the general operator array algebra of previous sections, see Ref. [15] for more details. Instead we will focus on what is essential in order to appreciate the consequences of the arguments needed to formulate ZEUS, the Zero-Energy Universe Scenario, as an all-inclusive concept that in addition incorporates the paradigm of evolution.

As is well known it is usually resolved that the many-body Schrödinger equation in particular and quantum mechanics in general portray reality to unmatched perfection. This anticipation acquiesced Löwdin [16] to establish the foundation of a new journal, the International Journal of Quantum Chemistry. With the emergence

³ Note that the probability function/operator p in this paragraph should not be confused with the absolute value of the momentum variable of previous sections.

of the computer revolution, the field of quantum chemistry prospered, and it is viewed today as a fundamental area becoming more or less synonymous with the fields of theoretical chemistry and chemical physics.

Despite these successes there remain many inconsistencies and conundrums plaguing the fundamental physical formulation. Primas [17] in his thought provoking evaluation of the *myth* of universal laws brings up ten profound problems connected with the incapabilities of traditional quantum chemistry promoting the so-called structural approach. Although many of the puzzles have a metaphysical flavour, they aim at the deeper meaning of chemistry and a worldview, *unus mundus*, which should also incorporate the dimensions of a semiotic analysis. The present author has reformulated some of the most serious ones in Brändas [6], in particular the well-known issues of the uni-directedness of time and the associated irreversibility of the macro-world (e.g. molecular chirality), as well as the elimination of the law of causality in the microscopic domain. Closely related is also the inquiry of the absolute nature of the second law, Sklar [18]. These problems have been reconsidered in the light of recent non-Hermitian quantum mechanics, see Nicolaides and Brändas [19] and Moiseyev [20] suggesting potential solutions to the paradox, see also Ref. [6].

Much could be said about the necessity to realize and accomplish a quantum mechanical extension,⁴ however it should be enough to briefly explain what we mean when saying that the Schrödinger equation is extended or continued beyond Hermitian territory. In the portrayal we refer to the popular analytic dilation technique for a simple case of a proper potential, V , exhibiting a point spectrum below a positive continuum.

The method simply amounts to multiplying the space coordinate x with a complex scale factor $\eta = e^{i\theta}$, with $\theta = \arg(\eta)$ for some $0 \leq \theta < \theta_0$, where θ_0 depends on the potential V , leading to a simple but nontrivial analytic extension of the spectrum of the differential operator that derives from a standard molecular Schrödinger equation. A comparison between the spectrum of the Schrödinger differential operator, before and after scaling, in the simple case where the point spectrum σ_p accumulates at a given point, defining the onset of the absolutely continuous spectrum σ_c , yields a rotation of the absolutely continuous spectrum around the accumulation point (threshold) with the angle $-2\arg(\eta)$, originating from the (dominating) kinetic part of the Hamiltonian being related the second order differential operator $\Delta = \nabla^2$. The mathematical theorem that provides the bound states, the continuum and the so-called resonance states, in the sector between the real axis and its rotated analogue, is due to Balslev and Combes [21]. For rigorous treatments including also the electromagnetic field, see e.g. resonance studies in

⁴ This extension rests on a rigorous mathematical theory, i.e. the Balslev-Combes theorem [21], see also Simon [22], and it is vital to understand and appreciate non-Hermitian quantum mechanics and its consequences for the dynamics of resonance states embedded in the continuum and their properties for higher order dynamics.

connection with Stark Hamiltonians, Hohenberger et al. [23], Brändas and Froelich [24] and for Floquet Hamiltonians, Howland [25].

Even if we have greatly oversimplified the details of the spectral decomposition, the dilatation analytic theory covers the whole analytic family of Hamiltonians and provides important testing grounds for extended investigations of dynamical quantum chemical systems, which goes beyond traditional approaches of quantum mechanics, Nicolaides and Brändas [19]. It will be shown below that most of the quantum mechanical machinery will remain intact in accounting for the “move into” the complex energy plane, nevertheless allowing for a much more general set of solutions, usually denoted “unstable states in the continuum”, at the same time giving rise to a more realistic contractive time evolution. However there is an important difference, i.e. the traditional use of matrix transformations via unitary transformations must be generalized to educe complex symmetric similitudes. As a consequence one might encounter situations where the Hamiltonian matrix cannot be diagonalised. This is usually considered to be a nightmare in contemporary numerical analysis, but is here a blessing in disguise, allowing important conceptual notions and fundamental abstractions.

6 Statistical Mechanics far from Equilibrium—Off-Diagonal Long-Range Order

Our objective is here to incorporate these so-called “unstable states” in a more general non-equilibrium quantum statistical framework. Obviously our formulation must go beyond the Maxwell-Boltzmann distribution and the traditional Fermi-Dirac or Bose-Einstein statistics. According to Nernst’s theorem, sometimes called the third law of thermodynamics, a perfect crystal has zero entropy in the limit when the absolute temperature $T \rightarrow 0$. Slightly generalized we could use a similar argument for any system with a nondegenerate ground state denoted by a properly antisymmetrised N -particle (fermionic) wavefunction Ψ . From this follows a sequence of N -representable reduced fermionic density matrices, see e.g. Löwdin [26]

$$\begin{aligned} & \Gamma^{(q)} \left(x_1, x_2, \dots, x_q | x'_1, x'_2, \dots, x'_q \right) \\ &= \binom{N}{q} \int \Psi(x_1, x_2, \dots, x_q, x_{q+1}, \dots, x_N) \Psi^*(x'_1, x'_2, \dots, x'_q, x_{q+1}, \dots, x_N) dx_{q+1}, \dots, dx_N \end{aligned} \tag{6.1}$$

The matrices above are characterized as N -representable as they derive from a pure state Ψ , i.e. $\Gamma^{(N)} = |\Psi\rangle\langle\Psi|$, with $q = N$ inserted in Eq. (6.1). Since our (crude) atomic- and molecular Coulomb Hamiltonian involves only two-body interactions, $H = \sum_{k=1}^N h_k + \sum_{k < l} h_{kl}$, special focus descends on the second order reduced density matrix $\Gamma^{(2)}$, $q = 2$ in Eq. (6.1). Finding proper ways to determine variational techniques for a suitably described $\Gamma^{(2)}$ would indeed yield a remarkable simplification as the total energy of the system simply obtains in terms of the reduced Hamiltonian $H_2 = \frac{1}{N-1}(h_1 + h_2) + h_{12}$, where $\text{Tr}\{A\}$ means the trace over the operator A ,

$$E = \text{Tr}\{H_2\Gamma^2\} \quad (6.2)$$

Unfortunately, the existence of general conditions to guarantee an N -representable form of $\Gamma^{(2)}$, are impractical at present, except in the strongly correlated case to be discussed below; see the monograph by Coleman and Yukalov [27].

One observes that our N -particle system (if restricted to N electrons) involves $\binom{N}{2}$ pairings with the total energy expressed as a sum of the corresponding pair energies. Equation (6.2), however, entails a reduction to one reduced pair energy, with the complications, due to the fundamental electronic correlations, now hidden in a correctly gauged $\Gamma^{(2)}$. A further reduction appears when the system might condense to $M = N/2$ bosons (or fermionic pairs), cf. the superfluid or the superconducting phase, believed to emerge for most systems at sufficiently low temperatures. The phase is rendered by and explained in terms of Yang's celebrated concept of ODLRO,⁵ Off-Diagonal Long-Range Order [28]. In this particular representation the density matrix becomes essentially (for proofs see Brändas [6])

$$\begin{aligned} \Gamma^{(2)} &= \lambda_L|g_1\rangle\langle g_1| + \lambda_S \sum_{k=2}^n |g_k\rangle\langle g_k| \\ \lambda_L &= \frac{N}{2} - \frac{N(N-2)}{n}; \quad \lambda_S = \frac{N(N-2)}{4n(n-1)} \end{aligned} \quad (6.3)$$

with $\lambda_L \rightarrow \frac{N}{2}$; $\lambda_S \rightarrow 0$; $n \rightarrow \infty$. The basis $|g\rangle$ is obtained from a preferred localized basis of geminals, $|h\rangle$, i.e. of paired fermions (antisymmetric with respect to permutation of the fermionic space-spin degree of freedom) and with $\omega = e^{i\pi/n}$, i.e.

⁵ The concept of ODLRO, although developed after the famous Bardeen-Cooper-Schrieffer theory of super-conductivity, is a formulation with focus on the collective properties of matter at sufficiently low temperatures. For a material system at zero temperature with a non-degenerate ground state the entropy is zero. Under specific conditions the system may develop superconductivity.

$$|\mathbf{g}\rangle = \mathbf{B}|\mathbf{h}\rangle$$

$$\mathbf{B} = \frac{1}{\sqrt{n}} \begin{pmatrix} 1 & \omega & \omega^2 & \cdot & \omega^{n-1} \\ 1 & \omega^3 & \omega^6 & \cdot & \omega^{3(n-1)} \\ \cdot & \cdot & \cdot & \cdot & \cdot \\ \cdot & \cdot & \cdot & \cdot & \cdot \\ 1 & \omega^{2n-1} & \omega^{2(2n-1)} & \cdot & \omega^{(n-1)(2n-1)} \end{pmatrix} \quad (6.4)$$

There exists a very simple proof of the extreme state formula above, which captures the importance of the finite dimensional result of Eq. (6.3), see e.g. [6]. The theorem, originally derived by Coleman [29], using a rather subtle counting argument of Sasaki [30], see also the discussion⁶ in Coleman, Yukalov [27], was mainly known under the name of an extreme state represented as an Antisymmetrized Geminal Power. The AGP writes as, $g = g_1$

$$\Psi(g) \propto g \wedge g \wedge \cdots \wedge g \quad (6.5)$$

i.e. the wavefunction is proportional to the “wedge” product of $N/2$ pairfunctions (geminals), with the wedge \wedge symbolizing antisymmetric product of paired fermions. Note that $g = g_1$ is both the key element of $\Psi(g)$ and an eigenfunction of $\Gamma^{(2)}(g)$.

The simplified proof, which will be briefly given below, entails a quantum logical argument, whose validity depends on the exact interpretation of Yang’s ODLRO and the Coleman-Sasaki theorem. Consider the density operator for a general system of $N/2$ paired fermions described by the preferred localized basis $|\mathbf{h}\rangle$ of dimension $n > N/2$ (the basis vector $|h_k\rangle$ should not to be confused with the one body operator h_1 , the former only occurring under the bra-ket symbols),

$$\Gamma^{(2)} = \varrho = \sum_{k,l}^n |h_k\rangle \varrho_{kl} \langle h_l|; \quad \text{Tr}\{\varrho\} = \frac{N}{2} \quad (6.6)$$

The matrix element ϱ_{kk} defines the probability p to find the paired fermion particle at the state k (or site since the basis is localised at the defining sites of the system) and $\varrho_{kl}; k \neq l$ the probability $p(1 - p)$ for making the transition from site k to site l . Hence the matrix ϱ is defined as follows

$$\varrho_{kk} = p; \quad \varrho_{kl} = p(1 - p); \quad k \neq l; \quad p = \frac{N}{2n} \quad (6.7)$$

⁶ Regarding reference [30], Coleman makes the following quote in [27]: “This article, which was based on Sasaki’s Report 77 (1962) Quantum Chemistry Group, Uppsala, was actually submitted in 1962 but was inadvertently misplaced by the publisher. It was in this paper that, independently of Yang, Sasaki observed that it is for AGP type functions that the largest possible eigenvalues of the 2-matrix occur.”

Solving for the eigenvalues and eigenfunctions of Γ or ϱ in (6.6) gives

$$\Gamma^{(2)} = \varrho = \lambda_L |g_1\rangle\langle g_1| + \lambda_S \sum_{k,l=1}^n |h_k\rangle(\delta_{kl} - \frac{1}{n})\langle h_l| \quad (6.8)$$

with one nondegenerate eigenvalue λ_L and an $(n - 1)$ -degenerate eigenvalue λ_S , i.e.

$$\lambda_L = np - (n - 1)p^2; \quad \lambda_S = p^2 \quad (6.9)$$

A slightly more detailed analysis would trivially yield the result in Eq. (6.3), but the present calculation will be as accurate for large N and n .

Applying the transformation (6.4) and noting that $\lambda_L \rightarrow \frac{N}{2}$; $\lambda_S \rightarrow 0$; as $n \rightarrow \infty$, one concludes that (6.3) and (6.8) are in fact fundamentally identical, i.e. $\Gamma^{(2)} = \varrho$. A closer analysis reveals that an exact identification with Coleman's extreme state, the precursor for Yang's ODLRO, can be made explicitly via the present argument, Brändas and Chatzidimitriou-Dreismann [31].

In summary we have obtained without explicit derivations, a second order reduced density matrix for an N -particle fermionic ($M = N/2$ quasi-bosonic) system derived from $\Gamma^{(N)}(g) = |\Psi(g)\rangle\langle\Psi(g)|$, yielding an N -representable representation for $\Gamma^{(2)}(g)$ according to (6.3–6.9). Since we are describing the system exhibiting a nondegenerate ground state at the temperature $T = 0$ there is no loss of information and the entropy equals zero. In order to rigorously incorporate the temperature, the corresponding thermalization requires the extension of the quantum dynamical framework accounting for the structures of the previously specified “unstable states in the continuum”. In this context we will appreciate the importance of the transformation Eq. (6.4) and its subsequent remarkable properties, see e.g. Ref. [6] for more details.

7 The Liouville Equation and the Prigogine Energy Operator

While proceeding on the plan laid out in the introduction, one notes that our present ansatz is general enough to incorporate, not only usual applications in chemical physics, but also more specialised portraits, like superconductivity, superfluidity and analogous spatio-temporal configurations. Our specific aim is to demonstrate how the present density matrix formalism, in concert with the generalized non-Hermitian extension, see Sect. 5, permits a more realistic time conception yielding a microscopic reading of self-organizational traits as they emerge in the formulation of the paradigm of evolution.

In order to examine the dynamical condition that relates to the appropriate density matrix ϱ , it is convenient to turn to the Liouville equation

$$i \frac{\partial \varrho}{\partial t} = \mathcal{L} \varrho \quad (7.1)$$

where the definition of the Liouvillian, as usual, is based on the Hamiltonian H describing the system of atomic and molecular configurations under investigation, i.e.

$$\mathcal{L} \varrho = H \varrho - \varrho H^\dagger \quad (7.2)$$

The insertion of H^\dagger above guarantees that the non-Hermitian extension yields complex eigenvalues with the proper sign of their imaginary parts.

Although Eq. (7.1) is formally equivalent to the Schrödinger equation, the Liouville equation allows a more general representation, i.e. it directly renders quantum transitions, portraying also ensemble-representable situations, not to mention the possibility to mimic both quantum and classical systems with a common algebra. The formulation prompts higher-level interpretations in terms of super-operators defined on a super-operator space of operators, i.e. density matrices, the latter defined on a carrier space of preferred basis vectors. In principle, standard linear algebra, (super-) propagators and (super-) resolvents and their transforms follow analogous patterns as the description outlined in the previous sections, see e.g. Prigogine [32], Obcemea and Brändas [33], Löwdin [9]. The objectives of our undertaking is to build hierarchies of complex structures, e.g. defining a suitable carrier space of quantum states from which an appropriate operator space yields the input for the Liouville dynamics on a higher level of complexity with the notion of cellular and neural organization in focus.

As a starting point we begin with the conceptual object of a non-degenerate ground state of our molecular system, i.e. $\Gamma^{(2)}$ of Eqs. (6.3) and (6.6–6.9). There are two interconnecting problems facing the development: (i) the thermal bath surrounding the system and (ii) the mixed dynamics of light fermionic carriers and the heavier nuclear skeleton. Let us first discuss the issues associated with the nuclear-electronic correlations. As has been mentioned in earlier work [12, 34], it is necessary to go beyond the Born-Oppenheimer approximation. One approach would be to view the dynamical interaction as a scattering experiment, which will be described in more detail below. Another way out would be to work with density matrices, where, for the light fermionic portion, the nuclear degrees of freedom are traced out, and vice versa for the nuclear problem. In both pictures there is a mirroring relation between the two entangled subsystems consisting of (I) the light fermion carriers and (II) the nuclear skeleton, see Löwdin [9] and Brändas and Hessmo [34].

The theorem says that the mapping of the system (I) to (II) followed by a mapping back to (I) and the mapping with (I) and (II) interchanged have the same nonvanishing eigenvalues and can be brought to the same classical canonical forms. In principle this defines the mapping between the carrier system and the nuclear

frame and imparts mirroring relations⁷ as the total system (I + II) is subject to endogenous perturbations. Thus we can use our preferred basis $|\mathbf{h}\rangle$ in two ways: first identifying $\langle \vec{r} | h_k \rangle = h_k(\vec{r}) = \mathcal{f}(\vec{r} - \vec{r}_k)$, with \vec{r} essentially being the coordinate for the center of mass of the fermionic pair and \vec{r}_k the coordinate for the nucleus k, with \mathcal{f} being a function localized at the origin. One can hence, mutatis mutandis use the Dirac ket $|\vec{r}_k\rangle$ to denote the nuclear degree of freedom at site k . As a metaphor one might denote system (II) as a device or target for measurements on the structure, organization, assembly or arrangement, i.e. the system (I). The obvious objection that the two mappings may have different dimensions is naturally resolved by the realization the difference corresponds to the appropriate number of zero eigenvalues of the larger dimensional mapping.

With the aforementioned link between (i) and (ii) in mind, we will address the query related to the description of the molecular system in their thermal environment. By redefining the Liouvillian, the commutator with H , we introduce the corresponding anticommutator

$$\mathcal{L}_B \varrho = \frac{1}{2} (H\varrho + \varrho H) \quad (7.3)$$

where the Prigogine energy superoperator \mathcal{L}_B is subject to the Bloch equation ($\beta = \frac{1}{kT}$)

$$-\frac{\partial \varrho}{\partial \beta} = \mathcal{L}_B \varrho \quad (7.4)$$

where k is Boltzmann's constant and T the absolute temperature. Since Eq. (7.3) includes the addition in contrast to the minus sign in Eq. (7.2), the density matrix during analytic continuation needs to be represented as a complex symmetric form, i.e. $|\cdot\rangle\langle\cdot| \rightarrow |\cdot\rangle\langle\cdot^*|$, signifying a complex conjugate in the bra-position. In particular for the density matrix given by Eqs. (6.7–6.9) one obtains directly the thermalized solution for an open system (note that, as an example, system I is open with respect to its coupling to system II and vice versa) at temperature T , defining the total energy to be zero, the arbitrarily chosen zero energy level,

$$e^{-\beta \mathcal{L}_B} \varrho = \lambda_L \sum_{k,l=1}^n |h_k\rangle e^{i\beta_1^L(\epsilon_k + \epsilon_l)} \langle h_l| + \lambda_S \sum_{k,l=1}^n |h_k\rangle e^{i\beta_2^L(\epsilon_k + \epsilon_l)} (\delta_{kl} - \frac{1}{n}) \langle h_l| \quad (7.5)$$

The derivation rests on the assumptions that the basis functions can be chosen real without restrictions and that the energy relations straightforwardly follow from

⁷ The classical mirror theorem as reformulated by Löwdin [9] is a much underrated and underused idea. It affects the measurement dilemma through the precise quantum mechanical relations between the system and the gauging device before decoherence. Here it opens a possibility to go beyond the rigidity of the Born-Oppenheimer approximation. For an account of some novel trends in theoretical and experimental quantum phenomena, see Karlsson and Brändas [35].

the partitioning of the exact dynamics [12]. Using the model of nuclei as vibrating oscillators, we can use the partitioning technique to estimate the complex energy of each oscillator dressed by the correlations from the other ones and from the environment. Hence one obtains for each oscillator (remember the mirror relation between $|h_k\rangle$ and $|\vec{r}_k\rangle$ and the reciprocal relationship between the energy width ϵ_k and the life time τ_k)

$$z_k = E_k - i\epsilon_k = -i\epsilon_k = -i\hbar/2\tau_k \quad (7.6)$$

where we have used the fact that the thermal excitations push the free energy just above the threshold (here assigned as the zero energy level) deducing that $E_k = 0$.

The unusual properties of the solution, Eq. (7.5), will be further explored in connection with a derivation of the boundary conditions for the representation of a free energy principle and the associated Correlated Dissipative Ensemble, CDE. It will be demonstrated that CDE, by integration of an irreducible unification of fundamental quantum-thermal correlations exhibits a microscopic law of self-organisation.

8 Free Energy Configurations and the Correlated Dissipative Ensemble, CDE

We will demonstrate the importance of the Free Energy Configuration above by briefly returning to the problem related to the inconsistent practice of employing the Born-Oppenheimer approximation, i.e. essentially treating the nuclei adiabatically. From the mirror theorem we will adopt a simple scattering model involving the electron carriers and the oscillating nuclei. At the same time we have learned from previous derivations of the representable and the quantum thermalized density matrix that merged quantum-thermal correlations might display strong off-diagonal order.

We will establish this point by considering our open structure as an elementary set-up for a scattering experiment. We will imagine our system (I), comprising n bosonic or paired fermionic degrees of freedom being “scattered” or correlated with system (II), the nuclear part, on a process relaxation timescale given by τ_{rel} , which in general should be much larger than the thermal timescale. Note that the system (I) is dissipative, i.e. it exchanges energy and/or entropy with its environment here system (II).

In principle the system may consist of fundamental building blocks that are primarily correlated in a complex biological system. One may e.g. describe scattering-like changes of nucleotide base pairs inside the DNA helical order of the gene, or polypeptide foldings translated into a linear chain of amino acids producing a well-defined three-dimensional structure in the cell, intrinsic genome-wide organisations of nucleosomes, extending the study all the way up from the chromosome to the whole cell, or to the collection of certain aggregations of cells belonging to a particular hierarchical position in the organism assigned to build

specific material structures and to foster communication channels for the spinal cord, the central nervous system.

We complete the model by defining the “incoming beam” of the light carriers arriving on an area or region occupied by the correlated nuclei, corresponding to a spherically averaged total cross section, σ_{tot} , being consistent with the physical parameters of the model. The outcome of the process is defined so that on average one will detect one particle degree of freedom in the differential solid-angle element $d\Omega$ during the timescale $\tau_{\text{corr}} \propto \tau_{\text{lim}}$ here given by Heisenberg’s uncertainty relation ($\tau_{\text{corr}} \approx 2.46 \times 10^{-14}$ s at 310 K)

$$\tau_{\text{corr}} = \frac{\hbar}{kT} \quad (8.1)$$

Note that the purpose is to find consistent relations between the temperature, the size of the dissipative structure, their various inherent timescales, reaction rates etc., and to use this information as input for our generalized quantum statistical analysis. With these ingredients we obtain via the application of conventional scattering theory that the incident flux, N_{inc} of the number of particles/degrees of freedom per unit area and time obtains as

$$N_{\text{inc}} = \frac{n}{\sigma_{\text{tot}} \tau_{\text{rel}}} \quad (8.2)$$

Furthermore, since number $N_s d\Omega$ of particles scattered into $d\Omega$ per unit time is

$$\sigma_{\Omega} d\Omega = N_s d\Omega = \frac{d\Omega}{\tau_{\text{corr}}} = \frac{kT}{\hbar} d\Omega \quad (8.3)$$

one obtains for the total cross section

$$\sigma_{\text{tot}} = \int \sigma_{\Omega} d\Omega = \int \frac{N_s}{N_{\text{inc}}} d\Omega \quad (8.4)$$

from which one gets the following relation between our physical parameters of the model

$$n = \frac{4\pi kT}{\hbar} \tau_{\text{rel}} \quad (8.5)$$

Organizing the correlated cluster of harmonic oscillators with the energies $\varepsilon_l = \hbar\tau_l^{-1}$ with the (smallest) energy difference between the equidistant harmonic oscillator levels being $\hbar\tau_{\text{rel}}^{-1}$ displaying a spectrum from the zero-point energy to $\hbar\tau_{\text{lim}}^{-1}$. The quantized oscillators are in a sense reminiscent of Planck’s law. Straightforward examination of the situation reveals (the proportionality factor 4π between τ_{lim} and τ_{corr} essentially corresponds to a an integral over solid angle)

$$\tau_{\text{rel}} = (l-1)\tau_l = \tau_2 = n\tau_{\text{lim}} = 4\pi n\tau_{\text{corr}}; \quad l = 2, 3, \dots, n \quad (8.6)$$

From Eqs. (7.6), (8.5–8.7) one gets

$$\beta\epsilon_l = \frac{2\pi(l-1)}{n} \quad (8.7)$$

which inserted into Eq. (7.5) yields, $\Gamma_T = e^{-\beta\mathcal{L}_B}\varrho = \varrho_T$

$$\Gamma_T = \varrho_T = \lambda_L \sum_{k,l=1}^n |h_k\rangle e^{i\frac{\pi}{n}(k+l-2)} \langle h_l| + \lambda_S \sum_{k,l=1}^n |h_k\rangle e^{i\frac{\pi}{n}(k+l-2)} \left(\delta_{kl} - \frac{1}{n} \right) \langle h_l| \quad (8.8)$$

The result (8.8) may not appear very exciting unless one carries out the transformation \mathbf{B}^{-1} , i.e. introduce the new basis $|\mathbf{h}\rangle\mathbf{B}^{-1} = |\mathbf{f}\rangle$ the outcome becoming

$$\Gamma_T = \varrho_T = \lambda_L \mathcal{J}^{(n-1)} + \lambda_S \mathcal{J} \quad (8.9)$$

with \mathcal{J} being the nilpotent operator defined by $\mathcal{J}^{(n)} = 0$; $\mathcal{J}^{(n-1)} \neq 0$ signifying the quantum transitions below

$$\mathcal{J} = \sum_{k=1}^{n-1} |f_k\rangle \langle f_{k+1}| \quad (8.10)$$

Incidentally the matrix representation of \mathcal{J} is an n -dimensional matrix with one's above the diagonal and the remaining elements equal to zero. The largest dimension of the so defined Jordan block is called the Segre characteristic of the degenerate eigenvalue. This thermalized configuration has previously been designated a coherent-dissipative structure [31, 36]. However, in order to signify its thermal characteristics and relevance for free energy principles, see below, we will denote Eqs. (8.8–8.10) as the Correlated Dissipative Ensemble, CDE. At the same time the energy given by Eq. (6.2) over the CDE defines a correlated free energy configuration being a authentic proxy of the (Helmholtz) free energy, here signified as zero energy gauge.

The result above is of crucial importance implying that $\Gamma^{(N)} = |\Psi(g)\rangle\langle\Psi(g)|$, after reduction, analytic continuation and thermalization yields $\Gamma_T^{(N)} = |\Psi(f)\rangle\langle\Psi(f^*)|$, $f = f_1$ and with $\Psi(f)$ and $\Psi(f^*)$ orthogonal to each other as imparted by Eqs. (8.8–8.10). We will use this result in two ways, (a) *to develop relevant building blocks for biological systems* and (b) *to use the properties of the transformation \mathbf{B} in (6.4) as a means for communication between entities on the molecular level*. Once it is realized that communication is ascertained between molecules and cells, this will extend to higher order levels of semiotic interactions and communications.

9 The CDE as a Spatio-Temporal Mnemonic Configuration, STEM

Returning to the general issue portrayed in the introduction, we will use the Correlated Dissipative Ensemble, CDE, to examine complex enough examples⁸ from the biological field. As a background for this undertaking we remind the reader of the important work of the leading evolutionary biologist of the twentieth century, Ernst Mayr. In particular we revisit his concept of so-called biological teleonomic processes, i.e. those influenced upon by an evolved program, cf. the genetic code, Mayr [37, 38]. To do so we will reconnect with our main result of the previous sections, i.e. the correlated free energy configuration, Eqs. (8.8–8.10).

In passing we note that the present result leads to a mathematical generalization of the self-referential argument given in Sect. 4. While the translation of Gödel's paradox into a Jordan matrix of dimension two (the Segré characteristic equals 2), the dissipative structure of Eq. (8.9) contains an n -dimensional Jordan block, i.e. with the Segré characteristic equal to n . Although the situations between the two scenarios are vastly different, we will demonstrate that such an analogy imparts fundamental consequences for the (teleo-)dynamics of the dissipative system, cf. the analogy between Gödel's self-referential argument, translated to unconventional algebraic form, and its identical gravitational formulation in terms of conjugate physical observables.

For instance, in our portrayal of a complex enough biological system, the preferred basis \mathbf{h} may represent important sites in the cell, reflecting the mirror-structure between the light fermion-carriers and the nuclear dynamics, the latter referring to the molecular double-proton tunnelling motion, see e.g. Löwdin [39] for a simple illustrative account, of the various base pairs, adenine-thymine, AT, and guanine-cytosine GT (and uracil instead of thymine in RNA).

In order to continue the build-up of a biological organisation, in terms of the dissipative units just defined, we will characterize the cell C^i , as derived from the molecular motion associated with the M base pairs, rewriting Eqs. (8.8–8.10) and utilizing Eq. (6.9)

$$\varrho = C^i = \frac{1}{\sqrt{1+q^2}} \left\{ q|f_1^i\rangle\langle f_n^i| + \frac{1}{(n-1)} \sum_{k=1}^{n-1} |f_k^i\rangle\langle f_{k+1}^i| \right\} \quad (9.1)$$

$$\text{Tr}\{\varrho\varrho^\dagger\} = 1; \quad q = p/(1-p) \quad (9.2)$$

For e.g. $n = 2M = N$; one obtains that $p = 1/2$, and hence $q = 1$. This choice is commensurate with a given selection of M base pairs, noting that we have in each

⁸ “Complex enough” is an unprecise statement that is prompted by the need to go from teleomatic to teleonomic processes. For more on the rules of evolving organization processes, see note added in proof.

particular entry in the string the choice between two pairs, AT (AG in RNA) and GT. Note also that this version prompts information capacities in bits, but because of the reduced density matrix formalism the formulation exhibits quantum mechanical linearity (linear in an n -dimensional space) in contrast to the full number of possible configurations being $\binom{n}{M}$. In general q will always be a natural number if n is a multiple of M . If considering the genetic alphabet, e.g. having four possible letters, this implies $p = 1/4$ and $q = 3$.

Recapitulating, the basis f obtains from the transformation $\mathbf{h} = \mathbf{fB}$, where \mathbf{B} becomes the crucial bearer of “phonon induced” channel information according to Eq. (6.4). Remember also that $\mathbf{g} = \mathbf{hB}$ simultaneously transforms the original second order reduced density matrix of the total system at temperature $T = 0$ to canonical (diagonal) form, while simultaneously bringing the thermally excited, quantum correlated system to the (non-diagonal) classical canonical form.

Before analysing the time evolution and the statistical properties of the base pair organisation, given by Eqs. (9.1 and 9.2), we will emphasize two things: *(i) the requisite reference to non-hermitian extension of quantum mechanics allows physically meaningful solutions in the complex energy plane (the “unphysical Riemann sheet”) with broken time reversal symmetry and including fundamental resonance structures, (ii) the irreducible merger of quantum- and thermal correlations produces a dissipative free energy configuration, which converts the pure density matrix at absolute temperature zero, into a quantum-thermally correlated transition matrix with precise spatio-temporal properties.* The conditions Eqs. (8.5–8.7) define the relations between the number of degrees of freedom, the temperature and relevant timescales of the system; hence we speak of a spatio-temporal structure. The precise adjustment or fine-tuning regulates the developments inside the cell and builds up the teleonomic character of the cell in its hierarchical order of the living organism.

A living system (in vivo) is, in contrast to a normal probabilistically determined physical system (ex vivo), a confined dissipative self-organising structure, characterized by *(a) its (dissipative) coupling to the environment, (b) its metabolic processes, including microscopic self-organisation (anabolism fuelled by catabolism) (c) the genetic function, and finally (d) homeostasis for appropriate spatio-temporal regulation.* Obviously, our representation, Eq. (9.1), by exchanging energy and entropy with the environment, will automatically satisfy (a) and (b). It has been shown, see Refs. [40, 41] that the Correlated Dissipative Ensemble (CDE), defined in Sect. 8, will evolve teleodynamically. Furthermore, as will be demonstrated below, see also Ref. [12], this property imparts protocols for communication as a genetic functionality (and beyond) satisfying also points (c) and (d) including an important temporal quality, i.e. with its regulative decoherence into classical states (also quantum states) being forbidden by the code protection protocol of the irreducible Jordan block structure.

As cases of confined living systems, we may list genes, chromosomes, cells, the spinal cord, the brain etc. In the past these features have led to the notion of either

coherent-dissipative structures or a spatio-temporal breathing edifice, cf. the flagellar movement in cytochemistry or gamma waves in the brain, commensurate with estimates resulting from the present configurations. Since the non-material spatio-temporal structure to be presented in more detail below, will remind of the steps regulated by enzymatic pathways as the response to changes in the cell's environment or signals from other cells, the semiotic character of the cell above motivates the name STEM or Spatio-TEmporal Mnemonic entity.

Thus defining a “cell basis” of the STEM units, Eq. (9.1), we will build a higher order Liouville super operator structure based on the propagator/generator \mathcal{P} . Note that we can form in analogy with $\mathbf{h}, \mathbf{g}, f$ of Sects. 6 and 7, the corresponding cell basis $\mathbf{H}, \mathbf{G}, \mathbf{F}$ subject to the same fundamental transformation (where n maybe different to the one in (6.4), yet might be related, and $\omega = e^{i\pi/n}$, see more below)

$$|\mathbf{G}\rangle = \mathbf{B}|\mathbf{H}\rangle \quad (9.3)$$

The probability argument, cf. the discussion leading up to Eqs. (6.6–6.9), can now be augmented, appropriately modified with $\mathcal{I} = \sum_{k=1}^n |F_k\rangle\langle F_k|$ to define the propagator \mathcal{P} , see e.g. Refs. [40, 41] for details

$$\mathcal{P} = (\omega_0\tau - i)\mathcal{I} + \mathcal{J} \quad (9.4)$$

with ω_0 the thermal frequency, $\tau = \tau_{\text{rel}}$ the average lifetime of the cell and τ_{corr} the short timescale, here essentially equal to τ_{lim} of the thermal molecular motion. Note the fundamental difference in the higher level description, Eq. (9.4) and the thermalization derived on the lower one from Eq. (7.4), with each thermally excited nuclear oscillation, coupled to the environment (of the other degrees of freedom of the system), yielding the threshold zero energy and the appropriate width. The Liouville configuration imparts the thermal frequency ω_0 and correlation time $\tau_{\text{corr}} = \hbar/kT$ from the interaction with the environment consisting of other cells. Hence the build-up of (9.4) is straightforward, including the appearance of the non-conventional operator \mathcal{J} , see e.g. the analogy with Eq. (8.10).

$$\mathcal{J} = \sum_{k=1}^{n-1} |F_k\rangle\langle F_{k+1}| \quad (9.5)$$

The n -dimensional Jordan block \mathcal{J} appears in analogy with our previous discussion, resulting in prolonged timescales of multiples of τ . Hence with the dimension n of \mathcal{J} in resonance (or equal for simplicity) with the dimension appearing in Eqs. (6.6–6.9) and (8.5–8.10), important information and associated communication will be transcended from the molecular- to the cellular level. The scaling-up from the intra-cell degrees of freedom to the inter-cell ones provides the verification of \mathcal{J} above. Consequently, there must be a resonating relation between

the inside degrees of freedom of the cell and its higher order structure in the hierarchy of the cell organisation.

Expressing the propagator in dimensionless units, we obtain a cellular Q -value, defined via

$$Q = \omega_0 \tau \quad (9.6)$$

Here we may easily determine Q as follows. From Eq. (8.5) one finds, with $\tau = \tau_{\text{rel}}$,

$$n = \frac{4\pi kT}{\hbar} \tau_{\text{rel}} = 4\pi \frac{\tau_{\text{rel}}}{\tau_{\text{lim}}} \propto Q \quad (9.7)$$

and provided we have defined τ as the average lifetime for the cell C_i , we can divide out the integration over the solid angles and obtain the result

$$Q = n \quad (9.8)$$

Equation (9.8) contains an especially valuable piece of information. The Q -value of the cell reveals not only the dimension n of the transformation \mathbf{B} , see e.g. (6.4) but also a more subtle property. Due to the factorizing nature of the transformation and the ensuing cyclic properties of the column vectors, the Q -value in effect calls for an encoding incorporating simultaneously the molecular, the super-molecular, and the cellular levels.

10 The Poisson Distribution and its Implication for STEM

As is well-known, the Poissonian distribution is to be found in many situations related to counting, from e.g. radioactivity via mutations in biology to telecommunications between human agents. Our aim will be to derive this law as a general property of a teleodynamically evolved universe.

Alongside this association it is natural to replace the spatial analysis in terms of the localization argument that led to the derivation of the density matrix, Eq. (6.8), and after thermalization to the dissipative ensemble, Eq. (8.9), with temporal inquiries related to “phone calls” or communications between e.g. molecular and cellular entities. In analogy with considerations providing the transformation \mathbf{B} and constituting a platform for the genetic code, it is imperative to recognize that the off-diagonal correlations between the cells, while analogously providing justification for the correlations (9.5), should be commensurate with the cell’s Q -value.

Within the stipulated time-direction (the time reversal symmetry is broken) and the appropriate time scales of the setup, the causal propagator $\mathcal{G}(t)$ and the resolvent $\mathcal{G}_R(z)$ defined by

$$\mathcal{G}(t) = e^{-i\mathcal{P}\frac{t}{\tau}}; \quad \mathcal{G}_R(\omega\tau) = (\omega\tau\mathcal{I} - \mathcal{P})^{-1} \quad (10.1)$$

yield directly inserting the Liouvillian, Eq. (9.4),

$$e^{-i\mathcal{P}\frac{t}{\tau}} = e^{-i\omega_0 t} e^{-\frac{t}{\tau}} \sum_{k=0}^{n-1} \left(\frac{-it}{\tau} \right)^k \frac{1}{k!} \mathcal{J}^k \quad (10.2)$$

$$(\omega\tau\mathcal{I} - \mathcal{P})^{-1} = \sum_{k=1}^n [(\omega - \omega_0)\tau + i]^{-k} \mathcal{J}^{(k-1)} \quad (10.3)$$

From the degenerate situation with $F_k(t) = e^{-i\omega_0 t} e^{-\frac{t}{\tau}} F_k(0)$ one finds for the r th power of t (note that only F_1 is an eigenfunction of \mathcal{P} while the remaining F_k 's complete the root manifold)

$$N(t) \propto |\langle F_1 | \mathcal{J}^r | F_{r+1} \rangle| \left(\frac{t}{r} \right)^r \frac{1}{r!} e^{-\frac{t}{\tau}} = \left(\frac{t}{r} \right)^r \frac{1}{r!} e^{-\frac{t}{\tau}} \quad (10.4)$$

which follows directly from the definition (9.5), i.e.

$$\mathcal{J}^r = \sum_{k=1}^{n-r} |F_k\rangle \langle F_{k+r}| \quad (10.5)$$

For the highest power $n-1$ one obtains

$$dN(t) = t^{n-2} \left(n-1 - \frac{t}{\tau} \right) N(t) dt \quad (10.6)$$

which imparts an altered microscopic law of evolution, i.e.

$$dN(t) > 0; \quad t < (n-1)\tau \quad (10.7)$$

It is important to realize that Eqs. (10.6) and (10.7) implies a higher level timescale $\tau_{\text{com}} = (n-1)\tau$, since the cellular model is based on the molecular lifetimes $\tau = \tau_{\text{rel}}$. In other words it modifies the boundary conditions Eqs. (8.6) and (8.7), with $\tau_{\text{corr}} \rightarrow \tau_{\text{rel}}$ and $\tau_{\text{rel}} \rightarrow \tau_{\text{com}}$.

Incidentally one observes that $\mathcal{G}(t)$ as defined in Eq. (10.1), needs to be modified to include the temperature explicitly and the commutation relation $E_{\text{op}} t = i\hbar + tE_{\text{op}}$ when requested by the specific quantum situation. Hence, with an adjustment back to the microscopic timescale $\tau_{\text{corr}} = \tau_{\text{lim}} = \hbar/kT$, one writes, cf. Zubarev [42],

$$\mathcal{G}(t + i\hbar\beta) = e^{-i\mathcal{P}\frac{(t+i\hbar\beta)}{\tau}} \quad (10.8)$$

from which one gets

$$N(t + i\hbar\beta) = \sum_{r=0}^{n-1} \left(\frac{4\pi}{n}\right)^r \frac{1}{r!} e^{-\frac{(t-\tau)}{\tau}} \quad (10.9)$$

Dividing the lifetime τ into $n/4\pi$ discrete time units, or going from $\tau - t$ to t in single steps, defines a cumulative Poisson statistics for the intra-cell quantum-thermal correlated ensemble with the intensity (rate) parameter $\lambda = 4\pi/n$, i.e.

$$P\{(t - \tau)/\tau < n/4\pi\} = \sum_{k=0}^{n-1} \left(\frac{4\pi}{n}\right)^k \frac{1}{k!} e^{-\frac{4\pi}{n}} \quad (10.10)$$

It is important to realize that there must exist an underlying microscopic level for the interpretation, here consisting of the molecular motions characterizing the cell. The boundary conditions that equate the intra-cell quality number n with the cell's Q -value and the dimension of \mathcal{J} in Eq. (9.4) (or provide appropriate multiple relationships) define the cell's actual position in the hierarchy of the organism and the corresponding assignment of the authentic purpose recognized by the collection of cells that it belongs to.

Summarizing, we have augmented the conventional decay law with a self-organizing trait derived via the time evolution of the propagator, Eq. (10.2), the latter verifying an inherent Poissonian statistics of the STEM. The STEM structure for each cell with its origin descending on the molecular (e.g. DNA-RNA) level exhibits its spatio-temporal properties from emerging quantum-thermal correlations of the dissipative ensemble. Examining the evolution with a degeneracy analysis, one finds that the so-called Segrè characteristic, n , defines the cell's Q -value factor in analogy with the quality aspects of an oscillator-resonator. As already mentioned, the cell's characteristic Q -value, conveys vital information as it specifies the precise semiotic structure of the transformation \mathbf{B} , allowing extrinsic communication, i.e. memory storage and retrieval along the Poissonian distributed broadband channel as will be seen in detail below.

11 Memory and Communication on Channel SELF

In order to present the communication protocol that derives from our extended quantum formulation, one needs to understand the possibilities disclosed by the properties of the transformation \mathbf{B} , see Eq. (6.4). In Eq. (11.1) below, we will display $\sqrt{12}\mathbf{B}$ as a simple diagram, where the dimensions of the cyclic vectors of \mathbf{B} are given in the appropriate entry. For simplicity we will not display the first column vector of one-dimensional units "1", and therefore we will only have 11 columns,

$$\begin{array}{ccccccccc}
 & & 2 & & & & & & \\
 & 6 & 4 & 3 & 2 & 3 & 4 & 6 & 12 \\
 12 & 6 & 4 & 3 & 12 & 2 & 12 & 3 & 4 \\
 & 6 & 4 & 3 & 2 & 2 & 3 & 4 & 6 \\
 & & 3 & & 2 & & 3 & & \\
 & & & & 2 & & & & \\
 & & & & & 2 & & & \\
 \end{array} \quad (11.1)$$

moreover noting the obvious symmetry between the columns of the graph. Alternatively one could also belabour the seven non-commuting factors, including the twelve ones and leaving out the final repetitions, i.e.

$$\{12\} = \{12 \times (1) \oplus 1 \times (12) \oplus 2 \times (6) \oplus 3 \times (4) \oplus 4 \times (3) \oplus 1 \times (12) \oplus 6 \times (2)\} \quad (11.2)$$

Using the notation in Eq. (11.2) we conclude that among the 12 columns of \mathbf{B} there are 4 that are of the type $1 \times (12)$, and hence that one third of them cannot be factorized, while the remaining two thirds can. In addition the choice $n = 12$ has a particular relevance since the graph supports the codon triplets as fundamental cycles. Including higher dimensional cycles, e.g. those corresponding to 20 amino acids, one could append $n = 12 \times 5 = 60$, i.e. including the factor “5”, which will add columns divisible by 5, 10, 15, 20, 30. One concludes that 40 columns of 60 are not factorizable, increasing the abundance of the latter ($n = 12$) from $1/3$ to $2/3$. Therefore one predicts that a large number of vectors do not convey any information as they contain no closed cycles of order smaller than n , compared to the number of those that do contain such cycles (not to mention the case n equals a prime!). This piece of information provides nested information bearing cycle structures for encoding information concerning cell differentiation and communication regarding quality recognition and hierarchical cellular order and organisation, indeed also suggesting a possible understanding of the exon-intron mechanism of the genes.

One might continue to exploit the metaphor seeing the phonon-assisted communication as a number of “phone calls” between the cells during a given time, t , being multiples of the characteristic time $\tau = \tau_{\text{rel}}$. Accordingly the probability that k “calls” are exchanged during a specific time interval, with each “telephone call” occurring with a known average (intensity) parameter $\lambda_l = (l-1)\tau_{\text{rel}}/\tau_{\text{rel}} = (l-1)$; $l = 2, 3, \dots, n$, i.e. with a specific distribution for each value of l , is simply given by

$$P_{\lambda_l}(k) = \frac{(l-1)^k}{k!} e^{-(l-1)} \quad (11.3)$$

with the mean equal to the variance equal being $\lambda = l - 1$. The number of calls during $\mathcal{T}_{l-1} = (l - 1)\tau_{\text{rel}}$ is at maximum for $l = n$. If counting $l = 0$ as an event the community of cells comprises, during \mathcal{T}_{n-1} , with a probability according to (11.3),

n communications between M cells distributed over n possible “sites” in the organism. Hence the length, n , of a message is directly matched with the variance and the mean (a well-known property of the Poisson distribution).

In summary, each cell is characterized as an STEM system, i.e. a dissipative system, which encompasses nested encodings, as programmed in the factorized canonical vectors of the transformation \mathbf{B} . Communication runs from the genetic to higher order codes, e.g. the scheme for the accretion of proteins, stored in the genetic alphabet and transformed via resonant mechanisms, depending on the cell’s quality value, from cell to cell. Similarly the intra-cell mechanism imparts a cumulative Poisson statistics based on the intensity parameter $\lambda = 4\pi/n$, with information divided up into smaller spatial packages as n increases. While the inter-cell communication is mainly temporal the intra-cell statistics is predominantly spatial.

Even if semantic or semiotic mappings centred on \mathbf{B} need further analysis, it is clear that our representational explanation exudes some common sense. The modern state of the art, i.e. how information from sensory input, coding for perception and coupling the information via interneurons, to motor output, is to a large part due to the Nobel Laureate Kandel [43] studying the giant marine snail Aplysia. In general, various forms of learning give rise to different patterns of neural activity, and long-term memory to the synthesis of new proteins. The important point is that chemical synapses predominate in the brain. Consequently it is tempting to analyse neuronal activities related to the nervous system of the present model. Rather than presenting an exchange of numbers, see Brändas [12] for some possibilities, one might combine relevant factors, like 60 for the DNA-protein synthesis or 23 reflecting the precise number of chromosome pairs in humans. The corresponding diagrams emulate interlevel communication releasing active terminals serving as classical communication channels for synaptic transmission with shifting Q -values.

The present communicative semiotics, based on the law of self-reference, does produce teleodynamic encodings and permit collections of neurons to combine external signals with internal memories. Coded semantic information, communicated via synchronized spike trains, may accordingly be investigated in terms of Poisson statistics as a predestined general feature of the neural cell. Consequently, this supports the function of statistical distributions, with $\lambda = (l-1)$ for $l = 2, 3, \dots, n$ providing a broadband channel (mean and variance equal to λ) for communication. Furthermore, irrespective of the location of the spatio-temporal site for communication, resolve and action, the only agent making the decision is the SELF. In this sense we might say that we have been able to reduce biological accounts to chemistry and then to physics under the reflexive law of self-referentiality, cf. Gödel’s paradox. Along with this understanding it is conceivable to explain the so-called psychological arrow of time, as rationalized from our teleonomical physical law. Hence, as suggested already in Ref. [15], the analogy between gravitational interactions and the self-referential law expressed in Sect. 4, therefore will unify all arrows of time under the heading of the Gödelian arrow of time.

While modern communication, as perceived in our society, is founded on traditional broadcasting techniques, referring to the modulation of electromagnetic

waves, based on Maxwell's equations, we have here another metaphor: The interactive transmitter SERVING LIFE Broadcasting on Channel SELF: A Poisson Distributed Ultra-Wide Broadband. Obviously communication between life forms requires some form of intelligence. Although this is a highly controversial term, we will only use it in its most trivial sense, i.e. in the meaning to pick out or understand something, but also to discern, distinguish, differentiate and recognize. One may e.g. refer to the laws of physics, like gravity or the second law of thermodynamics, as governing teleomatic processes, or as a programmed activity, restricted to action or behaviour owing its goal-directedness to the influence of an evolved program during evolution.

12 Conclusion

In the introduction we elaborated on the essential ingredients to promote a reliable and consistent scenario for the evolution of cosmos from the “Beginning” to the “End”. We did start with conjugate operator arrays presenting a platform for a theoretical discourse of maximum generality, including quantum-classical treatments, relativistic practices, teleomatic laws and teleodynamic processes from Gödel's incompleteness theorem to Einstein's laws and the extension of Darwin's theories to the Paradigm of Evolution.

In order to augment the present formulation with the cosmological challenges, we return to one of the key quantities in the gravitational enigma, viz. the emergence of an initially nonrotating black-hole object, Eq. (3.7), with M characterized as a spherical mass distribution, which does not change sign when $m \rightarrow -m$, see Sect. 3 for details.

As might be anticipated from the density matrix representation in Sect. 6, there exist proximate relations between the simple form derived, Eqs. (6.7–6.9) and Yang's celebrated concept of ODLRO, Off-Diagonal Long-Range Order, [28], and Coleman's notion of an extreme state [29], see e.g. [6, 31, 36] as well as references therein. We will here demonstrate that our black hole type entity is a direct analogue of the organization of ODLRO. In addition we will extend the discussion to a Kerr-type [8] rotating black hole characterized by its mass and angular momentum, see also Ref. [44].

From Eq. (3.7), with $r \leq 2\mu$, i.e. with the particle-antiparticle superposition inside the Schwarzschild boundary, solving for the canonical vectors in analogy with Eqs. (4.14') and (4.15') one obtains for the “vacuum” base vectors $|0\rangle$ and $|\bar{0}\rangle$ in terms of the mass m for the particle and with \bar{m} for the antiparticle, i.e.

$$|0\rangle = \frac{1}{\sqrt{2}}(|m\rangle - i|\bar{m}\rangle) \quad (12.1)$$

$$|\bar{0}\rangle = \frac{1}{\sqrt{2}}(|m\rangle + i|\bar{m}\rangle) \quad (12.2)$$

from which we will consider a finite number of fermion particle-anti-particle pairs in a vacuum (or particle-like environment, cf. Cooper pairs in a superconductor) written as

$$|0\rangle \wedge |\bar{0}\rangle = i|m\rangle \wedge |\bar{m}\rangle \quad (12.3)$$

Using the formulas of Sect. 6 to simplify the energy relations for the extreme state, which are equivalent to the ones acquiring Yang's ODLRO for superconductors, forming the bosonic condensate of particle-antiparticle pairs, Eq. (12.3), one obtains, in close analogy with the organisation of the superconducting state, that a large eigenvalue of macroscopic order develops consistent with a bound state of the condensate.

At the same time there is a fundamental difference as regards the energy relations Eqs. (6.2–6.5), i.e. there are here only rotational degrees of freedom available for the “black hole” system. Modelling the interaction by the reduced Hamiltonian of Eq. (6.2), the energy relation for the particle-antiparticle condensate yields

$$E = \text{Tr}\{H_2\Gamma^2\} = \lambda_L \langle g_1 | H_{12} | g_1 \rangle + \lambda_S \sum_{k=2}^n \langle g_k | H_{12} | g_k \rangle \quad (12.4)$$

Now considering an adequately orthogonal rotational basis \mathbf{h} , one would expect that

$$\langle h_k | H_{12} | h_l \rangle = \langle h_k | H_{12} | k \rangle \delta_{kl} \quad (12.5)$$

giving the result (for large n)

$$E \approx \frac{N}{2} w; \quad w = \frac{1}{n} \sum_{k=1}^n \langle h_k | H_{12} | k \rangle \quad (12.6)$$

However, since localized pairing in the “black hole” does not make sense inside the Schwarzschild boundary, one instead obtains an original rotational interaction mechanism with all matrix elements

$$\langle h_k | H_{12} | h_l \rangle = w_{LS}; \quad w_{LS} < 0 \quad (12.7)$$

independent of the indexes k and l . Fortunately we are able to characterize the present “condensate” entirely in terms of its mass and angular momentum, leading to a dramatically increased energy stabilization

$$E = \lambda_L \langle g_1 | H_{12} | g_1 \rangle = \frac{N}{2} n w_{LS} \quad (12.8)$$

The macroscopically large lowering of the energy, E , consist of the product between the mass $M \propto N/2$ and the number n of rotational degrees of freedom, i.e. with the rotational quantum number $J \approx n/2$. Thus, from the fundamental rotational mass generating interaction, a quantum mechanical version of a fermionic-antifermionic pair superfluid phase forms the black hole. Since one will always find an equal amount of particle-antiparticle pairs in the condensate it cannot be charged, see also the comment made in Sect. 3, that the mass M would not change sign under the transformation $m \rightarrow -m$.

We have discussed this situation in some more detail in Ref. [44], where the rotationally excited black hole is analysed further in terms of the renowned Kerr metric [8]. Comparing the situation between the Kerr- and the Schwarzschild gauge, one distinguishes in the former case between two physical surfaces, an inner surface that corresponds to the event horizon and an outer one, touching the inner one at the poles of the rotation axis, and with the space in between called the ergosphere.

One may, see Sect. 8, analyse the exchange of matter and energy in the system and its environment, portrayed as a gigantic non-elastic resonance scattering process. Let us first model the n degrees of freedom of the baryonic matter waves falling into the black hole being correlated on a so-called relaxation time scale τ_{rel} before being expelled by the rotational motion of the condensate in the excited state. The scale corresponds to the average lifetime of the “scattering process” (lifetime of our universe) and depends generally on the type of particles or properties of the units being represented cf. the Einstein relation in physical chemistry, which, e.g. connects transport displacements with the diffusion constant D in applications to soft condensed matter. Thus portraying the situation of Sect. 8, one might define an spherically averaged total reaction cross section denoted by σ_{tot} . This area, cf. the surface of the event horizon, should be consistent with the physical parameters of the model. As before one obtains the result, Eq. (8.9)

$$\Gamma_T^{(2)} = \varrho_T = \lambda_L \mathcal{J}^{(n-1)} + \lambda_S \mathcal{J}$$

being the thermalized counterpart to Eqs. (6.3) and (6.8)

$$\Gamma^{(2)} = \varrho = \lambda_L |g_1\rangle\langle g_1| + \lambda_S \sum_{k=2}^n |g_k\rangle\langle g_k|$$

The rotationally excited black hole can now be characterized by the quantum numbers (J, M_J, K) , i.e. in terms of the total angular momentum, the components along the laboratory- and the principal “molecular axis”. Like the case of symmetric rotors one can organize the rotational spectra according to oblate, prolate and spherical rotors, each with their own particular degeneracies and symmetries. Note that the Jordan form above shows a very special structure. From the thermalized density matrix, Eq. (8.9), one learns that the corresponding energy, being precisely zero at equilibrium, exhibits an exceptionally large degeneracy with Segré

characteristic n , the dimension of the irreducible Jordan block. Since the “responsible crossover states” refer to rotational degrees of freedom, we realize that the first term, with the largest weight λ_L , refers to transitions between $K = -J$ and $K = J$, while the second term displays all the other ones from $K = -J$ via $K = -J + 1, -J + 2, \dots, J - 1, J$.

The eigenvalue of $\Gamma_T^{(2)}$ is zero, which corresponds to $K = 0$. Since the direction of the (scattering) flux into the black hole is arbitrary, the orthogonal projection to the (arbitrary) symmetry axis must also be zero. Hence our generalized quantum state is characterized by the quantum numbers $2J + 1 = n; M_J = 0; K = 0$, i.e. with an gigantic rotational energy (large n) but with the rotational z -component in any arbitrary direction equal to zero! Hence from the view of an external observer one would experience its effects all around us, since $M_J = 0$, i.e. one would infer to have the cosmological horizon limited by the event horizon or in other words the cosmological or particle horizon equal to the event horizon. This interpretation is consistent with properties of the conjugate pair, viz. angular momentum and orientation. For instance, if the direction of the angular momentum of the universe is arbitrary, then its orientation is fixed.

Ideas of similar nature have been voiced recently, see e.g. Ref. [45]. The situation occurs in two families of solutions to the Einstein equations. One is the collapse of spherical shells of matter forming a black hole, the other models large structures as our Universe evolves. The first one is inside the black hole behind an event horizon, in the other case we actually live inside the cosmological horizon (outside the event horizon). It is interesting that the present quantum model of a black hole displays a similar representation, thereby providing a reasonable evolution scenario from the Beginning to the End of our Universe, or if one prefers “beginnings to ends”.

Precising the present resonance scattering model: we have modelled our universal scenario as an inbound flux of matter and radiation attracted to the “black hole”, exciting the “black-hole” from a lower to a higher state during the process, getting rid of matter and radiation, leaving the “target” in a free-energy-like configuration, the CDE-like state, characterized by its mass M and angular momentum quantum numbers J, M_J and K . The lower state has low entropy, $S \approx 0$ (a black hole ground state has of course zero entropy), while the “excited state” (or rather the CDE structure) + ejected matter and energy has high entropy. The CDE state, or the free energy configuration, is essentially a zero energy state. With the ejection of matter and radiation, the black hole de-excites to a lower state below the energy threshold, balancing the energy so that one essentially has a zero-energy (and also low entropy) scenario. Actually the entropy relates to the separation of matter-antimatter brought about during the black hole’s excitation and expulsion phase suggesting time-reversed settings for the matter-antimatter asymmetry.

It is possible that the entropy, which appears to grow in the evolving phase of the universe, is also balanced out by the inbound phase so that the entropy of the universe (including the black hole) is effectively constant, while the entropy obviously grows in a universe, considered as an open system (not including the black hole). Nevertheless our model supports and explains the conundrum, i.e. the

puzzling observed cosmological acceleration, without the need to introduce exotic forms of matter or unusual concepts like dark energies, anomalous gravitational interactions and unreasonable cosmological constants. Taking all these points into consideration, advancing evolution as a teleodynamic processes, our rather simple zero-energy universe scenario, ZEUS, is fully commensurate with an intrinsic ontology of entangled physical and mental worlds conjecturing a more basic and detailed theoretical formulation of Darwin's Evolution Paradigm.

Note Added in Proof:

Footnote 1: The notion of the Zero-Energy Universe is not new, see e.g. Berman [46].

Footnote 8: For accounts of the rules for the increase of complexity, see Maruani [47].

Acknowledgments The author thanks the organiser of QSCP XVIII, Prof. Marco Chaer Nascimento, Instituto de Química, Universidade Federal do Rio de Janeiro, Brazil for friendly cooperation, providing an excellent programme and organization. The present research has, over the years, been supported by the Swedish Natural Science Research Council, the Swedish Foundation for Strategic Research, The European Commission and the Nobel Foundation.

References

1. Tegmark M (2003) Parallel Universes. *Sci Am*
2. Greene B (2011) Hidden reality parallel Universes and the deep laws of the Cosmos. Alfred A. Knopf, New York
3. Green MB, Schwarz JH, Witten E (2012) Superstring theory: volume 2, Loop amplitudes, anomalies and phenomenology. Cambridge University Press, Cambridge
4. Gödel K (1931) Über Formal Unentscheidbare Sätze der Principia Mathematica und Verwandter Systeme I. *Monatschäfte für Mathematik und Physik* 38:173–198
5. Brändas EJ (2011) Gödelian structures and self-organization in biological systems. *Int J Quantum Chem* 111:1321
6. Brändas EJ (2012) Examining the limits of physical theory: analytical principles and logical implications (Adv. Quantum Chem.). In: Nicolaides CA, Brändas EJ (eds) *Unstable states in the continuous spectra, part II: interpretation, theory, and applications*, vol 63. Elsevier, Amsterdam, p 33
7. Brändas EJ (2012) The relativistic Kepler problem and Gödel's Paradox. In: Nishikawa K, Maruani J, Brändas EJ, Delgado-Barrio G, Piecuch P (eds) *Quantum systems in chemistry and physics*, vol 26. Springer, Dordrecht, p 3
8. Kerr RP (1963) Gravitational field of a spinning mass as an example of algebraically special metrics. *Phys Rev Lett* 11:237
9. Löwdin P-O (1998) *Linear algebra for quantum theory*. Wiley, New York
10. Feferman S (2009) Gödel, Nagel, minds and machines. *J Philos* 106(4):201
11. Turing AM (1937) On computational numbers, with an application to the Entscheidungsproblem. *Proc London Math Soc* 42(2):230; *ibid.* 43:544
12. Brändas EJ (2013) Some biochemical reflections on information and communication. In: Hotokka M, Maruani J, Brändas EJ, Delgado-Barrio G (eds) *Quantum systems in chemistry, physics and biology*, vol 27. Springer, Dordrecht, p 75
13. Penrose R (1994) *Shadows of the mind: a search for the missing science of consciousness*. Oxford University Press, Oxford

14. Domcke W, Yarkony DR (2012) Role of conical intersections in molecular spectroscopy and photoinduced chemical dynamics. *Ann Rev Phys Chem* 63:325
15. Brändas EJ (2013) Arrows of time and fundamental symmetries in chemical physics. *Int J Quantum Chem* 113:173
16. Löwdin P-O (1967) Program. Nature of quantum chemistry. *Int J Quantum Chem* 1:1
17. Primas H (1983) Chemistry, quantum mechanics and reductionism. *Perspectives in theoretical chemistry*. Springer, Berlin
18. Sklar L (1993) Physics and chance philosophical issues in the foundations of statistical mechanics. Cambridge University Press, Cambridge
19. Nicolaides CA, Brändas EJ (eds) (2010) Unstable states in the continuous spectra, part I: analysis, concepts, methods, and results. *Adv Quantum Chem* 60:1–549
20. Moiseyev N (2011) Non-hermitian quantum mechanics. Cambridge University Press, New York
21. Balslev E, Combes JM (1971) Spectral properties of many-body Schrödinger operators with dilatation-analytic interactions. *Commun Math Phys* 22:280
22. Simon B (1973) The definition of molecular resonance curves by the method of exterior complex scaling. *Ann Math* 97:247
23. Hehenberger M, McIntosh HV, Brändas E (1974) Weyl's theory applied to the Stark effect in the hydrogen atom. *Phys Rev A* 10:1494
24. Brändas E, Froelich P (1977) Continuum orbitals, complex scaling and the extended Virial theorem. *Phys Rev A* 16:2207
25. Howland JS (1983) Complex scaling of ac Stark Hamiltonians. *J Math Phys* 24:1240
26. Löwdin P-O (1955) Quantum theory of many-particle systems. I. Physical interpretations by means of density matrices, natural spin orbitals, and convergence problems in the method of configuration interaction. *Phys Rev* 97:1474
27. Coleman AJ, Yukalov VI (2000) Reduced density matrices. Coulson's challenge. *Lecture notes in chemistry*, vol 72. Springer, Berlin
28. Yang CN (1962) Concept of off-diagonal long-range order and the quantum phases of liquid helium and of superconductors. *Rev Mod Phys* 34:694
29. Coleman AJ (1963) Structure of fermion density matrices. *Rev Mod Phys* 35:668
30. Sasaki F (1965) Eigenvalues of fermion density matrices. *Phys Rev* 138B:1338
31. Brändas EJ, Chatzidimitriou-Dreismann CA (1991) On the connection between certain properties of the second-order reduced density matrix and the occurrence of coherent-dissipative structures in disordered condensed matter. *Int J Quantum Chem* 40:649
32. Prigogine I (1980) *From being to becoming*. Freeman W. H. Freeman and Company, San Francisco
33. Obcemea CH, Brändas EJ (1983) Analysis of Prigogine's theory of subdynamics. *Ann Phys* 151:383
34. Brändas E, Hessmo B (1998) Indirect measurements and the Mirror Theorem: a Liouville formulation of quantum mechanics. In: Bohm A, Doeblner H-D, Kielanowski P (eds) *Irreversibility and causality. Semigroups and rigged hilbert spaces. Lecture notes in physics*, vol 504, p 359
35. Karlsson EB, Brändas EJ (1998) Modern studies of basic quantum concepts and phenomena, In: Karlsson EB, Brändas E (eds) *Proceedings nobel symposium*, vol 104. World Scientific Publishing, Singapore, p 7
36. Brändas E, Elander N (eds) (1989) *Resonances: the unifying route towards the formulation of dynamical processes—Foundations and applications in nuclear, atomic and molecular physics*. *Lecture notes in physics*, vol 325. Springer, Berlin, pp 1–564
37. Mayr E (1974) *Teleological and teleonomic: a new analysis*. Boston Studies in the Philosophy of Science 14:91
38. Mayr E (2004) *What makes biology unique?*. Cambridge University Press, New York
39. Löwdin P-O (1965) Quantum genetics and the aperiodic solid. Some aspects on the biological problems of heredity, mutations, aging, and tumours in view of the quantum theory of the DNA molecule. *Adv Quantum Chem* 2:213

40. Brändas EJ (1995) Relaxation processes and coherent dissipative structures. In: Lippert E, Macomber JD (eds) *Dynamics during spectroscopic transitions*. Springer, Berlin, p 148
41. Brändas EJ (1995) Applications of CSM theory. In: Lippert E, Macomber JD (eds) *Dynamics during spectroscopic transitions*. Springer, Berlin, p 194
42. Zubarev DN (1960) Double-time green functions in statistical physics. Sov Phys Usp 3:320
43. Kandel ER (2006) *In search of memory the emergence of a new science of mind*. W. W. Norton & Company, New York
44. Brändas EJ (2012) Time asymmetry and the evolution of physical laws. In: Hoggan PE, Brändas EJ, Maruani J, Piecuch P, Delgado-Barrio G (eds) *Advances in the theory of quantum systems in chemistry and physics. Progress in theoretical chemistry and physics*, vol 22. Springer, Berlin, p 3
45. Rinaldi M (2012) Aspects of quantum gravity in cosmology. *Mod Phys Lett A* 7:1230008
46. Berman MS (2009) On the zero-energy universe. *Int J Theor Phys* 48(11):3278
47. Maruani J (2013) The Dirac electron as a massless charge spinning at light speed: implications on some basic physical concepts. In: Hotokka M, Maruani J, Brändas EJ, Delgado-Barrio G (eds) vol. 27. Springer, Dordrecht, p 53

Index

A

Absolutely continuous spectrum, 260
Absorption cross section, 42
Accessible surface, 121, 122
Adiabatic approach, 135, 137, 139
Adiabatic broadening, 69, 70
Adiabatic potentials, 138, 141
Adiabatic theory
 coupled channel equations, 137
 instantaneous solutions, 137
 photodissociation rates, 140
Aether, 22
Alzheimer's disease, 116
AMBER Force Field
 Generalized (GAFF), 117
Analytic dilation technique, 260
Anandamide, 115–119, 121–123, 125–127
Angular momentum, 46, 159–165, 167, 168, 170–174, 219, 224–227, 235–237, 240, 243, 249, 253, 278–281
Anticancer, 91
Anticommutator, 266
Antisymmetrized Geminal Power, 263
Anti-Wronscian, 209, 210
Arrow of time, 248
Artificial intelligence, 249, 254
Aufbau principle, 4, 8
Axial chirality, 160

B

Bands, 183
Bathochromic shift, 77, 78, 84, 86–88
Bias chart, 257
Biological teleonomic processes, 270
Biomolecular homochirality, 249
Bispherical coordinate system, 29–31, 36
Black hole, 249
Bloch equation, 266
Born–Oppenheimer approximation, 265

Bose-Einstein condensate, 225

Bosonic condensate, 279
BSSE using the counterpoise method, 94

C

Cannabinoid receptors, 116
Car-Parrinello PIMD algorithm, 81
CASPT2, 7
Catalytic triad, 116
Causality, 260
Cellular Q-value, 273
Chemical synapses, 277
Chiral aromatic molecules, 160
Circularly polarized photons, 241
Circularly polarized UV laser pulses, 160
Coherent, 117, 159–162, 165–172, 174, 187, 241, 269, 272
Coherent-dissipative structures, 272
Coherent ring current, 167, 174
Coleman-Sasaki theorem, 263
Collisional shift
 temperature dependence, 70
Communication protocol, 275
Compton angular frequency, 225, 226, 229
Compton wavelength, 225, 227, 234, 236, 238, 243
Conclusion, 145
Conduction band transitions, 38
Configuration interaction (CI)
 SAC-CI, 147–156
Confined photon, 237
Conical intersections, 255
Conjugate gradient method, 41
Conjugate operators, 247, 252, 278
Conjugate variables, 249
Contact surface, 122–124, 126
Continuum pressure effects, 73
Convoluted spectrum, 152
Correlated dissipative ensemble, 267

- Corresponding anticommutator, 266
 Coupled cluster, 6, 20
 CCSD(T), 6
 T1 and D1 diagnostics, 7
 Curvature of spacetime, 219, 227–229, 243
- D**
 Damped dipole, 41
 Dark energy, 248
 Darwinian evolution, 248
 de Broglie waves, 233
 Density functional theory (DFT), 37
 local density approximation (LDA)
 Pade LDA model, 46
 B3LYP, 8, 22–24, 26, 80, 84, 91–95, 97,
 99–105, 107–109, 149, 165
 M06, 8, 22, 24, 25
 M11, 8, 22, 25, 26
 PBE0, 8, 22–24, 26
 frequency domain (FD-TDDFT), 37, 40,
 42–44, 50
 real-time TDDFT, 40
 time-dependent Kohn-Sham equations, 39,
 40
 Density matrix
 reduced, 264, 271
 Density matrix element, 162, 163
 Density of states, 37, 44–46
 Dephasing, 41, 162, 167
 Dephasing constant, 162, 167
 Diabatic functions, 141
 1,1-diamino-2,2-dinitroethylene (FOX-7 or
 DADNE), 149
 Diatomic, 7–9
 Diffusion, 178, 180, 181, 183, 187–191, 280
 Diffusion broadening, 188, 189
 Diffusion rate, 189–191
 Dipole wave in spacetime, 222, 237, 243
 Dirac equation with complex energy, 201
 Dirac-Kohn-Sham-like equations, 197
 Dirac-Sturm approach, 65, 67
 Direct inversion of iterative subspace (DIIS), 5
 Dissipative system, 277
 Distortion of the spacetime, 228, 236, 243
 Drug-design, 117
 Dynamic polarizability, 61, 62
 Dynamic dissociation quenching, 139
 Dynamical structure factor, 178
- E**
 Effective barrier for the diffusion, 189
 Effective ring current, 165
- Einstein’s laws of general relativity, 253
 Einstein’s laws of special and general relativity,
 249
 Electron correlation, 148
 Electron-hole pairs, 178
 Electronic coherence, 166, 167, 170, 174
 Electronic state, 5, 18, 22, 23, 25
 Electronic state density, 44
 Electrostatic force, 219, 230–234
 Energetic materials, 147
 Energetic vacuum, 220
 Energy density, 221–228, 234, 240, 241, 243,
 244
 Entropy, 281
 Evolution comprises teleomatic, 249
 Exchange-correlation effects, 57, 67, 68, 71
 Exchange perturbation theory, 55–59, 71, 73
 Excited state, 6, 8, 17, 23–26, 148
 Explosives, 147, 148
 Explosophore, 148
 Extended Hartree-Fock, 4
- F**
 Fatty Acid Amide Hydrolase (FAAH),
 115–118, 120, 121, 124–126
 Feynman diagrams, 198
 Feld-assisted nuclear dynamics, 136
 Finite difference method, 83
 First ionization potential, 155
 Floquet theorem, 140
 Floquet theory
 coupled channel equations, 140
 quasi-adiabatic formulation, 140–144
 direct solution of the time-dependent
 Schrodinger equation, 144–145
 Fluctuations of spacetime, 221, 223
 Foley law, 70, 73
 Free energy configuration, 267
 Free energy of solvation, 94, 108, 109
 Frequency domain (FD-TDDFT), 40
- G**
 Gaussian basis set, 42, 149
 Geminals, 262, 263
 General relativity, 219, 228, 248, 249, 252, 253
 Geometry of spacetime, 232
 Gepol model, 93
 Gödel paradox, 249
 Gödel’s incompleteness theorem, 248
 Gödelian arrow of time, 277
 Gold clusters, 38, 39
 Governing teleomatic processes, 278

- Genetic code, 249
 Geometric description, 29
 Gravitational, 4–6, 11–17, 22, 23, 25
 Gravitational force, 219, 229, 230–234, 244
 Gravitational interactions, 277
 Gravitational waves, 222, 223, 240, 241, 244
 Green operator, 65
 Green's function method
 electron Green's function, 198, 199, 213
 electron radial Green's function, 203
 propagator, 198, 208
 two-time Green's function, 199
 Ground state, 4–6, 11, 14, 15, 23, 25
 Group velocity, 251
- H**
 Hartree-Fock, 3–5, 7, 26
 instability, 4
 Multiconfiguration Time Dependent, 177, 181
 multiple stable solutions, 27
 restricted (RHF, ROHF), 8
 Unrestricted (UHF, UOHF), 8
 Heterogeneous broadening, 38
 Homogeneous spacetime field, 226
 Hot electron, 49
 Hot electron population, 49
 Huntington's disease, 116
 Hydrogen bond, 77, 78, 80, 82, 91, 92, 95, 96, 99, 108, 112, 113, 115, 117, 123, 125–127
 Hydrogen bonding, 78, 92, 125, 127
 Hydrophobic character, 108, 110
 Hyperfine interaction hamiltonian, 58
 Hyperfine structure, 55–59, 70, 73
 Hypsochromic shift, 85, 86
- I**
 Impedance of spacetime, 1, 5, 26
 Induced dipole resulting, 39
 Inertial force, 238
 Inner ionizations, 152
 Integral Equation Formalism model (IEF), 93
 Intensity parameter, 276, 277
 Interband transition, 37, 38, 43–45, 47, 49, 50
 Inter-focal separation, 31, 33
 Intermediate scattering function (ISF), 177, 191
 Intraband transition, 43, 45–47, 49, 50
 Intrinsic energy broadening, 178
 Inverse points, 31
 Ionization processes, 147, 148
- Ionization potential (I.P.), 150
 Iterative Lanczos (SIL) integrator, 181
- J**
 Jellium model, 39, 41, 45, 46
 Jordan block, 253, 258, 269–271, 272, 281
- K**
 Kerr metric, 248, 254
 Klein-Gordon-like equation, 251
 Koopmans' theorem, 150, 152, 154
- L**
 Linear response, 42
 Liouville equation, 264, 265
 Living system (in vivo), 271
 Lorentzian, 179
 Löwdin's symmetry dilemma, 27
- M**
 Markov approximation, 160, 162
 Matter-antimatter asymmetry, 281
 Maximum Overlap Method (MOM), 8, 17, 18, 25
 MCSCF, 7
 Michelson-Morley experiment, 240, 241
 Molecular chirality, 260
 Møller-Plesset perturbation theory, 92
 Monopole approximation, 147–152, 154, 156
 Muchimangin B, 91–93, 95–99, 102, 103–105, 109, 112, 113
 Multiconfigurational time-dependent Hartree, 181
 Multireference methods, 3, 7
- N**
 Newton-Raphson (NR), 5
 N,N-dimethylnitramine, $(\text{CH}_3)_2\text{NNO}_2$, 149
 Nitramide, H_2NNO_2 , 149
 Nilpotent operator, 269
 Nitro compounds, 147, 148
 Nitromethane, 151
 NO_2 group, 148
 Non-adiabatic chemistry, 255
 Non-equilibrium statistical mechanics, 261, 249
 Non-Hermitian quantum mechanics, 259, 260
 Non-Hermitian hamiltonians, 146
 Nonplanar aromatic ring molecules, 174
 Nonplanar chiral aromatic molecule, 160, 165

N-representable representation, 264
Nuclear finite size effect, 213

O

Off-diagonal correlations, 273
Off-Diagonal Long-Range Order (ODLRO), 262, 278
Organic electronic devices, 160
Oscillator strengths, 208

P

Pairwise interactions, 29, 30
Paradigm of evolution, 249, 278
Parallel universe, 248
Parkinson's Disease, 116
Particle-antiparticle pairs, 279
Path Integral Molecular Dynamics (PIMD), 79, 81
 π -electron ring current, 159–161
Photoelectron cross sections, 148
Photoionization, 148
Photon propagator, 208
Plasmonic, 37
Pixelation model of spacetime, 222
Planck amplitude, 222–226, 236, 238
Planck amplitude waves, 222, 224, 225, 226
Planck charge, 230, 232–234, 238
Planck force, 231, 232, 240, 244
Planck length, 221, 223, 224, 227, 241, 243
Planck time, 221, 223, 224, 243
Plane wave basis sets, 41
Plasmonic nanoparticles, 38
Poisson distribution, 273, 277
Poisson statistics, 275
Polarisable Continuum Model (PCM), 93, 97, 104, 105, 108
Polarizability, 39, 41, 42, 61, 62, 66, 70
Polarized distortion of spacetime, 239
Potential energy curve (PEC), 4, 6, 8, 11, 18, 25, 26
Prigogine energy superoperator, 266
Propellants, 147
Propositional logics, 255
Proton quantum confinement, 86
Protonated ammonia dimer, 79
Pseudopotential, 39, 40–42, 45, 46, 50, 81

Q

QM/MM calculations, 117, 126
Quantitative Structure Activity Relationship (QSAR), 106
Quantum beat, 169
Quantum chromodynamics, 221

Quantum-classical dichotomy, 00
Quantum confinement, 86, 88
Quantum electrodynamics, 221, 243
Quantum switching, 159, 161, 170, 172
Quantum wave packet, 178
Quasi-adiabatic solutions, 137, 140
Quasi-elastic broadening, 178
Quasiparticles, 207

R

Radial distribution function, 115, 118, 122, 124, 125, 127
Radiation pressure, 223
Random phase approximation, 42
Rayleigh–Schrodinger perturbation theory, 56
Reaction cross section, 280
Real-time TDDFT, 40
Relativistic Dirac–Kohn–Sham, 66
Relativistic electrons, 235
Relativistic many-body perturbation theory, 57, 62, 64
Relativistic mean-field nuclear potential, 200
Relativistic orbitals, 57, 63, 71
Relativistic perturbation theory, 55, 73
Relativistic quantum chemistry, 199
Relaxation, 41, 155, 178, 190, 267, 280
Response function, 42, 49, 50
Ring current, 159–161, 165–169, 174
RMF model, 203, 204

S

Satellite or correlation peaks, 154
Schwarzschild line element, 253
Schwarzschild metric, 248, 249
Schwarzschild radius, 242, 254
Second law, 260
Segré characteristics, 252
Self-energy, 197, 199–201, 212, 213
Self-organisation, 248
SHAKE algorithm, 118
Short iterative Lanczos, 181
Silver clusters, 37–40, 42
Solute-solvent interactions, 108
Solvent Accessible Surface Accessible Area (SASA), 115, 117, 118, 121, 122, 124
Solvent polarity, 92, 108, 110
Spacetime field, 2, 4, 6, 7, 9, 10, 15–18, 20, 22, 25, 220, 222, 224, 226, 227, 228, 233–236, 238, 240, 241, 243, 244
Spacetime model, 221, 225, 227, 229, 231, 235, 236, 238, 243
Spatio-temporal mnemonic entity, 249, 272

Spectral decomposition, 261
Spectral line profiles, 56
Spectral lines shape, 58
Sphere-sphere interactions, 29
Spin contamination, 11, 12, 18
Spin flip method, 6, 7
Static polarizability, 70
Strain amplitude, 223, 225, 226, 228, 230, 231
Sturm expansions, 66
Sturm orbitals, 62
Superconductors, 279
Super-operator, 265
(2×2) surface cell, 181
Surface enhance Raman spectroscopy, 38
Surface-to-surface separation, 29–36
Symmetry-Adapted-Cluster (SAC), 147–149
Symmetry-Adapted-Cluster Configuration Interaction (SAC-CI), 149
Symmetry violations, xix
Synchrotron radiation, 148

T

Teleomatic- and teleonomic physical laws, 249
Teleodynamic encodings, 277
Theory of consciousness, 249
Theory of everything, 2, 220, 248
Time-dependent coherent ring currents, 159, 174
Time-dependent density functional theory (TDDFT), 39
Time-dependent dipole moment, 41
Time-dependent Schrödinger equation, 135, 136
Time evolution of the ring currents, 167
Transition dipole moment, 136, 162, 166
Transition metal diatomics, 14
Tunneling, 188, 189, 191

Two-dimensional quantum switching, 161
Two-dimensional switching, 174

U

Ultimate ensemble, 248
Ultrafast quantum switching, 172
Uncertainty principle, 220–222, 236
Unification of forces, 13
United Atom Topological Model, 93
Unstable states in the continuum, 261

V

Vacuum fluctuations, 220
van der Waals coefficient, 59, 61
van der Waals constants, 55, 58, 61, 62, 67, 68, 71, 73
van der Waals interactions, 122
Van Hove formula, 179
Vibrational lifetimes, 178, 190
Vibrational predissociation, 78
Virtual particles, 198

W

Ward identities, 200
Whittaker functions, 199
Wronskian, 203, 209, 210
Wavefunction, 7, 14, 148

X

Xanthone derivatives, 91

Z

Zero-Energy Universe Scenario (ZEUS), 247–249, 259
Zero Point Energy (ZPE), 2, 25, 94, 268